Since 1955

Strojniški vestnik
Journal of Mechanical Engineering

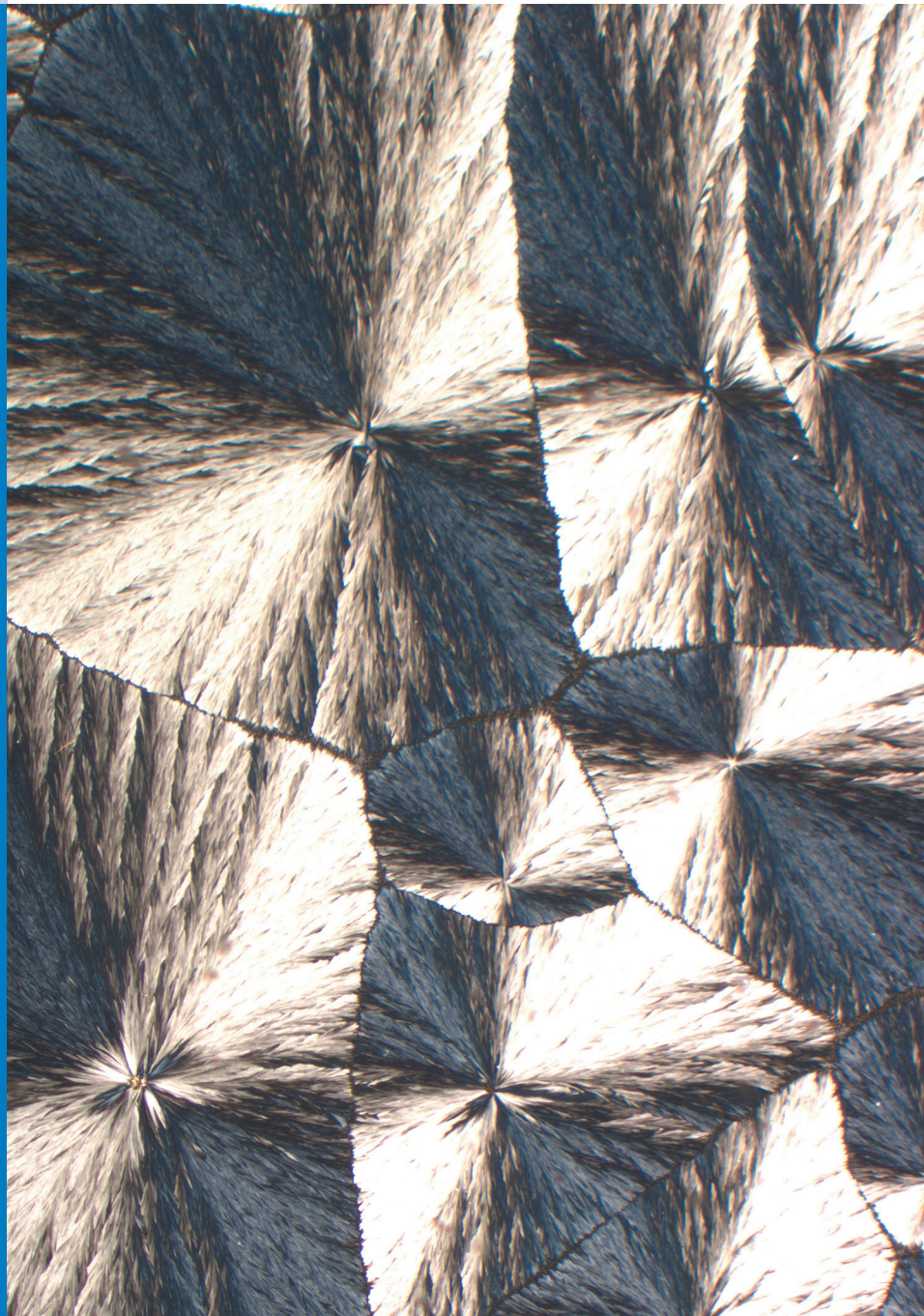

no. 9
year 2021
volume 67

Strojniški vestnik – Journal of Mechanical Engineering (SV-JME)

Aim and Scope

The international journal publishes original and (mini)review articles covering the concepts of materials science, mechanics, kinematics, thermodynamics, energy and environment, mechatronics and robotics, fluid mechanics, tribology, cybernetics, industrial engineering and structural analysis.

The journal follows new trends and progress proven practice in the mechanical engineering and also in the closely related sciences as are electrical, civil and process engineering, medicine, microbiology, ecology, agriculture, transport systems, aviation, and others, thus creating a unique forum for interdisciplinary or multidisciplinary dialogue.

The international conferences selected papers are welcome for publishing as a special issue of SV-JME with invited co-editor(s).

Editor in Chief

Vincenc Butala

University of Ljubljana, Faculty of Mechanical Engineering, Slovenia

Technical Editor

Pika Škraba

University of Ljubljana, Faculty of Mechanical Engineering, Slovenia

Founding Editor

Bojan Kraut

University of Ljubljana, Faculty of Mechanical Engineering, Slovenia

Editorial Office

University of Ljubljana, Faculty of Mechanical Engineering

SV-JME, Aškerčeva 6, SI-1000 Ljubljana, Slovenia

Phone: 386 (0)1 4771 137

Fax: 386 (0)1 2518 567

info@sv-jme.eu, http://www.sv-jme.eu

Print: Demat d.o.o., printed in 250 copies

Founders and Publishers

University of Ljubljana, Faculty of Mechanical Engineering, Slovenia

University of Maribor, Faculty of Mechanical Engineering, Slovenia

Association of Mechanical Engineers of Slovenia

Chamber of Commerce and Industry of Slovenia, Metal Processing Industry Association

President of Publishing Council

Mitjan Kalin

University of Ljubljana, Faculty of Mechanical Engineering, Slovenia

Vice-President of Publishing Council

Bojan Dolšak

University of Maribor, Faculty of Mechanical Engineering, Slovenia

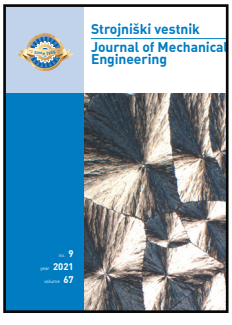

Cover: SEMI-CRYSTALLINE STRUCTURE OF POLYPROPYLENE POLYMER. Some polymers form partially crystalline structures when cooled from the melt. The size and density of the crystals, to a large extent, determine the polymer materials' physical properties. The crystalline structure and, consequently, the properties can be controlled during polymer production (cooling). This means that the same polymer can be made in a way that will be almost completely transparent or completely opaque and that it can show either ductile or brittle behaviour. The figure shows a polypropylene material made with a polarized microscope. Rather large crystals (~ 1mm) formed when polymer melt was gradually cooled to ambient temperature.

Image Courtesy: Marko Bek, PhD, University of Ljubljana, Faculty of Mechanicaal Engineering, Laboratory for Experimental Mechanics

ISSN 0039-2480, ISSN 2536-2948 (online)

International Editorial Board

Kamil Arslan, Karabuk University, Turkey
Hafiz Muhammad Ali, King Fahd U. of Petroleum & Minerals, Saudi Arabia
Josep M. Bergada, Politechnical University of Catalonia, Spain
Anton Bergant, Litostroj Power, Slovenia
Miha Boltežar, University of Ljubljana, Slovenia
Filippo Cianetti, University of Perugia, Italy
Janez Diaci, University of Ljubljana, Slovenia
Anselmo Eduardo Diniz, State University of Campinas, Brazil
Igor Emri, University of Ljubljana, Slovenia
Imre Felde, Obuda University, Faculty of Informatics, Hungary
Imre Horvath, Delft University of Technology, The Netherlands
Aleš Hribernik, University of Maribor, Slovenia
Soichi Ibaraki, Kyoto University, Department of Micro Eng., Japan
Julius Kaplunov, Brunel University, West London, UK
Iyas Khader, Fraunhofer Institute for Mechanics of Materials, Germany
Jernej Klemenc, University of Ljubljana, Slovenia
Milan Kljajin, J.J. Strossmayer University of Osijek, Croatia
Peter Krajnik, Chalmers University of Technology, Sweden
Janez Kušar, University of Ljubljana, Slovenia
Gorazd Lojen, University of Maribor, Slovenia
Darko Lovrec, University of Maribor, Slovenia
Thomas Lübben, University of Bremen, Germany
George K. Nikas, KADMOS Engineering, UK
Tomaž Pepelnjak, University of Ljubljana, Slovenia
Vladimir Popović, University of Belgrade, Serbia
Franci Pušavec, University of Ljubljana, Slovenia
Mohammad Reza Safaei, Florida International University, USA
Marco Sortino, University of Udine, Italy
Branko Vasić, University of Belgrade, Serbia
Arkady Voloshin, Lehigh University, Bethlehem, USA

General information

Strojniški vestnik – Journal of Mechanical Engineering is published in 11 issues per year (July and August is a double issue).

Institutional prices include print & online access: institutional subscription price and foreign subscription €100,00 (the price of a single issue is €10,00); general public subscription and student subscription €50,00 (the price of a single issue is €5,00). Prices are exclusive of tax. Delivery is included in the price. The recipient is responsible for paying any import duties or taxes. Legal title passes to the customer on dispatch by our distributor. Single issues from current and recent volumes are available at the current single-issue price. To order the journal, please complete the form on our website. For submissions, subscriptions and all other information please visit: *http://www.sv-jme.eu.*

You can advertise on the inner and outer side of the back cover of the journal. The authors of the published papers are invited to send photos or pictures with short explanation for cover content.

We would like to thank the reviewers who have taken part in the peer-review process.

© 2021 Strojniški vestnik - Journal of Mechanical Engineering. All rights reserved. SV-JME is indexed / abstracted in: SCI-Expanded, Compendex, Inspec, ProQuest-CSA, SCOPUS, TEMA. The list of the remaining bases, in which SV-JME is indexed, is available on the website.

The journal is subsidized by Slovenian Research Agency.

Strojniški vestnik - Journal of Mechanical Engineering is available on *https://www.sv-jme.eu*.

Contents

Strojniški vestnik - Journal of Mechanical Engineering
volume 67, (2021), number 9
Ljubljana, September 2021
ISSN 0039-2480

Published monthly

Papers

Khurram Ali, Adeel Mehmood, Israr Muhammad, Sohail Razzaq, Jamshed Iqbal: Control of an Anthropomorphic Manipulator using LuGre Friction Model - Design and Experimental Validation 401
Dragan Milčić, Amir Alsammarraie, Miloš Madić, Vladislav Krstić, Miodrag Milčić: Predictions of Friction Coefficient in Hydrodynamic Journal Bearing Using Artificial Neural Networks 411
Almatbek Kydyrbekuly, Gulama-Garip Alisher Ibrayev, Tangat Ospan, Anatolij Nikonov: Multi-parametric Dynamic Analysis of a Rolling Bearings System 421
Youyu Liu, Yi Li, Xuyou Zhang, Bo Chen: Trajectory-Tracking Control for Manipulators Based on Fuzzy Equivalence and a Terminal Sliding Mode 433
Yanxiong Liu, Yuwen Shu, Wentao Hu, Xinhao Zhao, Zhicheng Xu: Active Vibration Control of a Mechanical Servo High-speed Fine-Blanking Press 445
Xuan Bo Tran: Nonlinear Control of a Pneumatic Actuator Based on a Dynamic Friction Model 458

Strojniški vestnik - Journal of Mechanical Engineering 67(2021)9, 401-410
© 2021 Journal of Mechanical Engineering. All rights reserved.
DOI:10.5545/sv-jme.2021.7258 Original Scientific Paper
Received for review: 2021-05-28
Received revised form: 2021-08-17
Accepted for publication: 2021-08-18

Control of an Anthropomorphic Manipulator using LuGre Friction Model - Design and Experimental Validation

Khurram Ali [1] - Adeel Mehmood [1] - Israr Muhammad [1] - Sohail Razzaq [2] - Jamshed Iqbal [3,*]
[1]COMSATS University Islamabad, Department of Electrical and Computer Engineering, Islamabad, Pakistan
[2]COMSATS University Islamabad, Department of Electrical and Computer Engineering, Abbottabad, Pakistan
[3]University of Hull, Faculty of Science and Engineering, Department of Computer Science and Technology, Hull, UK

Automation technology has been extensively recognized as an emerging field in various industrial applications. Recent breakthrough in flexible automation is primarily due to deployment of robotic arms or manipulators. Autonomy in these manipulators is essentially linked with the advancements in non-linear control systems. The objective of this research is to propose a robust control algorithm for a five degree of freedom (DOF) robotic arm to achieve superior performance and reliability in the presence of friction. A friction compensation-based non-linear control has been proposed and realized for the robotic manipulator. The dynamic model of the robot has been derived by considering the dynamic friction model. The proposed three-state model is validated for all the joints of the manipulator. The integral sliding mode control (ISMC) methodology has been designed; the trajectories of system every time begin from the sliding surface and it eliminates the reaching phase with assistance of integral term in the sliding surface manifold. The designed control law has been first simulated in Matlab/Simulink environment to characterize the control performance in terms of tracking of various trajectories. The results confirm the effectiveness of the proposed control law with model-based friction compensation. The transient parameters like settling and peak time have improvement as well have better results with friction than without considering the friction. The proposed control law is then realized on an in-house developed autonomous articulated robotic rducational platform (AUTAREP) and NI myRIO hardware interfaced with LabVIEW. Experimental results also witnessed the trajectory tracking by the robotic platform.

Keywords: robotic manipulator, lugre friction model, sliding mode control

Highlights

- *A dynamic model of robot manipulator is presented in this work by considering the friction between the joints.*
- *Dynamic LuGre model is used for friction which reflects the real friction phenomenon by considering stick-slip motion and stribeck effect.*
- *Sliding mode control technique is used to design the control law using Lyapunov stability theorem.*
- *Controller performance is evaluated with and without friction compensation in Matlab.*
- *Proposed controller is also tested on experimental test bench using NI myRio 1900 and AUTAREP robot system.*

0 INTRODUCTION

Robotic arms are playing a pivotal role in today's industrial world [1]. The industrial automation methods are majorally affected by the development in the field of robotics. Robotic arms are basically the mechanical replication of the human body arm. Research shows that they can outperform the humans in terms of strength, precision, speed and repeatability, thus, they can save time with improved performance [2]. Owing to these concrete reasons, robotic arms have acquired an invaluable place in industry [3]. To achieve high precision in robotic manipulators, friction in joints is the major limitation [4]. A manipulator, being inherently non-linear in nature, can demonstrate steady-state error and limit cycles and hence may suffer from degraded performance [5]. It affects both dynamic and static performances and can results in instability due to coupling effects. Henceforth, joint friction compensation in robot has been one of the major research problem in control design throughout the years. Friction is one of the main reasons of unwanted effects and system performance degradation [6]. Friction is a force which mostly occurs in moving systems exhibiting a complex phenomenon and can be divided into two types. The first type is known as static friction F_s which is often defined for the bodies at rest. The other type is known as dynamic friction which occurs when one body is moving with respect to some other body in contact. It is further divided into three components. One component is recognized as sliding friction and others are rolling and pivot friction [7].

Static friction models like Karnopp model are difficult to implement while simulating the dynamic systems [8]. The dynamic friction models established so far cover majority of non-linear phenomena and they exhibit continuous behavior when the velocity is zero. These characteristics make the dynamic models more useful and convenient for software simulations and analysis of control algorithms. It is known that some of the foremost restrictions to realize

*Corr. Author's Address: Department of Computer Science and Technology, Faculty of Science and Engineering, University of Hull, HU6 7RX, UK, j.iqbal@hull.ac.uk

admirable breakthrough in mechanical frameworks is the presence of friction, which is a non-linear phenomenon and hard to depict analytically [9]. Friction should be taken into account at an early stage throughout the system design by reducing it at probable minimum limit through careful design. Moreover, research shows that most of the dynamic models developed so far are incapable to capture the real friction phenomenon experienced by surfaces in contact [10]. The LuGre friction model is used in the current research since it describes important friction behaviour and characteristics such as stick-slip motion and stribeck effect etc. [11]. While demonstrating advantages of friction modelling, the LuGre friction model can result in numerically stiff and tough system dynamics. Moreover, the LuGre model performs like a linear spring pair when it is linearized for small motions. For a control engineer, it is suitable to analyse the impact of friction on the feedback system in order to design a control law that reduces the effect of friction.

In robotics, non-linear, centralized trajectory tracking refers to the input torque computation which guarantees precise tracking of reference trajectory. The research community has suggested numerous control approaches varying from simple linear feedback control to sophisticated algorithms. Sliding mode control (SMC) is one of the robust non-linear control techniques based on principle of the variable structure control theory. The key features of SMC include system robustness [12] and its stability against matched uncertainties [13]. The dynamics of a robotic manipulator having multi-DOF is complicated and highly non-linear [14]. The position of a single joint and its two higher derivatives have a strong impact on all joints of robotic manipulator. Moreover, gravity, external forces, modelling uncertainties, and friction can impact the robot motion. The state-of-the-art research works have been reported in the literature on robotic manipulator that uses friction models instead of a disturbance. An adaptive robust control (ARC) algorithm has been proposed for an electric cylinder with the LuGre friction model in [15] and the Lyapunov approach has been suggested for system stability and ARC handles external disturbances. In [16], to lessen the impact of estimation errors the robust sliding mode controller with an adaptive block compensation controller is proposed. The inverted pendulum and planar multi-joint robot with friction model are used to validate the controller. Authors in [17] used adaptive ISMC with time-delay estimation.

In this paper, an ISMC for anthropomorphic manipulator based on modified LuGre model with friction compensation is proposed. The following is a brief description of the main contribution:

- Mathematical model of AUTAREP robotic manipulator is centered on a five DOF has been derived by considering the kinematics and dynamics of the robot manipulator, as well as the LuGre friction model.
- Robust controller has been designed to compensate the dynamic friction behaviors and drive the position and speed to track the desired trajectories. The integral sliding mode control (ISMC) law, which is based on the Lyapunov function, is used to compensate for the system's parametric and load torque uncertainties.
- The proposed control law is then implemented on a custom developed platform using LabVIEW interface with NI myRIO hardware having motors driving circuits.

This article is organised as follows; Section 1 derives the mathematical model of a single joint along with LuGre friction model. In Section 2, SMC based control law is designed. After the control design, in section 3, outcomes of control design have been analysed and experimental results are discussed. Section 4 concludes the article.

1 MATHEMATICAL MODELLING

A robotic manipulator usually consists of servo motors, optical encoders, and one or more controllers. The robotic manipulator used for research and analysis in the current research is AUTAREP ED-7220C [18] shown in Fig. 1. The robotic manipulator has five degrees of movement actuated with DC servo motors. A single motor is used to move each joint except the wrist joint where pitch and roll motions are controlled by two motors. The model characterizes an extremely non-linear system since velocities as well as positions of links are coupled dynamically. For feedback from joints, the robotic arm has optical encoders mounted on each joint servo motor axis, which provides information about its position. An adequate motion control algorithm could be accomplished through mathematical modelling by considering the dynamics of the robot manipulator.

Kinematics of a robot gives the relationship between joint angles/translations and the location (position and orientation) of its end-effector [19]. The kinematic model of the manipulator established on

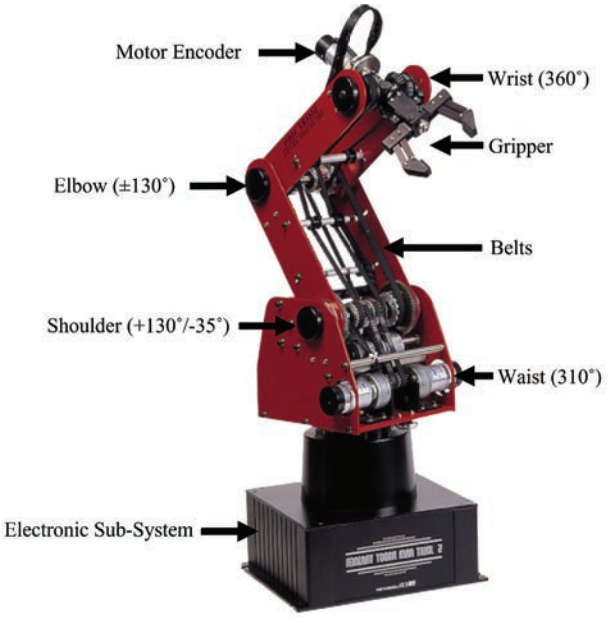

Fig. 1. *AUTAREP Manipulator ED-7220C with joints corresponding range of motions*

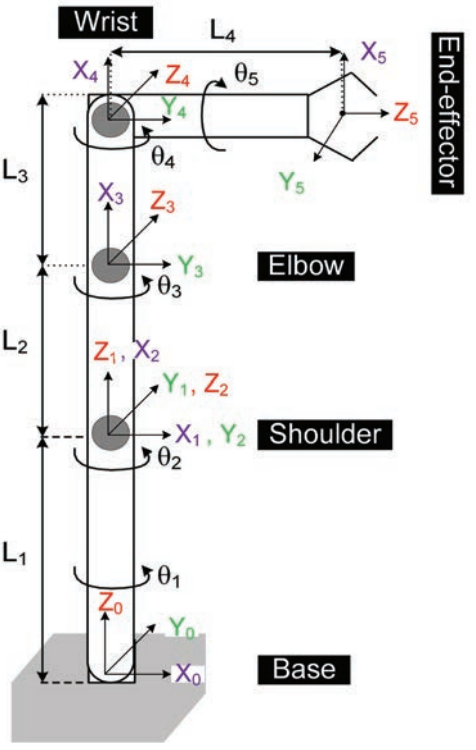

Fig. 2. *Kinematic representation of the robotic arm where ($L_1 =$ 385 mm, $L_2 =$ 220 mm, $L_3 =$ 220 mm, $L_4 =$ 155 mm)*

Denavit-Hartenberg (D-H) parameters is reported in [**20**]. The process of modelling the robot dynamics involves derivation of velocities and inertia matrices, computation of kinetic and potential energies and final formulation of torque equation [**21**]. Each link of the manipulator is considered as a set of number of elements for which potential and kinetic energies are developed. In the present research work, the Lagrangean approach is used for the formulation of dynamics [**22**]. Fig. 2 illustrates the kinematic representation of AUTAREP manipulator. In order to function motors, the model should be able to evaluate the joint torques which are system control input [**23**]. The manipulator's dynamic equation is given by Eq. (1):

$$\tau_f = M(q_i)\,\ddot{q}_i + C_c(q_i,\dot{q}_i)\,\dot{q}_i + G(q_i) + T_f(\dot{q}_i), \quad (1)$$

where for n joints, $M(q_i) \in R^{n\times n}$ is the mass/inertial matrix, $C_c(q_i) \in R^{n\times n}$ represents the coriolis and centripetal forces, $G(q_i) \in R^{n\times 1}$ is the gravitational matrix, $T_f(\dot{q}_i) \in R^{n\times 1}$ represents friction torques. The term $\tau_f \in R^{n\times 1}$ is the vector of input torques applied to the joints of the robot. Friction is one of the major causes of undesirable effects. Numerous dynamic models for friction have been suggested in literature, including the Dahl model and LuGre model [**24**], etc.

The dynamic Dahl friction model forms the origin of the LuGre friction model and is an integrated dynamic model of friction. However, it does not consider all the non-linear phenomena caused by friction. In the literature, it has been shown that static models cannot capture certain characteristics of true frictional phenomena that are experimentally seen in high friction systems. Therefore, LuGre model of friction is a dynamic friction model related to the bristle interpretation of friction and the average deflection force of elastic springs is used to model friction. The velocity determines the average bristle deflection for a steady state motion. It is lower at low speeds, implying that steady-state deflection decreases with increasing velocity. Rate dependent friction phenomena such as varying break-away force and frictional lag are also included in the model. Therefore, the LuGre model is used here for friction modeling and is given as

$$T_f = \sigma_0\, z + \sigma_1 \dot{z} + f(v), \quad (2)$$

where $f(v) = \sigma_2 v$, z is internal friction state and the term T_f is predicted friction torque.

$$T_f = \sigma_0\, z + \sigma_1 \dot{z} + \sigma_2 v. \quad (3)$$

The dynamics of friction state z can be defined as:

$$\dot{z} = v - \sigma_0 \frac{|\,v\,|}{g\,(v)}\, z, \quad (4)$$

where $g(v)$ is given by:

$$g(v) = F_c + (F_s - F_c)\exp^{-(|v/v_s|)}. \quad (5)$$

The LuGre model can illustrate several properties of real friction, for example the limit cycle displacement in stick-slip motion. For steady-state friction measurement the functions $f(v)$ and $g(v)$ can be used. The model has a significant drawback in that, this does not take into account the dwell time effect, which implies that it cannot model variations in friction force when two surfaces are maintained in contact at rest for a set period. The LuGre model is a dynamical system with the following properties: internal state dissipativity, boundedness, I/O dissipativity with constant σ_1 and velocity-dependent $\sigma_1(v)$ [**25**]. Most of these are reasonable characteristics of a model illustrating friction. Parameters of LuGre friction model are obtained from literature [**26**] and are given in Table 1.

Table 1. *Parameters of LuGre friction model*

Parameter	Value	Unit	Description
σ_0	2750	Nm/rad	Stiffness coefficient
F_s	8.875	Nm	Static friction torque
F_c	6.975275	Nm	Coulomb friction torque
σ_1	45.2	Nm·s/rad	Damping coefficient
σ_2	1.819	Nm·s/rad	Viscous friction coefficients
v_s	$6.109 \cdot 10^{-2}$	rad/s	Velocity

Let q_1 is the position vector, q_2 is the velocity vector and z_3 is internal friction state. Thus the state-space model of a single joint can be represented by Eq. (6):

$$\begin{aligned} \dot{q}_1 &= q_2 \\ \dot{q}_2 &= M^{-1}\left(\tau_f - C_c q_2 + G q_1 + \sigma_0 z_3 + \sigma_2 q_2 + \sigma_1 \dot{z}_3\right) \\ \dot{z}_3 &= q_2 - \sigma_0 \frac{|q_2|}{g(q_2)} z_3. \end{aligned} \quad (6)$$

2 CONTROL DESIGN

SMC technique permits control of non-linear processes subjected to high model uncertainties and external disturbances [**27**]. In present research, SMC based law with friction compensation is implemented on AUTAREP manipulator. SMC law is divided into two phases i.e. the sliding phase and the reaching phase [**28**]. The system trajectories achieve the required sliding surface in the case of reaching phase, defined as:

$$\dot{q}_i = f(q_i) + g(q_i)u + \Delta(q_i, t). \quad (7)$$

The vector fields $f(q_i)$ and $g(q_i)$ are the non linear functions representing the system with matched uncertainties $\Delta(q_i, t)$. For the control design, the first step is to define a sliding surface and the whole system states are forced in such a way that the sliding surface converges to zero in a finite time and remains there as long as there is no change in reference input [**29**]. The control objective in this work is to make sure that the robot should track the predefined trajectory q_{di}. To accomplish this aim, a sliding surface based on error signal for each link is described in Eq. (8):

$$S_{si} = C_s \dot{e}_s i + \lambda_{si} e_{si} + I_{si} \int e_{si} dt, \quad (8)$$

where C_s, λ_{si} and I_{si} are positive constants. The tracking function is established for well-defined sliding surface in Eq. (8). Thus, the sliding surface will converge to zero with the applied control effort. This will ensure the tracking error e_{si} converges to the origin. The control input of SMC law comprises of two parts. The first part is equivalent control law (u_{seq}) and it is a continuous term. The second part is discontinuous control law (u_{sdis}) with the signum function.

$$u = u_{seq} + u_{sdis}. \quad (9)$$

The equivalent control input (u_{seq}) is acquired through sliding surface by considering $\dot{S}_{si} = 0$ which is obtained after taking the time derivative of Eq. (8):

$$\dot{S}_{si} = C_s \ddot{e}_{si} + \lambda_{si} \dot{e}_{si} + I_{si} e_{si}. \quad (10)$$

In SMC, the objective is accomplished by setting $\dot{S}_{si} = 0$. Substituting this value in Eq. (10):

$$0 = C_s \ddot{e}_{si} + \lambda_{si} \dot{e}_{si} + I_{si} e_{si}, \quad (11)$$

where $\dot{e}_{si} = \dot{q}_{di} - \dot{q}_i$ and $\ddot{e}_{si} = \ddot{q}_{di} - \ddot{q}_i$ are the first and second time derivatives of error function respectively. Substituting error dynamics, we get:

$$0 = C_s(\ddot{q}_{di} - \ddot{q}_i) + \lambda_{si}(\dot{q}_{di} - \dot{q}_i) + I_{si}(q_{di} - q_i), \quad (12)$$

$$\ddot{q}_i = (C_s)^{-1}\left[(\lambda_{si}(\dot{q}_{di} - \dot{q}_i) + I_{si}(q_{di} - q_i)\right] + \ddot{q}_{di}. \quad (13)$$

The equivalent control effort u_{seq} is chosen as:

$$\begin{aligned} u_{seq} = M(q_i)(C_s)^{-1}\left[(\lambda_{si}(\dot{q}_{di} - \dot{q}_i) + I_{si}(q_{di} - q_i)\right] \\ + \ddot{q}_d + (C_c)(q_i, \dot{q}_i) + G(q_i) + T_f(\dot{q}_i). \end{aligned} \quad (14)$$

In order to compensate the dynamic model uncertainties, the discontinuous function u_{sdis} is defined as given in Eq. (15):

$$u_{sdis} = -k_{si} sign(S_{si}) - \zeta S_{si}, \quad (15)$$

where k_{si} and ζ are positive constants. The equivelant control input u_{seq} drives the system from initial

state to sliding surface and ensures that $\dot{S} = 0$. However, due to different uncertainties and external disturbances the sliding surface may not converge to zero. Lyapunov stability-based method is used for analysis and control design which guarantees the system stability. For stability analysis, a positive definite Lyapunov energy-function for SMC is chosen as Eq. (16):

$$V = \frac{1}{2} S_{si}^2. \tag{16}$$

Taking derivative of Eq. (16), we obtain:

$$\dot{V} = S_{si}\dot{S}_{si}. \tag{17}$$

By substituting the value of $\dot{S}_{si}$ given in Eq. (12) and substituting u_{seq} as well u_{sdis} in Eq. (17), we get:

$$\dot{V} = S_{si}(-k_{si} sign(S_{si}) - \zeta S_{si}), \tag{18}$$

$$\dot{V} \leq -k_{si}|S_{si}| - \zeta (S_{si})^2. \tag{19}$$

The derivative of Lyapunov function $\dot{V}$, turns out to be negative semi-definite function which is sufficient condition for Lyapunov stability. Therefore, the dynamics of system will converge in finite time and the error will converge to zero for the applied input given in Eq. (20):

$$\begin{aligned} \tau_f = {} & M(q_i) {C_s}^{-1} [(\lambda_{si}(\dot{q}_{di} - \dot{q}_i) + I_{si}(q_{di} - q_i)] \\ & + \ddot{q}_{di} + C_c(q_i, \dot{q}_i) + G(q_i) + T_f(\dot{q}_i) \\ & - ksign S_{si} - \zeta S_{si}. \end{aligned} \tag{20}$$

2.1 Experimental Setup

The proposed control algorithm is also tested on the experimental setup using LabView environment and NI myRIO-1900 hardware. The experimental setup is shown in Fig. 3. The myRIO-1900 is a tool used to implement multiple design concepts with one reconfigurable input/output (I/O) device. It is a portable device that can be used to design and develop various applications in robotics as well in mechatronic systems. It consists of a Xilinx Field Programmable Gate Arrays (FGPA), digital I/O lines and analog inputs as well as analog outputs. It has a built-in accelerometer with distinct features such as Universal asynchronous receiver-transmitter (UART), audio input and output terminals and a pulse width modulator. The myRIO-1900 is a WiFi-enabled edition which allows for speedy integration into remotely control embedded applications. The myRIO-1900 is programmed with LabVIEW using graphical programming language (G-Programming)

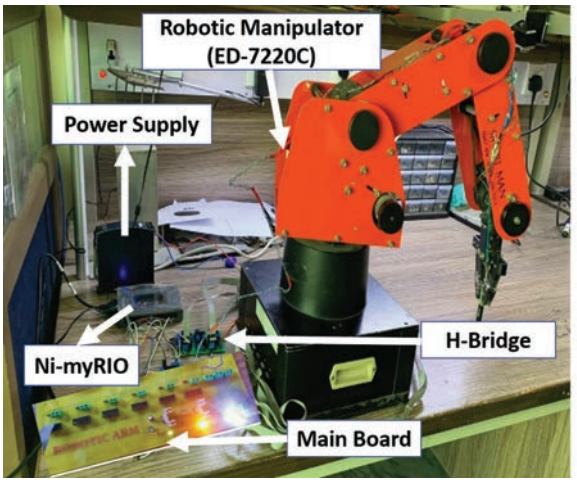

Fig. 3. *Hardware setup*

(a) *Motor driving board* **(b)** *Main board*

Fig. 4. *Motors driver board for robotic manipulator*

with a high data flow and a building block that can be used for link data acquisition, logical operations, and analysis.

In the proposed solution, digital outputs are used for controlling the actuators that are interfaced through indigenously designed H-bridges by using power transistors TIP147 and TIP142 as shown in Fig. 4a with current rating of five Amperes. The movement of rotary joints in a robot manipulator is controlled by using motor driver circuitry and the Fig. 4b presents the main board which connects the robotic manipulator with motor driving board. The desired speed of the motor is accomplished by controlling the voltage via pulse width modulation of the corresponding duty cycle. The actuators are integrated with optical encoders to determine the joint positions and their signals are sent to the myRIO for data processing.

3 RESULTS AND DISCUSSIONS

Matlab/Simulink is used for simulation. To validate the model, simulations are conducted using Matlab R2016a installed on a core i5 processor system having 6 GB random access memory. Step response is presented for the elbow joint of the robot manipulator

as shown in Fig. 5 while sinusoidal response is plotted for the base joint as presented in Fig. 6.

The desired step input signal of amplitude of 0.1 rad is given to the closed loop system and Fig. 5a shows simulation results for a control law that is designed to track a unit step function with and without friction compensation. Although there is no overshoot in Fig. 5a, but it shows an improvement in settling time in the case of the controller with friction compensation. The controller with friction compensation has settling time of 1 second as compared to 2 second settling time without considering the friction. The results show that the response of ISMC is better for friction taking into account in terms of steady-state error. The Fig. 5b demonstrates the control effort in elbow joint of robotic manipulator. The results clearly indicate that the more control effort is required for controller without friction and control input exhibits an unwanted chattering phenomenon, which can be damaging to the system's mechanical and electrical components. The trajectories of system begin from the sliding surface and the reaching phase is removed with the help of integral term in the sliding surface manifold. However, a discontinuous term of the switching control appears in the resulting joint torque. The chattering impact is the main hurdle in the practical realization of the sliding mode control. An integral term of SMC improves the outcomes by simplifying the higher order derivatives of the system. In the figure, it can be observed from the result that the control effort with friction compensation-based SMC allows the system to track the required trajectory with more precision and accuracy as compared to SMC without considering the friction model. Fig. 5c demonstrates the tracking error signal with and without friction compensation. As figure shows that at time of one second the error signal is zero with friction compensation as compared to 0.15 with out considering friction. The internal state of friction in elbow joint of robotic manipulator is illustrated in 5d.

In Fig. 6, to test the closed loop tracking performance of the robot manipulator system, the desired differentiable sinusoidal input signal is generated with an amplitude and frequency of 0.1 rad and 0.016 Hz, respectively. The simulation results are generated with and without friction compensation. 6a illustrates the sinusoidal response of base. At some point actual position attains the required trajectory then it follows the desired path for remaining time. In the figure, It can be observed from the results that the control effort with friction compensation-based control allows the system to track the required trajectory with more precision and accuracy as compared to SMC without considering the friction model. Fig. 6b illustrates the control effect in the form of applied torque to the base. The control effort is calculated using the control law defined in Eq. (19). The SMC based law reduces the chattering effect, when the dynamics of the system are weak against the uncertainties. Fig. 6c shows the error signal between actual and desired positions of the base. These results show that SMC with friction compensation demonstrates better performance with nearly zero error signal compared to SMC without friction compensation. In the figure, it can be observed that without friction compensation error signal has greater amplitude of error in comparison to friction compensation error signal. Fig. 6d shows the internal state of LuGre friction model in base joint of the AUTAREP robot manipulator.

Figs. 7a and b present the experimental results of joints of the robot manipulator. Fig. 7a demonstrates the step input response for base joint of the robot manipulator and shows that the joint reaches the desired position in 0.6 sec with overshoot. It can be seen that both transient and steady-state parameters are within acceptable limits. Sinusoidal response of base joint is also shown in Fig. 7b. The results demonstrate the well-known chattering phenomenon. This behavior of the system is undesirable and it may cause heat and energy dissipation and wear and tear of various components in the system. The chattering phenomenon can be reduced by implementing other variants of SMC such as higher order SMC.

The proposed ISMC technique and the adaptive sliding mode control (ASMC) methodology implemented in [**30**] are compared in Fig. 7c. By employing SMC's reaching condition, these trajectories approach zero and provide asymptotic stability to the system. Fig. 7c demonstrates the tracking behavior between both the current and desired positions which does not exceed 1.5 s for both techniques. The ISMC method has settling time of 1.25 s with friction compensation in comparison to 1.45 s for control law proposed in [**30**]. It has rise time of 214.9 milli second with overshoot of 0.792 % in comparison to ASMC technique having 270.63 milli-second rise time and overshoot of 0.658 %. The passivity based adaptive control of a serial robotic manipulator is implemented in [**31**] using joint frictions depending upon temperature. The position tracking of said technique along with the method implemented in this paper is shown in Fig. 7d. The position tracking in ISMC has better convergence performance and asymptotic convergence in comparison to method proposed in [**31**]. The

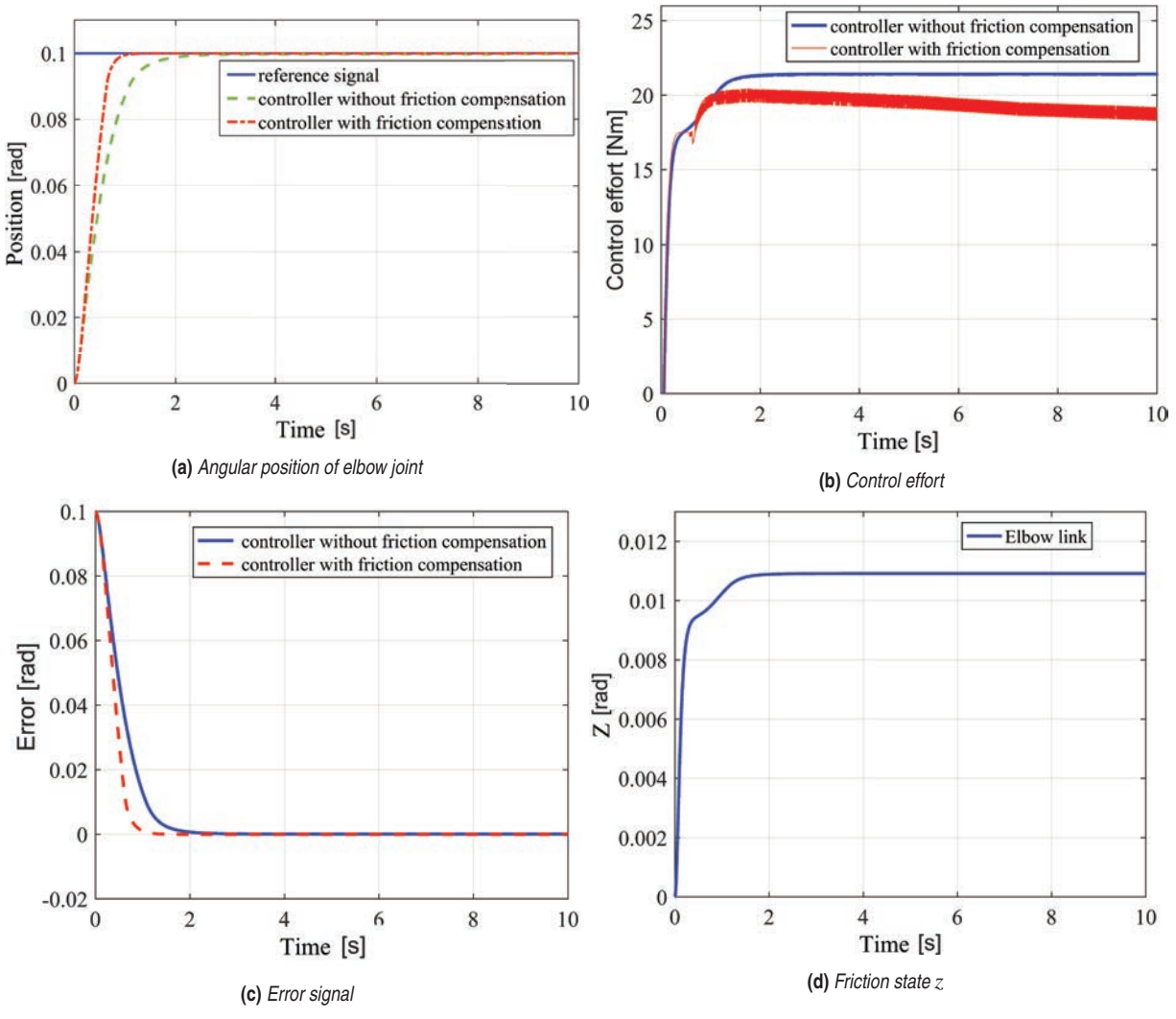

(a) *Angular position of elbow joint*

(b) *Control effort*

(c) *Error signal*

(d) *Friction state z*

Fig. 5. *Step response obtained by the elbow joint of the robotic manipulator*

negative aspect in the proposed technique ISMC with friction compensation is that the temperature effect of joints are not considered as well high control gains and high control efforts related to chattering issues. As robotic manipulators are often used in various applications where the joints get warmer due to the friction after the manipulator operates for some time. They may also be used when the temperature varies from very low to very hot degrees. The temperature effects must therefore be considered.

4 CONCLUSIONS

In this research work, a sliding mode control with an integral term is proposed for the desired trajectory tracking and robotic manipulator is modeled using dynamic LuGre friction model. The effectiveness of the proposed ISMC technique is initially validated in Matlab and simulation findings are shown to illustrate the effectiveness of the designed robust controller with and without considering the friction. The proposed control scheme is then evaluated by comparing with the other sliding mode control techniques. The ISMC technique performs superior in terms of system control efforts and transient parameters involving percentage overshoot, rise time and settling time etc. have been witnessed to be within certain bounds as anticipated. The proposed control law is also being tested on the custom developed experimental test bench using LabVIEW and NI-myRIO.

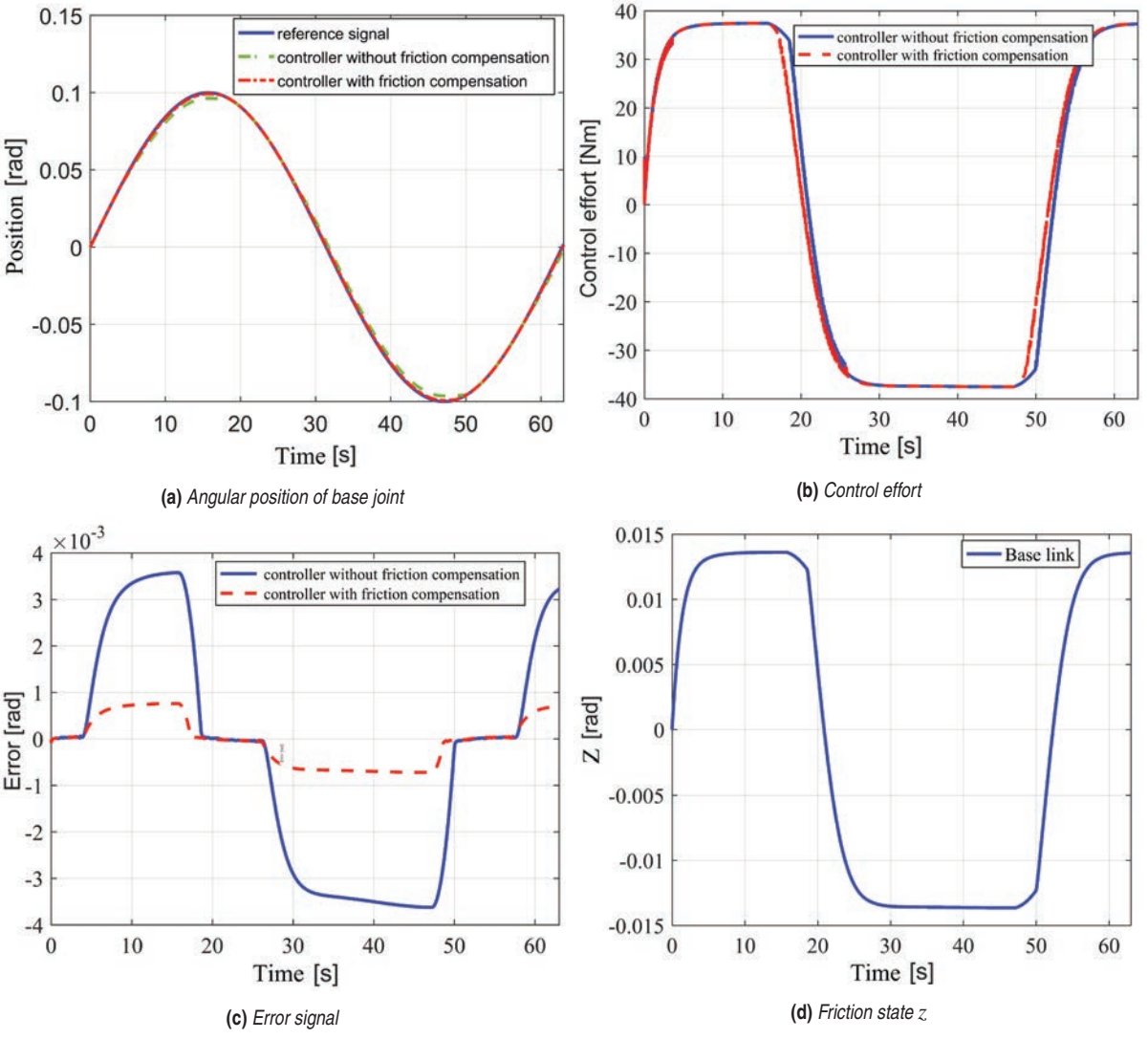

(a) *Angular position of base joint*

(b) *Control effort*

(c) *Error signal*

(d) *Friction state z*

Fig. 6. *Sinusoidal input signal response obtained by the base joint of the robotic manipulator*

5 REFERENCES

[1] Iqbal, J., Islam, R.U., Abbas, S.Z., Khan, A.A., Ajwad, S.A. (2016). Automating industrial tasks through mechatronic systems–A review of robotics in industrial perspective. *Technical Gazette - Tehnički vjesnik*, vol. 23, no. 3, p. 917-924, **DOI:10.17559/TV-20140724220401**.

[2] Mei, J., Zang, J., Ding, Y., Xie, S., Zhang, X. (2017). Rapid and automatic zero-offset calibration of a 2-DOF parallel robot based on a new measuring mechanism. *Strojniški vestnik - Journal of Mechanical Engineering*, vol. 63, no. 12, p. 715-724, **DOI:10.5545/sv-jme.2017.4529**.

[3] Ajwad, S.A., Iqbal, J., Khan, A.A., Mehmood, A. (2015). Disturbance-observer-based robust control of a serial-link robotic manipulator using SMC and PBC techniques. *Studies in Informatics and Control*, vol. 24, no. 4, p. 401-408, **DOI:10.24846/v24i4y201504**.

[4] Liu, H., Tian, X., Wang, G., Zhang, T. (2016). Finite-Time H_∞ Control for high-precision tracking in robotic manipulators using backstepping control. *IEEE Transactions on Industrial Electronics*, vol. 63, no. 9, p. 5501-5513, **DOI:10.1109/TIE.2016.2583998**.

[5] Erkaya, S. (2018). Effects of joint clearance on the motion accuracy of robotic manipulators. *Strojniški vestnik - Journal of Mechanical Engineering*, vol. 64, no. 2, p. 82-94, **DOI:10.5545/sv-jme.2017.4534**.

[6] Podgornik, B., Hogmark, S., Sandberg, O. (2004). Wear and friction properties of coatings for forming tools. *Strojniški vestnik – Journal of Mechanical Engineering*, vol. 50, no. 3, p. 156.

[7] Linderoth, M., Stolt, A., Robertsson, A., Johansson, R. (2013). Robotic force estimation using motor torques and modeling of low velocity friction disturbances.

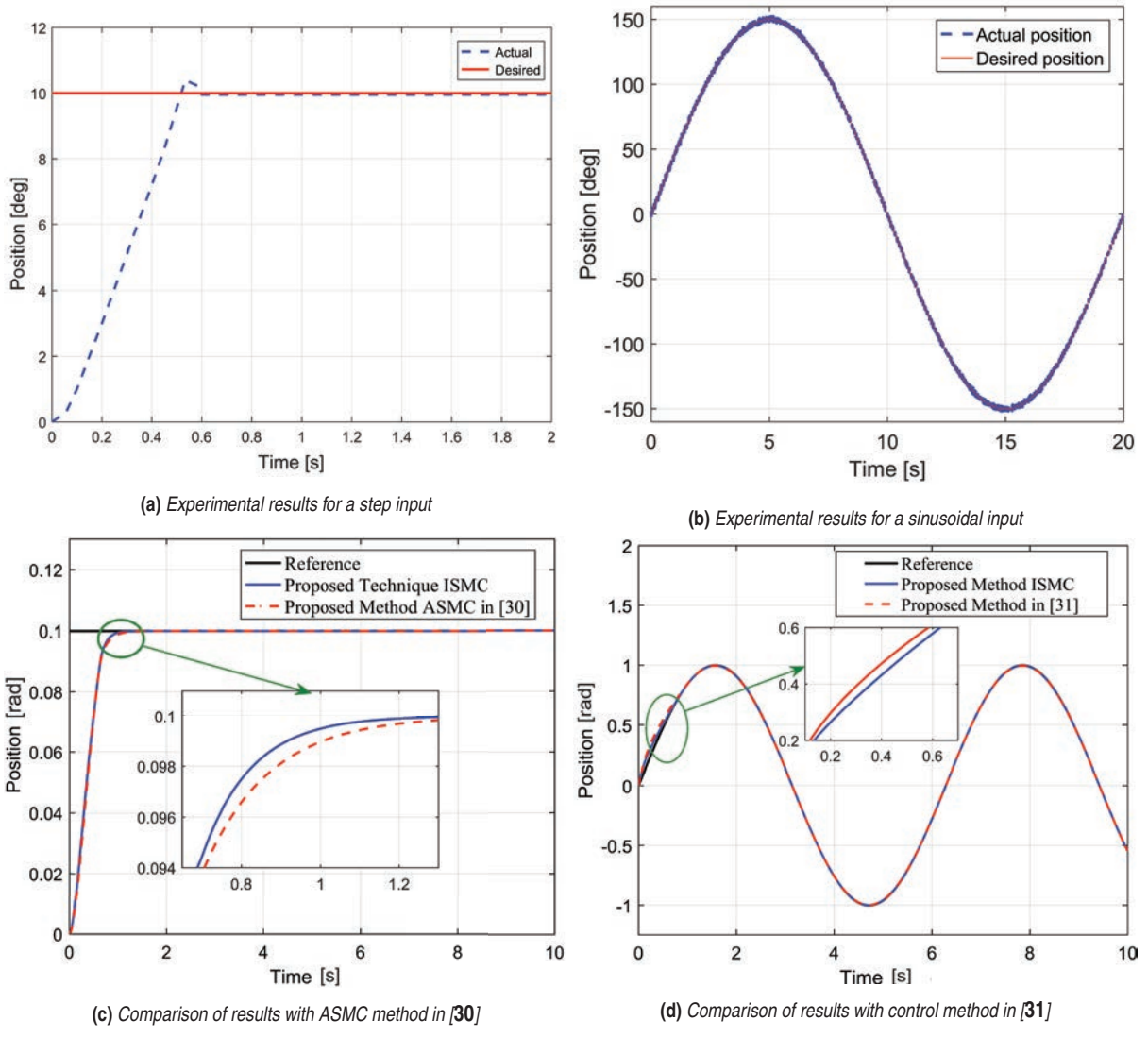

(a) *Experimental results for a step input*

(b) *Experimental results for a sinusoidal input*

(c) *Comparison of results with ASMC method in [***30***]*

(d) *Comparison of results with control method in [***31***]*

Fig. 7. *Experimental results and proposed technique comparisons*

In 2013 *IEEE/RSJ International Conference on Intelligent Robots and Systems*, p. 3550-3556, **DOI:10.1109/IROS.2013.6696862**.

[8] Correia, M.D., Gustavo, A., Conceição, S. (2012). Modeling of a three wheeled omnidirectional robot including friction models. *IFAC Proceedings Volumes*, vol. 45, no. 22, p. 7-12, **DOI:10.3182/20120905-3-HR-2030.00002**.

[9] Zhang, D., Niu, Y., Sun, L., Tomizuka, M. (2019). A position-based friction error model and its application to parameter identification. *IEEE* Access, vol. 7, p. 7759-7767, **DOI:10.1109/ACCESS.2018.2890669**.

[10] Segalman, D.J. (2006). Modelling joint friction in structural dynamics. *Structural Control and Health Monitoring*, vol. 13, no. 1, p. 430-453, **DOI:10.1002/stc.119**.

[11] Ma, W., Deng, W., Yao, J. (2018). Continuous integral robust control of electro-hydraulic systems with modeling uncertainties. *IEEE Access*, vol. 6, p. 46146-46156, **DOI:10.1109/ACCESS.2018.2866270**.

[12] Erenturk, K. (2008). Nonlinear two-mass system control with sliding-mode and optimised proportional-integral derivative controller combined with a grey estimator. *IET Control Theory & Applications*, vol. 2, no. 7, p. 635-642, **DOI:10.1049/iet-cta:20070330**.

[13] Ajwad, S.A., Iqbal, J., Ullah, M.I., Mehmood, A. (2015). A systematic review of current and emergent manipulator control approaches. *Frontiers of Mechanical Engineering*, vol. 10, no. 2, p. 198-210, **DOI:10.1007/s11465-015-0335-0**.

[14] Hacioglu, Y., Yagiz, N. (2019). Fuzzy robust backstepping with estimation for the control of a robot manipulator. *Transactions of the Institute of Measurement and Control*, vol. 41, no. 10, p. 2816-2825,

DOI:10.1177/0142331218814290.

[15] Li, D.Y., Zheng, J., Hao, W.R. J., Wang, S.K., Shen, W. (2017). Adaptive robust controller for electric cylinder with fast parameter estimation based on modified lugre model. *36th Chinese Control Conference (CCC)*, p. 3315-3320, **DOI:10.23919/ChiCC.2017.8027870**.

[16] Wu, Z. (2019). Adaptive block compensation trajectory tracking control based on LuGre friction model. *International Journal of Advanced Robotic Systems*, vol. 16, no. 5, **DOI:10.1177/1729881419873212**.

[17] Lee, J., Chang, P.H., Jin, M. (2017). Adaptive integral sliding mode control with time-delay estimation for robot manipulators. *IEEE Transactions on Industrial Electronics*, vol. 64, no. 8, p. 6796-6804, **DOI:10.1109/TIE.2017.2698416**.

[18] Manzoor, S., Islam, R.U., Khalid, A., Samad, A., Iqbal, J. (2014). An open-source multi-DOF articulated robotic educational platform for autonomous object manipulation. *Robotics and Computer-Integrated Manufacturing*, vol. 30, no. 3, p. 351-362, **DOI:10.1016/j.rcim.2013.11.003**.

[19] Serrezuela, R.R., Chavarro, A.F.C., Cardozo, M.A.T., Toquica, A.L., Martinez, L.F.O. (2017). Kinematic modelling of a robotic arm manipulator using Matlab. *ARPN Journal of Engineering and Applied Sciences*, vol. 12, no. 7, p. 2037-2045.

[20] Ajwad, S.A., Iqbal, J., Islam, R.U., Alsheikhy, A., Almeshal, A., Mehmood, A. (2018). Optimal and robust control of multi DOF robotic manipulator: Design and hardware realization. *Cybernetics and Systems*, vol. 49, no. 1, p. 77-93, **DOI:10.1080/01969722.2017.1412905**.

[21] Han, S., Wang, H., Tian, Y. (2017). Integral backstepping based computed torque control for a 6 DOF arm robot. *29th Chinese Control And Decision Conference (CCDC)*, p. 4055-4060, **DOI:10.1109/CCDC.2017.7979210**.

[22] Siciliano, B., Sciavicco, L., Villani, L., Oriolo, G. (2010). *Robotics: Modelling, Planning and Control*. Springer Science & Business Media, London, **DOI:10.1007/978-1-84628-642-1**.

[23] Khan, O., Pervaiz, M., Ahmad, E., Iqbal, J. (2017). On the derivation of novel model and sophisticated control of flexible joint manipulator. *Revue Roumaine des Sciences Techniques-Serie Electrotechnique et Energetique*, vol. 62, no. 1, p. 103-108.

[24] Yao, J., Deng, W., Jiao, Z. (2015). Adaptive control of hydraulic actuators with LuGre model-based friction compensation. *IEEE Transactions on Industrial Electronics*, vol. 62, no. 10, p. 6469-6477, **DOI:10.1109/TIE.2015.2423660**.

[25] Astrom, K.J. (2008). Revisiting the LuGre friction model. *IEEE control systems Magazine*, vol. 28, no. 6, p. 101-114, **DOI:10.1109/MCS.2008.929425**.

[26] Wang, X., Wang, S. (2015). Output torque tracking control of direct-drive rotary torque motor with dynamic friction compensation. *Journal of the Franklin Institute*, vol. 352, no. 11, p. 5361-5379, **DOI:10.1016/j.jfranklin.2015.08.021**.

[27] Zhang, L., Liu, L., Wang, Z., Xia, Y. (2018). Continuous finite-time control for uncertain robot manipulators with integral sliding mode. *IET Control Theory & Applications*, vol. 12, no. 11, p. 1621-1627, **DOI:10.1049/iet-cta.2017.1361**.

[28] Alam, W., Mehmood, A., Ali, K., Javaid, U., Alharbi, S., Iqbal, J. (2018). Nonlinear control of a flexible joint robotic manipulator with experimental validation. *Strojniški vestnik - Journal of Mechanical Engineering*, vol. 64, no. 1, p. 47-55. **DOI:10.5545/sv-jme.2017.4786**.

[29] Dumlu, A., Erentürk, K., Kaleli, A., Ayten, K.K. (2017). A comparative study of two model-based control techniques for the industrial manipulator. *Robotica*, vol. 35, no. 10, p. 2036-2055, **DOI:10.5545/sv-jme.2017.4786**.

[30] Tu'ma, D.H., Hamoudi, A.K. (2020). Performance of 2-link robot by utilizing adaptive sliding mode controller. *Journal of Engineering*, vol. 26, no. 12, p. 44-65, **DOI:10.31026/j.eng.2020.12.03**.

[31] Azizi, Y., Yazdizadeh, A. (2019). Passivity-based adaptive control of a 2-DOF serial robot manipulator with temperature dependent joint frictions. *International Journal of Adaptive Control and Signal Processing*, vol. 33, no. 3, p. 512-526, **DOI:10.1002/acs.2968**.

Strojniški vestnik - Journal of Mechanical Engineering 67(2021)9, 411-420
© 2021 Journal of Mechanical Engineering. All rights reserved.
DOI:10.5545/sv-jme.2021.7230 Original Scientific Paper
Received for review: 2021-04-19
Received revised form: 2021-07-13
Accepted for publication: 2021-08-20

Predictions of Friction Coefficient in Hydrodynamic Journal Bearing Using Artificial Neural Networks

Dragan Milčić[1,*] – Amir Alsammarraie[2] – Miloš Madić[1] – Vladislav Krstić[3] – Miodrag Milčić[1]

[1] University of Niš, Faculty of Mechanical Engineering, Serbia
[2] Tikrit University, Engineering Faculty, Iraq
[3] Ljubex International, Belgrade, Serbia

This paper explores the influence of the frequency of shaft sleeve rotation and radial load on a journal bearing made of tin-babbitt alloy (Tegotenax V840) under hydrodynamic lubrication conditions. An experimental test of the frictional behaviour of a radial plain bearing was performed on an originally developed device for testing rotating elements: radial and plain bearings. Using the back-propagation neural network, based on experimental data, artificial neural network models were developed to predict the dependence of the friction coefficient and bearing temperature in relation to the radial load and speed. Using experimental data of the measured friction coefficient with which the artificial neural network was trained, well-trained networks with a mean absolute percentage error on training and testing of 0.0054 % and 0.0085 %, respectively, were obtained. Thus, a well-trained neural network model can predict the friction coefficient depending on the radial load and the speed.

Keywords: artificial neural network, hydrodynamic journal bearing, babbitt metal tin-based alloy, friction coefficient

Highlights

- *An artificial neural network was used to predict the friction coefficient of the hydrodynamic radial journal bearings.*
- *For the training and testing of artificial neural network (ANN), experimental data obtained by testing radial hydrodynamic journal bearings made of a tin- Babbitt alloy (Tegonenax V840) were used.*
- *The ANN model allows the prediction of the friction coefficient based on the radial load of the bearing and the speed.*
- *Prediction of the coefficient of friction using ANN has proven to be a competitive and efficient method.*

0 INTRODUCTION

Hydrodynamic bearings support a rotating shaft with its associated loads, through a pressure field developed within the lubricant that separates the solid surfaces. Journal bearings made of tin-babbitt alloy (Tegotenax V840) under hydrodynamic lubrication conditions are widely used in compressors, turbines, pumps, electric motors, electric generators, mining ore crushers, etc. Sliding friction in the contact surfaces between the material of the shaft and the sleeve material is a dissipative process of a complex nature, accompanied by a series of phenomena: mechanical, physicochemical, electrical, metallurgical, and thermal characteristics, which lead to the wear and tear of coupled bodies.

The coefficient of friction is significantly influenced by: normal load, geometry, relative surface motion, sliding velocity, the surface roughness of the rubbing surfaces, the type of material, system rigidity, temperature, stick-slip, relative humidity, lubrication and vibration.

Among these factors, normal load and sliding velocity are the two major factors that play significant roles in the variation of the friction coefficient **[1]** to **[4]**.

The effect of radial load on the friction coefficient and loss material of different polymer and composite materials was investigated **[2]**; it was found that the amounts of friction coefficient and loss material are different for different materials. The tribological actions of Babbitt alloy 16-16-2 sliding against aluminium bronze ZnCuAl9Mn2 lubricated by seawater were systematically investigated by Wu et al. **[3]**. The results indicated that the friction coefficient decreased as the load increased to 30 N and then remained steady at high loading but decreased with an increase in sliding speed. Zeren et al. **[4]** studied the tribological behaviour of two different tin-based bearing materials in dry sliding conditions: one of these alloys with low Sb content (7 %) is known as SAE 12 and is widely used in the automotive industry and the other with a high Sb content (20 %) is an Sn–Sb–Cu alloy. Although search results have proved that WM-2 and WM-5 alloys can be used in dry sliding conditions, it is shown that the performance of WM-5 under heavy service conditions is better than WM-2 due to its alloying elements.

Artificial neural networks (ANN) are a successful tool for predicting some tribological properties. ANN is a mathematical model inspired by the biological nervous system. ANN technology is used to solve

*Corr. Author's Address: Faculty of Mechanical Engineering, University of Niš, Aleksandra Medvedeva 14, Niš, Serbia, dragan.milcic@masfak.ni.ac.rs

complex scientific and engineering problems. The significance of this technology is that ANN models can be trained based on experimental data to recognize solutions. The ANN prediction method has been used in several applications, such as wear and friction.

Asafa and Fadare [5] have presented an ANN predictive model that captures the dynamic behaviour of the tool wear and can be deployed effectively for online monitoring processes. Nine different structures of multi-layer perceptron neural networks with feed-forward and back-propagation learning algorithms were designed using the MATLAB neural network toolbox. An optimal ANN architecture of 5-12-4-2 with the Levenberg-Marquardt training algorithm and a learning rate of 0.1 was obtained using the Taguchi experimental design method. Durmuş et al. [6] have presented the effects of ageing conditions at various temperatures, load, sliding speed, and abrasive grit diameter in 6351 aluminium alloy have been investigated using artificial neural networks. The experimental results were trained in the ANN's program, and the results were compared with experimental values. It is observed that the experimental results coincided with ANN's results. Knowing friction coefficient is important for determination of wear loss conditions at Al-Si alloys. Nagaraj et al. [7] investigated the effects of load, sliding velocity and sliding duration on the wear loss of the alloy. The experimental results were used to train the ANN program and the results were compared with experimental values. It was observed that the experimental results are very close to ANN's results.

Kalidass et al. [8] focuses on two different models, regression mathematical and ANN models for predicting tool wear. Experiments have been conducted for measuring tool wear based on the design-of-experiment (DOE) technique in a vertical machining centre on AISI 304 steel using a solid carbide end mill cutter. The experimental values are used in Six Sigma software for finding the coefficients to develop the regression model. The experimentally measured values are also used to train the feed-forward back-propagation ANN for the prediction of tool wear. Liujie et al. [9] used a back-propagation (BP) neural network to study the effects of the pv factor and sliding distance on the friction and wear behaviour of 30 wt. % carbon fibre reinforced poly (ether-ether-ketone) advanced composite (PEEK-CF30) at the contact temperature of 120 ºC. An experimental plan was performed on a pin-on-disc machine for obtained experimental results under unlubricated conditions. Hassan and Mohammed [10] experimentally investigated the parameters affecting the wear debris and the temperature rise due to friction, as well as developing the model ANN using MATLAB program for predicting the wear and temperature of disc and pad. Since the hybrid materials had not been enough researched, Sathyabalan et al. [11] have presented application of ANN on the MMC (hybrid LM6 aluminium), which is reinforced by SiC and flyash. The aim of this study was the prediction of the influence of additives (reinforcement materials) on the wear and hardness of hybrid material. The best results were obtained with ANN (4-6-2). Input parameters are defined by variables (flyash size, SiC size, flyash in % and SiC in %) while the outputs are wear and hardness. Prediction accuracy was high, so the ANN has been validated for practical application by weight definition of the above-mentioned reinforcement materials for the hybrid material with good resistance against wear. An ANN model for the prediction of the wear process with glass-filled polytetrafluoroethylene (PTFE) composites is presented by Varade and Kharde [12]. An additional task of this research was establishing the dependence between load-sliding and time-sliding speed. The input parameters were velocity, load, time and percentage of glass fill, while the output was wear. Taguchi's orthogonal array of 27 experiments was used. The results revealed that the material with the highest percentage of glass fill possesses better resistance against wear. As the friction coefficient also depends on selected lubricant, Durak et al. [13] have presented a back-propagation neural network (BPNN) for the prediction of the concentration of the additive (based on PTFE) in the base oil in order to decrease the friction coefficient of the journal bearing. A bearing for testing was made of ZnAl alloy. The best results were obtained by using BPNN (3-5-1). Prediction accuracy is high, so the presented BPNN can be used in practice.

In order to research the applicability of the ANNs by friction coefficient prediction of the composite carbon-fibre-reinforced polymer (CGRP) material, Nasir et al. [14] have developed suitable ANN for this purpose. They have developed few different models, but the best results were with ANN (4-40-1), which used the Levenberg–Marquardt algorithm for training. The input parameters were fibre orientation, testing speed, normal force and duration time, while the output parameter was the friction coefficient.

Artificial intelligence (AI) has many tools and techniques that can be applied in the prediction of different parameters. One of these is the adaptive neuro-fuzzy inference system (ANFIS). This methodology was used in combination with experimental research [15]. This work focuses on

establishing a correlation between friction coefficient and load by sliding bushing, made of a tin-based white metal alloy (TEGOTENAX V840). Experimental research [16] and [17] attempted to provide values (i.e., parameters), which will be used for ANFIS design: friction coefficient, speed and radial load. All mentioned values were measured in equal time intervals. The newly designed ANFIS was tested, and the results were compared, which showed that the prediction accuracy is high. As the final result, an expression was obtained that describes correlation friction coefficient - load under conditions of lubrication defined in advance.

The present study's objective was to predict friction coefficient in the radial hydrodynamic journal bearing of the *white metal* bearing *alloys*, known commercially as babbitt metal - Tegotenax V840, based on experimental research [16] and [17] using ANN.

1 EXPERIMENTAL DETAILS AND PROCEDURE

1.1 Radial Journal Bearing Test Rig

Fig. 1 shows a test rig for testing rotating machine elements, developed at the Faculty of Mechanical Engineering in Niš, Serbia, adapted for testing the tribological properties of plain bearings. The test rig for testing hydrodynamically lubricated plain bearings consists of three main systems: the drive system, the hydraulic system for realizing the load of the plain bearing, and the hydraulic system for lubricating the plain bearing.

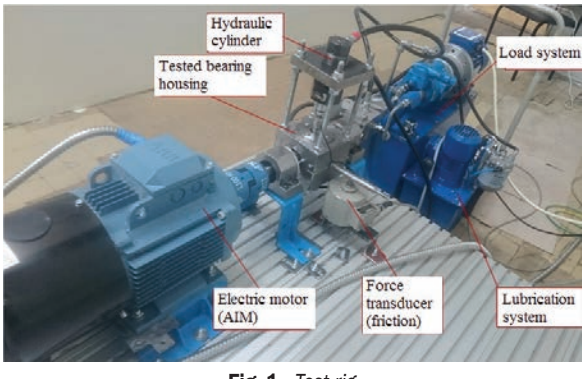

Fig. 1. *Test rig*

The drive system of the test rig consists of an asynchronous induction motor (ABB, 400 V, 50 Hz, 3 kW, 1460 rpm), which is connected to the shaft by an elastic coupling. The shaft is supported by two roller bearings and a test specimen (i.e., a journal bearing mounted between these two bearings). The motor is equipped with an E720 encoder for counting the engine speed.

The test specimen-journal bearings are hydrodynamically lubricated. The lubrication system consists of an electric motor (1450 rpm, 90 W), an ELP pump (AMGP-03C), and a 10 l hydraulic tank. The lubricating oil of the test plain bearing is ISO VG 32. A schematic representation of the part of the test rig with the bearing assembly is shown in Fig. 2.

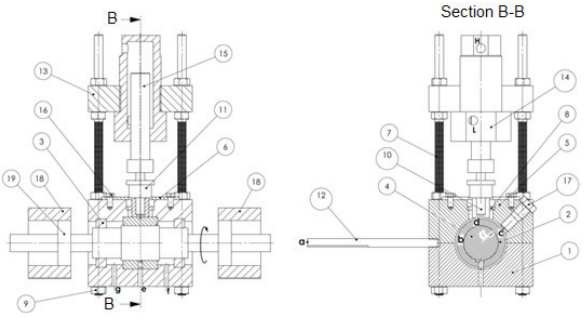

Fig. 2. *The bearing-housing assembly (1-lower bracket; 2-sleeve; 3-seal; 4-shaft; 5-top bracket; 6-top cover with seal; 7-screw; 8-seal; 9-nut; 10-lever with which the bearing is loaded; 11-force sensor; 12-beam; 13-cylinder carrier; 14-cylinder; 15-piston; 16-screw; 17-thermocouple; 18-roller bearing housing; 19-roller bearing; a-place of friction force measurement; c- thermocouple temperature measurement location; d-place of bearing loading by radial force, g, e, f- hydraulic ports)*

A hydraulic system was used to load the sliding bearing, which consists of an electric motor (EM) (0.75 kW, 380 V, 1420 rpm), a pump (EATON PVQ10), and a 30 l oil tank. The hydraulic cylinder is used to load the test of a sliding bearing. The working fluid is the above-mentioned oil. The hydraulic cylinder exerts a load on the journal bearing sleeve via a radial force sensor (HBM U9C / 10 kN).

Table 1 shows the properties of the operating fluid.

Table 1. *Properties of hydraulic oil ISO VG32*

Item		Value	Unit
Density at 15.6 °C	ρ	868	kg/m^3
Kinematic viscosity at 40 °C	v_{40}	32.2	mm^2/s
Kinematic viscosity at 100 °C	v_{100}	5.52	mm^2/s
Viscosity index		108	-
Flash point		212	°C
Pour point		–33	°C
Aniline point		104	°C

The bearing sleeve is given in Fig. 3. The dimensions of the bearing are: bearing diameter $d = 40$ mm + 0.05 mm, bearing axial length $B = 40$ mm,

outer bearing diameter D = 60 mm, bearing diametral clearance Z = 0.025 mm.

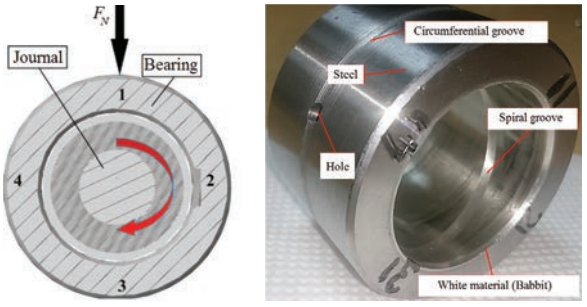

Fig. 3. *Bearing sleeve*

1.2 Preparation of Experimental Materials and Conditions

The journal bearing sleeve is made of AISI 440C stainless steel, and a 3 mm thick layer of white metal (Tegotenax V840) is applied to the sleeve. The shaft is made of AISI 440C stainless steel. The chemical properties of the steel layer and Babbitt layer materials are given in Table 2, and the mechanical and physical properties in Table 3.

Table 2. *Chemical composition of AISI 440C sleeve and material of internal sliding surface - white metal TEGOTENAX V840*

Element	TEGOTENAX V840 [wt. %]	AISI 440C [wt. %]
Sn	88.7	-
Sb	7.6	-
Cu	3.7	-
C	-	1.2
Si	-	1
Mn	-	1
Ni	-	1
Cr	-	18
Mo	-	0.75
P	-	0.04
S	-	0.03

Table 3. *Mechanical and Physical Properties*

	Tin-based white metal alloy: TEGOTENAX V840		Shaft: AISI 440C
Hardness HB 10/250/180	20 °C	23	269
	50 °C	17	-
	100 °C	10	-
	150 °C	8	-
Yield Strength, $R_{p0.2}$ [MPa]	46		448
Tensile Strength, R_m [MPa]	77		758
Young's modulus, E [MPa]	56500		200000
Density, ρ [kg/m^3]	7400		7650
Poisson ratio, υ	0.33		0.27 to 0.30

1.3 Determination of Frictional Properties

The friction coefficient is determined by the moment of friction. The friction moment $M_f(t)$ as a function of time is calculated as the product of the friction force $F_f(t)$ and the bearing radius r. As a reaction of the friction moment, the force $F_s(t)$ appears at the contact point of the force sensor, which is at a perpendicular distance L from the centre of the sleeve (Fig. 4).

$$M_f(t) = F_f(t) \cdot r = F_s(t) \cdot L\,. \tag{1}$$

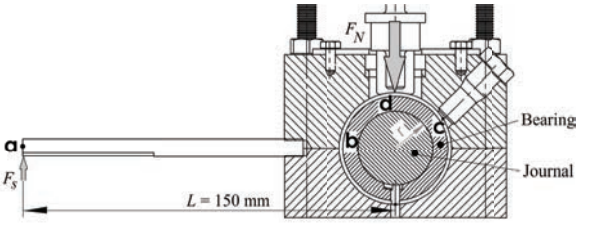

Fig. 4. *Friction force measurement scheme*

Based on the expression for determining the friction force:

$$F_f(t) = \mu(t) \cdot F_N(t). \tag{2}$$

The friction coefficient is determined by the expression:

$$\mu(t) = \frac{F_f(t)}{F_N(t)} = \frac{F_s(t) \cdot L}{r \cdot F_N(t)}. \tag{3}$$

The input parameters of the test are speed n, i.e., sliding speed v and bearing load F_N. The radial bearing load was varied in the range F_N = 1000 N to 4000 N, with the variation of the shaft speeds in the range n = 1000 rpm to 3000 rpm. The test parameters and specific bearing load are given in Table 4.

Table 4. *Defined parameters for testing plain bearings*

Speed, n [rpm]	Sliding speed, v [m/s]	Bearing load, F_N [N]	Specific bearing load, $p = F_N/(d{\cdot}B)$ [MPa]
1000	2.09	1000	0.625
		2000	1.25
		3000	1.875
		4000	2.5
2000	4.2	1000	0.625
		2000	1.25
		3000	1.875
		4000	2.5
3000	6.3	1000	0.625
		2000	1.25
		3000	1.875
		4000	2.5

For data acquisition within the experimental tests of tribological properties of the sliding bearing, a personal computer (PC) equipped with appropriate hardware (measuring and control interface) in conjunction with software developed in the LabVIEW environment is used. The data was transmitted to the recorder, which enabled monitoring and recording of the signals. The data about coefficient friction, radial load and sensor force were applied for 1/20 s and the temperature lubrication oil and load for 5 s.

1.4 Test Results

Based on the experimental plan given in Table 4, tests were performed on test specimens of plain bearings with a previously defined geometry.

Figs. 5 to 7 show the changes of temperature and friction coefficient with the change of the radial load of the bearing F_N = 1000 N to 4000 N and the speed n = 1000 rpm to 3000 rpm. Twelve different experiments were performed, each lasting an average of 5 hours (18000 s).

2 ANN MODEL DEVELOPMENT

In order to establish a mathematical relationship between the dependence of the experimental parameters of the journal bearing test in the conditions of hydrodynamic testing, two ANN models were developed. The first model was for the prediction of the friction coefficient, and the second was for the prediction of the bearing temperature. For training and testing of the network, the data of the measured values of the friction coefficient μ and the bearing temperature T for 18000 s were used as a function of the change of the radial load F_N and the speed of the shaft n.

The neural network architecture for both models had three neurons in the input layer (bearing load F_N, speed n and time t), one neuron in the output layer (friction coefficient μ respectively bearing temperature T) and one hidden layer with 6 neurons (Fig. 8).

For the ANN model, a linear activation function and a nonlinear sigmoid activation function were combined in the output and hidden layers,

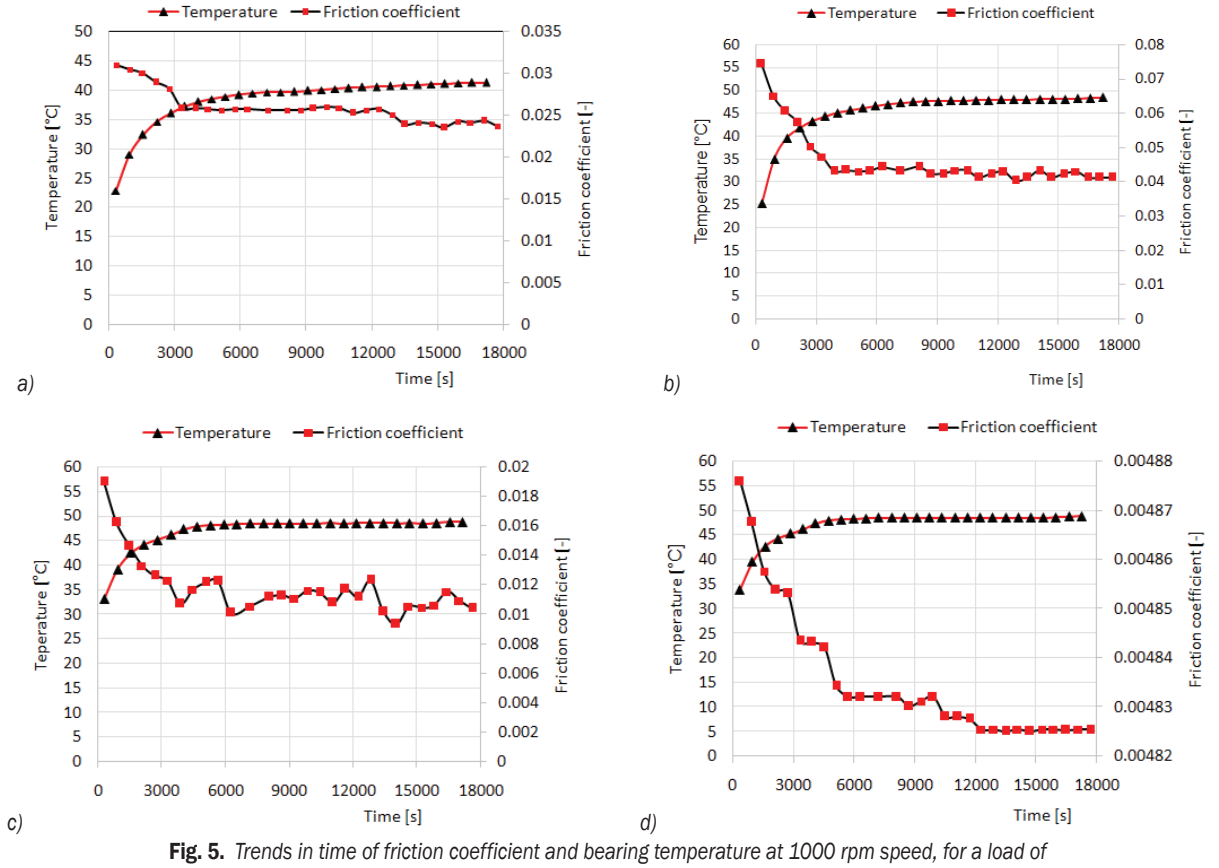

Fig. 5. *Trends in time of friction coefficient and bearing temperature at 1000 rpm speed, for a load of a) F_N = 1000 N; b) F_N = 2000 N; c) F_N = 3000 N and d) F_N = 4000 N*

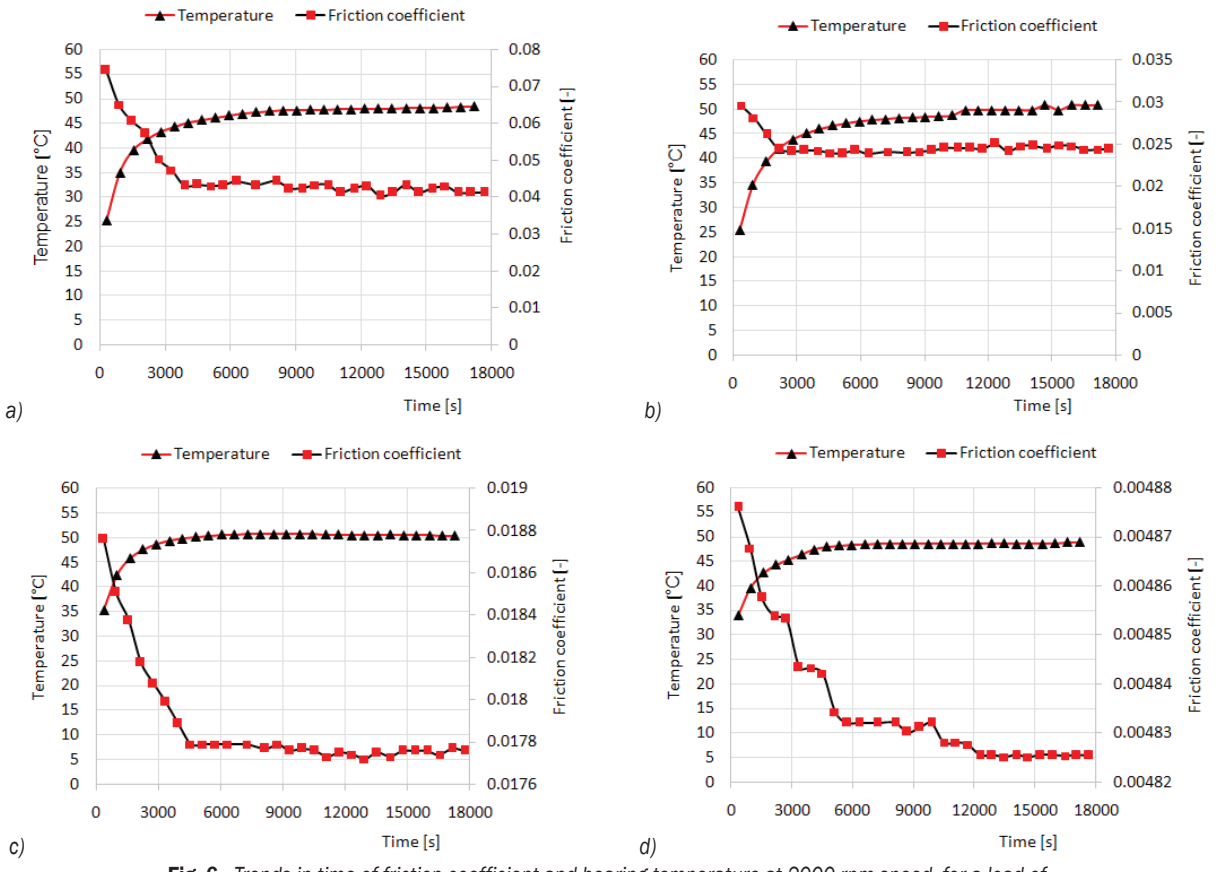

Fig. 6. *Trends in time of friction coefficient and bearing temperature at 2000 rpm speed, for a load of a) F_N = 1000 N; b) F_N = 2000 N; c) F_N = 3000 N and d) F_N = 4000 N*

respectively. Accordingly, the obtained experimental data were normalized in the range [–1, 1]. During the development of the ANN model, the available input/output data set was randomly divided into two sets: a training set and a test set for the ANN network model. 295 data points were used for ANN training, and 43 data points were used to test trained ANN network models.

The Levenberg-Marquardt algorithm was chosen for ANN training due to its high accuracy and fast convergence. In order to solve the convergence problem and minimize, as well as slow the convergence, the ANN training process was repeated several times with the help of different initial weights established by the Nguyen-Widrow method. During the ANN training process, although the maximum number of training iterations was set at 1000, it was observed that much fewer iterations were sufficient to train ANN models, Fig. 9.

Upon completion of the training process, the prediction performance of the trained ANN model was assessed. For this purpose, the mean absolute percentage error (MAPE) was calculated according to the Eq (4):

$$MAPE = \frac{1}{N}\sum_{N}\left|\frac{\text{Experimental value} - \text{Estimed value}}{\text{Experimental value}}\right| \cdot 100[\%], \quad (4)$$

where N is the number of data.

The average errors for training and testing data for the first model are 0.0054 % and 0.0085 %, respectively, which are very small indeed. The average errors for training and testing data for the second model are 0.12 % and 0.023 %, respectively, which are very small.

3 ANALYSIS AND DISCUSSION

Fig. 10 shows the prediction of the friction coefficient as a function of bearing load and speed for the white metal alloy bearing internal sliding surface of Tegotenax V840. The prediction of the friction coefficient of the sliding bearing's internal surface made of tin-based white metal alloy showed that the

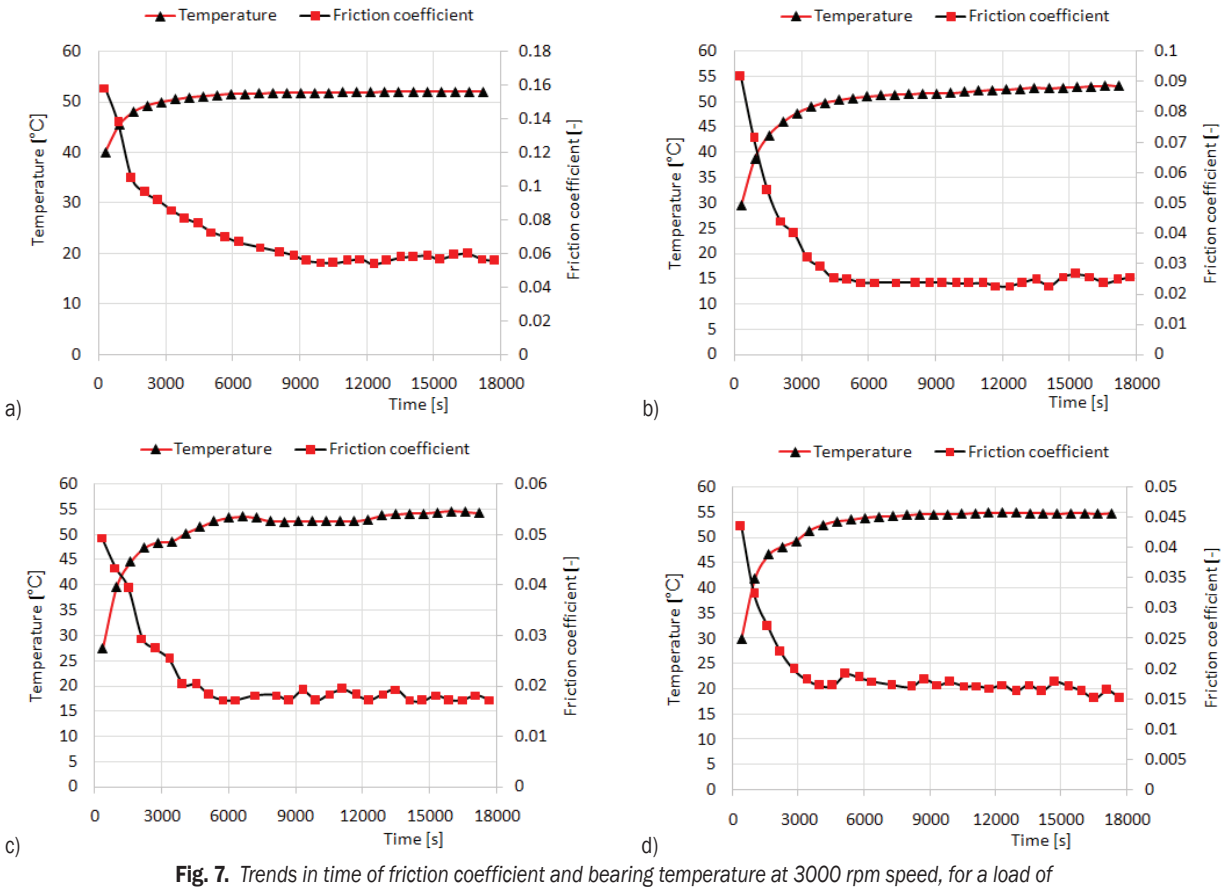

Fig. 7. *Trends in time of friction coefficient and bearing temperature at 3000 rpm speed, for a load of a) F_N = 1000 N; b) F_N = 2000 N; c) F_N = 3000 N and d) F_N = 4000 N*

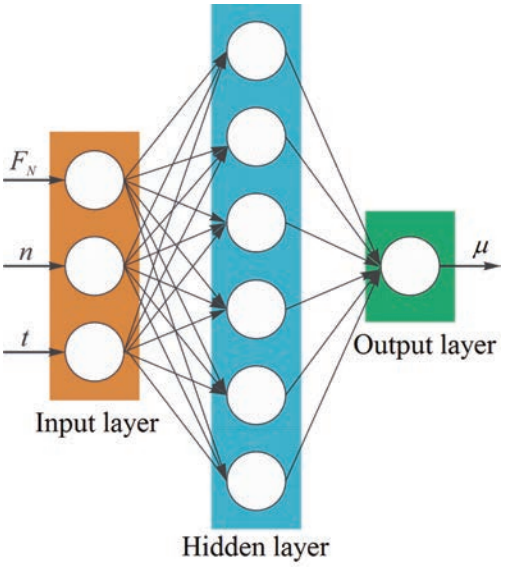

Fig. 8. *Neural network architecture*

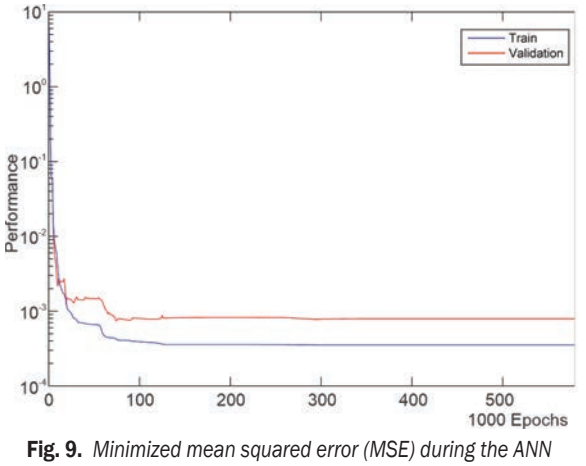

Fig. 9. *Minimized mean squared error (MSE) during the ANN training process for friction coefficient prediction*

friction coefficient has a downward trend with an increased bearing load.

The values of the change of the friction coefficient take the form of a downward trend - curve with increasing bearing load and decreasing speed, as shown in Fig. 10.

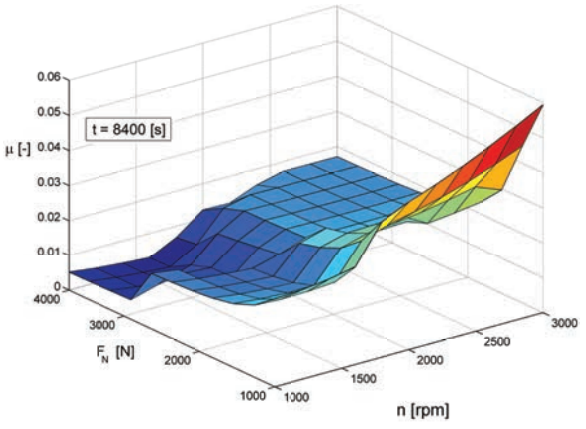

Fig. 10. *Prediction of friction coefficient μ as a function of bearing load F_N and speed n with the help of BP neural network*

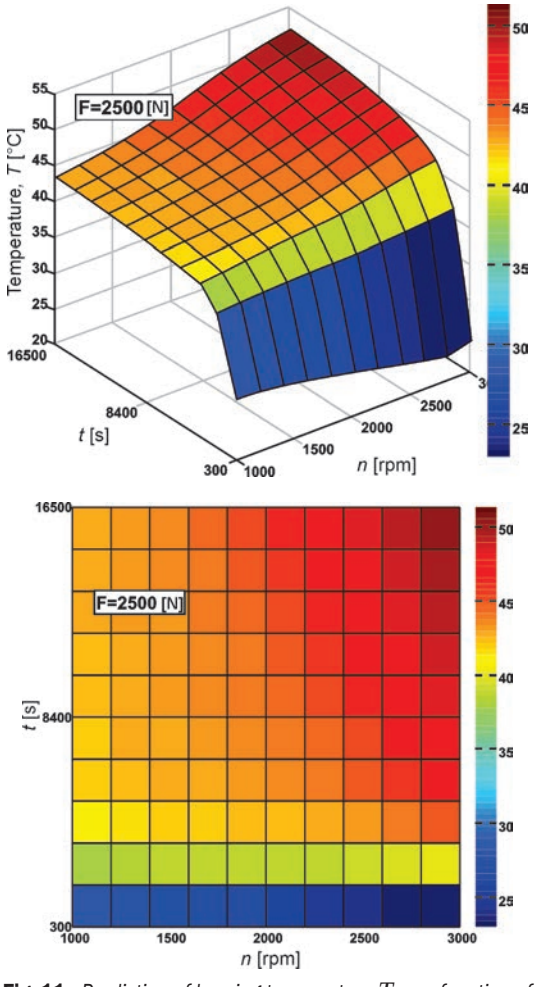

Fig. 11. *Prediction of bearing temperature T as a function of speed n and sliding time t with the help of BP neural network*

The sliding friction between the shaft sleeve, bearing, and lubricant causes an increase in the lubricant temperature, which results in a decrease in the shear stress of the lubricant, which leads to a decrease in the viscosity of the lubricant and hence a decrease in the friction coefficient.

Fig. 11 shows the prediction of bearing temperature T as a function of the speed n and a sliding time t for the bearing load F_N = 2500 N. This change has a growing trend with an increasing sliding time and speed.

It can be seen that the bearing temperature T increases with time t, as shown in Fig. 11. As the friction coefficient is directly proportional to the dynamic viscosity η, and the increase in oil temperature leads to a decrease in dynamic viscosity, which certainly leads to a decrease in friction coefficient. In Fig. 11, two zones can be observed, the unstable zone and the stable zone. In the zone of an unstable state, the temperature inside the system increases with time. The duration of this zone is estimated at about 4000 s. The second zone is a stable state in which the temperature remains approximately constant: somewhere around 41 °C to 54 °C.

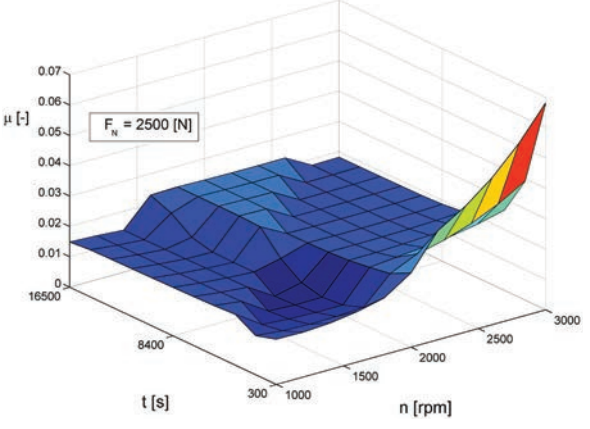

Fig. 12. *Prediction of the ratio of the friction coefficient μ, in relation to the speed n and the sliding time t with the help of BP neural network*

Fig. 12 shows the predicted friction coefficient μ in relation to the speed n and the sliding time t at constant load F_N = 2500 N. It can be seen that the friction coefficient μ increases with the speed n. As the sliding time increases, the friction coefficient decreases according to the increase in temperature and the decrease in the viscosity of the oil.

The optimization of the ANN model using metaheuristics indicated a maximum friction coefficient of 0.1513, which was obtained in a combination of values of process parameters: n = 3000 rpm, F_N = 1072 N and t = 300 s. With regard to

the stochastic nature of metaheuristics, i.e., inability to guarantee the optimality of the found solution, the solution was checked by creating a three-dimensional (3D) diagram of the friction coefficient for t = 300 s, which is shown in Fig. 13.

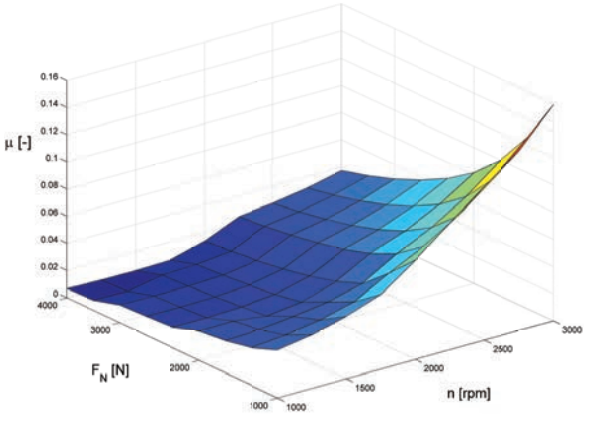

Fig. 13. *The highest friction coefficient μ, obtained by optimizing the ANN model*

As can be seen from Fig. 13, the value of the maximum friction coefficient of 0.1591 is obtained in a combination of the force F_N = 1000 N and the speed n = 3000 rpm.

Based on experimental data, it was determined that for F_N = 1000 N, n = 3000 rpm and t = 300 s, the resulting coefficient of friction has a value of 0.1579, which once again confirms the accuracy of the created ANN model.

4 CONCLUSIONS

The research into tribological properties of sliding bearings was performed on the originally developed equipment for testing rotating elements at the Faculty of Mechanical Engineering in Niš in the Laboratory for Mechanical Constructions, Development, and Engineering. A bearing made of tin-based white metal alloy-TEGOTENAX V840 were tested under hydrodynamic lubrication conditions with selected ISO VG 32 hydraulic oil.

Based on the conducted experimental research and developed ANN models for the prediction of the friction coefficient (first model) and bearing temperature (second model), the following conclusions can be drawn:

The ANN architecture for both models was 3-6-2, and the Levenberg-Marquardt algorithm was used to train the ANN. The result of ANN prediction shows that the models are extremely good with minimal mean square error training and testing data for the first model 0.0054 % and 0.0085 % and for the second model 0.12 % and 0.023 %, respectively.

The optimization of the ANN model, the highest friction coefficients 0.1513 were obtained at a bearing load of 1072 N and a speed of 3000 rpm, while the lowest coefficients of friction 0.00288 were obtained at a maximum load of 4000 N and a speed of 1675.22 rpm.

The bearing temperature prediction model indicates a growing trend of change with increasing sliding time and speed. The bearing temperature T increases with time t; after a little more than 1 hour (about 4000 s), the bearing temperature stabilizes at approximately 50 °C at all bearing loads and all bearing rotation frequencies.

5 ACKNOWLEDGEMENT

This research was financially supported by the Ministry of Education, Science and Technological Development of the Republic of Serbia (Contract No. 451-03-9/2021-14/200109).

6 REFERENCES

[1] Chowdhury, M.A., Nuruzzaman, D.M., Mia, A.H., Rahaman, M.L. (2012). Friction coefficient of different material pairs under different normal loads and sliding velocities. *Tribology in Industry*, vol. 34, no. 1, p. 18-23.

[2] Nuruzzaman, D.M., Chowdhury, M.A., Rahaman, M.L. (2011). Effect of duration of rubbing and normal load on friction coefficient for polymer and composite materials. *Industrial Lubrication and Tribology*, vol. 63, no. 5, p. 320-326, **DOI:10.1108/00368791111154931**.

[3] Wu, H., Bi, Q., Zhu, S., Yang, J., Liu, W. (2011). Friction and wear properties of Babbitt alloy 16-16-2 under sea water environment. *Tribology International*, vol. 44, no. 10, p. 1161-1167, **DOI:10.1016/j.triboint.2011.05.007**.

[4] Zeren, A., Feyzullahoglu, E., Zeren, M. (2007). A study on tribological behaviour of tin-based bearing material in dry sliding. *Materials & Design*, vol. 28, no. 1, p. 318-323, **DOI:10.1016/j.matdes.2005.05.016**.

[5] Asafa, T., Fadare, D.A. (2012). Artificial neural network predictive modeling of uncoated carbide tool wear when turning NST 37.2 steel. *Journal of Engineering and Applied Sciences*, vol. 7, no. 4, p. 396-406.

[6] Durmuş, H.K., Özkaya, E., Meric, C. (2006). The use of neural networks for the prediction of wear loss and surface roughness of AA 6351 Aluminum Alloy. *Materials & Design*, vol. 27, no. 2, p. 156-159, **DOI:10.1016/j.matdes.2004.09.011**.

[7] Nagaraj, A., Shivalingappa, D., Koti, H., Channankaiah (2012). Modeling and predicting adhesive wear behaviour of aluminium-silicon alloy using neural networks. *International Journal of Recent Scientific Research*, vol. 3, no. 5, p. 378-381.

[8] Kalidass, S., Palanisamy, P., Muthukumaran, V. (2012). Prediction of tool wear using regression and artificial neural network models in end milling of AISI 304 austenitic stainless steel. *International Journal of Engineering and Innovative Technology (IJEIT)*, vol. 1, no. 2, p. 29-36.

[9] Liujie, X., Cardoso, R., Davim, J.P. (2008). Modelling of tribological behaviours of composite PEEK-CF30 using BP neural networks. *Materials Science-Poland*, vol. 26, no. 3, p. 495-504.

[10] Hassan, A.K.F., Mohammed, S. (2016). Artificial neural network model for estimation of wear and temperature in pin-disc contact. *Universal Journal of Mechanical Engineering*, vol. 4, no.2, p. 39-49, **DOI:10.13189/ujme.2016.040204**.

[11] Sathyabalan, P., Selladurai, V., Sakthivel, P. (2009). ANN based prediction of effect of reinforcements on abrasive wear loss and hardness in a hybrid MMC. American Journal of Engineering and Applied Sciences, vol. 2, no. 1, p. 50-53, **DOI:10.3844/ajeassp.2009.50.53**.

[12] Varade, B.V., Kharde, Y.R. (2012). Prediction of specific wear rate of glass filled PTFE composites by artificial neural networks and Taguchi approach. *International Journal of Engineering Research and Applications*, vol. 2, no. 6, p. 679-683.

[13] Durak, E., Salman, Ö., Kurbanoglu, C. (2008). Analysis of effects of oil additive into friction coefficient variations on journal bearing using artificial neural network. *Industrial Lubrication and Tribology*, vol. 60, no. 6, p. 309-316, **DOI:10.1108/00368790810902241**.

[14] Nasir, T., Yousif, B.F., McWilliam, S., Salih, N.D., Hui, L.T. (2010). An artificial neural network for prediction of the friction coefficient of multi-layer polymeric composites in three different orientations. *Proceedings of the Institution of Mechanical Engineers, Part C: Journal of Mechanical Engineering Science*, vol. 224, no. 2, p. 419-429, **DOI:10.1243/09544062JMES1677**.

[15] Anđelković, B., Al-Sammarraie, A., Milčić, D., Stamenković, D., Banić, M., Marinović, J.S., Đorđević, B., Zdravković, N. (2018). Consideration of the use of artificial intelligence methods for determining the friction coefficient of lubricated sliding bearings. *IOP Conference Series: Materials Science and Engineering*, vol. 393, **DOI:10.1088/1757-899X/393/1/012063**.

[16] Al-Sammarraie, A., Milčić, D., Banić, M., Milčić, M. (2017). Tribological behavior of radial plain bearing made of TiN-based white metal alloy- Tegotenax V840. *15th International Conference on Tribology*, p. 258-266.

[17] Al Sammarraie, A., Milčić, D., Banić, M., Milčić, M. (2018). Tribological behavior of Tin- based materials - Tegotenax V840 in oil lubricated conditions. *Annals of Faculty Engineering Hunedoara*, vol. 16, no.1, p.149-152.

Strojniški vestnik - Journal of Mechanical Engineering 67(2021)9, 421-432
© 2021 Journal of Mechanical Engineering. All rights reserved.
DOI:10.5545/sv-jme.2021.7178 Original Scientific Paper
Received for review: 2021-03-21
Received revised form: 2021-06-24
Accepted for publication: 2021-09-17

Multi-parametric Dynamic Analysis of a Rolling Bearings System

Almatbek Kydyrbekuly[1] – Gulama-Garip Alisher Ibrayev [1] – Tangat Ospan[1] – Anatolij Nikonov[2,*]
[1] Al-Farabi Kazakh National University, Kazakhstan
[2] Faculty of Industrial Engineering Novo mesto, Slovenia

A method for calculating amplitudes and constructing frequency characteristics of forced and self-excited vibrations of a rotor-fluid-foundation system on rolling bearings with a non-linear characteristic based on the method of complex amplitudes and harmonic balance has been developed. Non-linear equations of motion of the rotor-fluid-foundation system are derived, and analytical methods of their solution are presented. Frequencies of fundamental and ultra-harmonic resonances are determined. The intervals between self-oscillation frequencies are estimated. The dependence of amplitudes on the amount of fluid in the rotor cavity, the mass of the foundation, linear imbalance, the value of the stiffness coefficient, and the damping coefficient is shown.

Keywords: forced vibrations, resonance, fluid, rolling bearing, self-oscillations, ultra-harmonic

Highlights

- *A dynamic model of the rotor-fluid-foundation system on rolling bearings with a non-linear characteristic has been constructed.*
- *The specific features of the system with many degrees of freedom are defined.*
- *The prerequisites under which the fluid stabilizes the behaviour of a non-linear system are determined.*
- *The optimal parameters of the system, providing its stable operating mode, are determined.*

0 INTRODUCTION

One of the main tasks of dynamics of rotors and design of rotary machines is the choice of parameters that provide their stable operation. The damping of forced and purely non-linear self-excited rotor vibrations by selecting parameters of the system, taking into account vibrations of the foundation, elasticity of supports, imbalance and other parameters, is of great interest from both technical and economic points of view.

Currently, many works on the study of non-linear oscillations of rotor systems exist **[1]**. However, their dynamics is insufficiently studied because of difficulties arising in taking into account the mutual influence and combined actions of factors such as the presence of fluid in the rotor cavity, external non-conservative forces **[2]**, different types of linear and angular imbalances and nonlinearities **[3]** and **[4]**.

In the design of rotary machines, one of the most important mechanical components described by non-linear models is elastic support, which ensures the operability and reliability of the system **[5]** to **[7]**. In this paper, rolling bearings act as elastic supports **[8]**. The neglect of non-linear properties of bearings prevents correct qualitative and quantitative results for rotor systems from being obtained **[9]** to **[11]**. This phenomenon can be explained by the fact that when analysing linear rotor systems with rolling bearings, an approximate estimate of stiffness and damping properties of bearings is most often used, whereas in reality the bearing stiffness heavily depends on the load, i.e., on the operating mode of the rotor system, on the geometry and size of the bearing clearances, on the size of the fit of the inner and outer rings in the bearing, and other factors **[12]** and **[13]**.

To obtain a detailed description of the process, it is necessary to consider the influence of such factors as imbalance, asymmetry of the rotor on the shaft, external friction, changes in inertial parameters and positional forces of various kinds **[14]** to **[16]**. Such complications of the model in the analysis of dynamics make it possible to study the influence of the gap size, rotation frequency on frequency spectra, and amplitude-frequency characteristics for any rotor system on rolling bearings.

Mathematical models of bearings that take into account nonlinearity factors are distinguished by complexity and primarily by the loads that they consider. In our case, to describe the bearing model, the Hertz contact theory is used, which connects the radial loads acting on the bearing and the deformation at the contact points between the rolling element and the bearing rings **[17]**. In the bearing model, it is assumed that there are no types of sliding of bodies and rolling surfaces. Damping is considered in terms of equivalent viscous and linear friction.

1 STATEMENT OF PROBLEM AND EQUATIONS OF MOTION

A symmetrical vertical rotor of mass m with a cylindrical cavity of radius R, partially filled with an ideal fluid, is rotating on rolling bearings with a constant angular velocity Ω_0. The angular velocity is considered sufficiently large so that the fluid in the

*Corr. Author's Address: Faculty of Industrial Engineering Novo mesto, Šegova ulica 112, 8000 Novo mesto, Slovenia, anatolij.nikonov@fini-unm.si

rotor cavity takes the form of a cylindrical ring. Due to the different positions of the centre of mass and the geometric centre, the rotor has a static imbalance (or linear eccentricity) e. The foundation of mass M rigidly connected to the outer ring is mounted on elastic supports with an equivalent linear stiffness coefficient c_2 (see Fig. 1); below, all the dimensional parameters shown in this figure are appropriately dimentionalized, see Section 3. The radial compliance of bearings occurs due to deformation of the rolling elements and raceways at the contact points. In this case, the non-linear restoring force in bearings can be generally described using the Hertz contact formula [14] and [18]:

$$F_C = C_b \delta_r^{\frac{3}{2}}. \tag{1}$$

However, for the sake of simplicity, in what follows, the restoring force in rolling bearings is approximated by a power series according [16]:

$$F_C = c_0 \delta_r + c_1 \delta_r^3, \tag{2}$$

where F_C is a component of the restoring force in the radial direction, δ_r is the deformation in the radial direction, C_b is the stiffness coefficient, c_0 and c_1 are stiffness coefficients for the linear and cubic terms, respectively. This expansion at $\delta_r < 1000$ μm agrees with the experimental results in [18].

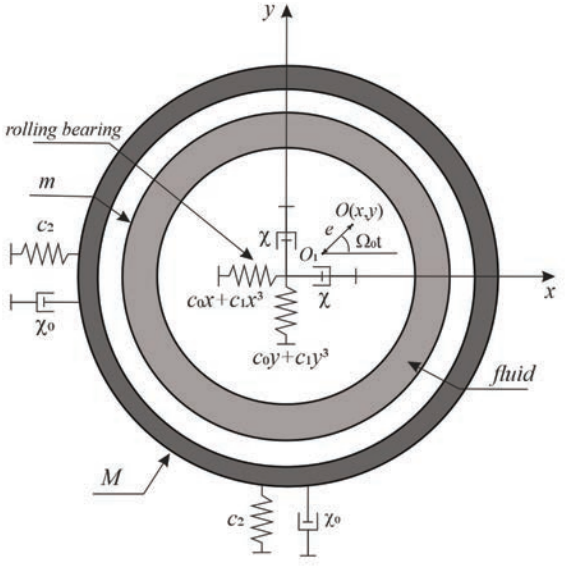

Fig. 1. *Scheme of a rotor on rolling bearings, with a cavity partially filled with an ideal fluid and mounted on a foundation*

The motion of the system is considered concerning the fixed coordinate system $Oxyz$. The coordinates of the centre of mass of the rotor are denoted as $A(x,y)$, and the coordinates of the centre of mass of the foundation are denoted as $A_2(x_2,y_2)$, χ and χ_0 are the external friction coefficients, $O\xi\eta$ the coordinate system associated with the rotor, η is its polar axis, and axis ξ is arbitrarily drawn through the eccentricity vector of the rotor mass.

Let us introduce complex variables in the form:

$$x + iy = z, \quad x_2 + iy_2 = z_2, \tag{3}$$

for analysing plane-parallel motion of the rotor and foundation. Then, assuming that damping force acting on rotor depends on velocities of the rotor itself, and similarly, damping force acting on foundation depends on the velocities of the foundation itself, we present the equations of motion of the system in question in the form, here and below see [8] and references therein,

$$\ddot{z} + n_0^2 (z - z_2) + n_1 (z - z_2)^3 + 2k\dot{z} = \\ = e\Omega_0^2 \exp(i\Omega_0 t) + \frac{F_r}{m},$$
$$\ddot{z}_2 + n_2^2 z_2 - n_{01}^2 (z - z_2) - n_{10} (z - z_2)^3 + 2k_0 \dot{z}_2 = 0, \tag{4}$$

where

$$n_0^2 = \frac{2c_0}{m}, \; n_1 = \frac{2c_1}{m}, \; 2k = \frac{\chi}{m}, \; n_2^2 = \frac{2c_2}{M},$$
$$n_{01}^2 = \frac{2c_0}{M} = \mu n_0^2, \; n_{10} = \frac{2c_1}{M} = \mu n_1, \; 2k_0 = \frac{\chi_0}{M}, \; \mu = \frac{m}{M},$$

and F_r is a complex expression for the reaction force of a fluid, which is defined as:

$$F_r = Rh \int_0^{2\pi} P|_{r=R} e^{i(\Omega_0 t + \varphi)} d\varphi, \tag{5}$$

where h is the rotor cavity height, $P|_{r=R}$ is the fluid pressure on the rotor wall.

The equations of motion for fluid are written as:

$$\frac{\partial u}{\partial t} - 2\Omega_0 \upsilon = -\frac{1}{\rho}\frac{\partial P}{\partial r} - \ddot{x}\cos(\Omega_0 t + \varphi) \\ -\ddot{y}\sin(\Omega_0 t + \varphi),$$
$$\frac{\partial \upsilon}{\partial t} + 2\Omega_0 u = -\frac{1}{\rho r}\frac{\partial P}{\partial \varphi} + \ddot{x}\sin(\Omega_0 t + \varphi) \\ -\ddot{y}\sin(\Omega_0 t + \varphi), \tag{6}$$

where u and υ are the radial and tangential components of the velocity of the fluid particle, P and ρ are pressure and density of the fluid.

The continuity equation at ρ = const is given by:

$$\frac{\partial (ur)}{\partial r} + \frac{\partial \upsilon}{\partial \varphi} = 0. \tag{7}$$

The boundary conditions for the Eqs. (6) and (7) can be written as:

$$u|_{r=R}=0, \tag{8}$$

and

$$\left.\frac{\partial P}{\partial t}\right|_{r=r_0}=-\rho\Omega_0{}^2 r_0 u|_{r=r_0}, \tag{9}$$

where r_0 is the radius of the free fluid surface. These relations express the impenetrability condition at the rotor wall and the conditions on the fluid pressure along the free surface, respectively.

Eqs. (3) to (7) with boundary conditions Eqs. (8) and (9) in combination with the continuity equation form a closed system of equations.

2 NON-LINEAR FORCED VIBRATION AND SELF-OSCILLATIONS OF THE ROTOR-FLUID-FOUNDATION SYSTEM

Assuming that the rotor and the foundation perform harmonic oscillations, we seek the solution of the system of equations Eq. (4) in the form **[20]** and **[21]**,

$$z=Z_r\exp\left(i\left(\Omega_0 t-\phi\right)\right)+A_r\exp\left(i\omega t\right), \tag{10}$$

$$z_2=Z_f\exp\left(i\left(\Omega_0 t-\phi\right)\right)+B_f\exp\left(i\omega t\right), \tag{11}$$

where ω is natural frequency, Z_r and Z_f are forced vibration amplitudes of rotor and foundation, while A_r and B_f are natural vibration amplitudes of rotor and foundation, respectively.

The presence of an angle ϕ i.e., a phase lag, is caused by the presence of resistance forces in the system.

As an expression describing the action of the hydrodynamic force on the system, which arises due to the presence of fluid in the cavity, we start from formulae in **[8]** and **[19]**, taking into account Eqs. (10) and (11):

$$F_r=F_x+iF_y=Z_r m_L\Omega_0{}^2\exp\left(i\left(\Omega_0 t-\phi\right)\right)+ +A_r m_L\omega^2\frac{\left(\sigma^2-2\Omega_0\sigma-\Omega_0{}^2\right)}{\left(\gamma\sigma^2-2\Omega_0\sigma-\Omega_0{}^2\right)}\exp(i\omega t), \tag{12}$$

where

$$q=\frac{R}{r_0},\quad \sigma=\omega-\Omega_0, \tag{13}$$

$m_L=\pi\rho R^2 h$ is the mass of fluid required to completely fill the rotor cavity, σ vibration frequency of the free surface of the fluid.

Substituting Eqs. (10), (11) and (12) in Eq. (4), we obtain a system of algebraic equations for the unknowns A_r, B_f, Z_r and Z_f. Its solution is given by:

$$Z_r=\frac{f_0}{f_1},\quad Z_f=\frac{f}{f_1}, \tag{14}$$

$$B_f=(p_1+ip_2)A_r, \tag{15}$$

$$Z_r-Z_f=\frac{f_0-f}{f_1}=f_2, \tag{16}$$

$$A_r=\left(\frac{p_1}{p^2{}_1+p_2{}^2}-\frac{ip_2}{p^2{}_1+p_2{}^2}\right)B_f, \tag{17}$$

where

$$f_0=rp_0-pr_0,\quad f=pq_0+qp_0,\quad f_1=rq_0+qr_0,$$
$$q=\mu\Omega_0^2(1+\mu_L),\quad p=\mu e\Omega_0^2\cos\phi,\quad r=n_2{}^2-\Omega_0^2,$$
$$q_0=2\mu\Omega_0 k,\quad p_0=\mu e\Omega_0^2\sin\phi,\quad r_0=2k_0\Omega_0,$$

$$p_1=\frac{\mu\omega^2\left(n_2{}^2-\omega^2\right)\left(1+\mu_L\frac{D_3}{D_4}\right)-4kk_0\omega^2}{m_1},$$

$$p_2=-\frac{2\mu\left(\left(1+\mu_L\frac{D_3}{D_4}\right)\omega^2 k_0+\left(n_2{}^2-\omega^2\right)k\right)\omega}{m_1},$$

$$m_0=n_2^2-\Omega_0^2+2k_0\Omega_0 i,\quad m_1=\left(n_2^2-\omega^2\right)^2+4k_0{}^2\omega^2,$$
$$m_2=n_2^2-\omega^2+2k_0\omega i,\quad D_3=\sigma^2-2\Omega_0\sigma-\Omega_0^2,$$
$$D_4=\gamma\sigma^2-2\Omega_0\sigma-\Omega_0^2.$$

$\mu_L=m_L/m$ is the ratio of the mass of fluid required to completely fill the rotor cavity to the mass of the rotor.

Thus, to determine the unknown amplitudes, we may derive two non-linear equations from the relations above:

$$m_0 Z_f-(Z_r-Z_f)\cdot\left(n_{01}+n_{10}\left(\frac{3}{4}(Z_r-Z_f)^2+\frac{3}{2}(A_r-B_f)^2\right)\right)=0, \tag{18}$$

$$m_2 B+(A_r-B_f)\cdot\left(-n_{01}-n_{10}\left(\frac{3}{2}(Z_r-Z_f)^2+\frac{3}{4}(A_r-B_f)^2\right)\right)=0. \tag{19}$$

After substituting Eqs. (14) to (16) into Eq. (18), a quadratic equation for A_r can be obtained. Using the values of the amplitudes Z_r, Z_f, A_r and B_f calculated from Eq. (19), we can determine the phase angle ϕ.

The linearized form of Eqs. (18) and (19) becomes:

$$\ddot{z} + n_0^2(z - z_2) + 2k\dot{z} = 0,$$
$$\ddot{z}_2 + n_2^2 z_2 - n_{01}^2(z - z_2) + 2k_0\dot{z}_2 = 0. \quad (20)$$

Since the resistance forces do not strongly affect the value of the natural frequency [22], in this case, it is sufficient to find the frequency equation for $k = k_0 = 0$, i.e., for the equation in the form:

$$\begin{bmatrix} 1 & 0 \\ 0 & 1 \end{bmatrix}\begin{bmatrix} \ddot{z} \\ \ddot{z}_2 \end{bmatrix} + \begin{bmatrix} n_0^2 & -n_0^2 \\ -\mu n_0^2 & n_2^2 + \mu n_0^2 \end{bmatrix}\begin{bmatrix} z \\ z_2 \end{bmatrix} = \begin{bmatrix} 0 \\ 0 \end{bmatrix}. \quad (21)$$

To obtain a frequency equation, we seek the solution in the form:

$$z = z_s \exp\left(i\left(\omega t - \varphi\right)\right), z_2 = z_{2s} \exp\left(i\left(\omega t - \varphi\right)\right). \quad (22)$$

Substituting Eq. (22) into Eq. (21), we obtain:

$$\begin{bmatrix} n_0^2 - \omega^2 & 0 & -n_0^2 & 0 \\ 0 & n_0^2 - \omega^2 & 0 & -n_0^2 \\ -\mu n_0^2 & 0 & n_2^2 + \mu n_0^2 - \omega^2 & 0 \\ 0 & -\mu n_0^2 & 0 & n_2^2 + \mu n_0^2 - \omega^2 \end{bmatrix} \cdot \begin{bmatrix} A_s \\ B_s \\ C_s \\ D_s \end{bmatrix} = \begin{bmatrix} 0 \\ 0 \\ 0 \\ 0 \end{bmatrix}, \quad (23)$$

where

$$z_s = \sqrt{A_s^2 + B_s^2}, \quad z_{2s} = \sqrt{C_s^2 + D_s^2}. \quad (23)$$

Then, to find the values of the natural frequencies ω, it is sufficient to find the determinant of system Eq. (23), i.e.:

$$\det \begin{Vmatrix} n_0^2 - \omega^2 & 0 & -n_0^2 & 0 \\ 0 & n_0^2 - \omega^2 & 0 & -n_0^2 \\ -\mu n_0^2 & 0 & n_2^2 + \mu n_0^2 - \omega^2 & 0 \\ 0 & -\mu n_0^2 & 0 & n_2^2 + \mu n_0^2 - \omega^2 \end{Vmatrix} = 0. \quad (24)$$

Then, the frequency equation is written as:

$$\omega^8 + \lambda_1\omega^6 + \lambda_2\omega^4 + \lambda_3\omega^2 + \lambda_4 = 0, \quad (25)$$

where

$$\lambda_1 = -\left(\Delta_1 + 2\Delta_4\right), \quad \lambda_2 = \Delta_1^2 - \Delta_2\Delta_3 + 4\Delta_1\Delta_4 + \Delta_4^2,$$
$$\lambda_3 = -2\Delta_1\Delta_4\left(\Delta_1 + \Delta_4\right), \quad \lambda_4 = \Delta_1^2\Delta_4^2 - \Delta_2^2\Delta_3^2,$$
$$\Delta_1 = n_0^2, \quad \Delta_2 = -\mu n_0^2, \quad \Delta_3 = -n_0^2, \quad \Delta_4 = n_2^2 + \mu n_0^2.$$

Thus, four natural frequencies are obtained, where the lowest frequency is taken as the first frequency. The accuracy of the approximate formulae for natural frequencies are discussed in [19], [21], and [22].

It should be noted that the search for a solution in the form of Eqs. (10) and (11) makes it possible to study both forced and self-excited vibrations in general; however, at the same time, this approach excludes the possibility of studying steady-state vibrations (which is typical for the case of an empty or a completely filled rotor), since the partial filling of the cavity with fluid causes the appearance of self-oscillations.

Thus, by slowly changing the angular velocity of the rotor, it is possible to construct the amplitude-frequency characteristics of the system while varying the parameters of the rotor, foundation, and fluid.

3 RESULTS AND DISCUSSION

To analyse the system and determine the optimal operating mode, the amplitude-frequency characteristics of the rotor and foundation were constructed. They were obtained from Eqs. (18) and (19) and numerical solution of the differential equations of motion of the system for different degrees of filling of the rotor cavity with fluid, different values of the damping coefficient (χ), non-linear stiffness (c_1), imbalance (e) and different values of the foundation mass (M). For qualitative analysis of the system, the following dimensionless parameters were introduced:

$$s = \frac{\Omega_0}{\omega}, \quad E = \frac{e}{R}, \quad K = \frac{k}{\Omega_0}, \quad C = \frac{n_1 e^2}{\Omega_0^2}, \quad (26)$$

where s is a dimensionless frequency, E is a dimensionless parameter of linear imbalance, Z_r is a dimensionless amplitude of the rotor, Z_f is a dimensionless amplitude of the foundation, K is a dimensionless damping coefficient, C is a dimensionless coefficient of stiffness at the cubic term, R is a cavity radius (see Figs. 2 to 11).

When an insignificant amount of fluid is present in the cavity, e.g. $r_0 = 0.93R$, (see Figs. 2 and 3), three self-oscillation zones and three resonance amplitudes are observed for both the rotor and the foundation. All figures show examples when the system parameters take the values: $\chi = 4200$ kg/s, $\chi_0 = 6.59$ kg/s, $c_0 = 1.1 \cdot 10^7$ kg/s^2, $c_1 = 0.87 \cdot 10^7$ kg/m^{2}s^2, $c_2 = 3.26 \cdot 10^5$ kg/s^2, $M = 25$ kg, $m = 2.4$ kg, $e = 0.001$ m. The amplitude-frequency characteristic, in this case, demonstrates a monotonic increase over the interval $0 < s < 0.065$ up to the first resonance peak. The first resonance occurs at $s = 0.065$, where the amplitudes are $Z_r = 0.083$ and $Z_f = 0.0091$. Then, over the interval $0.065 < s < 0.65$, a self-oscillating mode occurs (see Figs. 2 and 3) with maximum amplitudes of 0.028 for the rotor and 0.001 for the foundation, respectively. At $s = 0.65$, the second resonance occurs with the

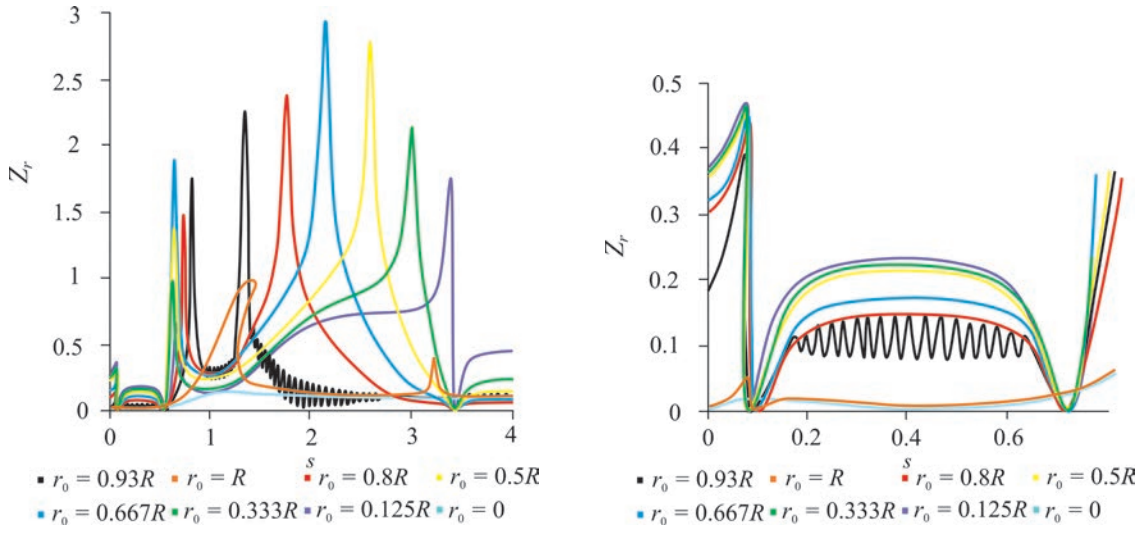

Fig. 2. *Amplitude-frequency characteristics of the rotor at different degrees of the rotor cavity filling, r_0*

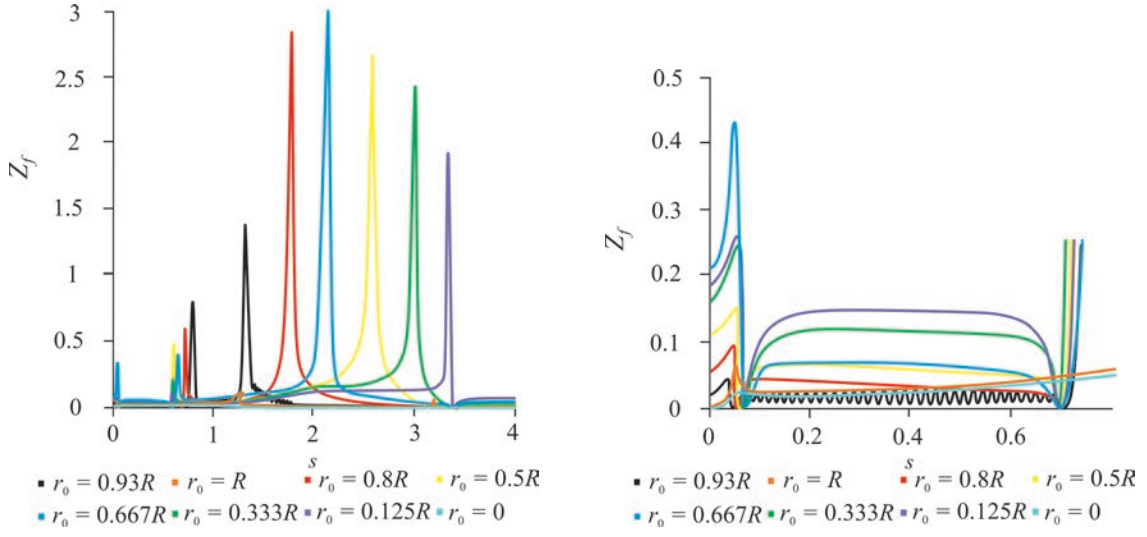

Fig. 3. *Amplitude-frequency characteristics of the foundation at different degrees of the rotor cavity filling, r_0*

amplitudes 1.72 and 0.79 for the rotor foundation, respectively. Further, over the interval $0.65<s<1$, the vibration amplitudes decrease monotonically to the values 0.07 and 0.013. Next, over the interval $1<s<1.35$, the amplitude of vibrations grows rather intensively up to the third resonance, where $s=1.35$, and the amplitudes are $Z_r=2.23$ and $Z_f=1.38$. Further, in the interval $1.35<s<3.41$, the amplitudes monotonically decrease to the third self-oscillation zone, which occurs at $s=3.41$, where the amplitudes take constant values $Z_r=0.057$, $Z_f=0.0003$, which is caused by the effect of self-centring and non-conservative circulation-type forces arising due to the presence of fluid in the rotor cavity. Here, the self-oscillation zones are presented as a curve showing the oscillatory process. In all other cases, the curves corresponding to self-oscillations are smoothed.

With the increase of the fluid volume in the cavity at $r_0=0.8R$, it can be seen that the first and second resonances, as well as the first self-oscillation zone, occur at the same frequencies as at $r_0=0.93R$, but with larger amplitudes. For example, at the first resonance, i.e., at $s=0.065$, the amplitudes are $Z_r=0.15$ and $Z_f=0.015$, that is, a 4.74-times increase of the fluid volume leads to 1.82- and 1.65-times increase in the amplitudes of the rotor and foundation, respectively. The maximum amplitudes of self-oscillations, in this case, also have higher values. For example, they reach

0.088 for the rotor, and 0.0097 for the foundation, which is 3.14- and 9.7-times higher than in the previous case, respectively. At the second resonance ($s=0.65$), the amplitudes are $Z_r=1.5$ and $Z_f=0.59$, which practically does not differ from the previous case. The third resonance peak in this case shifts to higher frequency range and occurs at $s=1.75$, where $Z_r=2.36$, $Z_f=2.83$. Then, for $s>3.41$, a self-oscillation zone is formed, where the amplitudes take on constant values $Z_r=0.139$ and $Z_f=0.0006$.

When the fluid volume in the rotor cavity is one third of the total volume, i.e., $r_0=0.667R$ (see, e.g., Figs. 2 and 3), the maximum resonance amplitudes are observed. The first and second resonances, as well as the first self-oscillation zone, occur at the same frequencies as in the two previous cases, the amplitudes are, respectively, $Z_r=0.198$, $Z_f=0.033$ and $Z_r=1.9$, $Z_f=0.38$; the maximum amplitudes of the first self-oscillation zone are $Z_r=1.9$, $Z_f=0.38$. In this case, the third resonance peak also appears at a greater angular velocity occurring at $s=2.12$, with amplitudes $Z_r=2.93$, $Z_f=2.99$. Then, as before, at $s>3.41$, a self-oscillation zone is formed, where the amplitudes take on constant values $Z_r=0.15$ and $Z_f=0.0008$. The maximum amplitudes when one third of the cavity is fluid-filled and are associated with a specific behaviour of a "coupled" solid-fluid system **[8]**, **[19]**, and **[23]**.

Furthermore, for cases $r_0=0.5R$, $r_0=0.333R$ and $r_0=0.125R$, frequencies of the first and second resonances, i.e., $s=0.065$ and $s=0.65$, as well as the frequencies of formation of self-oscillation zones, i.e., $0.065<s<0.65$, $0.65<s<3.41$ and $s>3.41$, do not change. The values of the first and second resonance amplitudes are damped. The third resonant amplitude is also damped, while the related resonance frequency is shifted to the right (see, e.g., Figs. 2 and 3), due to the increase of the fluid volume. At the same time, the fluid volume does have a significant effect on the amplitudes over the first, second and third zones of self-oscillations.

For an empty rotor, a breakdown of the amplitude-frequency characteristics of both the rotor and foundation, corresponding to the fundamental resonance, is typical for the studied cubic nonlinearity, as for a Duffing oscillator. This phenomenon, which arises as a result of a monotonic increase in the amplitudes and their sharp decrease after a certain frequency, has been studied in detail by many authors, e.g. **[24]** to **[26]**. In this case, the breakdown of the amplitude of the empty rotor with a gradual increase in frequency occurs at $Z_r=1.05$ and $s=1.33$, then the amplitudes of the rotor decrease to 0.15. A similar behaviour of the amplitude at $s=1.33$ is observed for the foundation; in this case, the maximum amplitude is $Z_f=0.115$, which is almost an order of magnitude less than the rotor amplitudes. The foundation amplitudes after the breakdown decrease to 0.01. This difference between the amplitudes of the forced vibrations of the rotor and the foundation is primarily due to the ratio of the masses of the rotor and the foundation, as well as the value of linear eccentricity. As might be expected, an additional (first) linear resonance appears at $s=0.065$, according to the general theory in the book **[27]**. It should be noted that the third resonance is a specific feature of a non-linear system; this feature is addressed in greater detail below. For a fully fluid-filled rotor, the first and third resonances are suppressed, while the second resonance looks similar in a sense to the linearized case.

Thus, maximum amplitudes of forced oscillations of the rotor and the foundation are observed when one third of the rotor cavity is filled with fluid. In addition, a decrease in the fluid volume leads to a shift of the third resonance towards lower angular frequencies.

Decrease of the damping coefficient ($K=0.01$) causes a shift of the third resonance to higher angular velocities (see Figs. 4 and 5). The first and second resonances are observed at virtually the same frequencies as for $r_0=0.667R$ and $K=1$, i.e., at $s=0.065$ and $s=0.65$ with amplitudes $Z_r=0.62$, $Z_f=0.33$ and $Z_r=0.52$, $Z_f=0.07$. The first resonance at $K=0.01$ coincides in magnitude with the resonance at $K=1$. The second resonance of the rotor and foundation for $K=0.01$ is 6.35 and 54.28 times lower than the corresponding resonances for $K=1$. The number of self-oscillating zones does not change, i.e., three self-oscillation zones are observed, the first in the interval $0.065<s<0.65$, the second in the interval $0.65<s<3.41$, and the third at $s>3.41$ with maximum amplitudes $Z_r=0.43$, $Z_f=0.043$, $Z_r=0.9$, $Z_f=0.19$ and $Z_r=0.104$, $Z_f=0.017$, respectively. The shifted third resonance appears at $s=3.4$ with amplitudes $Z_r=8$ and $Z_f=13.3$, which is 2.76 times and 1.34 times less than the amplitudes of the third resonance of the rotor and foundation, respectively, at $K=1$.

With a significant increase in the damping coefficient, i.e., for $K=0.1$, the amplitudes of self-oscillations are damped and coincide with those at $K=1$. The resonance amplitudes of the rotor and the foundation increase in magnitude. The first, second and third resonances appear at the same frequencies as for $K=1$, that is, at $s=0.065$, $s=0.65$ and $s=2.12$, with amplitudes $Z_r=0.9$, $Z_f=0.3$, $Z=2.9$, $Z_f=4.1$ and $Z_r=25.5$, $Z_f=9.1$, which coincides in magnitude with

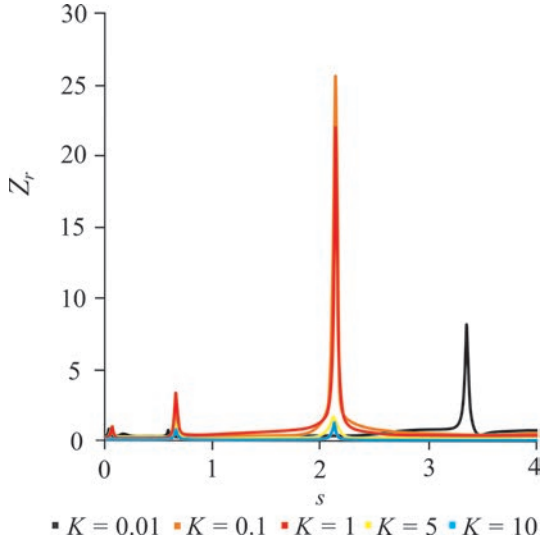

Fig. 4. *Amplitude-frequency characteristics of the rotor Z_r for various damping coefficients K*

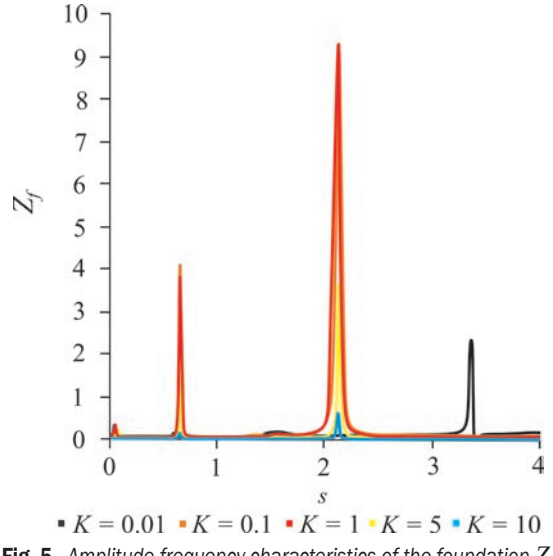

Fig. 5. *Amplitude-frequency characteristics of the foundation Z_f for various damping coefficients K*

the first, second, and third amplitudes of both the rotor and the foundation for $K=1$.

Further increase in the damping coefficient (cases $K=5$ and $K=10$) leads to significant damping of self-oscillations and resonance amplitudes, for example, for $K=5$, the amplitudes of the first, second, and third resonances are equal to $Z_r=0.02$, $Z_f=0.003$, $Z_r=1.15$, $Z_f=0.4$ and $Z_r=1.7$, $Z_f=3.6$, respectively. For $K=10$, the amplitudes of the first, second, and third resonances are $Z_r=0.02$, $Z_f=0.003$, $Z_r=0.66$, $Z_f=0.1$ and $Z_r=1.1$, $Z_f=2.5$, respectively.

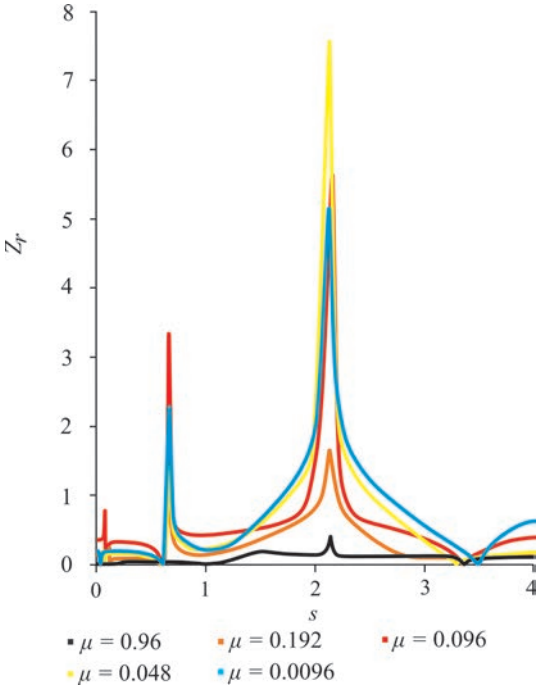

Fig. 6. *Amplitude-frequency characteristics of the rotor Z_r for different values of the foundation mass, μ*

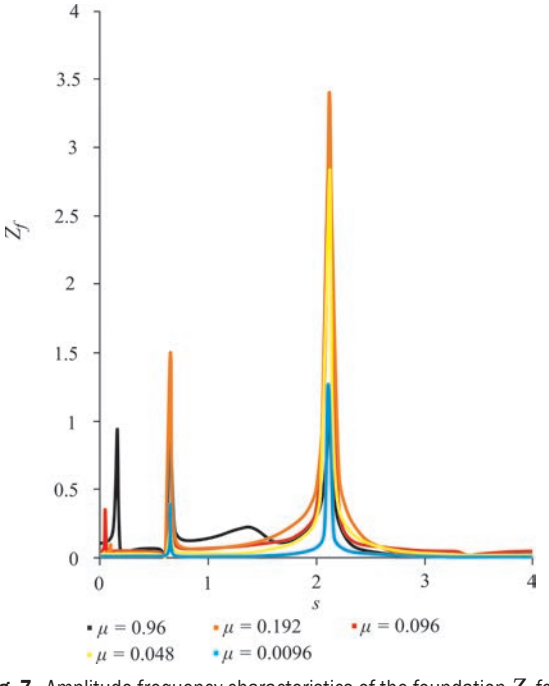

Fig. 7. Amplitude-frequency characteristics of the foundation Z_f for different values of the foundation mass, μ

In addition, with a significant decrease of the damping coefficient, a shift of the third resonance to higher angular velocities occurs. In particular, for a third fluid filled rotor, the aforementioned resonance

is observed at the same frequency as that of an empty rotor ($s=3.4$), which is a distinctive feature of non-linear vibrations.

To assess the effect of the foundation mass on self-oscillations and resonance amplitudes at $r_0=0.667R$, various ratios of the rotor and foundation masses $\mu=0.96$, $\mu=0.192$, $\mu=0.096$, $\mu=0.048$ and $\mu=0.0096$ were considered and for each case the amplitude-frequency characteristics were constructed (see Figs. 6 and 7).

In all of the above cases, the first, second, and third resonances were observed at $s=0.065$, $s=0.65$, and $s=2.12$, respectively. With an increase in the mass of the foundation (cases $\mu=0.096$, $\mu=0.048$), there is an increase in the amplitudes of the rotor at the third resonance (at $s=2.12$, $Z_r=5.6$, $Z_f=7.53$) and self-excited vibrations in general, whereas the resonance amplitudes and amplitudes of self-oscillations of the foundation decrease in magnitude. In the case in which the mass of the foundation is slightly greater than the mass of the rotor (cases $\mu=0.192$ and $\mu=0.96$), the minimum amplitudes of the third resonances of both the rotor and the foundation are observed ($Z_r=1.94$ and $Z_f=3.39$, $Z_r=0.34$ and $Z_f=1.01$). It should be noted that at $\mu=0.96$ in the interval $0.65<s<2.125$, a zone of intense self-oscillations of the foundation with a maximum amplitude of 0.28 appears (see Fig. 7). Damping the rotor amplitudes with a decrease in the mass of the foundation is a specific feature of the non-linear system. In the linear case, a decrease in the rotor amplitudes is observed with an increase in the mass of the foundation, as in this case the foundation itself acts as an anti-load.

To study the influence of nonlinear effects arising from nonlinearity of the restoring force, different values of the stiffness coefficient at the cubic term were considered, i.e., $C=0.01$, $C=0.1$, $C=1$, $C=10$ and $C=100$, and for each case the amplitude-frequency characteristics with a rotor fluid filled by one third, i.e., for $r_0=0.667R$, are obtained (see Figs. 8 and 9).

An increase in the stiffness coefficient at the cubic term leads to a decrease in both the resonance amplitudes and the amplitudes of self-oscillations of the rotor and the foundation. The maximum amplitudes are observed in the case of $C=0.01$, for which the amplitudes of the first resonance for $s=0.065$ are $Z_r=1.86$ and $Z_f=0.15$, the amplitudes of the second resonance for $s=0.65$ are $Z_r=19.215$ and $Z_f=3.84$, and the amplitudes of the third resonance for $s=2.125$ are $Z_r=23.47$ and $Z_f=14.09$. The minimum resonance amplitudes are, respectively, observed in the case of $C=100$, where the amplitudes of the first

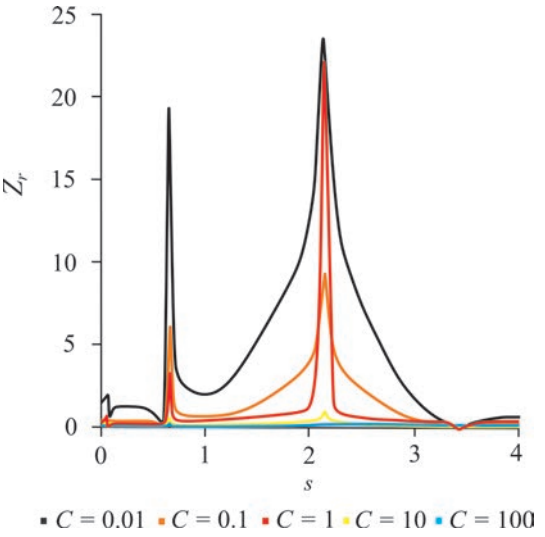

Fig. 8. *Amplitude-frequency characteristics of the rotor Z_r for different values of the stiffness coefficient of the cubic term, C*

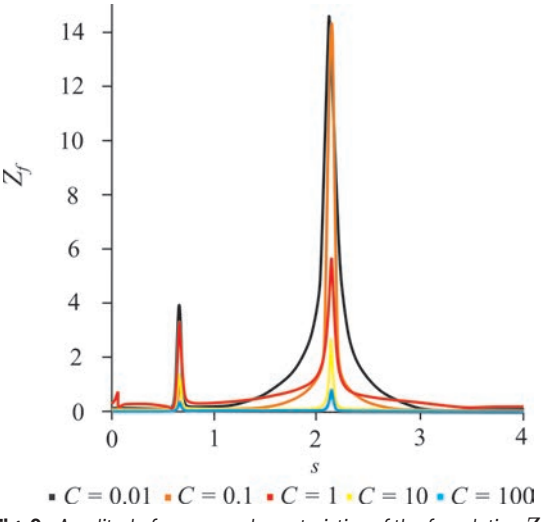

Fig. 9. *Amplitude-frequency characteristics of the foundation Z_f for different values of the stiffness coefficient of the cubic term, C*

resonance for $s=0.065$ are equal to $Z_r=0.03$ and $Z_f=0.01$, the amplitudes of the second resonance for $s=0.65$ are equal to $Z_r=0.07$ and $Z_f=0.37$, and the amplitudes of the third resonance for $s=2.125$ are $Z_r=0.31$ and $Z_f=0.83$, i.e., with an increase in the stiffness coefficient by two orders of magnitude, the resonance amplitudes of the rotor and foundation decrease in 54.78 and 15 times for $s=0.065$, in 266.87 and 10.37 times for $s=0.65$, and in 76.21 and 16.97 times for $s=2.125$. Any significant shift of resonant frequencies and self-oscillation zones is observed when the stiffness coefficient changes. In this case, as in linear cases, an increase in stiffness leads to damping of all vibrations. Analysis of greater values

of the stiffness coefficient is not of practical interest for the original engineering system.

Due to the imperfection of equipment and other factors at high operating speeds, it is important to determine the range of critical values of inbalance e, and to identify its impact on the behaviour of the system. In this work, the cases $E=0.5$, $E=1$, $E=5$ and $E=10$ were considered; for each case the amplitude-frequency characteristics were constructed (see Figs. 10 and 11).

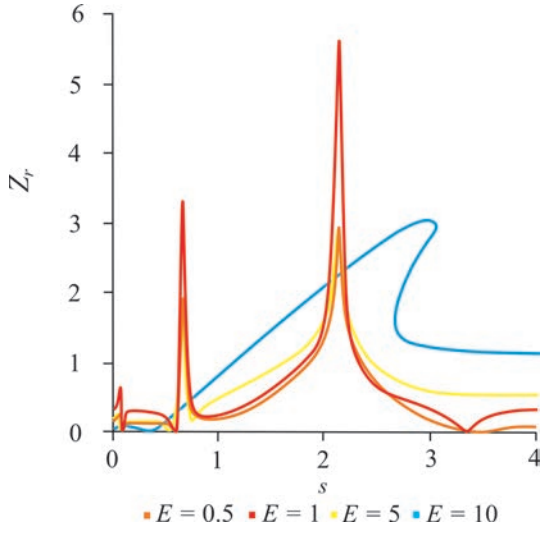

Fig. 10. *Amplitude-frequency characteristics of the rotor Z_r for different values of imbalance, E*

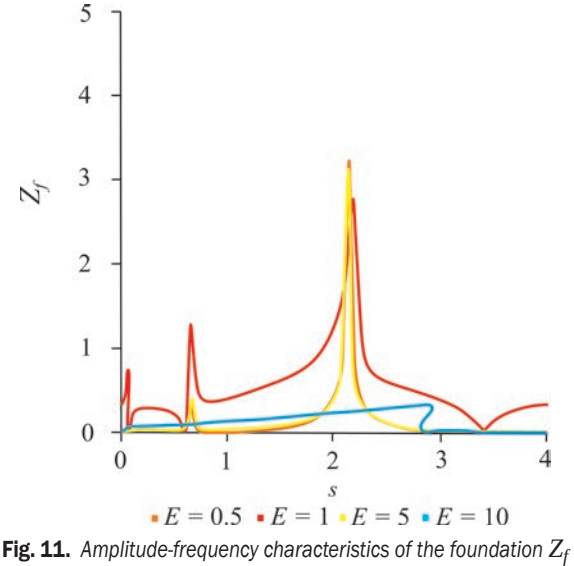

Fig. 11. *Amplitude-frequency characteristics of the foundation Z_f for different values of imbalance, E*

For $E=0.5$, $E=1$ and $E=5$, as before, three resonance amplitudes are observed for $s=0.065$, $s=0.65$, and $s=2.125$. In this case, the change in the imbalance value practically does not affect the values of the resonance amplitudes and amplitudes of self-oscillations.

As the value of imbalance increases by an order of magnitude, i.e., at $E=10$, the amplitude-frequency characteristic of the rotor and the foundation is given by the nonlinearity of a hardening (stiff) type. Thus, with an increase in linear imbalance, self-oscillations arising from the action of the fluid are suppressed by forced vibrations. In this case, the characteristic breakdown of the amplitudes is shifted towards higher frequencies of the system. Further, after the breakdown, due to the self-centring effect, operation of the system is stabilized, and vibrations occur with an amplitude of about $Z_r=1.26$, which slightly exceeds the amplitude of self-oscillations. During rotor vibrations, one self-oscillation zone is observed in the interval $0<s<0.346$ with maximum amplitudes $Z_r=0.08$. During vibrations of the foundation, a sharp variation of the amplitude up to the value $Z_f=0.09$ is observed over the interval $0<s<0.112$. Further, with an increase in frequency, a gradual increase in foundation vibrations is observed until its amplitude breaks down, and, then, as in the case of the rotor, vibrations stabilize with an amplitude of about $Z_f=0.03$. In both cases, for the rotor and for the foundation, breakdown is observed at $s=2.817$.

To understand the nature of the first and third resonances, we construct the amplitude-frequency characteristics of the linear and non-linear "rotor-foundation" system without fluid (see Figs. 12 and 13), which can be obtained from the equations of motion, Eq. (13) for $F_r=0$ as

$$\ddot{z}+n_0^2(z-z_2)+2k\dot{z}=e\Omega_0^2\exp(i\Omega_0 t),$$
$$\ddot{z}_2+n_2^2 z_2-n_{01}^2(z-z_2)+2k_0\dot{z}_2=0, \qquad (27)$$

and

$$\ddot{z}+n_0^2(z-z_2)+n_1(z-z_2)^3+2k\dot{z}=e\Omega_0^2\exp(i\Omega_0 t),$$
$$\ddot{z}_2+n_2^2 z_2-n_{01}^2(z-z_2)-n_{10}(z-z_2)^3+2k_0\dot{z}_2=0. \qquad (28)$$

The linear system of equations, Eq. (27) can be solved with sufficient degree of accuracy by numerical methods (see Figs. 12 and 13, black (solid) curve).

A cubic nonlinearity supports ultra-harmonic ($\Omega_0=3\omega$, or $s=3$) -harmonic resonances ($\Omega_0=\omega/2$ and $\Omega_0=\omega/3$, or $s=0.5$ and $s=0.333$). The frequencies of the latter are multiples of the fundamental one ($\Omega_0=\omega$, or $s=1$). The solution of non-linear equations in Eq. (28) is found analytically, in order to incorporate explicitly the contribution of higher harmonics corresponding to sub- and ultra-harmonic oscillations.

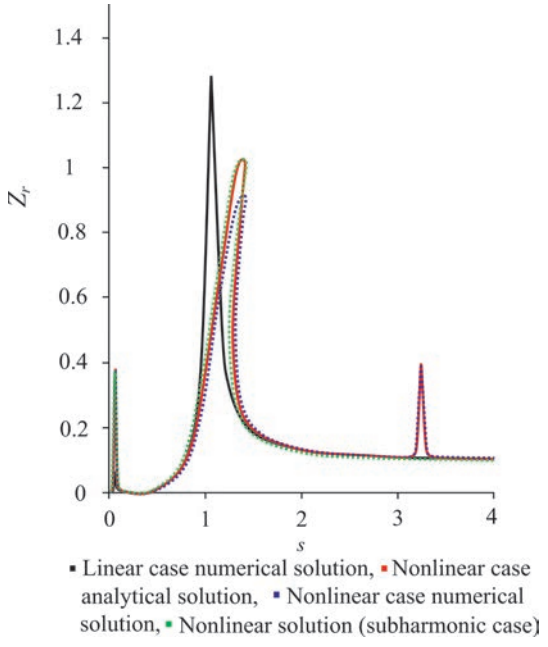

Fig. 12. *Amplitude-frequency characteristics of the rotor Z_r in the linear and non-linear cases*

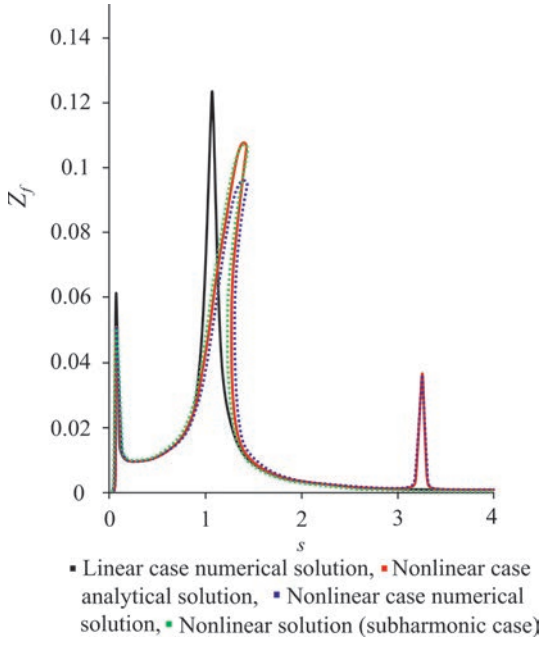

Fig. 13. *Amplitude-frequency characteristics of the foundation Z_f in the linear and non-linear cases*

The restoring force F_c approximated by Eq. (2) does not support sub-harmonic resonance in the system. Then, to find third-order sub-harmonic resonances, we introduce a notation $\Omega_0=3\omega_f$, (ω_f is sub-harmonic frequency) and search for a solution in the form [28]:

$$z=\tilde{B}_{1/3}\exp\left(i\left(\omega_f t-\phi\right)\right)+\tilde{B}_1\exp\left(3i\left(\omega_f t-\phi\right)\right), \quad (29)$$

and

$$z=\tilde{D}_{1/3}\exp\left(i\left(\omega_f t-\phi\right)\right)+\tilde{D}_1\exp\left(3i\left(\omega_f t-\phi\right)\right). \quad (30)$$

Substituting Eqs. (29) and (30) into Eq. (28) and using the harmonic balance method, we obtain a system of algebraic equations:

$$\left(n_0^2-9\omega_f^2\right)\tilde{B}_{1/3}-n_0^2\tilde{D}_{1/3}+\frac{3}{4}n_1\left(\tilde{B}_{1/3}-\tilde{D}_{1/3}\right)^3-$$
$$-\frac{3}{4}n_1\left(\tilde{B}_{1/3}-\tilde{D}_{1/3}\right)^2\left(\tilde{B}_1-\tilde{D}_1\right)-$$
$$-\frac{3}{2}n_1\left(\tilde{B}_{1/3}-\tilde{D}_{1/3}\right)\left(\tilde{B}_1-\tilde{D}_1\right)^2=9e\omega_f^2, \quad (31)$$

$$\left(n_0^2-81\omega_f^2\right)\tilde{B}_1-n_0^2\tilde{D}_1-\frac{1}{4}n_1\left(\tilde{B}_{1/3}-\tilde{D}_{1/3}\right)+$$
$$+\frac{3}{2}n_1\left(\tilde{B}_{1/3}-\tilde{D}_{1/3}\right)^2\left(\tilde{B}_1-\tilde{D}_1\right)+\frac{3}{4}n_1\left(\tilde{B}_1-\tilde{D}_1\right)^3=0, \quad (32)$$

$$\left(n_2^2+n_{01}^2-9\omega_f^2\right)\tilde{D}_{1/3}-n_{01}^2\tilde{B}_{1/3}-\frac{3}{4}n_{10}\left(\tilde{B}_{1/3}-\tilde{D}_{1/3}\right)^3+$$
$$+\frac{3}{4}n_{10}\left(\tilde{B}_{1/3}-\tilde{D}_{1/3}\right)^2\left(\tilde{B}_1-\tilde{D}_1\right)+$$
$$+\frac{3}{2}n_{10}\left(\tilde{B}_{1/3}-\tilde{D}_{1/3}\right)\left(\tilde{B}_1-\tilde{D}_1\right)^2=0, \quad (33)$$

$$\left(n_2^2+n_{01}^2-81\omega_f^2\right)\tilde{D}_1-n_{01}^2\tilde{B}_1+\frac{1}{4}n_{10}\left(\tilde{B}_{1/3}-\tilde{D}_{1/3}\right)-$$
$$-\frac{3}{2}n_{10}\left(\tilde{B}_{1/3}-\tilde{D}_{1/3}\right)^2\left(\tilde{B}_1-\tilde{D}_1\right)-\frac{3}{4}n_{10}\left(\tilde{B}_1-\tilde{D}_1\right)^3=0. \quad (34)$$

Solving Eqs. (31) to (34), we obtain the amplitudes of the steady-state forced vibrations $\tilde{B}_{1/3},\tilde{B}_1,\tilde{D}_{1/3}$ and $\tilde{D}_1$, which can be used to construct the amplitude-frequency characteristics of the rotor and foundation in the case of sub-harmonic vibrations.

To determine ultra-harmonic resonances, the solution is sought in the form:

$$z=Z_r\exp\left(i\left(\Omega_0 t-\phi\right)\right)+B\exp\left(3i\left(\Omega_0 t-\phi\right)\right), \quad (35)$$

and

$$z_2=Z_f\exp\left(i\left(\Omega_0 t-\phi\right)\right)+D\exp\left(3i\left(\Omega_0 t-\phi\right)\right). \quad (36)$$

In this case, the force of reaction of the fluid on the rotor wall has the form:

$$F_r=m_L{\Omega_0}^2A\exp\left(i(\Omega_0 t-\phi)\right)+$$
$$+9m_L{\Omega_0}^2B\exp\left(3i(\Omega_0 t-\phi)\right). \quad (37)$$

Substituting Eqs. (35) and (36) into Eq. (4) and using the harmonic balance method, we obtain a system of non-linear algebraic equations resulting in

$$B = d_0 D, \tag{38}$$

and

$$D = dB, \tag{39}$$

where

$$d_0 = a_0 + ia_1, \quad dd_0 = 1, \quad d = \frac{a_0 - ia_1}{a_0^2 + a_1^2},$$

$$a_0 = \frac{-(b_0 c_0 + b_1 c_1)}{b_3}, \quad a_1 = \frac{-(b_0 c_1 - b_1 c_0)}{b_3},$$

$$b_3 = b_0^2 + b_1^2, \quad b_0 = -9\Omega_0^2 \mu (1 + \mu_L D_0),$$

$$b_1 = 6\Omega_0 k\mu, \quad D_0 = \frac{1}{4\gamma - 3}, \quad c_0 = n_2^2 - 9\Omega_0^2,$$

$$c_1 = 6\Omega_0 k_0, \quad b_1 = 6\Omega_0 k\mu.$$

To determine the unknowns, we also have a system of two equations, which takes the form:

$$e_0 C - n_{01}(Z_r - Z_f) + n_{10}(Z_r - Z_f) \cdot \left(\frac{3}{4}(Z_r - Z_f)^2 + \right.$$

$$\left. + \frac{3}{2}(B - D)^2 + \frac{3}{4}(B - D)(Z_r - Z_f) \right) = 0,$$

$$e_1 D - n_{01}(B - D) - n_{10} \cdot \left(\frac{3}{4}(B - D)^3 + \right.$$

$$\left. + \frac{3}{2}(Z_r - Z_f)^2 (B - D) + \frac{1}{4}(Z_r - Z_f)^3 \right) = 0, \tag{40}$$

where

$$e_0 = n_2^2 - \Omega_0{}^2 + i2k_0\Omega_0, \quad e_1 = n_2^2 - 9\Omega_0{}^2 + i6k_0\Omega_0.$$

From the system in Eq. (40), taking into account Eqs. (38) and (39), we have:

$$B^2 + gB + l = 0, \tag{41}$$

where

$$g = \frac{f_2}{2(1-d)}, \quad l = \frac{-e_{01} f + f_1 (f_2 n_{01} + \frac{3}{4} n_{10} f_2{}^3)}{\frac{3}{2} f_2 f_1 n_{01} (1-d)^2}.$$

Solving Eq. (41), we obtain the values of the amplitudes $B_{1,2}$, and using Eqs. (38) to (40), we can find all the amplitudes of ultra-harmonic oscillations and the phase angle.

Thus, by comparing the amplitude-frequency characteristics obtained from the system in Eq. (27) and the amplitude-frequency characteristics obtained from systems in Eqs. (4) and (28), it is possible to determine whether sub-harmonic and ultra-harmonic resonances are present.

As sub-harmonic and ultra-harmonic resonances are observed only in non-linear systems, and (as in the linear case) there is no third resonance, which is observed at $s = 3.24$ (see Figs. 12 and 13, black (solid) curve), we can conclude that this resonance is ultra-harmonic, which is also confirmed by the fact that $\Omega_0 \approx 3\omega$; in doing so, a shift in frequency is due foundation vibrations, whereas the presence of the first resonance is typical for a multi-degree of freedom system.

The numerical solution of the non-linear system in Eq. (28) does not indicate the presence of sub-harmonic resonances (see Figs. 12 and 13, purple curve).

To design rotor installation with these parameters, the optimal value of the foundation mass has to be up to 1.042 of the rotor mass, with linear eccentricity not exceeding $E = 10$. It is recommended to increase the stiffness coefficient at the cubic term by five orders of magnitude relative to the linear term and to decrease the damping coefficient by two orders, which will result in smaller amplitudes and will increase ultra-harmonic resonances.

Thus, for stable operation of the system at any filling of the cavity, it is necessary that the operating speed is in the range $0.065 < s < 0.65$ or $s > 3.41$.

4 CONCLUSIONS

A method for calculating amplitudes and constructing frequency characteristics of forced and self-excited vibrations of the "rotor-fluid-foundation" system on rolling bearings with a non-linear characteristic based on the method of complex amplitudes and harmonic balance has been developed. The specific features of the non-linear dynamic behaviour characterised by ultra-harmonic vibrations are studied. The optimal parameters of linear imbalance, the mass of the foundation, the fluid volume in the rotor cavity, the stiffness and damping coefficients, for which the amplitudes take optimal values, have been determined.

5 ACKNOWLEDGEMENTS

This work has been supported financially by the research project AP08856167 of the Ministry of Education and Science of the Republic of Kazakhstan and was performed at Research Institute of Mathematics and Mechanics in Al-Farabi Kazakh National University, which is gratefully acknowledged by the authors. The corresponding author gratefully acknowledges financial support from the Slovenian Research Agency (ARRS), Grant Ref. J2-9224.

6 REFERENCES

[1] Sharma, A., Upadhyay, N., Kankar, P. K., Amarnath, M. (2018). Non-linear dynamic investigations on rolling element bearings: A review. *Advances in Mechanical Engineering*, vol. 10, no. 3, p. 1-15, **DOI:10.1177/1687814018764148**.

[2] Wang, G., Yuan, H., Sun, H. (2020). An investigation on the instability of a flexible liquid-filled rotor. *Proceedings of the Institution of Mechanical Engineers, Part G: Journal of Aerospace Engineering*, vol. 234, no. 2, p. 165-172, **DOI:10.1177/0954410019854262**.

[3] Zhang, X., Han, Q., Peng, Z., Chu, F. (2013). Stability analysis of a rotor-bearing system with time-varying bearing stiffness due to finite number of balls and unbalanced force. *Journal of Sound and Vibration*, vol. 332, no. 25, p. 6768-6784, **DOI:10.1016/j.jsv.2013.08.002**.

[4] Kumar Avshist, R., Peng, Q. (2018). Non-linear dynamic modeling of the cracked rotor ball bearing system with emphasis on damage detection capabilities. *Journal of Vibration and Acoustics*, vol. 140, no. 4, p. 041018-1-041018-10, **DOI:10.1115/1.4039404**.

[5] Li, Z., Li, J., Li, M. (2018). Non-linear dynamics of unsymmetrical rotor-bearing system with fault of parallel misalignment. *Advances in Mechanical Engineering*, vol. 10, no. 5, p. 1-17, **DOI:10.1177/1687814018772908**.

[6] Xu, Q., Niu, J., Yao, H., Zhao, L., Wen, B. (2019). Non-linear dynamic behavior and stability of a rotor/seal system with the dynamic vibration absorber. *Advances in Mechanical Engineering*, vol. 11, no. 1, p. 1-17, **DOI:10.1177/1687814018819578**.

[7] Nan, G., Tang, M., Chen, E., Yang, A. (2016). Non-linear dynamic mechanism of rolling element bearings with an internal clearance in a rotor-bearing system. *Advances in Mechanical Engineering*, vol. 8, no. 11, p. 1-9, **DOI:10.1177/1687814016679588**.

[8] Kydyrbekuly, A., Khajiyeva, L., Ybraev, G.G.A.Y., Kaplunov, J. (2016). Non-linear vibrations of a rotor-fluid-foundation system supported by rolling bearings. *Strojniški vestnik - Journal of Mechanical Engineering*, vol. 62, no. 6, p. 351-362, **DOI:10.5545/sv-jme.2016.3423**.

[9] Ishida, Y., Liu, J. (2010). Elimination of unstable ranges of rotors utilizing discontinuous spring characteristics: An asymmetrical shaft system, an asymmetrical rotor system, and a rotor system with liquid. *Journal of Vibration and Acoustics*, vol. 132, no. 1, p. 011011-1-011011-8, **DOI:10.1115/1.4000842**.

[10] Xia, Z., Qiao, G., Zheng, T., Zhang, W. (2009). Non-linear modelling and dynamic analysis of the rotor-bearing system. *Nonlinear Dynamics*, vol. 57, no. 4, p. 559-577, **DOI:10.1007/s11071-008-9442-3**.

[11] Luczko, J. (2002). A geometrically non-linear model of rotating shafts with internal resonance and self-excited vibrations. *Journal of Sound and Vibrations*, vol. 255, no. 3, p. 433-456, **DOI:10.1006/jsvi.2001.4164**.

[12] Friswell, M., Penny, J., Garvey, S., & Lees, A. (2010). *Dynamics of Rotating Machines (Cambridge Aerospace Series)*. Cambridge University Press, Cambridge, **DOI:10.1017/CBO9780511780509**.

[13] Vance, J.M., Zeidan, F.Y., Murphy, B. (2010). Machinery Vibration and Rotordynamics. John Wiley & Sons, Inc., Hoboken, **DOI:10.1002/9780470903704**.

[14] Harris, T.A. (2001). *Rolling Bearing Analysis*. John Wiley & Sons, Inc., Hoboken

[15] David, P.F., Poplawski, J.V. (2004). Transient vibration prediction for rotors on ball bearings using load-dependent non-linear bearing stiffness. *International Journal of Rotating Machinery*, vol. 10, no. 6, p. 489-494, **DOI:10.1080/10236210490504102**.

[16] Yamamoto, T., Ishida, Y. (1977). Theoretical discussions on vibrations of a rotating shaft with non-linear spring characteristics. *Ingenieur-Archiv*, vol. 46, no. 2, p. 125-135, **DOI:10.1007/BF00538746**.

[17] Changsen, W. (1991). *Analysis of Rolling Element Bearings*. Mechanical Engineering Publications Limited.

[18] Jin, Y., Lu, Z., Yang, R., Hou, L., Chen, Y. (2018). A new non-linear force model to replace the Hertzian contact model in a rigid-rotor ball bearing system. *Applied Mathematics and Mechanics*, vol. 39, no. 3, p. 365-378, **DOI:10.1007/s10483-018-2308-9**.

[19] Ishida, Y., Yamamoto, T. (2013). *Linear and Nonlinear Rotordynamics: A Modern Treatment with Applications*. John Wiley & Sons, Weinheim, **DOI:10.1002/9783527651894**.

[20] Isayuk-Sayevskaya, A.R., Kelzon, A.S. (1995). Dynamics of a high-revolution scroll centrifuge. *Machine Vibration*, vol. 3, no. 4, p. 233-237.

[21] Tondl, A. (1965). *Some Problems of Rotor Dynamics*. Chapman and Hall, London.

[22] Rao, S. (2018). *Mechanical Vibrations*. Pearson Education, Inc., London.

[23] Kollmann, F.G. (1962). Experimentelle und theoretische Untersuchungen uber die kritischen Drehzahlen flussigkeitsgefullter Hohlkorper. *Forschung auf dem Gebiete des Ingenieurwesens A*, vol. 28, no. 4,p. 115-123, vol. 28, no. 5, p. 147-153, **DOI:10.1007/BF02557449**.

[24] Schmidt, G., Tondl, A. (1986). Non-linear Vibrations. Cambridge University Press, Cambridge, **DOI:10.1017/CBO9780511735752**.

[25] Kovacic, I., Brennan, J. (2011). *The Duffing Equation: Non-linear Oscillators and Their Behaviour*. John Wiley & Sons, Hoboken, **DOI:10.1002/9780470977859**.

[26] Cveticanin, L. (2018). Strong Non-linear Oscillators. Springer, Cham, **DOI:10.1007/978-3-319-58826-1**.

[27] Krämer, E. (1993). *Dynamics of Rotors and Foundations*, Springer-Verlag, New York, **DOI:10.1007/978-3-662-02798-1**.

[28] Hayashi, C. (2014). *Non-linear Oscillations in Physical Systems*. Princeton University Press, Princeton.

Strojniški vestnik - Journal of Mechanical Engineering 67(2021)9, 433-444
DOI:10.5545/sv-jme.2021.7220
Original Scientific Paper
Received for review: 2021-04-08
Received revised form: 2021-08-21
Accepted for publication: 2021-08-24
© 2021 Journal of Mechanical Engineering. All rights reserved.

Trajectory-Tracking Control for Manipulators Based on Fuzzy Equivalence and a Terminal Sliding Mode

Youyu Liu[1,2,*] – Yi Li[1,2] – Xuyou Zhang[1,2] – Bo Chen[1,2]

[1] Key Laboratory of Advanced Perception and Intelligent Control of High-end Equipment, Ministry of Education, China
[2] Anhui Polytechnic University, School of Mechanical Engineering, China

To suppress the chattering of manipulators under heavy-load operations, a control method called fuzzy equivalence & terminal sliding mode (FETSM) was applied to the trajectory tracking of motion curves for manipulators. Based on the switching term of the equivalent sliding mode (ESM), a fuzzy parameter matrix processed by the simple fuzzy rules was introduced, and the fuzzy switching term was obtained. By summing the fuzzy switching term and the equivalent term of the equivalence and a terminal sliding mode (ETSM), the control law of the FETSM for manipulators was obtained. On this basis, the stability of the system was analysed and the finite arrival time of it was deduced. On the premise of ensuring the stability of the system, the fuzzy rules and membership functions were designed for the fuzzy constants in the fuzzy switching term. Simulation tests show that the proposed FETSM can ensure sufficient trajectory-tracking precision, error convergence speed, and robustness. Compared with the ETSM, the proposed FETSM can reduce the chattering time by 94.75 % on average; compared with the proportion-integral-differential (PID) control method, the maximum chattering amplitude by the FETSM can be reduced by at least 99.21 %. Thus, the proposed FETSM is suitable for those manipulators under heavy-load operations.

Keywords: sliding mode control, fuzzy switch term, chattering, manipulator, trajectory tracking

Highlights

- *The law of the FETSM control system for manipulators is obtained.*
- *The stability and finite arrival time of the FETSM system are proved.*
- *Fuzzy rules are used to estimate the external disturbances of the system and uncertainties of the system.*
- *The chattering of the sliding mode system can be suppressed by the proposed control method.*

0 INTRODUCTION

Manipulator is a non-linear and time-varying system with multi-input, multi-output, strong coupling, in which there are usually uncertain modelling and external disturbances [1] and [2]. Moreover, the trajectory tracking of motion curves for manipulators has always been a hot and difficult topic. Manipulators are mostly used for heavy-load operations, such as palletizing, handling, and so on, in which small chattering and high torque control ability are required, while the trajectory tracking precision and robustness requirements are insignificant [3]. At this present, some control methods are used in trajectory tracking for manipulators, mainly including sliding mode control [4] and [5], neural network control [6] to [8], the proportional–integral–derivative (PID) control [9] to [11] and robust control [12] and [13]. In order to reduce the chattering of manipulators under heavy-load operations, a fuzzy equivalence and a terminal sliding mode (FETSM) control method for manipulators has been proposed in this article.

Sliding mode control has been receiving increasing attention due to its characteristics of fast response and small influence by parameter changing and external disturbances. However, there is a serious chattering phenomenon in sliding mode control, which affects the stability of trajectory-tracking system and increase energy consumption. In order to overcome the chattering of the sliding mode system for manipulators, researchers have conducted some studies. For example, Liu et al. [14] constructed an approaching law with *fal* function to adjust the speed of approaching motion. When the state is far from the sliding mode surface of system, the speed of approaching motion is faster; when the state is close to the sliding mode surface, the speed decreases greatly. Therefore, the system can pass through the sliding mode surface at a lower speed to reduce its chattering. However, it is not easy to select the deceleration position. The overall time of approaching motion will be increased if the position chosen is too far from the sliding mode surface; otherwise, the chattering will be increased to a certain extent. Combining with the dynamic surface, which prevented the complex differential of the virtual control laws, Jiang et al. [15] designed a fuzzy adaptive system to approximate the observation errors of the uncertain disturbances and to reduce the chatter of the control law. The fuzzy parameters and fuzzy rules of this method are complex, which will reduce the computational efficiency. Xi et al. [16] set

*Corr. Author's Address: Anhui Polytechnic University, School Mechanical Engineering. Wuhu 241000, China, liuyyu@ahpu.edu.cn

the deceleration position change with the state of the sliding mode system by using fuzzy rules to deal with the exponent in power approach laws and replaced sign functions with hyperbolic tangent functions. This method can reduce the approaching time of the sliding mode system and the chattering of them. However, the chattering of the sliding mode system is still at a high level; consequently, some constants are still set to offset the disturbances and uncertainties. Tran et al. [17] used radial basis function neural networks to approximate the unknown non-linear dynamics of the system and designed an adaptive compensation mechanism of approximation error and adaptive law of weights of neural networks to realize model-free control. Chang et al. [18] proposed an adaptive sliding mode control scheme by introducing an adaptive term derived from a radical basis function network, which does not require knowledge of the bound of the system uncertainties and external disturbances. It simultaneously eliminates the chattering phenomenon without deteriorating the system fast-response characteristic and robustness. The chattering of the system is reduced by the above two methods. However, with the increase of the degree of freedom (DOF) of manipulators, the number of parameters in each matrix in a controlled model increases geometrically, which will lead to a significant increase in the computational complexity and the time required to control the system.

In this article, the FETSM control method is proposed. a fuzzy parameter matrix is introduced into the switching term of the equivalent sliding mode (ESM), and the matrix is processed with simple fuzzy rules, so that it can approach the sum of the uncertainties and external disturbances to the greatest degree possible while ensuring the stability of the system. The purpose is to reduce chattering and optimize the input torque control of manipulators under heavy-load operations on the premise of ensuring sufficient joint control precision, error convergence speed, and robustness. The feasibility and effectiveness of the proposed method are verified by comparing the trajectory tracking and input torque with several existing methods.

1 DESIGN ON CONTROL LAW OF FETSM

In order to obtain the control law of the FETSM, the equivalence term and the fuzzy switching term need to be designed. The former makes the trajectory tracking move on the sliding mode surface, and the latter is used to offset the uncertainties and external disturbances to ensure that the state of the trajectory-tracking system moves towards the sliding mode surface.

1.1 Design on Equivalent Term

The dynamic equation of *N*-DOF manipulator can be described as follows [19]:

$$\mathbf{M}(\mathbf{q})\ddot{\mathbf{q}} + \mathbf{V}(\mathbf{q},\dot{\mathbf{q}})\dot{\mathbf{q}} + \mathbf{G}(\mathbf{q}) + \Delta(\mathbf{q},\dot{\mathbf{q}}) + \mathbf{d} = \tau, \quad (1)$$

where $\mathbf{q}$ is an *N*-dimensional joint position vector; $\dot{\mathbf{q}}$ is the first-order derivative of $\mathbf{q}$. $\ddot{\mathbf{q}}$ is the second-order derivative of $\mathbf{q}$. $\mathbf{M}(\mathbf{q})$ is an *N*-order symmetric positive definite inertial matrix; $\mathbf{V}(\mathbf{q},\dot{\mathbf{q}})$ is an *N*-order centrifugal force matrix; $\mathbf{G}(\mathbf{q})$ is an *N*-dimensional gravity vector; $\Delta(\mathbf{q},\dot{\mathbf{q}}) = [\Delta_1, \Delta_2, ..., \Delta_N]^{\mathrm{T}}$ is the uncertainties of modelling and friction; $\mathbf{d} = [d_1, d_2, ..., d_N]^{\mathrm{T}}$ is an *N*-dimensional external disturbance, and $\|\Delta(\mathbf{q},\dot{\mathbf{q}}) + \mathbf{d}\| \le \Delta + d$; $\boldsymbol{\tau}$ is an *N*-dimensional joint input torque.

$\mathbf{M}(\mathbf{q})$ is an invertible matrix because $\mathbf{M}(\mathbf{q})$ is a symmetric positive definite inertia matrix. From Eq. (1),

$$\ddot{\mathbf{q}} = \mathbf{M}^{-1}(\mathbf{q})\left[\tau - \mathbf{V}(\mathbf{q},\dot{\mathbf{q}})\dot{\mathbf{q}} - \mathbf{G}(\mathbf{q}) - \Delta(\mathbf{q},\dot{\mathbf{q}}) - \mathbf{d}\right]. \quad (2)$$

Order $\mathbf{x}_1 = \mathbf{q}$ and $\mathbf{x}_2 = \dot{\mathbf{q}}$, the dynamics equation of manipulators can be inferred from Eq. (2), namely,

$$\begin{cases} \dot{\mathbf{x}}_1 = \mathbf{x}_2 \\ \dot{\mathbf{x}}_2 = \mathbf{M}^{-1}(\mathbf{x}_1) \\ \quad \cdot\left[\tau - \mathbf{V}(\mathbf{x}_1,\mathbf{x}_2)\mathbf{x}_2 - \mathbf{G}(\mathbf{x}_1) - \Delta(\mathbf{x}_1,\mathbf{x}_2) - \mathbf{d}\right] \end{cases}. \quad (3)$$

Order $\mathbf{e} = \mathbf{q}_d - \mathbf{x}_1$ ($\mathbf{q}_d$ is the desired position trajectory of joints), a non-linear sliding surface is designed as follows [20]:

$$\mathbf{s} = \mathbf{e} + \boldsymbol{\beta}^{-1}\dot{\mathbf{e}}^{\frac{p}{q}}. \quad (4)$$

where $\mathbf{e}$ is the position tracking error of joints; $\boldsymbol{\beta} = \mathrm{diag}\{\beta_1, \beta_2, ..., \beta_N\}$, and $\beta_1, \beta_2, ..., \beta_N > 0$; p and q are odd numbers, and $p > q$, $1 < p/q < 2$.

Taking the derivative of Eq. (4), then,

$$\dot{\mathbf{s}} = \dot{\mathbf{e}} + \frac{p}{q}\boldsymbol{\beta}^{-1}\mathrm{diag}\{\ddot{\mathbf{e}}\}\dot{\mathbf{e}}^{\frac{p-q}{q}}, \quad (5)$$

where $\mathrm{diag}\{\ddot{\mathbf{e}}\}$ is an *N*-order diagonal matrix in which the principal diagonal elements are the corresponding elements of $\ddot{\mathbf{e}}$.

Let $\dot{\mathbf{s}} = 0$, thus,

$$\dot{\mathbf{e}} + \frac{p}{q}\boldsymbol{\beta}^{-1}\mathrm{diag}\{\ddot{\mathbf{q}}_d - \dot{\mathbf{x}}_2\}\dot{\mathbf{e}}^{\frac{p-q}{q}} = 0. \quad (6)$$

Ignoring the uncertainties and external disturbances, and substituting Eq. (3) into Eq. (6),

$$\dot{\mathbf{e}}+\frac{p}{q}\boldsymbol{\beta}^{-1}\mathrm{diag}\left\{\ddot{\mathbf{q}}_d-\mathbf{M}^{-1}\left(\mathbf{x}_1\right)\cdot\left[\boldsymbol{\tau}-\mathbf{V}\left(\mathbf{x}_1,\mathbf{x}_2\right)\mathbf{x}_2-\mathbf{G}\left(\mathbf{x}_1\right)\right]\right\}\dot{\mathbf{e}}^{\frac{p-q}{q}}=0. \quad (7)$$

From Eq. (7),

$$\mathrm{diag}\left\{\ddot{\mathbf{q}}_d-\mathbf{M}^{-1}\left(\mathbf{x}_1\right)\cdot\left[\boldsymbol{\tau}-\mathbf{V}\left(\mathbf{x}_1,\mathbf{x}_2\right)\mathbf{x}_2-\mathbf{G}\left(\mathbf{x}_1\right)\right]\right\}=-\frac{q}{p}\boldsymbol{\beta}\dot{\mathbf{e}}^{2-\frac{p}{q}}. \quad (8)$$

diag^{-1} is defined as an operation that has the following characteristics: If $\boldsymbol{\Lambda}=\mathrm{diag}\{\Lambda_1,\Lambda_2,...,\Lambda_N\}$ is a diagonal matrix, then,

$$\mathrm{diag}^{-1}\left\{\boldsymbol{\Lambda}\right\}=\left[\Lambda_1,\Lambda_2,...,\Lambda_N\right]^{\mathrm{T}}. \quad (9)$$

Both sides of Eq. (8) are diagonal matrices. From Eqs. (8) and (9),

$$\ddot{\mathbf{q}}_d-\mathbf{M}^{-1}\left(\mathbf{x}_1\right)\left[\boldsymbol{\tau}-\mathbf{V}\left(\mathbf{x}_1,\mathbf{x}_2\right)\mathbf{x}_2-\mathbf{G}\left(\mathbf{x}_1\right)\right]=\mathrm{diag}^{-1}\left(-\frac{q}{p}\boldsymbol{\beta}\dot{\mathbf{e}}^{2-\frac{p}{q}}\right). \quad (10)$$

From Eq. (10), the equivalent term can be designed as Eq. (11),

$$\boldsymbol{\tau}_{eq}=\mathbf{M}\left(\mathbf{x}_1\right)\left[\ddot{\mathbf{q}}_d+\mathrm{diag}^{-1}\left(\frac{q}{p}\boldsymbol{\beta}\dot{\mathbf{e}}^{2-\frac{p}{q}}\right)\right]+\mathbf{V}\left(\mathbf{x}_1,\mathbf{x}_2\right)\mathbf{x}_2+\mathbf{G}\left(\mathbf{x}_1\right). \quad (11)$$

1.2 Design on Fuzzy Switching Term

In order to ensure that it can compensate uncertainties and external disturbances, the fuzzy switching term is designed as follows,

$$\boldsymbol{\tau}_{sw}=\mathrm{diag}\left\{\varepsilon_1,\varepsilon_2,\ldots,\varepsilon_N\right\}\cdot\mathrm{diag}\left\{\kappa_1,\kappa_2,\ldots,\kappa_N\right\}\mathrm{sgn}\left(\mathbf{s}\right), \quad (12)$$

where $\mathrm{diag}\{\kappa_1,\kappa_2,...,\kappa_N\}$ is a constant matrix, and $\kappa_1,\kappa_2,...,\kappa_N\geq\Delta+d$, $\kappa=\max(|d(t)|)+\eta$; $\mathrm{diag}\{\varepsilon_1,\varepsilon_2,...,\varepsilon_N\}$ is a fuzzy parameter matrix ($\boldsymbol{\tau}_{sw}$ is a basic switching item when $\varepsilon_1,\varepsilon_2,...,\varepsilon_N$ are all equal to 1, and $\boldsymbol{\tau}_{sw}$ is a fuzzy switching item while one of $\varepsilon_1,\varepsilon_2,...,\varepsilon_N$ is not equal to 1; and $\varepsilon_1\kappa_1,\varepsilon_2\kappa_2,...,\varepsilon_N\kappa_N\geq\Delta+d$; sgn is a symbolic function [21], and $\mathrm{sgn}(\mathbf{s})=[\mathrm{sgn}(s_1),\mathrm{sgn}(s_2),...,\mathrm{sgn}(s_N)]^{\mathrm{T}}$. If Z is a real number, then, $\mathrm{sgn}\left(Z\right)=\begin{cases}1, Z>0\\0, Z=0\\-1, Z<0\end{cases}$.

Order $\boldsymbol{\kappa}=\mathrm{diag}\{\kappa_1,\kappa_2,...,\kappa_N\}$ and $\boldsymbol{\varepsilon}=\mathrm{diag}\{\varepsilon_1,\varepsilon_2,...,\varepsilon_N\}$, The control law of the FETSM can be obtained by adding Eq. (11) to Eq. (12).

$$\boldsymbol{\tau}=\mathbf{M}\left(\mathbf{x}_1\right)\left[\ddot{\mathbf{q}}_d+\mathrm{diag}^{-1}\left(\frac{q}{p}\boldsymbol{\beta}\dot{\mathbf{e}}^{2-\frac{p}{q}}\right)\right]+\mathbf{V}\left(\mathbf{x}_1,\mathbf{x}_2\right)\mathbf{x}_2+\mathbf{G}\left(\mathbf{x}_1\right)+\boldsymbol{\varepsilon}\boldsymbol{\kappa}\mathrm{sgn}\left(\mathbf{s}\right). \quad (13)$$

2 ANALYSIS ON STABILITY AND FINITE ARRIVAL TIME

2.1 Stability Analysis

For the sliding mode control of a rigid manipulator, a Lyapunov function [22] was defined as follows:

$$\mathbf{L}_y=\frac{1}{2}\mathbf{s}^{\mathrm{T}}\mathbf{s}, \quad (14)$$

taking the derivative of Eq. (14),

$$\dot{\mathbf{L}}_y=\mathbf{s}^{\mathrm{T}}\dot{\mathbf{s}}. \quad (15)$$

From Eqs. (3), (13) and (15),

$$\dot{\mathbf{L}}_y=\mathbf{s}^{\mathrm{T}}\left\{\dot{\mathbf{e}}+\frac{p}{q}\boldsymbol{\beta}^{-1}\mathrm{diag}\left\{\ddot{\mathbf{q}}_d-\mathbf{M}^{-1}\left(\mathbf{x}_1\right)\cdot\left[\boldsymbol{\tau}-\mathbf{V}\left(\mathbf{x}_1,\mathbf{x}_2\right)\mathbf{x}_2-\mathbf{G}\left(\mathbf{x}_1\right)-\Delta\left(\mathbf{x}_1,\mathbf{x}_2\right)-\mathbf{d}\right]\right\}\dot{\mathbf{e}}^{\frac{p-q}{q}}\right\}. \quad (16)$$

Substituting Eq. (13) into Eq. (16) and simplifying it,

$$\dot{\mathbf{L}}_y=\frac{p}{q}\left[\frac{1}{\beta_1},\ldots,\frac{1}{\beta_N}\right]\mathbf{M}^{-1}\left(\mathbf{x}_1\right)\left(\dot{\mathbf{q}}_d-\mathbf{x}_2\right)^{\frac{p-q}{q}}\cdot\left\{\left(\Delta\left(\mathbf{x}_1,\mathbf{x}_2\right)+\mathbf{d}\right)\mathbf{s}^{\mathrm{T}}-\mathrm{diag}\left\{\boldsymbol{\varepsilon}\boldsymbol{\kappa}|\mathbf{s}|\right\}\right\}, \quad (17)$$

where $|\mathbf{s}|$ is the absolute value of $\mathbf{s}$, namely $|\mathbf{s}|=[|s_1|,|s_2|,...,|s_N|]^{\mathrm{T}}$.

For $1<p/q<2$, then $0<(p-q)/q<2$; and both p and q are positive odd numbers. Therefore, the elements of $\left(\dot{\mathbf{q}}_d-\mathbf{x}_2\right)^{\frac{p-q}{q}}$ are non-negative numbers. $\beta_1,\beta_2,...,\beta_N$ are positive numbers and $\mathbf{M}^{-1}(\mathbf{x}_1)$ is a symmetric positive definite matrix, when $\mathbf{x}_2\neq\dot{\mathbf{q}}_d$,

$$\frac{p}{q}\left[\frac{1}{\beta_1},\ldots,\frac{1}{\beta_N}\right]\mathbf{M}^{-1}(\mathbf{x}_1)(\dot{\mathbf{q}}_d-\mathbf{x}_2)^{\frac{p-q}{q}}>0. \quad (18)$$

The sign of $\dot{\mathbf{L}}_y$ is determined by the N-order diagonal matrix $(\boldsymbol{\Delta}(\mathbf{x}_1,\mathbf{x}_2)+\mathbf{d})\mathbf{s}^{\mathrm{T}}-\mathrm{diag}\{\boldsymbol{\varepsilon}\boldsymbol{\kappa}|\mathbf{s}|\}$, which is written in matrix form as follows:

$$\begin{aligned}&\left[\Delta(\mathbf{x}_1,\mathbf{x}_2)+\mathbf{d}\right]\mathbf{s}^{\mathrm{T}}-\mathrm{diag}\left\{\boldsymbol{\varepsilon}\boldsymbol{\kappa}|\mathbf{s}|\right\}\\&=\begin{bmatrix}(\Delta_1+d_1)s_1-\varepsilon_1\kappa_1|s_1| & \cdots & 0\\ \vdots & \ddots & \vdots\\ 0 & \cdots & (\Delta_N+d_N)s_N-\varepsilon_N\kappa_N|s_1|\end{bmatrix}.\end{aligned} \quad (19)$$

Due to $|s_1|\geq s_1,\ldots,|s_N|\geq s_N$, all of the principal diagonal elements of $(\boldsymbol{\Delta}(\mathbf{x}_1,\mathbf{x}_2)+\mathbf{d})\mathbf{s}^{\mathrm{T}}-\mathrm{diag}\{\boldsymbol{\varepsilon}\boldsymbol{\kappa}|\mathbf{s}|\}$ are non-positive numbers. Moreover, when the fuzzy parameter matrix works normally, $\varepsilon_1\kappa_1,\varepsilon_2\kappa_2,\ldots,\varepsilon_N\kappa_N\geq\Delta+d$. Thus, $\dot{\mathbf{L}}_y\leq 0$.

When $\mathbf{x}_2\neq\dot{\mathbf{q}}_d$, the trajectory-tracking system employed by the FETSM is stable according to Lyapunov's second method [23]. In addition, the sliding mode surface of it is non-singular. Substituting Eq. (13) into Eq. (3),

$$\begin{aligned}\dot{\mathbf{x}}_2=\ddot{\mathbf{q}}_d+\mathrm{diag}^{-1}\left[\frac{q}{p}\boldsymbol{\beta}(\dot{\mathbf{q}}_d-\mathbf{x}_2)^{2-\frac{p}{q}}\right]+\mathbf{M}^{-1}(\mathbf{x}_1)\\ \cdot\left\{\Delta(\mathbf{x}_1,\mathbf{x}_2)+\mathbf{d}-\mathrm{diag}\left[\boldsymbol{\varepsilon}\boldsymbol{\kappa}\mathrm{sgn}(\mathbf{s})\right]\right\},\end{aligned} \quad (20)$$

when $\mathbf{x}_2=\dot{\mathbf{q}}_d$, for $\ddot{\mathbf{e}}=\dot{\mathbf{q}}_d-\mathbf{x}_2$,

$$\ddot{\mathbf{e}}=\mathbf{M}^{-1}(\mathbf{x}_1)\left\{\Delta(\mathbf{x}_1,\mathbf{x}_2)+\mathbf{d}-\mathrm{diag}\left\{\boldsymbol{\varepsilon}\boldsymbol{\kappa}\mathrm{sgn}(\mathbf{s})\right\}\right\}. \quad (21)$$

When $\mathbf{s}>0$, $\ddot{\mathbf{e}}<0$, namely, $\dot{\mathbf{e}}$ will decrease rapidly. While $\mathbf{s}<0$, $\ddot{\mathbf{e}}>0$,, namely, $\dot{\mathbf{e}}$ will increase rapidly. Obviously, $\mathbf{s}$ can reach 0 within a finite time when $\mathbf{x}_2=\dot{\mathbf{q}}_d$ [20]. Therefore, the sliding mode of the N-DOF manipulator with the FETSM control law exists and can be reached.

2.2 Analysis on Finite Arrival Time

Eq. (4) can be written in scalar form: $s_j=e_j+\beta_j(\dot{e}_j)^{\frac{p}{q}}$ j=1, 2, ..., N. Order $s_j=0$,

$$e_j+\beta_j\left(\frac{\mathrm{d}e_j}{\mathrm{d}t}\right)^{\frac{p}{q}}=0. \quad (22)$$

From Eq. (22),

$$\mathrm{d}t=\left(-\frac{e_j}{\beta_j}\right)^{-\frac{q}{p}}\mathrm{d}e_j. \quad (23)$$

If the trajectory-tracking system spends time t_j from $e_j(0)\neq 0$ to $e_j(t_j)=0$, then,

$$\int_0^{t_j}\mathrm{d}t=\int_{e_j(0)}^{0}\left(-\frac{e_j}{\beta_j}\right)^{-\frac{q}{p}}\mathrm{d}e_j. \quad (24)$$

From Eq. (24), The effective time to reach equilibrium state is as follows:

$$t_j=\beta_j\frac{p}{p-q}\left(\frac{e_j(0)}{\beta_j}\right)^{\frac{p-q}{p}}. \quad (25)$$

If $t_{\max}=\max\{t_1,t_2,\ldots,t_N\}$, the trajectory-tracking error of the system must reach 0 within $t_{\max}$, which is finite according to Eq. (25). Therefore, the trajectory-tracking error of the system can reach 0 within a finite time.

3 DESIGN ON FUZZY RULES AND SYSTEM STRUCTURE

3.1 Design on Fuzzy Rules

Supposing there is no fuzzy parameter matrix $\boldsymbol{\varepsilon}$ in Eq. (18), $\dot{\mathbf{L}}_y\leq 0$ is still proper for $\kappa_1,\kappa_2,\ldots,\kappa_N$ are constants and not less than $\Delta+d$.Therefore, the FETSM system of manipulators remains stable. In contrast, uncertainties and external disturbances are time-varying, and $\kappa_1,\kappa_2,\ldots,\kappa_N$ are constants. Therefore, constant matrix cannot follow the change of $\boldsymbol{\Delta}(\mathbf{x}_1,\mathbf{x}_2)+\mathbf{d}$, which leads to every main diagonal element of κsgn(s) always being large, and then the chattering of the sliding mode system is increased. On the premise of stability, the difference between the corresponding parameters of $\boldsymbol{\varepsilon}\boldsymbol{\kappa}\mathrm{sgn}(\mathbf{s})$ and $\boldsymbol{\Delta}(\mathbf{x}_1,\mathbf{x}_2)+\mathbf{d}$ are as small as possible by using the fuzzy method to adjust $\boldsymbol{\varepsilon}$, so as to reduce the chattering.

NE, PO and ZE are used to represent negative, positive and zero, respectively. The input and output of the fuzzy system are defined as follows:

$$\begin{cases}\mathrm{input}: s_j=\{\mathrm{NE},\mathrm{ZE},\mathrm{PO}\}\\ \mathrm{output}: \varepsilon_j=\{\mathrm{ZE},\mathrm{PO}\}\end{cases},\quad j=1,2,\ldots,N. \quad (26)$$

"If-then" statement [24] is used to define fuzzy rules between the input and output.

$$\begin{cases}\mathrm{Rule3}\ j-2:\mathrm{If}\ s_j\ \mathrm{is\ NE\ then}\ \varepsilon_j\ \mathrm{is\ PO}\\ \mathrm{Rule3}\ j-1:\mathrm{If}\ s_j\ \mathrm{is\ ZE\ then}\ \varepsilon_j\ \mathrm{is\ ZE}\\ \mathrm{Rule3}\ j:\mathrm{If}\ s_j\ \mathrm{is\ PO\ then}\ \varepsilon_j\ \mathrm{is\ PO}\end{cases}. \quad (27)$$

3.2 Design on Membership Function

As for the input s, the membership function is designed as follows [25]: its domain is $[-1, 1]$; NE is a trapezoidal membership function, $[-1, -1, -2\times\sigma, 0]$; ZE is a triangular membership function, $[-2\times\sigma, 0, 2\times\sigma]$; PO is a trapezoidal membership function, $[0, 2\times\sigma, 1, 1]$. As for the output ε, the membership function is designed as follows [25]: its domain is $[0, 1]$; ZE is a triangular membership function, $[0, 1\times10^{-5}, 2]$; PO is a trapezoidal membership function, $[0, 1, 1, 1]$. The σ in the function represents the thickness of the boundary layer. When $-\sigma < s < \sigma$, s and ε belong to ZE. In addition, the variation range of the ε is between 1×10^{-5} and 1. While the s approaches the boundary layer, the ε approaches 1. Conversely, when the s approaches 0, the ε approaches 1×10^{-5}; When the s is outside the boundary layer, the ε is 1. The membership function curves of the input and output of the proposed control method are shown in Fig. 1 [26].

3.3 System Structure

The structure of the trajectory-tracking system of the FETSM for manipulators is shown in Fig. 2.

4 SIMULATION VERIFICATION

4.1 Analysis on Trajectory Tracking

MATLAB R2019b is applied as the simulation platform to track the ideal curve trajectories by using the FETSM, the ETSM [27], the ESM [28], and the PID [10] methods, respectively. By comparing the error of position tracking of each joint, the effects of the trajectory tracking of the above four control methods are analysed. Two curves are chosen as the ideal position curves of the joints 1 and 2. The coefficient of the curves is listed in Tables 1 to 4. The

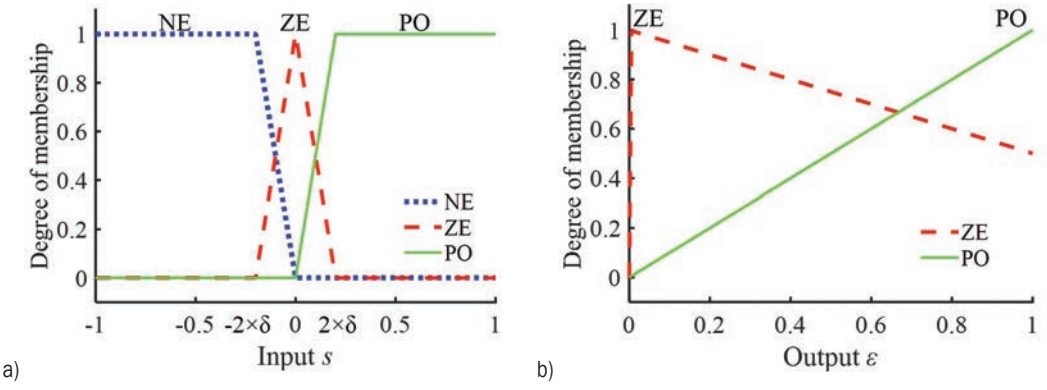

Fig. 1. *The membership function of input and output of the FETSM; a) input s; b) output ε*

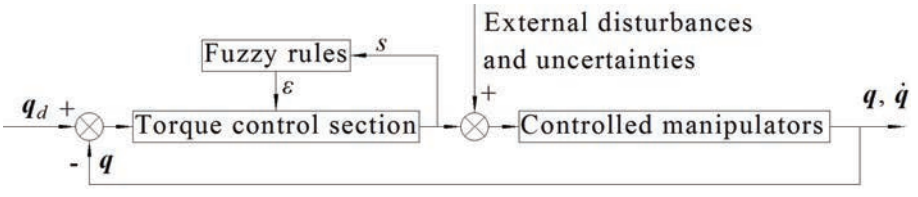

Fig. 2. *Structure diagram of the FETSM trajectory-tracking system*

Table 1. *The coefficients of the 1st position curve of the 1st joint*

Intervals [s]	q_4 [rad]	q_3 [rad]	q_2 [rad]	q_1 [rad]	q_0 [rad]
[0.0000, 2.3806)	–0.0152	0.0731	0.0000	0.0000	0.0000
[2.3806, 3.5057)	0.0243	–0.3034	1.3445	–2.1338	1.2699
[3.5057, 4.2751)	–0.0125	0.2120	–1.3659	4.2007	–4.2817
[4.2751, 6.6127)	0.0005	–0.0093	0.0535	0.1554	0.0418
[6.6127, 7.8886)	–0.0034	0.0942	–0.9729	4.6803	–7.4387
[7.8886, 10.2557)	0.0114	–0.3746	4.5742	–24.4928	50.0953

Table 2. *The coefficients of the 1st position curve of the 2nd joint*

Intervals [s]	q_4 [rad]	q_3 [rad]	q_2 [rad]	q_1 [rad]	q_0 [rad]
[0.0000, 2.3806)	–0.0019	0.0093	0.0000	0.0000	0.5236
[2.3806, 3.5057)	–0.0020	0.0101	–0.0029	0.0045	0.5209
[3.5057, 4.2751)	0.0136	–0.2079	1.1433	–2.6743	2.8686
[4.2751, 6.6127)	–0.0032	0.0796	–0.7004	2.5805	–2.7475
[6.6127, 7.8886)	–0.0010	0.0213	–0.1216	0.0290	1.4707
[7.8886, 10.2557)	0.0029	–0.1033	1.3526	–7.7240	16.7608

Table 3. *The coefficients of the 2nd position curve of the 1st joint*

Intervals [s]	q_4 [rad]	q_3 [rad]	q_2 [rad]	q_1 [rad]	q_0 [rad]
[0.0000, 2.3806)	0.0020	–0.0097	0.0000	0.0000	–0.3491
[2.3806, 3.5057)	–0.0017	0.0253	–0.1249	0.1982	–0.4670
[3.5057, 4.2751)	–0.0002	0.0051	–0.0185	–0.0503	–0.2492
[4.2751, 6.6127)	–0.0029	0.0504	–0.3096	0.7791	–1.1356
[6.6127, 7.8886)	0.0147	–0.4147	4.3041	–19.5600	32.4885
[7.8886, 10.2557)	–0.0094	0.3443	–4.6773	27.6740	–60.6644

Table 4. *The coefficients of the 2nd position curve of the 2nd joint*

Intervals [s]	q_4 [rad]	q_3 [rad]	q_2 [rad]	q_1 [rad]	q_0 [rad]
[0.0000, 2.3806)	–0.0032	0.0156	0.0000	0.0000	0.3491
[2.3806, 3.5057)	0.0071	–0.0822	0.3493	–0.5543	0.6790
[3.5057, 4.2751)	–0.0116	0.1797	–1.0280	2.6645	–2.1421
[4.2751, 6.6127)	0.0044	–0.0941	0.7280	–2.3400	3.2066
[6.6127, 7.8886)	–0.0085	0.2460	–2.6457	12.5325	–21.3803
[7.8886, 10.2557)	0.0032	–0.1229	1.7198	–10.4260	23.8975

Table 5. *Stetting for external disturbances and uncertainties and starting points*

	External disturbances and uncertainties		Starting points [rad]	
	The 1st position curve	The 2nd position curve	The 1st position curve	The 2nd position curve
The 1st joint	$10\exp(-2(t-5)^2)$	$10\sin(t)$	0.02	–0.34
The 2nd joint	$2\exp(-0.5(t-5)^2)$	$2\cos(t)$	0.52	0.34

ideal trajectories in each period accords with Eq. (28), a reference trajectory formula.

$$y = q_4 t^4 + q_3 t^3 + q_2 t^2 + q_1 t + q_0. \quad (28)$$

The setting for the uncertainties and external disturbances and starting points for the four kinds of control methods is shown in Table 5. The parameter setting for the three sliding mode methods is shown in Table 6. The boundary layer thickness of the fuzzy controller is taken as 1×10^{-5}. The control parameters of the PID are as follows: $K_p=5000$, $K_i=500$, $K_d=2000$. The design of the two-DOF manipulator in this paper is as follows: $m_1=m_2=2$, $r_1=1$, $r_2=0.8$, $g=9.8$ [29].

Table 6. *Parameter setting for the three sliding modes*

Methods	p	q	η	β_1	β_2
FETSM	5	3	0.2	1	1
ETSM					
ESM	1	1			

The trajectory-tracking situation of the above four control methods is shown in Figs. 3 to 6, demonstrating that all four control methods can effectively implement the trajectory-tracking task and meet the basic requirements of practical application. According to Fig. 3, it is found that the tracking trajectories by the ETSM and the proposed FETSM coincide with the ideal trajectories with only slight

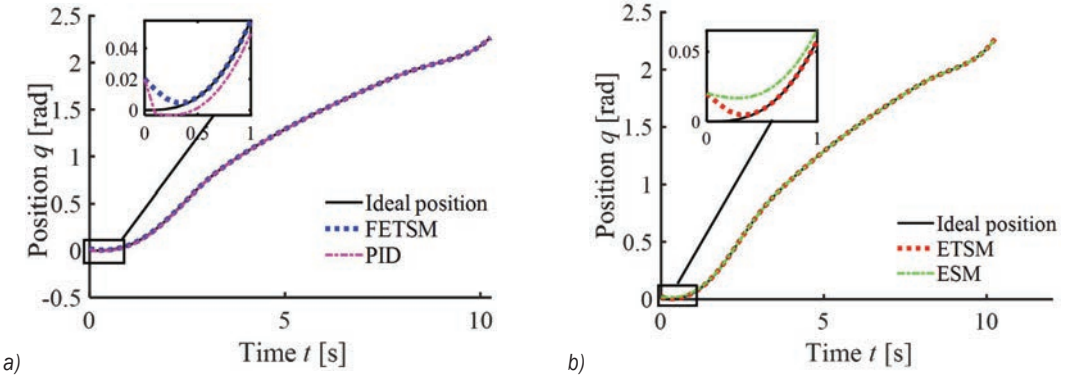

Fig. 3. *Tracking situation of the 1st position curve of the 1st joint; a) FETSM and PID; b) ETSM and ESM*

deviation in the initial stage. The phenomenon in Fig. 3 is similar to those in Figs. 4 to 6. However, the tracking trajectories by the ESM and PID have some obvious deviation from the ideal trajectories in some different periods. In order to further compare the control precision of the four methods, their tracking errors are quantitatively analysed by calculating the ordinate difference between the actual trajectories and the ideal ones at the same time and the same joint.

The averages of the tracking error are shown in Table 7. For the 1st curve, compared with the ETSM, the average error of the 1st joint by the proposed FETSM is increased by 1.88 %, and the average error of the 2nd joint is reduced by 15.33 %; compared with the ESM, those errors are reduced by 81.13 % and 94.20 % respectively; compared with the PID, those error is reduced by 88.58 % and 93.17 % respectively. As for the 2nd curve, compared with the ETSM, the

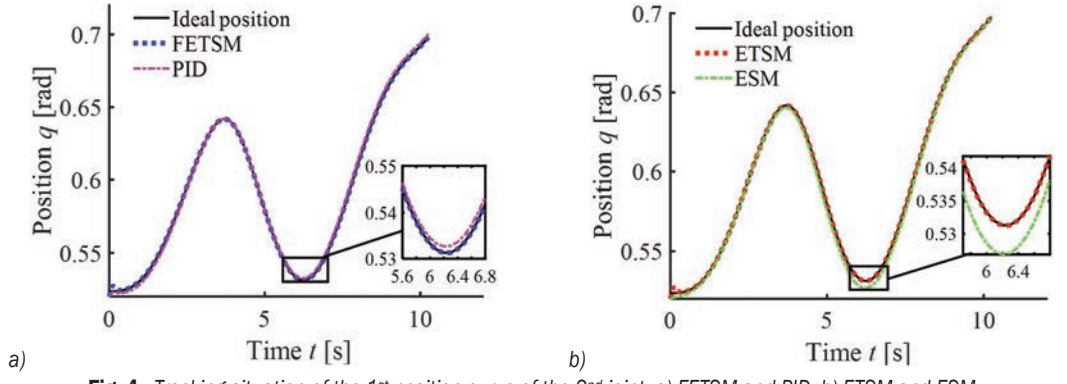

Fig. 4. *Tracking situation of the 1st position curve of the 2nd joint; a) FETSM and PID; b) ETSM and ESM*

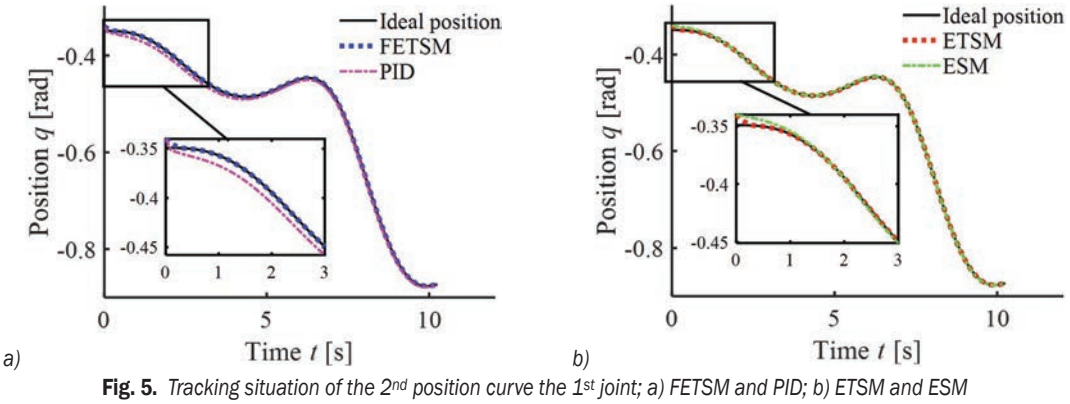

Fig. 5. *Tracking situation of the 2nd position curve the 1st joint; a) FETSM and PID; b) ETSM and ESM*

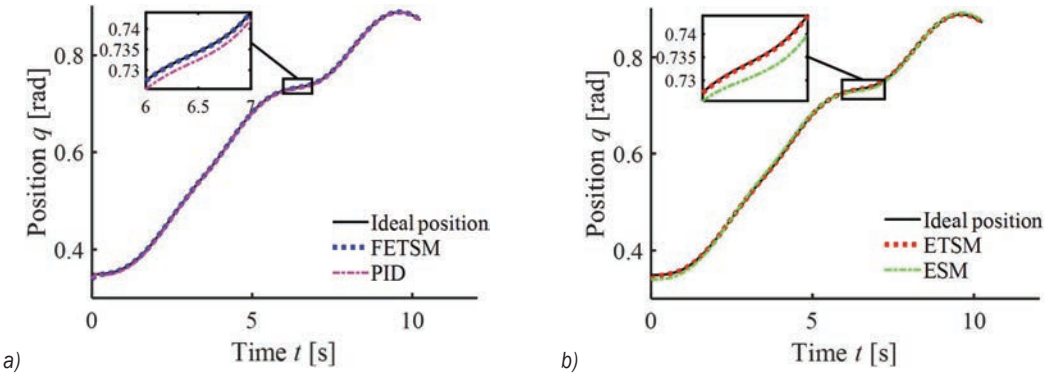

Fig. 6. *Tracking situation of the 2nd position curve of the 2nd joint; a) FETSM and PID; b) ETSM and ESM*

Table 7. *The averages of tracking error*

Control methods	The 1st curve & the 1st joint [rad]	The 1st curve & the 2nd joint [rad]	The 2nd curve & the 1st joint [rad]	The 2nd curve & the 2nd joint [rad]
FETSM	4.34×10^{-4}	1.16×10^{-4}	2.11×10^{-4}	2.14×10^{-4}
ETSM	4.26×10^{-4}	1.37×10^{-4}	1.70×10^{-4}	2.79×10^{-4}
ESM	2.30×10^{-3}	2.00×10^{-3}	1.40×10^{-3}	3.40×10^{-3}
PID	3.80×10^{-3}	1.70×10^{-3}	6.00×10^{-3}	2.00×10^{-3}

average error of the 1st joint by the proposed FETSM is increased by 24.12 %, and the average error of the 2nd joint is reduced by 23.30 %; compared with the ESM, those errors are reduced by 84.93 % and 93.71 % respectively; compared with the PID, those error is reduced by 96.43 % and 89.30 %, respectively.

In brief, the precision of the proposed FETSM dealing with the 1st joint is less than that of the ETSM, but the average error of the overall joints is reduced by 3.56 % compared with the latter; compared with the ESM and PID, the FETSM can reduce the average error of the overall joints by 89.30 % and 92.78 %, respectively. As a result, the proposed FETSM has better control precision compared with the other three methods.

The variation of the tracking error of joints 1 and 2 with time was shown in Fig. 7. The proposed FETSM is superior to the PID in error convergence speed and robustness. To compare the error convergence speed and robustness of three sliding mode methods, taking the error by the ESM at 1 s as the reference, the convergence time of the four curves by the proposed FETSM to achieve the reference error is 0.195 s, 0.260 s, 0.175 s, and 0.045 s, respectively; and that by the ETSM is 0.195 s, 0.260 s, 0.175 s, and 0.047 s, respectively. On the 2nd position curve of the 2nd joint, the error convergence speed by the FETSM is slightly better than that by the ETSM; in other cases, the error convergence time by the proposed FETSM is consistent with that by the ETSM. Moreover, the average speed of the error convergence by the above two is 83.13 % faster than that by the ESM. The averages of the maximum error caused by disturbances in the three sliding mode methods are shown statistically in Table 8. It shows that the robustness of the proposed FETSM is less than that of the ETSM in the 1st joint but better than the latter in the 2nd joint. The robustness of the FETSM is superior to that of the ESM in joints 1 and 2. The averages of the overall disturbance error by the FETSM, the ETSM and ESM are 9.39×10^{-5}, 1.35×10^{-4}, and 2.96×10^{-3}, respectively. In short, the overall robustness of the proposed FETSM is 30.24 % higher than that of the ETSM, and 96.83 % higher than that of the ESM. It can be seen from the above analysis that the proposed FETSM can ensure sufficient error convergence speed and robustness.

4.2 Analysis of Input Torque

In order to investigate the anti-chattering performance of the FETSM, the input torque characteristics of the different control systems, in the same joint and in the same position curve, are analysed. The ETSM, which has better trajectory-tracking precision than the ESM, is selected as a competitive sample of non-fuzzy control; the PID is selected as a competitive sample of non-sliding mode control. The comparison diagrams

for the input torques using the three methods are shown in Figs. 8 to 11.

As shown in Fig. 8a, there is chattering with an amplitude of approximately 10.24 N·m by the proposed FETSM in the period of 0 s to 0.55 s, but the input torque curve is smooth and continuous in other times. Combined with Fig. 7a, it is found that the error by the proposed FETSM converges to 0 s near 0.55 s, and the system reaches the sliding mode surface. Therefore, the reason for the chattering in the initial stage is that the system does not reach the sliding mode surface. The phenomenon in Fig. 8a is similar to those in Figs. 9a, 10a and 11a using the same the FETSM.

As shown in Fig. 8b, the chattering amplitude of the input torque curve by the ETSM is small in the period of 4.9 s to 5.1 s; in other periods, it is about 10.20 N·m. Currently, the disturbance term applied to the joint is Gaussian and reaches the maximum in 5 s. Obviously, the chattering amplitude of the system decreases only when the disturbance term approaches the switching term. The phenomenon in Fig. 8b is similar to those in Figs. 9b, 10b and 11b. Quantitatively comparing and analysing the chattering time of the systems by the ETSM and FETSM in the four cases shown in Figs. 8 to 11, The chattering time of these two methods is shown in Table 9. It is found that those by the proposed FETSM is less than those by the ETSM, can be reduced by 94.75 % on average.

As shown in Fig. 8c, the input torque curve using the PID is consistent with the proposed FETSM except that serious chattering occurs in the overshoot stage. The phenomenon in Fig. 8c is similar to those in Figs. 9c, 10c and 11c. Quantitatively comparing and

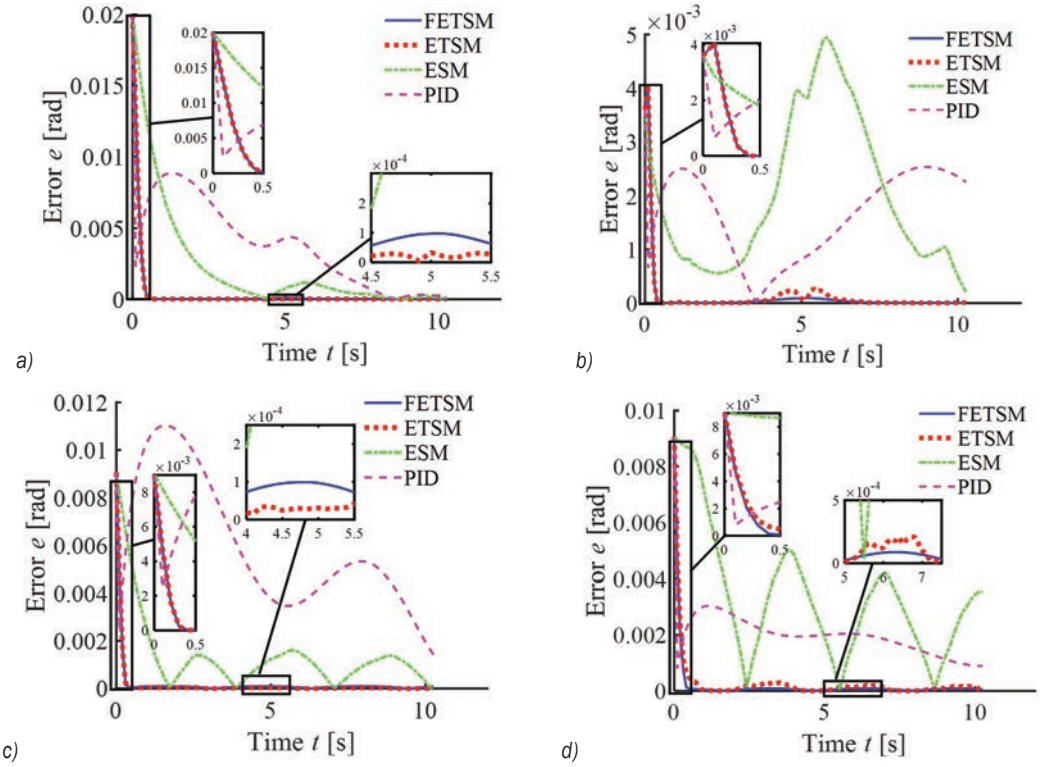

Fig. 7. *Variation of the error of joints; a) the 1st position curve of the 1st joint; b) the 1st position curve of the 2nd joint; c) the 2nd position curve of the 1st joint; d) the 2nd position curve of the 2nd joint*

Table 8. *The averages of the maximum error caused by disturbances*

Control methods	The 1st curve & the 1st joint [rad]	The 1st curve & the 2nd joint [rad]	The 2nd curve & the 1st joint [rad]	The 2nd curve & the 2nd joint [rad]
FETSM	9.74×10^{-5}	9.17×10^{-5}	9.84×10^{-5}	8.79×10^{-5}
ETSM	3.31×10^{-5}	2.53×10^{-4}	3.03×10^{-5}	2.22×10^{-4}
ESM	1.18×10^{-3}	4.94×10^{-3}	1.46×10^{-3}	4.25×10^{-3}

analysing the chattering amplitude of the systems by the PID and FETSM in the four cases shown in Figs. 8 to 11, The maximum amplitudes of these two methods are shown in Table 10. It is found that those by the proposed FETSM is less than those by the PID, can be reduced by 99.21 % at least.

Moreover, compared with similar methods proposed by other scholars [1], the proposed FETSM can achieve similar anti-chattering performance while the structure of the switching term is simple.

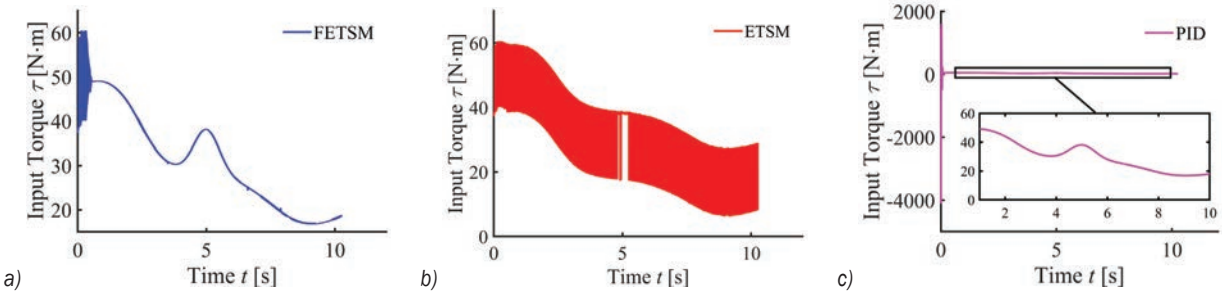

Fig. 8. *Input torque comparison of the 1st position curve of the 1st joint; a) FETSM; b) ETSM; c) PID*

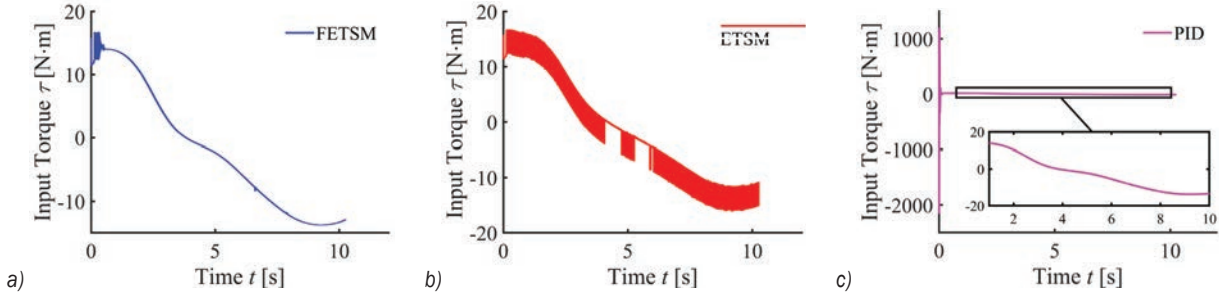

Fig. 9. *Input torque comparison of the 1st position curve of the 2nd joint; a) FETSM; b) ETSM; c) PID*

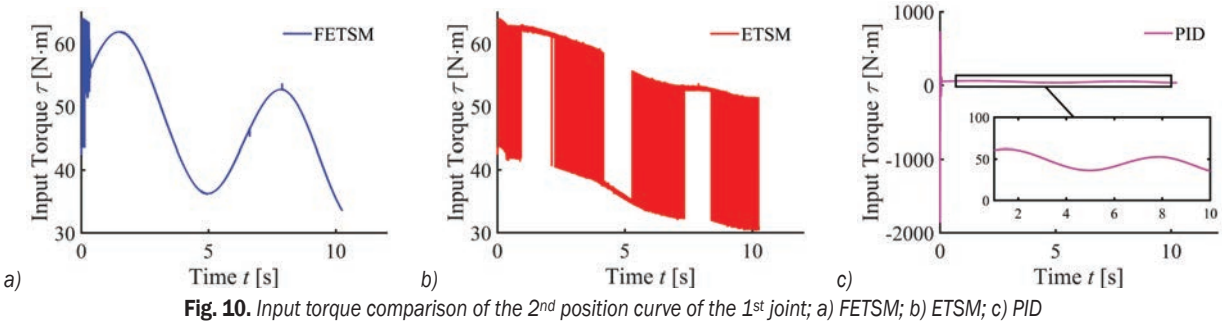

Fig. 10. *Input torque comparison of the 2nd position curve of the 1st joint; a) FETSM; b) ETSM; c) PID*

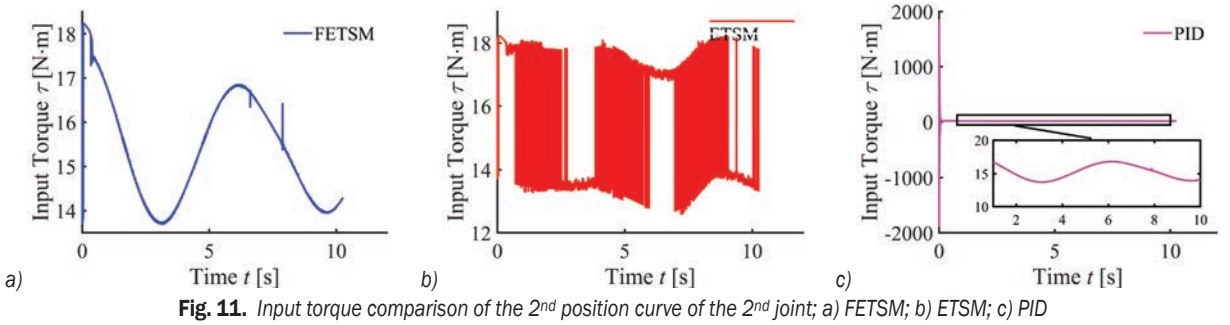

Fig. 11. *Input torque comparison of the 2nd position curve of the 2nd joint; a) FETSM; b) ETSM; c) PID*

Table 9. *The chattering time of the FETSM and ETSM*

Control methods	The 1st curve & the 1st joint [s]	The 1st curve & the 2nd joint [s]	The 2nd curve & the 1st joint [s]	The 2nd curve & the 2nd joint [s]
FETSM	0.55	0.58	0.42	0.11
ETSM	9.67	8.81	6.76	6.76

Table 10. *The maximum amplitudes of the FETSM and PID*

Control methods	The 1st curve & the 1st joint [N·m]	The 1st curve & the 2nd joint [N·m]	The 2nd curve & the 1st joint [N·m]	The 2nd curve & the 2nd joint [N·m]
FETSM	10.24	2.21	10.26	2.22
PID	2.85×10^3	1.6810^3	1.3010^3	1.8710^3

5 CONCLUSIONS

(1) The proposed FETSM control method can be used to track the actual motion position of each joint according to the ideal trajectory of the corresponding joint. This technology can be used to suppress the chattering of manipulators under heavy-load operations.

(2) Simulation results show that compared with the ETSM, the overall tracking precision by the proposed FETSM is improved by 3.56 %, and the overall robustness is improved by 30.24 %. Moreover, their error convergence speeds are basically the same. Compared with the ESM, the overall tracking precision by the proposed FETSM is improved by 89.30 %, the overall robustness is improved by 96.83 %, and the error convergence speed is improved by 83.13 %. Compared with the PID, the overall tracking precision by the proposed FETSM is improved by 92.78 %. Moreover, its error convergence speed and overall robustness are better than those by the PID. Consequently, the proposed FETSM can obtain sufficient trajectory-tracking precision, error convergence speed and robustness.

(3) Employing the proposed FETSM, chattering occurs only when the system does not reach the sliding mode surface. Compared with the ETSM, the proposed FETSM can reduce the chattering time by 94.75 % on average. Compared with the PID, the maximum chattering amplitude by the FETSM can be reduced by 99.21 % at least. Therefore, the proposed FETSM can reduce the chattering of systems, and optimize the input torque control.

6 ACKNOWLEDGEMENTS

This work was supported by the Natural Science Research Project of Higher Education of Anhui Province of China [grant numbers KJ2020A0357] and the University Synergy Innovation Program of Anhui Province of China [grant numbers GXXT-2019-048].

7 REFERENCES

[1] Wu A.G., Wu S.H., Dong N. (2019). Non-singular fast terminal sliding model fuzzy control of robotic manipulators. *Journal of Zhejiang University (Engineering Science)*, vol. 53, no. 5, p. 862-871, **DOI:10.3785/j.issn.1008-973X.2019.05.006**.

[2] Liu, P., Liu, Y.H., Wang, K., Wei, X.X., Xin, C., Wu, X.L. (2020). Design and Performance Analysis of Airbag-Soft-Manipulator According to Characteristic Parameters. *Strojniški vestnik - Journal of Mechanical Engineering*, vol. 66, no. 1, p. 38-50, **DOI:10.5545/sv-jme.2019.6228**.

[3] Fang, L.X., Wang, T., Wang, P.J., Hou, C.X., Wu, M. (2021). Kinematic cooperative optimization control algorithm for underground heavy-load robot. *Journal of Intelligent & Robotic Systems, Journal of intelligent & robotic systems*, vol. 102, no. 11, p. 1-15, **DOI:10.1007/s10846-021-01360-y**.

[4] Alam, W., Mehmood, A., Ali, K., Javaid, U., Alharbi, S., Iqbal, J. (2018). Non-linear control of a flexible joint robotic manipulator with experimental validation. *Strojniški vestnik - Journal of Mechanical Engineering*, vol. 64, no. 1, p. 47-55, **DOI:10.5545/sv-jme.2017.4786**.

[5] Wang, Y.Y., Yan, F., Jiang, S.R., Chen, B. (2020). Adaptive non-singular terminal sliding mode control of cable-driven manipulators with time delay estimation. *International Journal of Systems Science*, vol. 51, no. 8, p. 1429-1447, **DOI:10.1080/00207721.2020.1764659**.

[6] Kumar, N., Rani, M. (2021). Neural network-based hybrid force/position control of constrained reconfigurable manipulators. *Neurocomputing*, vol. 420, no. 3, p. 1-14, **DOI:10.1016/j.neucom.2020.09.009**.

[7] Shojaei, K., Kazemy, A., Chatraei, A. (2021). An observer-based neural adaptive PID2 controller for robot manipulators including motor dynamics with a prescribed performance.

IEEE/ASME Transactions on Mechatronics, vol. 26, no. 3, p. 1689-1699, **DOI:10.1109/TMECH.2020.3028968**.

[8] Zhang, Y.Y., Kim, D.G., Zhao, Y. D., Lee, J.M. (2020). PD control of a manipulator with gravity and inertia compensation using an RBF neural network. *Transactions on Control, Automation and Systems Engineering*, vol. 18, no. 12, p. 3083-3092, **DOI:10.1007/S12555-019-0482-X**.

[9] Liang, X.F., Yang, B. (2011). PID track following control of a 7-DOF manipulator based on ADAMS. *Advanced Materials Research*, vol. 1380, no. 636, p. 694-597, **DOI:10.4028/www.scientific.net/AMR.317-319.694**.

[10] Elkhateeb, N.A., Badr, R.I. (2017). Novel PID tracking controller for 2DOF robotic manipulator system based on artificial bee colony algorithm. *Electrical, Control and Communication Engineering*, vol. 13, no. 1, p. 55-62, **DOI:10.1515/ecce-2017-0008**.

[11] Haidegger, T., Kovács, L., Precup, R-E., Preitl, S., Benyó, B., Zoltán Benyó, Z. (2011). Cascade control for telerobotic systems serving space medicine. *IFAC Proceedings Volumes*, vol. 44, no. 1, p. 3759-3764, **DOI:10.3182/20110828-6-IT-1002.02482**.

[12] Neghreian, E., Koofugar, H.R., (2021). Robust tracking control of robot manipulators with friction and variable loads without velocity measurement: A switched control strategy. *Proceedings of the Institution of Mechanical Engineers, Part I: Journal of Systems and Control Engineering*, vol. 235, no. 4, p. 532-539, **DOI:10.1177/0959651820947944**.

[13] Izadbakhsh, A, Khorashadizadeh, S. (2020). Robust adaptive control of robot manipulators using Bernstein polynomials as universal approximator. *International Journal of Robust and Nonlinear Control*, vol. 30, p. 2719-2735, **DOI:10.1002/rnc.4913**.

[14] Liu, F.C., Liang, L.H., Li, Q., Wang, W.K. (2014). Sliding mode control for space manipulator trajectory tracking considering effects of gravity. *Control and Decision*, vol. 29, no. 10, p. 1856-1860, **DOI:10.13195/j.kzyjc.2013.0764**. (in Chinese)

[15] Jiang, S., Tian, F.Q., Sun, S.Y., Liang, W.G. (2020). Integrated guidance and control of guided projectile with multiple constraints based on fuzzy adaptive and dynamic surface. *Defence Technology*, vol. 16, no. 6, p. 1130-1141, **DOI:10.1016/j.dt.2019.12.003**.

[16] Xi, L.P., Chen, Z.L., Qi,X.H. (2012). Fast sliding mode variable structure control for manipulators with chattering suppression effect. *Electric Machines and Control*, vol. 16, no. 7, p. 97-102, **DOI:10.15938/j.emc.2012.07.002**. (in Chinese)

[17] Tran, M.D., Kang, H.J. (2016). A novel adaptive finite-time tracking control for robotic manipulators using non-singular terminal sliding mode and RBF neural networks. *International journal of precision engineering and manufacturing*, vol. 17, no. 7, p. 863-870, **DOI:10.1007/s12541-016-0105-x**.

[18] Chang, Y.F., Yuan, R.Y., Tan, X.M., Yi, J.Q. (2016). Observer-based adaptive sliding mode control and fuzzy allocation for aero and reaction jets' missile. *Proceedings of the Institution of Mechanical Engineers Part I - Journal of Systems and Control Engineering*, vol. 230, no. 6, p. 498-511, **DOI:10.1177/0959651816629540**.

[19] Wan, M., Tian. Q.G., Wang, M.C. (2018). adaptive sliding mode control of robot manipulator based on second order approximation accuracy and decomposed fuzzy compensator. *Wireless Personal Communications*, vol. 103, no. 2, p. 1207-1218, DOI:10.1007/s11277-018-5421-2.

[20] Feng, Y., Yu, X.H., Man, Z.H. (2002). Non-singular terminal sliding mode control of rigid manipulators. *Automatica*, vol. 38, no. 12, p. 2159-2167, **DOI:10.1016/S0005-1098(02)00147-4**.

[21] Wang, T.L., Tan, N.L., Zhang, X.W., L.i., G.Z., Su, S.Q., Zhou, J., Qiu, J.Z., Wu, Z.Q., Zhai, Y.K., Labati, RD, Piuri, V., Scotti, F. (2021). A time-varying sliding mode control method for distributed-mass double pendulum bridge crane with variable parameters. *IEEE ACCESS*, vol. 9, no. 5, p. 75981-75992, **DOI:10.1109/ACCESS.2021.3079303**.

[22] Cheng, C., Lai, R., Chen, Z., Liu, X.D. (2016) Adaptive non-singular terminal sliding mode control of 6-DOF manipulator with modified switch function. *Journal of Advanced Computational Intelligence and Intelligent Informatics*, vol. 20, no. 2, p. 294-301, **DOI:10.20965/jaciii.2016.p0294**.

[23] Shahri, E.S.A., Balochian, S. (2015). Analysis of fractional-order linear systems with saturation using Lyapunov' s second method and convex optimization. *International Journal of Automation and Computing*, vol. 12, no. 4, p. 4440-4447, **DOI:10.1007/s11633-014-0856-8**.

[24] Lv, Z.Y., Zhang, Y., Yu, M., Xia, Y.H.. (2020). Decentralised coordinated energy management for hybrid AC/DC microgrid by using fuzzy control strategy. *IET Renewable Power Generation*, vol. 14, no. 14, p. 2649-2656, **DOI:10.1049/iet-rpg. 2019.1281**.

[25] Precup, R.-E., Preitl, S. (2003). Development of fuzzy controllers with non-homogeneous dynamics for integral-type plants. *Electrical Engineering*, vol. 85, no. 3, p. 155-168, **DOI:10.1007/s00202-003-0157-7**.

[26] Li, Y. (2021). Anhui Polytechnic University School of Mechanical Engineering, from *https://github.com/LiYi199983/-fuzzycontrol*, accessed on 2021-08-28.

[27] Liang, X.C., Wan, Y., Zhang, C.G., Kou, Y.Y. Xin, Q.Q., Yi, W. (2018). Robust position control of hydraulic manipulators using time delay estimation and non-singular fast terminal sliding mode. *Proceedings of the Institution of Mechanical Engineers, Part I: Journal of Systems and Control Engineering*, vol. 232, no. 1, p. 50-61, **DOI:10.1177/0959651817733596**.

[28] Liu, T.R. (2019). Quadratic feedback–based equivalent sliding mode control of wind turbine blade section based on rigid trailing-edge flap. *Measurement & Control*, vol. 52, no. 1-2, p. 81-90, **DOI:10.1177/0020294018819548**.

[29] Li, Y. (2021). Anhui Polytechnic University School of Mechanical Engineering, from *https://github.com/LiYi199983/FETSM-matlab-simulink*, accessed on 2021-08-16.

Strojniški vestnik - Journal of Mechanical Engineering 67(2021)9, 445-457
© 2021 Journal of Mechanical Engineering. All rights reserved.
DOI:10.5545/sv-jme.2020.6959 Original Scientific Paper
Received for review: 2020-10-01
Received revised form: 2021-01-04
Accepted for publication: 2021-01-07

Active Vibration Control of a Mechanical Servo High-speed Fine-Blanking Press

Yanxiong Liu[1,3] – Yuwen Shu[1,3] – Wentao Hu[1,3] – Xinhao Zhao[1,2,*] – Zhicheng Xu[1,3]

[1]Wuhan University of Technology, Hubei Key Laboratory of Advanced Technology of Automotive Components, China
[2]Wuhan University of Technology, School of Materials Science and Engineering, China
[3]Wuhan University of Technology, Hubei Collaborative Innovation Center for Automotive Components Technology, China

The fine-blanking process as an advanced sheet metal forming process has been widely applied in industry. However, specially designed equipment is required for this process. In this paper, a novel mechanical servo high-speed fine-blanking press with the capacity of 3200 kN is proposed, and the vibration control for this machine is researched to achieve the requirement of fine-blanked parts of high dimensional accuracy, since the vibration of the fine-blanking machine will cause the machining displacement error and reduce the machining accuracy. Self-adaptive feed-forward control is used to simulate the active vibration control of the mechanical fine-blanking machine. The vibration control principle of the fine-blanking machine is described, and the control algorithm is established. At the same time, the mechanical vibration model of the fine-blanking machine as the controlled object is established, and the parameters of the excitation input and the mechanical model are obtained by the fine-blanking finite element simulation and the experiments of the vibration measurement of the press. Finally, the numerical simulation and analysis of active vibration control based on MATLAB are carried out. The results show that the control effect is good, and the vibration response is effectively reduced, thus greatly increasing the processing accuracy, saving a significant amount of energy, and reducing the energy consumption and defective rate.

Keywords: active vibration control; mechanical vibration model; mechanical servo high-speed fine-blanking press; self-adaptive feed-forward control

Highlights

- *The mechanical vibration model of the fine-blanking machine tool is established.*
- *The dynamic model parameters of the mechanical fine-blanking machine are obtained by using finite element analysis and empirical formula.*
- *An adaptive feed-forward vibration controller for the fine-blanking machine is designed and applied to active vibration control of the fine-blanking machine.*
- *The vibration response of the whole machine has been effectively reduced when the active control is applied, in which the time-domain vibration response has been reduced by more than 95 %, and the frequency-domain vibration response has been reduced by more than 80 %, which means that the vibration reduction effect is obvious.*

0 INTRODUCTION

The fine-blanking (FB) process as an advanced net shape or near-net shape plastic forming process has been widely applied in industry because of the advantages of high efficiency and high parts quality [1] and [2]. Many mid-thick sheet metal components with complicated shapes and high dimensional accuracy can be fabricated with the FB process in one operation, as shown in Fig. 1a. Compared with the conventional blanking process, a special designed fine-blanking press was required for this process, providing at least three separate forces: blanking force, blank holder force, and counter punch force [3]. Now, almost all FB presses are hydraulic machines with the capacity of 3200 kN to 12000 kN [4], and the forming efficiency is about 30 to 70 times per minute with a punch stroke of 40 mm. With the increasingly huge market demand for the mid-thick sheet metal parts, the FB efficiency should be further improved; the target is about 200 times per minute or higher.

A mechanical servo high-speed FB press was designed and fabricated by our research group and Huangshi Huali Co., Ltd., and the forming efficiency can reach up to 220 times per minute and the maximum forming capacity is 3200 kN. The mechanical construction of the main driving system is shown in Fig. 1b, and the main slide block can achieve the trajectory shown in Fig. 1c. With the increasing punch frequency, the vibration of the FB press will become increasingly severe. It is known that the vibration of the press not only affects the parts' quality, such as causing the crack on the cutting surface and reducing the dimensional accuracy but also reducing the service life of the machine. Moreover, the noise caused by the machine vibration will adversely affect working conditions and human health. Therefore, vibration control for the high-speed fine blanking press is urgently required.

*Corr. Author's Address: Wuhan University of Technology, Wuhan, China, zhaoxh@whut.edu.cn

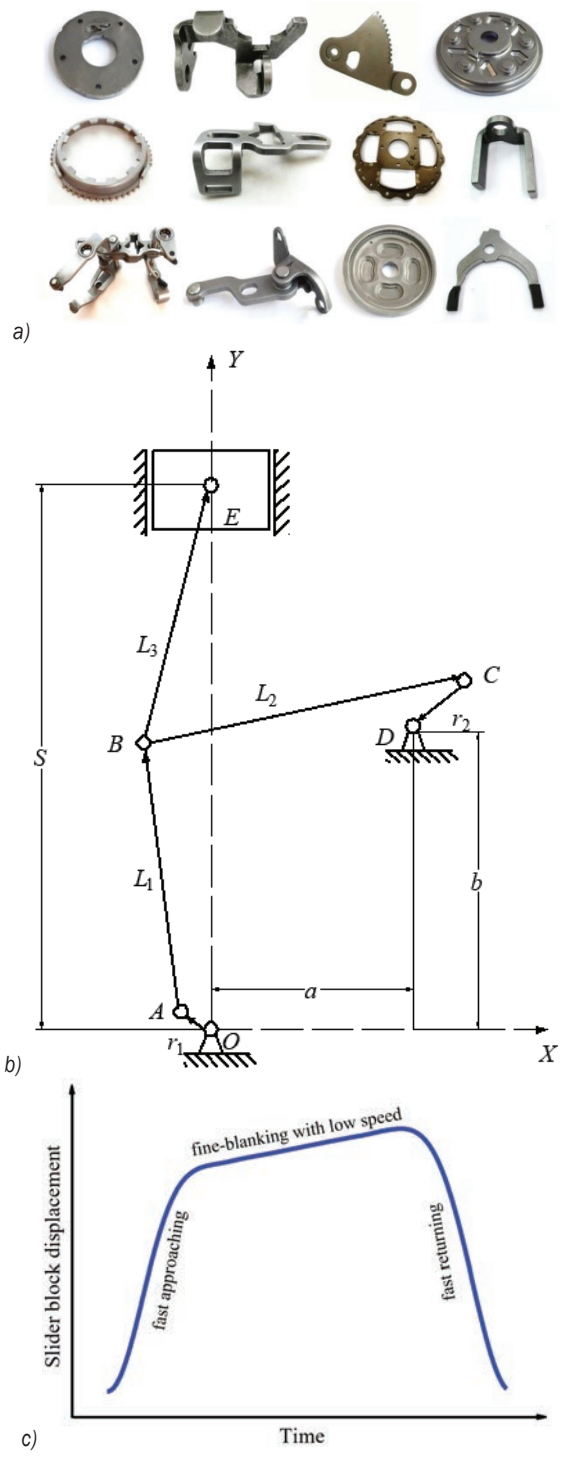

Fig. 1. *a) The mid-thick sheet metal parts fabricated by FB process, b) the mechanical construction of the main driving system of the high-speed FB press, and c) the slide block stroke diagram*

In general, the passive control method was applied for the vibration control of the traditional press, such as increasing the stiffness of the frame and adding the vibration isolation system, and the vibration control effort for the excitation source of the press is very rare. For the high-speed FB press proposed in this paper, except for the passive control method, the active vibration control method was also applied to restrain the vibration of the whole machine caused by the elastic restoring force produced by the FB process. Therefore, the low-frequency vibration can be effectively suppressed, so as to reduce the vibration of the mechanical servo high-speed FB press to the greatest extent.

For the research of the active control by Lueg, Guicking **[5]** submitted, early in 1933, a patent application describing for the first time the principle of active noise cancellation. The basic idea is that using the active control wave with the same amplitude of the noise to counteract the original noise. In 1953, Olson and May **[6]** invented the electronic sound absorption equipment, which proved the practical feasibility of the active vibration and noise control theory through experiments. Since then, active vibration control technology has been gradually applied to engineering machines. Winberg et al. **[7]** and Daley et al. **[8]** applied the active vibration control for the marine applications.

In recent years, many new active vibration control theories have been developed. Shao et al. **[9]** created the finite element (FE) active vibration control model of the piezoelectric flexible linkage by using the mixed Hamilton principle. Based on the complex mode theory, a hybrid independent mode controller, which consisted of the state feedback and disturbance feed-forward control, was developed. The results showed that the vibration was effectively suppressed for the flexible four-bar linkage. Li **[10]** studied the active control of submarine vibration system, and a corresponding adaptive control method was put forward. A good control effect of the vibration system by applying the periodic excitation force was obtained. Zhu et al. **[11]** proposed the active vibration control process for the marine diesel engine, and the x-LMS algorithm based on the off-line identification of error channel was used for the active vibration control. Belyi and Gan **[12]** studied and brought forward a combined bilateral and binaural active noise control algorithm for closed-back headphones. Soni et al. **[13]** published about the active vibration control of a ship-mounted flexible rotor-shaft-bearing system. Teo and Fleming **[14]** published optimal integral force feedback for active vibration control in 2015. Park and Kim **[15]** studied semi-active vibration control of space truss structures by friction damper for the maximization of modal damping ratio in 2013.

Through the inspiration of the active vibration control method mentioned above, the active vibration control strategy was researched for the mechanical servo high-speed FB press to suppress the periodic low-frequency vibration of the machine. The active vibration control principle of the high-speed FB press was analyzed, and the adaptive vibration controller was created. According to test results of the FB press vibration, the input parameters for the control model were obtained, and the active vibration control effect was predicted by using MATLAB software.

1 ADAPTIVE VIBRATION CONTROLLER DESIGN

1.1 Active Vibration Control System

The active vibration control system of a mechanical servo FB press is mainly composed of the following parts, as shown in Fig. 2.

(1) Controlled object. In this paper, the controlled object is the mechanical servo FB press. The main drive system of the press is the excitation source of the controlled object; the excitation force acts on the frame and then transfers to the whole machine. Since the elastic restoring force is mainly acted on in the vertical direction, the mathematical model of the controlled object is primarily focused on the vertical deformation.

(2) Measuring mechanics. The core component of the measuring mechanics is the sensor. An acceleration sensor is often used in the data acquisition of vibration response. The vibration signal of the whole machine measured by the acceleration sensor is transmitted to the control system through signal amplification and filtering, which is used as the input parameter of the active vibration control.

(3) Electric actuator. According to the command of the controller, the actuator applies the specified force or torque on the frame of the press and feeds back the action effect to the controller.

(4) Controller. The controller is the core part of the active vibration control system, which can provide the command and control rate of the actuator. Because the main driving system is motorial during the forming process, the adaptive controller which can adjust the parameters of the control system applied in this paper.

(5) Energy and auxiliaries. The external energy supplies the input energy of the actuator for the active vibration control system of the FB press.

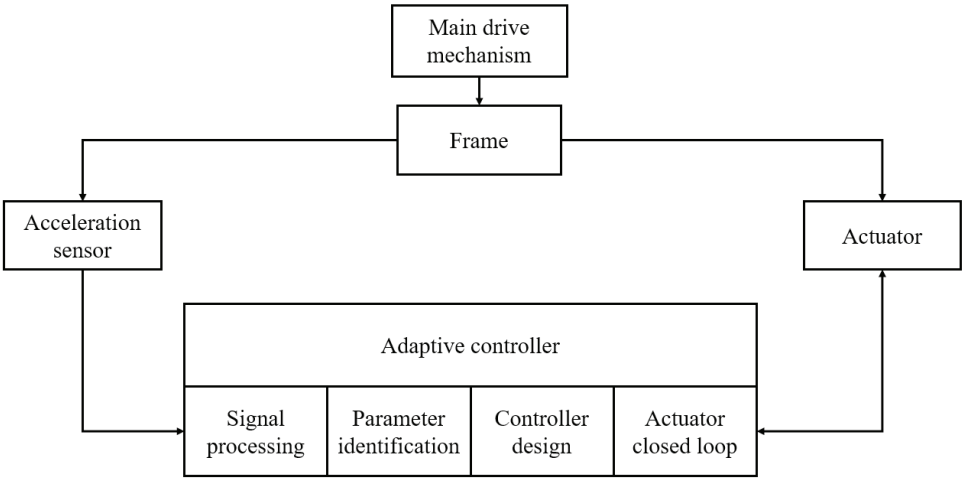

Fig. 2. *Schematic diagram of the active vibration control system for FB press*

1.2 Adaptive Vibration Control Algorithm

The selection and design of the algorithm play an important role in the adaptive vibration controller. Among many adaptive control methods, the least mean square (LMS) adaptive algorithm [16] has been widely used, in which the gradient search method is used, the convergence solution can be obtained quickly, and the implementation is relatively simple.

The LMS algorithm can be expressed by Eq. (1):

$$F(e(n)) = \varepsilon(n) = E(e^2(n)) = E\left[d^2(n) - 2d(n)y(n) + y^2(n)\right]. \quad (1)$$

The filter of the adaptive active vibration controller adopts the finite impulse response (FIR) structure, and its structure diagram is shown in Fig. 3.

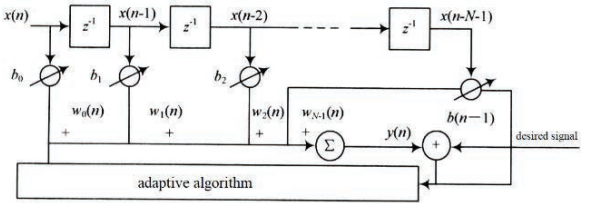

Fig. 3. *Adaptive FIR filter*

In Fig. 3 $x(n)$ represent the input of the adaptive active vibration control filter, $y(n)$ is the output of the adaptive active vibration control filter, $w(n)$ is the impulse response, $w(n)=\{w(0),w(1),...,w(n-1)\}$, then:

$$y(n)=\mathbf{W}^{\mathrm{T}}(n)\mathbf{X}(n)=\sum_{i=0}^{N-1}w_i(n)x(n-i). \tag{2}$$

For the filter with transverse structure, substitute the expression of into Eq. (1):

$$\varepsilon=E(\mathbf{d}^2(n))+\mathbf{W}^{\mathrm{T}}(n)\mathbf{R}\mathbf{W}(n)-2\mathbf{W}^{\mathrm{T}}(n)\mathbf{P}, \tag{3}$$

where where $\mathbf{R}=E[\mathbf{X}(n)\mathbf{X}^{\mathrm{T}}(n)]$ is the autocorrelation matrix of $\mathbf{N}\times\mathbf{N}$, is the cross-correlation vector for $\mathbf{N}\times1$, which represents the correlation between the ideal signal $\mathbf{d}(n)$ and the input vector.

Because the gradient descent method is adopted for the optimization process, so:

$$\frac{\partial\varepsilon}{\partial\mathbf{W}(n)_{w(n)=w^*}}=0. \tag{4}$$

When the mean square error reaches to the minimum value, the optimal weight coefficient can be obtained.

If the $\mathbf{R}$ matrix is full rank, the best value of the weight coefficient should be satisfied with $\mathbf{W}^*=\mathbf{R}^{-1}\mathbf{P}$, namely:

$$\begin{bmatrix} w_0^* \\ w_1^* \\ \vdots \\ w_{(n-1)}^* \end{bmatrix}=\begin{bmatrix} \phi_x(0) & \phi_x(1) & \cdots & \phi_x(n-1) \\ \phi_x(1) & \phi_x(0) & \cdots & \phi_x(n-2) \\ \vdots & \vdots & \ddots & \vdots \\ \phi_x(n-1) & \phi_x(n-2) & \cdots & \phi_x(0) \end{bmatrix}^{-1}\begin{bmatrix} \phi_{xd}(0) \\ \phi_{xd}(1) \\ \vdots \\ \phi_{xd}(n-1) \end{bmatrix}, \tag{5}$$

where, $\phi_x(m)=E[x(n)x(n-m)]$ shows the autocorrelation value of $x(n)$, $\phi_{xd}(k)=E[x(n)d(n-k)]$ represents the cross-correlation value between $x(n)$ and $d(n)$.

In practical applications, it is difficult to obtain the autocorrelation and cross-correlation values of signals. Therefore, gradient estimation value can be used, that is:

$$\begin{aligned}\hat{g}_w(n)&=-2d(n)x(n)+2x(n)x^{\mathrm{T}}(n)w(n)\\&=2x(n)(-d(n)+x^{\mathrm{T}}(n)w(n)).\end{aligned} \tag{6}$$

Using the gradient estimation value to replace the real values, then:

$$w(n+1)=w(n)+2\mu e(n)x(n). \tag{7}$$

This is the iterative equation of the LMS algorithm. In practical application, the step size is fixed, and the value of will affect the performance of the algorithm, resulting in the change of convergence speed, jump tracking ability and steady-state imbalance of the algorithm. Since the most appropriate value is very difficult to obtain, the variable step size normalized LMS algorithm is usually applied, which can be expressed as:

$$w(n+1)=w(n)+2\mu_n e(n)x(n)=w(n)+\Delta w(n). \tag{8}$$

According to the expression of the instantaneous square error of the LMS algorithm, the instantaneous square error of variable step size normalized LMS algorithm can be expressed as:

$$\begin{aligned}\tilde{e}^2(n)&=e^2(n)+2\Delta w^{\mathrm{T}}(n)x(n)x^{\mathrm{T}}(n)w(n)\\&+\Delta w^{\mathrm{T}}(n)x(n)x^{\mathrm{T}}(n)w(n)-2d(n)\Delta w^{\mathrm{T}}(n)x(n),\end{aligned} \tag{9}$$

then:

$$\begin{aligned}\Delta e^2(n)&=\tilde{e}^2(n)-e^2(n)=\\&-2\Delta w^{\mathrm{T}}(n)x(n)e(n)\\&+\Delta w^{\mathrm{T}}(n)x(n)x^{\mathrm{T}}(n)w(n).\end{aligned} \tag{10}$$

From $\Delta w(n)=2\mu_n e(n)x(n)$, we can get:

$$\begin{aligned}\Delta e^2(n)&=-4\mu_n e^2(n)x^{\mathrm{T}}(n)x(n)\\&+4\mu_n e^2(n)\left[x^{\mathrm{T}}(n)x(n)\right]^2.\end{aligned} \tag{11}$$

To minimize $\Delta e^2(n)$, which makes the instantaneous square error close to the square error, we can take $d\Delta e^2(n)/d\mu_n=0$, then,

$$\mu_n=\frac{1}{2x^{\mathrm{T}}(n)x(n)}. \tag{12}$$

In order to avoid the steady-state imbalance, a fixed numerical convergence factor μ_k is introduced to avoid a large step size when the denominator is very small during the iteration process. At the same time, another parameter γ is introduced to adjust the denominator. Then the updated iterative equation of the new variable step size normalized LMS algorithm is:

$$w(n+1) = w(n) + \frac{\mu_k}{\gamma + x^{\mathrm{T}}(n)x(n)} e(n)x(n). \quad (13)$$

1.3 Adaptive Feedforward Active Vibration Control of the Fine-Blanking Press

As mentioned in Section 1.1, the main drive system of the press applies vertical excitation force to the whole machine, including the frame. The actuator is installed on the frame, which can exert a controllable force with the opposite direction of the excitation force of the main drive system to offset the original vibration and realize active vibration reduction.

Because the vibration on the frame is easy to measure, the upper and lower cross-beams of the frame are selected as the vibration observation parts of the control system. The excitation force generated by the main drive system is transmitted to the frame through the primary channel to generate the vibration response, which can be used as the reference input of the adaptive active vibration control. is the control input, and the value is the estimated value of the excitation force. By adjusting the with the adaptive feed-forward control method, the vibration response of the frame can be reduced, and the effect of reducing the vibration of the whole machine can be achieved. The control block diagram is shown in Fig. 4.

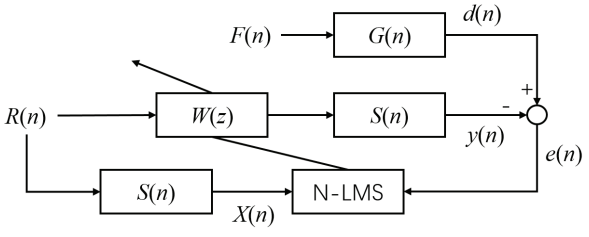

Fig. 4. *Active vibration control block diagram of the FB press*

In Fig. 4, $F(n)$ is the excitation force generated by the main drive system, $d(n)$ is the excitation force response used as the reference input, $e(n)$ is the control system error and also used as the controlled output when the control system is stable, $W(z)$ is the adaptive controller, $R(n)$ is the estimated value of the excitation force, $G(n)$ is the transfer function which reflects the excitation force transferred to the frame, $S(n)$ is the transfer function which reflects the control force transferred to the frame. The FIR filter described above is adopted as the filter.

Based on the above control block diagram, the mean square error of the whole control system can be expressed as Eq. (1).

Then the control output $y(n)$ of the n^{th} order filter is equal to the convolution operation:

$$y(n) = S(n) \times \sum_i^N w(n)R(n)$$

$$= \int_0^\infty S(n-\tau) \times (\sum_i^N w(\tau)R(\tau)), \quad (14)$$

then the gradient value of the mean square error can be calculated as:

$$g_w = \frac{dE\left[e^2(n)\right]}{dw} = -E\left[2e(n)S(n)R(n)\right]. \quad (15)$$

According to the variable step-size normalized LMS algorithm, the variable step-size factor μ needs to be transformed, that is:

$$\mu = \frac{1}{2(S(n)R(n))^{\mathrm{T}}(S(n)R(n))}, \quad (16)$$

then the iterative equation of the weight updating of the adaptive control algorithm can be obtained:

$$w(n+1) = w(n) + \frac{\mu_n}{\gamma + x^{\mathrm{T}}(n)x(n)} e(n)x(n), \quad (17)$$

where, $X(n) = S(n)\,R(n)$.

2 VIBRATION MECHANICAL MODEL DESIGN

2.1 Vibration Mechanical Model of the Fine Blanking Press

For the adaptive active vibration control system of the fine blanking machine, establishing the mechanical vibration model of the controlled object and obtaining the transfer function of the control system are required. It is assumed that the material distribution before each blanking process can be restored, and the material penetration is not considered. The punching force is located in the vertical direction, so the vertical direction, which has the maximum deformation, is mainly considered. Therefore, the structure of the FB press can be expressed as a combination of linear spring dampers.

Then the mechanical vibration model as shown in Fig. 5 can be established, and the motion equation for each mass block can be expressed as follows.

$$m_i \ddot{x}_i = \sum F_i^{imp} + \sum F_i^{el}, \quad (18)$$

where F_i^{imp} is the sum of the impact forces exerted on the mass m_i, F_i^{el} is the sum of the elastic forces applied to the mass m_i.

The excitation source of the whole press comes from the main drive system. The excitation force

acting on the main drive system is mainly composed of two parts. One part is the unbalanced inertia force F_y, generated by the main drive system itself. The other part mainly is the elastic restoring force from the main drive system at the ending of the FB process, which is relatively difficult to obtain; this can be done so with the FE simulation of the FB process. The FB FE model is shown in Fig. 5. The material for this simulation is TC4 titanium alloy with a thickness of 5 mm. The diameter of the fine-blanked part is 20 mm, and the FB speed is 5 mm/s. The relationship between the FB force and the time can be obtained, as shown in Fig. 6. When the punch force acts on the workpiece, the reaction force exerts on the main drive system in the opposite direction, which reflects the changing of the impact load acting on the main drive system.

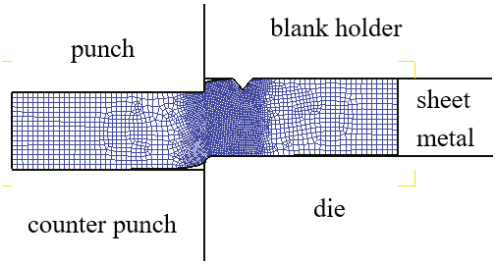

Fig. 5. *The FE model of the FB process*

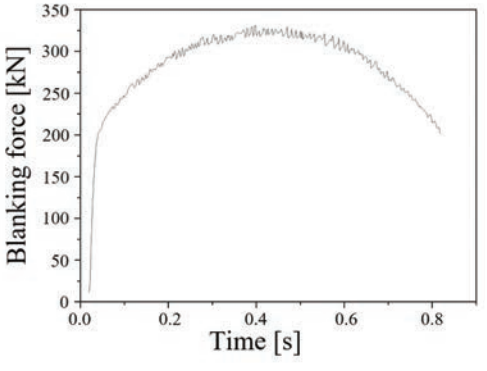

Fig. 6. *The relationship between the fine-blanking force and the time*

According to the mechanical vibration model, as shown in Fig. 7, the vibration equations of each mass block can be expressed by:

$$\begin{cases} m_7\ddot{x}_7 + c_7(\dot{x}_7 - \dot{x}_8) \\ \quad +k_7(x_7 - x_8) = F^{imp} + F_y \\ m_8\ddot{x}_8 + c_8(\dot{x}_8 - \dot{x}_9) + c_7(\dot{x}_8 - \dot{x}_7) \\ \quad + k_8(x_8 - x_9) + k_7(x_8 - x_7) = 0 \\ m_9\ddot{x}_9 + c_9\dot{x}_9 + c_8(\dot{x}_9 - \dot{x}_8) \\ \quad + k_9x_9 + k_8(x_9 - x_8) = 0 \end{cases}, \tag{19}$$

where m_7, k_7, c_7, and x_7 represent the mass, equivalent stiffness, equivalent damping and displacement of the main drive, respectively. m_8, k_8, c_8, and x_8 represent the mass, equivalent stiffness, equivalent damping and displacement of the frame, respectively. m_9, k_9, c_9, and x_9 represent the mass, equivalent stiffness, equivalent damping and displacement of the embedded footings, respectively. k_{10} and c_{10} represent the equivalent stiffness and damping of the upper worktable. $\ddot{x}_j$ and $\dot{x}_j$ $(j=6,7,8)$ represent the acceleration and velocity of the mass block.

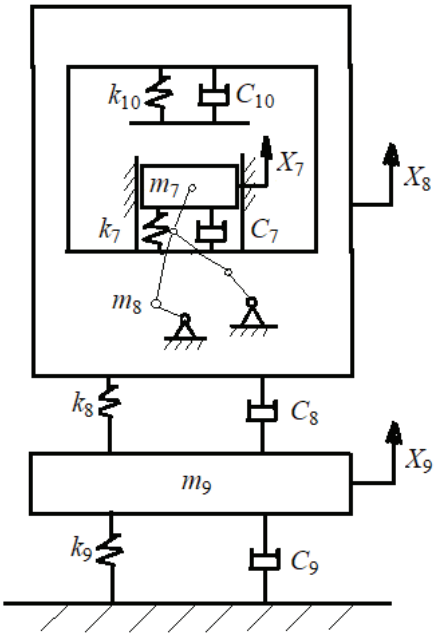

Fig. 7. *Vibration mechanical model of the FB press*

2.2 Parameters Determination of the Vibration Mechanical Equation

In order to solve the mechanical vibration equation, the parameters, such as the equivalent mass, equivalent stiffness, equivalent damping value and similar parameters, should be determined firstly based on the FB press structure.

2.2.1 Embedded Footings System

Fig. 8 shows the foundation installation system for the FB press. For the embedded foundation in the deep homogeneous layer, we can use the formulas presented in [17] and [18] to calculate the stiffness and damping value. That is:

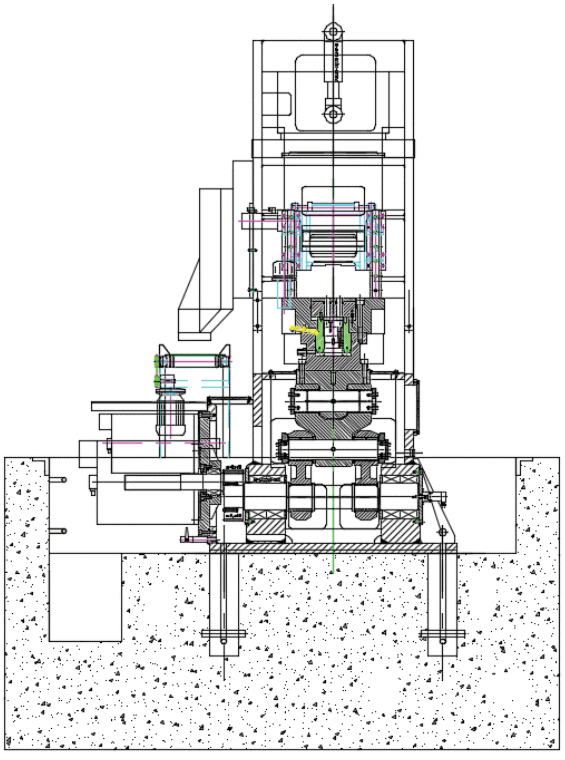

Fig. 8. *Foundation installation design of mechanical fine blanking machine*

$$\begin{cases} k = Gr_0(C_{v1} + \dfrac{G_S}{G}\dfrac{l}{r_0}S_{v1}) \\ c = r_0^2\sqrt{\rho G}(\bar{C}_{v2} + \bar{S}_{v2}\dfrac{l}{r_0}\sqrt{\dfrac{\rho_S}{\rho}\dfrac{G_S}{G}}) \end{cases}, \tag{20}$$

where G is the shear modulus of the soil, r_0 is the radius of circular foundation or the equivalent radius of non-circular foundation. ρ is the density of the soil, l is the depth of embedment, G_S and ρ_S are the shear modulus and density of the backfill side layer, respectively. Dimensionless stiffness and damping parameters C_{v1} and $\bar{C}_{v2}$ depend on the dimensionless frequency. S_{v1} and $\bar{S}_{v2}$ are the dimensionless stiffness and damping parameter of the side layer. Novak [19] provided the C_{v1}, $\bar{C}_{v2}$, S_{v1} and $\bar{S}_{v2}$ for most stamping equipment, as shown in Table 1.

Table 1. *Reference values of stiffness and damping for foundation installation system*

soil	Half-space		Side layer	
	C_{v1}	$\bar{C}_{v2}$	S_{v1}	$\bar{S}_{v2}$
Cohesive soil	7.5	6.8	2.7	6.7
Granular soil	5.2	5.0		

Based on the installation conditions of the mechanical servo FB press, the average shear wave velocity of soil is 150 m/s, and the density is 1900 kg/m³. The total mass of the foundation system is taken as 400,000 kg. The average shear wave velocity of backfill material is 120 m/s, and the mass density is 2400 kg/m³. The shear modulus of soil can be evaluated by $G=\rho V_S^2$, and it is 42.75 MPa for footing and 25.9 MPa for the side layer. Therefore, the stiffness and damping constants of the foundation installation system can be calculated by Eq. (21), which is $k = 8.1\times10^8$ N/m and $c = 1.1\times10^7$ (N/m)/s.

2.2.2 Frame Part

Because of the complexity of the frame structure, the FE method is usually used to obtain the equivalent stiffness of the frame mass. As shown in Fig. 9, the bottom surface is fixed by four points, and the upper cross-beam is applied with 200 N uniform force to get the deformation of the frame. According to the simulation results, the maximum deformation of the frame is 6.7324×10^{-8} m. Therefore, the equivalent stiffness of the frame can be calculated with:

$$k_f = \frac{F_f}{\Delta l} = \frac{200}{6.7324\times10^{-8}}\,[\mathrm{N/m}] = 2.971\times10^9\,[\mathrm{N/m}]. \tag{21}$$

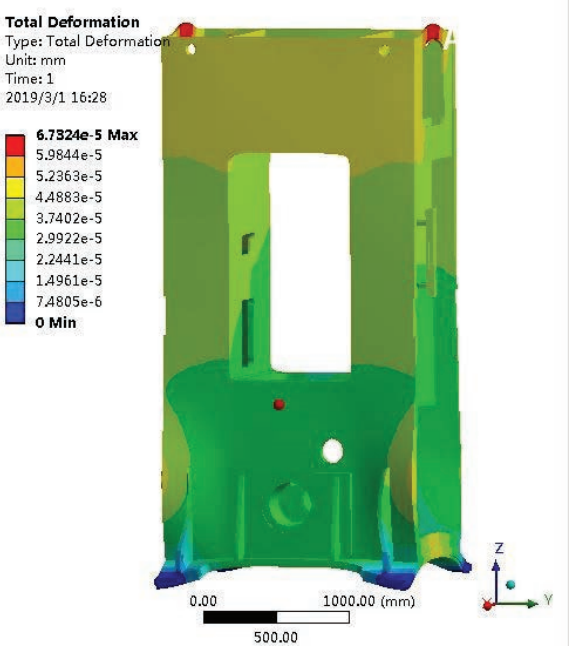

Fig. 9. *Frame deformation under the action of the constant load*

It is somewhat difficult to calculate the equivalent damping value of the frame. In general, it is required to calculate the logarithmic decrement rate δ of the system response under the impact vibration. The relationship between the logarithmic decrement rate and the structural damping ratio is shown in Eq. (22):

$$\delta = In\frac{x_i}{x_{i+T}} = \frac{2\pi\xi}{\sqrt{1-\xi^2}}, \quad (22)$$

where ξ is the damping ratio of the frame, x_i is the displacement, velocity or acceleration amplitude on the frame at the time of t_i, x_{i+T} is the displacement, velocity or acceleration amplitude on the same location at the time of t_{i+T}.

Because the value of ξ is very small, it can be ignored after the square. Then, Eq. (22) can be simplified as:

$$\delta = In\frac{x_i}{x_{i+t}} = 2n\pi\xi. \quad (23)$$

Based on Eq. (23), once the logarithmic decrement rate δ is determined, the damping ratio ξ of the frame can be obtained.

$$c = 2\xi\sqrt{mk}. \quad (24)$$

Therefore, to obtain the equivalent damping of the frame, the logarithmic decrement rate of the vibration amplitude of the system under the impact load should be calculated first. Based on the above FE model, 1 MN impact force is applied to the frame workbench and the bearing seat hole with a time of 0.02 s. According to the simulation result, the maximum acceleration and velocity changing point on the frame can be obtained, as shown in Fig. 10.

Based on the plots in Fig. 10, the following equivalent damping parameters can be obtained and summarized in Table 2.

Table 2. *Equivalent damping parameters of the frame*

	Value		Logarithmic decrement rate	Damping ratio of frame
	t_i	t_{i+T}	δ	ξ
Velocity v_7	0.272	0.103	0.971	0.154
Acceleration a_7	6.691	2.731	0.896	0.143

Based on the numbers in Table 2, it can be seen that the damping ratio of the frame is near 0.15. Therefore, it can be taken as 0.15. It is also known that the total mass of the frame is 12,314 kg. According to Eqs. (22) to (24), the equivalent damping value of the frame can be obtained as $c_7 = 1.81\times10^6$.

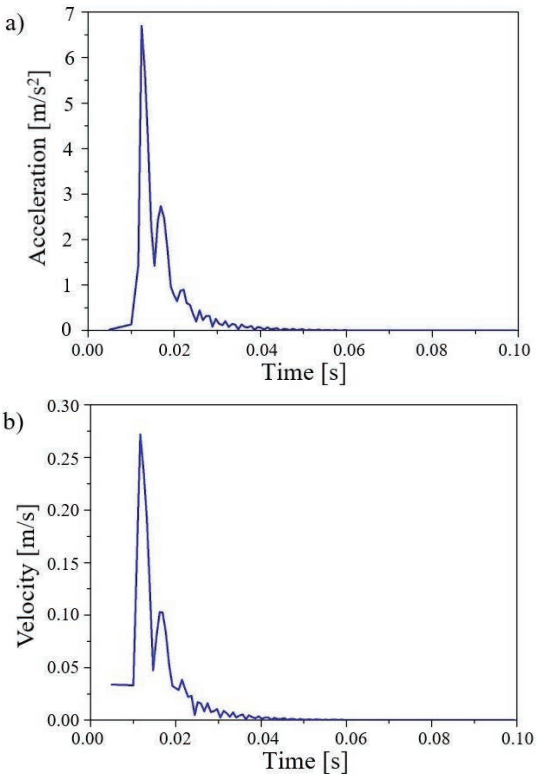

Fig. 10. *Acceleration and velocity attenuation on the frame under the impact load; a) acceleration, and b) velocity*

2.2.3 Main Drive System

For the main drive system, the equivalent stiffness and damping can be obtained with the same method applied for the frame part. The FE model for the main drive system was created as shown in Fig. 11, in which the support constraint is applied to the bearing pedestal at the bottom of the main drive system, and the horizontal displacement of the slide block is constrained. The deformation of the main drive system can be obtained by applying 200 N uniform force load on the top of the slider, as shown in Fig. 11.

Based on the plots in Fig. 10 that the maximum deformation of the main drive system under the constant load is 6.0265×10^{-7}. Then, the equivalent rigidity of the main drive system can be obtained by Eq. (25):

$$k_T = \frac{F_T}{\Delta l} = \frac{200}{6.0265\times10^{-7}} = 3.32\times10^8\,[\mathrm{N/m}]. \quad (25)$$

In order to obtain the equivalent damping of the main drive system, the 10^5 N impact is applied to the top surface of the slider for 0.02 s. The maximum acceleration and velocity changing point on the main

drive system can be obtained from the simulation results as shown in Fig. 12.

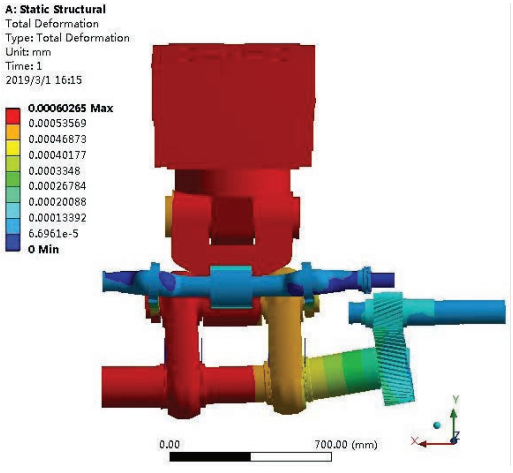

Fig. 11. *Deformation of the main drive system under the constant load*

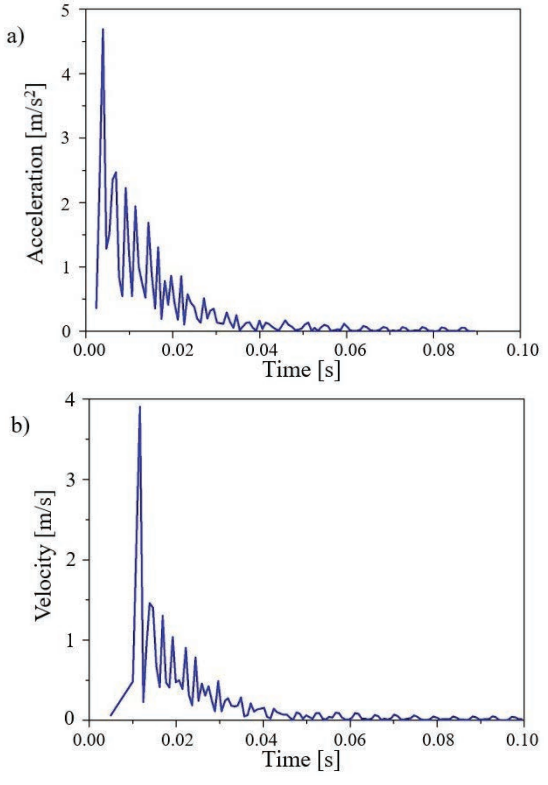

Fig. 12. *Acceleration and velocity attenuation of the main drive system under the impact load; a) acceleration, and b) velocity*

Based on the plots in Fig. 12, the following equivalent damping parameters can be obtained and summarized in Table 3.

Table 3. *Equivalent damping parameters of the main drive system*

	Value		Logarithmic decrement rate	Damping ratio of frame
	t_i	t_{i+T}	δ	ξ
Velocity v_6	1.601	1.038	0.433	0.069
Acceleration a_6	4.689	2.773	0.436	0.069

According to the parameters obtained in Table 3, the value of the damping ratio of the main drive system is approximately 0.069. It is also known that the total mass of the main drive system is 2,592 kg. According to Eqs. (23) to (25), the equivalent damping value of the main drive system can be obtained as $c_6 = 1.28 \times 10^5$.

After obtaining the parameters of each part, the mechanical vibration model of the controlled object can be finally established and used in the active vibration control simulation.

3 NUMERICAL SIMULATION AND DISCUSSION

3.1 Analog Excitation Input

Because the effect of the vertical excitation force on the forming accuracy is the most direct and the largest, the reference excitation force input of the active vibration control can be composed of the blanking force excitation during the FB process and the unbalanced inertia force excitation during the non-working process. In order to simulate the error during the active vibration control process, the random vibration interference is added to the reference excitation input, which is shown in Fig. 13.

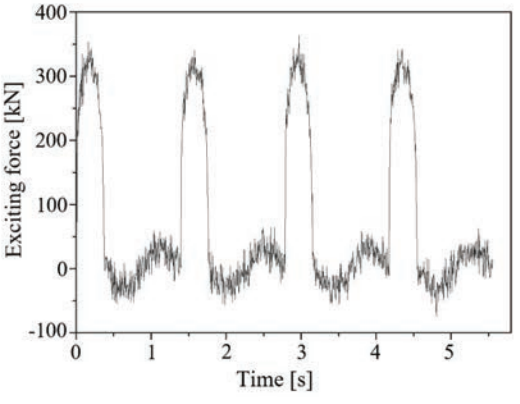

Fig. 13. *Reference excitation force input*

3.2 Reference Input Based on the Measured Vibration Response

3.2.1 Vibration Measurement Scheme of Fine-Blanking Machine

The composition of the vibration measurement system of the mechanical servo FB press can be depicted by the schematic diagram shown in Fig. 14. During the working process, the vibration at the working area is the most obvious, which has a direct impact on the forming accuracy. Therefore, the vibration in the working area needs to be measured. Meanwhile, the rigidity of the frame in the middle area is much smaller than that of the upper and lower cross-beams, and the guide rail of the slide block is arranged on the frame column in the middle area. Therefore, measuring points need to be arranged on the inner side of the stand column to reflect the vibration mode of the whole machine. Consequently, the measuring points arranged at the worktable area of the FB press are shown in Fig. 15, and 12 three-way acceleration sensors are even distributed at the working area.

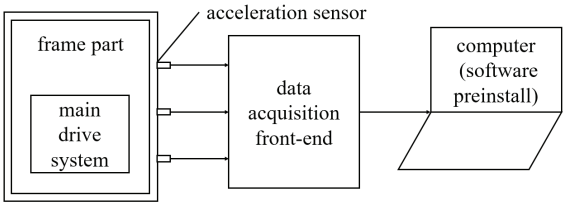

Fig. 14. *Vibration measurement schematic diagram*

3.2.2 Test Results of Measuring Points

During the test, the mechanical servo FB press works periodically with a speed of 87 times per minute under the no-load condition. In the movement process, the inertial load affects the lower cross-beam directly, and the vibration will be transmitted to the worktable, resulting in the forming error. The bottom of the lower cross-beam connected with the ground by installation system, the overall stiffness is very large. Therefore, the acceleration response of measuring points 1, 2, and 3 can reflect the overall response of the lower cross-beam, which is shown in Fig. 16.

Compared with the upper and lower cross-beams, the rigidity of the frame columns on the left and right sides in the middle is smaller, and the deformation will have a great impact on the whole press deformation. As the left and right columns are of symmetrical structure, the deformation situation is similar from the results, so the deformation situation on the right side is selected for the analysis. The response situations in time domain and frequency domain are shown in Fig. 17.

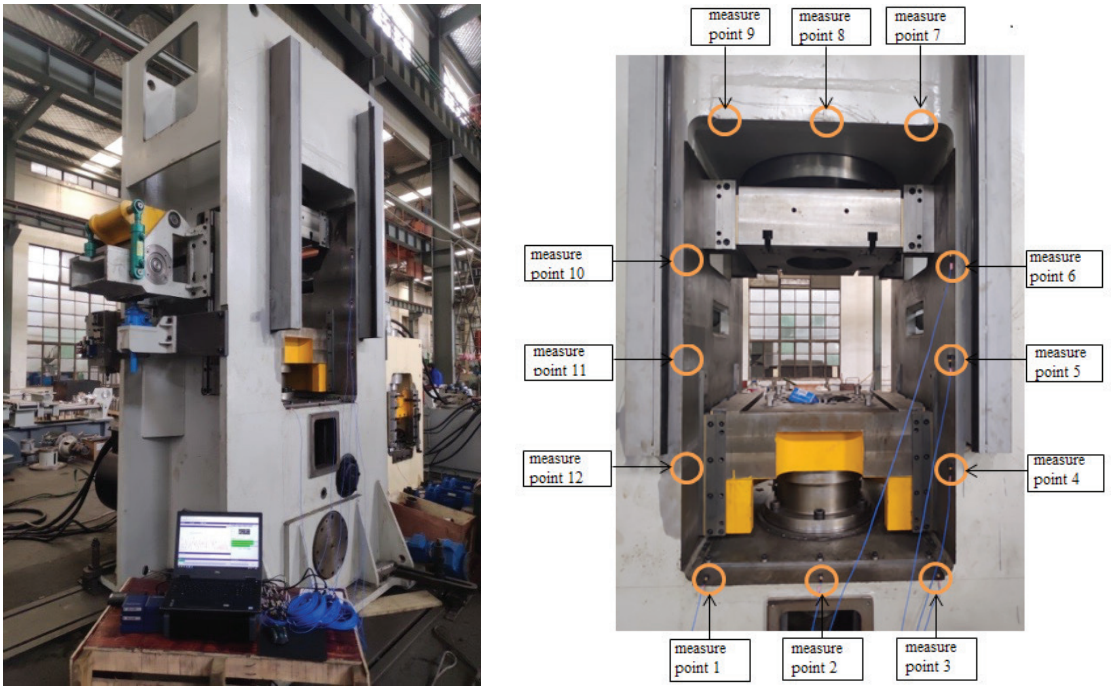

Fig. 15. *Measuring points distribution at the working area*

Based on the plots in Figs. 16 and 17, when the frequency is about 200 Hz, points of 4, 5 and 6 have a stronger frequency response than the points of 1, 2 and 3.

The overall rigidity of the upper cross-beam is very large. Because the upper cross-beam is far from the frame installation system, it is easy to produce large vibration response. The response situations in the time and frequency domain are shown in Fig. 18.

Based on the plots in Figs. 16 to 18, points of 7, 8 and 9 have a stronger frequency response when the frequency is about 150 Hz than points of 1, 2, 3, 4, 5 and 6. But have a weaker frequency response when the frequency is about 200 Hz.

3.3 Numerical Simulation Results

According to the self-adaptive vibration feed-forward control method, as described in Section 2, the control system simulation process is programmed in the MATLAB software platform, and the value of μ_k is 0.005, γ is 10^{-5}. Combined with the mechanical model of the controlled object, the time-domain vibration response of each observation point with and without control can be obtained, as shown in Fig. 19a. The simulation results show that the control effect of all measuring points is very good, so we use measuring point 2 to show. The frequency domain vibration response of observation point 2 with and without control can be obtained, as shown in Fig. 19b.

In Fig. 19, the blue line represents the vibration response output without control, and the red line represents the vibration response output adding active control. It can be seen from Fig. 19 that the vibration response of the press with the active vibration control is effectively reduced. The time-domain vibration response quickly achieves stability when the active control applied and the convergence speed is very fast, which means that it has a stable control effect at that time. It can be seen that the vibration of the frame

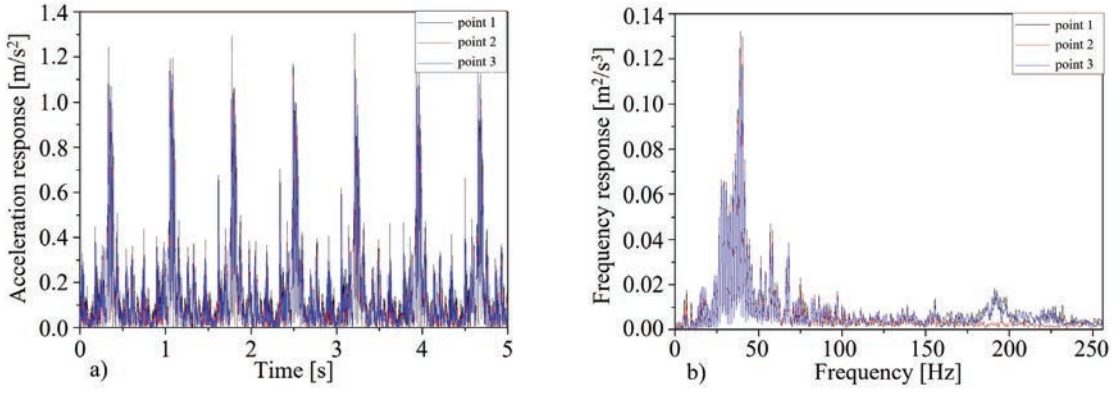

Fig. 16. *Response of Z-direction time domain and frequency domain of measuring points at the lower cross-beam area (measuring points of 1, 2 and 3); a) time domain response diagram, and b) frequency domain response diagram*

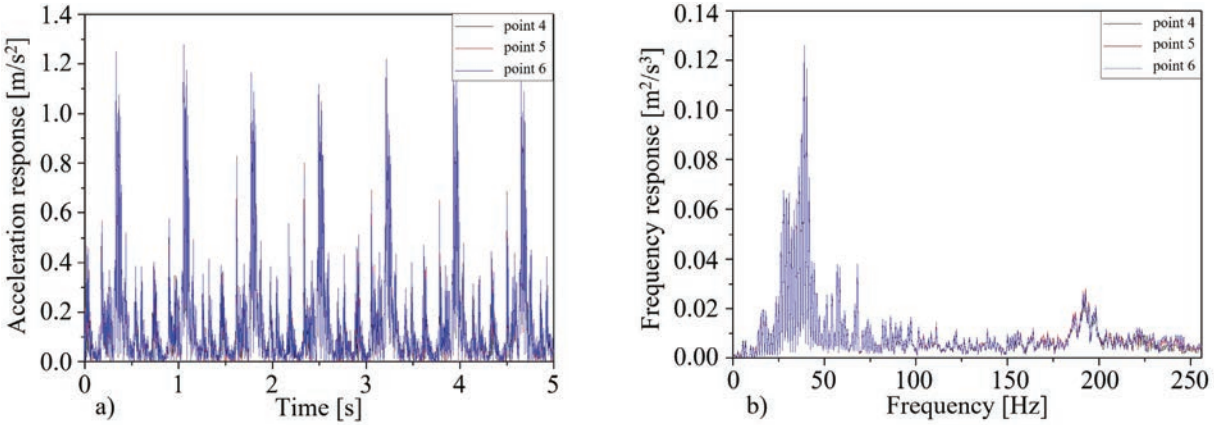

Fig. 17. *Response of Z-direction time domain and frequency domain of measuring point at frame column area (measuring points of 4, 5 and 6); a) time domain response diagram, and b) frequency domain response diagram*

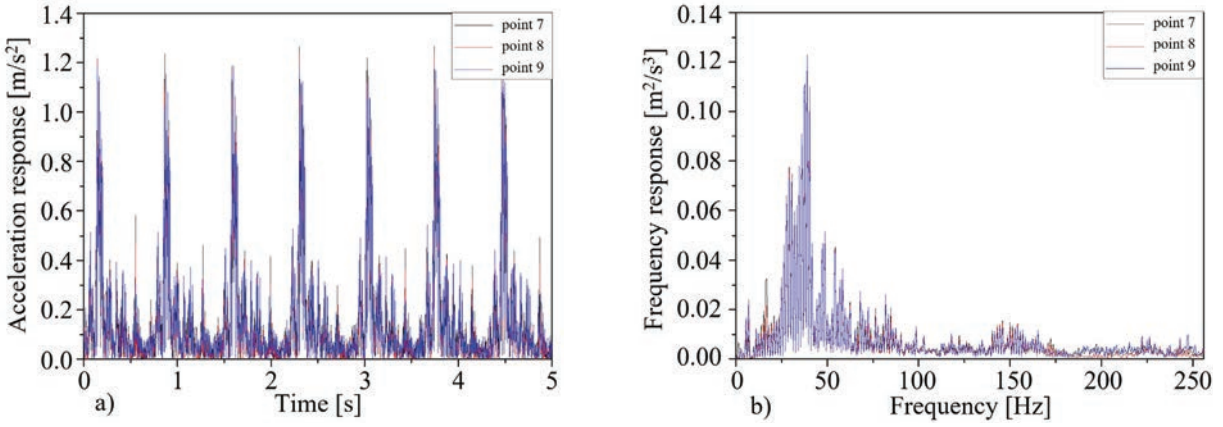

Fig. 18. *Response of Z-direction time domain and frequency domain of measurement point at upper cross-beam area (measuring points of 7, 8 and 9); a) time domain response diagram, and b) frequency domain response diagram*

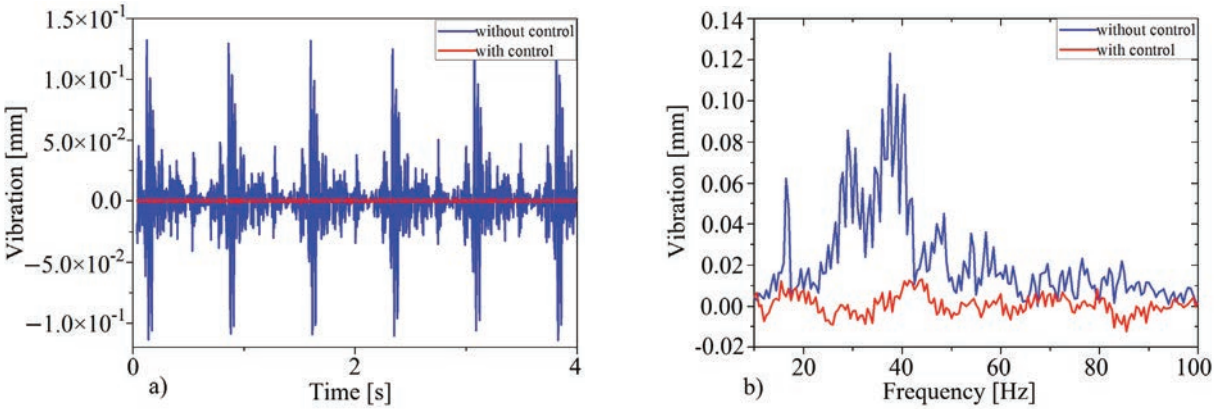

Fig. 19. *a) Time domain, and b) frequency domain vibration response with and without control*

has been significantly suppressed, and the maximum value of the vibration response has been reduced by more than 95 %; the amplitude variation of the vibration response is maintained within the range of m.

For the frequency domain control effect, it can be seen that after controlling the corresponding response of the first three modes, the vibration response amplitude reaches stability very fast, and the maximum value of the vibration response is reduced by more than 80 %. At the same time, the convergence speed of the system is very fast after the application of active vibration control.

From the simulation results, it can be seen that the active vibration control applied to the FB press does not suppress the vibration completely. However, the effect of vibration control is very significant, which shows a promising future for the application of the active vibration control method on the FB press.

4 CONCLUSION

In this paper, the mechanical vibration model of the fine-blanking press as the controlled object is established, the dynamic model parameters of a mechanical fine-blanking machine are obtained by using finite element analysis and empirical formula. The principle of vibration control of fine blanking press is described, the control algorithm is established, and the adaptive vibration control block diagram of fine blanking press is established.

The self-adaptive feed-forward control is used to simulate the vibration control of the mechanical FB press. The simulation results show that the vibration control effect is good, and the conclusion can be obtained as follows.

The vibration response of the whole machine has been effectively reduced when the active control is applied, in which the time-domain vibration response has been reduced by more than 95 %, and the frequency-domain vibration response has been

reduced by more than 80 %, which means that the vibration reduction effect is obvious. Effectively reducing the vibration effect of fine-blanking machine greatly increases the processing accuracy, saves significant amounts of energy, and reduces the energy consumption and defect rate.

5 ACKNOWLEDGEMENTS

The authors would like to thank the Fundamental Research Funds for the Central Universities (WUT: 2019III117CG), 111 Project (B17034) and Innovative Research Team Development Program of Ministry of Education of China (No. IRT_17R83) for the supports given to this research and the Huangshi Huali Metal Forming Machine Tool Co., Ltd. for their supports given to experiments.

6 REFERENCES

[1] Liu, Y., Tang, B., Hua, L., Mao, H. (2018). Investigation of a novel modified die design for fine-blanking process to reduce the die-roll size. *Journal of Materials Processing Technology*, vol. 260, p. 30-37, **DOI:10.1016/j.jmatprotec.2018.04.029**.

[2] Mao, H., Li, S., Liu, Y., Hua, L. (2017). An investigation on the microstructure of the fine-blanked sprocket. *The International Journal of Advanced Manufacturing Technology*, vol. 90, p. 3171-3185, **DOI:10.1007/s00170-016-9589-x**.

[3] Xu, Z., Liu, Y., Hua, L., Zhao, X., Guo, W. (2019). Energy analysis and optimization of main hydraulic system in 10,000 kN fine blanking press with simulation and experimental methods. *Energy Conversion and Management*, vol. 181, p. 143-158, **DOI:10.1016/j.enconman.2018.12.012**.

[4] Zhao, X., Liu, Y., Hua, L., Mao, H. (2016). Finite element analysis and topology optimization of a 12000kN fine blanking press frame. *Structural and Multidisciplinary Optimization*, vol. 54, p. 375-389, **DOI:10.1007/s00158-016-1407-4**.

[5] Guicking, D. (1990). On the invention of active noise control by Paul Lueg. *The Journal of the Acoustical Society of America*, vol. 87, p. 2251-2254, **DOI:10.1121/1.399195**.

[6] Olson, H.G., May, E.G. (1953). Electronic sound absorber. *The Journal of the Acoustical Society of America*, vol. 25, p. 1130, **DOI:10.1121/1.1907249**.

[7] Winberg, M., Johansson, S., L Lagö, T.L. (2001). Active control of engine induced noise in a naval application. *Pediatric Pulmonology*, vol. 22, no. 4, p. 280-282, **DOI:10.1002/1099-0496(199610)22:43.0.CO;2-K**.

[8] Daley, S., Johnson, F.A., Pearson, J.B., Dixon, R. (2004). Active vibration control for marine applications. *Control Engineering Practice*, vol. 12, no. 4, p. 465-474, **DOI:10.1016/S0967-0661(03)00135-7**.

[9] Shao, C., Zhang, X., Shen, Y. (2000). Active vibration controller designing for high-speed flexible linkage mechanisms. *Journal of Mechanical Engineering*, vol. 36, no. 12, p. 54-58, **DOI:10.3901/JME.2000.12.054**.

[10] Li, P. (2012). Theoretical analysis and experiment on active vibration control of a shaft-hull system. *Journal of Mechanical Engineering*, vol. 48, no. 19, p. 103-108, **DOI:10.3901/JME.2012.19.103**.

[11] Zhu, M.G., Jin, G.Y., Feng, N. (2011). Numerical study of active control of interior noise in a structural-acoustic enclosure. *Key Engineering Materials*, vol. 486, p. 103-106, **DOI:10.4028/www.scientific.net/KEM.486.103**.

[12] Belyi, V., Gan, W.-S. (2019). A combined bilateral and binaural active noise control algorithm for closed-back headphones. *Applied Acoustics*, vol. 160, art. ID 107129, **DOI:10.1016/j.apacoust.2019.107129**.

[13] Soni, T., Das, A.S., Dutt, J.K. (2020). Active vibration control of ship mounted flexible rotor-shaft-bearing system during seakeeping. *Journal of Sound and Vibration*, vol. 467, art. ID 115046, **DOI:10.1016/j.jsv.2019.115046**.

[14] Teo, Y.R., Fleming, A.J. (2015). Optimal integral force feedback for active vibration control. *Journal of Sound and Vibration*, vol. 356, p. 20-33, **DOI:10.1016/j.jsv.2015.06.046**.

[15] Park, Y.-M., Kim, K.-J. (2013). Semi-active vibration control of space truss structures by friction damper for maximization of modal damping ratio. *Journal of Sound and Vibration*, vol. 332, no. 20, p. 4817-4828, **DOI:10.1016/j.jsv.2013.04.032**.

[16] Sun, W., Zhang, F., Luo, S., Wang, H. (2017). Simulation analysis of adaptive active vibration control. *Noise and Vibration Control*, vol. 37, p. 23-28. (in Chinese)

[17] Beredugo, Y.O., Novak, M. (2011). Coupled horizontal and rocking vibration of embedded footings. *Canadian Geotechnical Journal*, vol. 9, no. 4, p. 477-497, **DOI:10.1139/t72-046**.

[18] Novak, M. (2010). Effect of soil on structural response to wind and earthquake. *Earthquake Engineering & Structural Dynamics*, vol. 3, no. 1 p. 79-96, **DOI:10.1002/eqe.4290030107**.

[19] Novak, M. (2011). Foundations for shock-producing machines. *Canadian Geotechnical Journal*, vol. 20, no. 1, p. 141-158, **DOI:10.1139/t83-013**.

Strojniški vestnik - Journal of Mechanical Engineering 67(2021)9, 458-472
© 2021 Journal of Mechanical Engineering. All rights reserved.
DOI:10.5545/sv-jme.2021.7236 Original Scientific Paper
Received for review: 2021-04-26
Received revised form: 2021-08-04
Accepted for publication: 2021-09-01

Nonlinear Control of a Pneumatic Actuator Based on a Dynamic Friction Model

Xuan Bo Tran
Hanoi University of Science and Technology, School of Transportation Engineering, Vietnam

This paper presents a new controller for the position of a pneumatic actuator. The controller is designed based on the multiple-surface sliding control method in combination with a frictional compensator. The multiple-surface sliding control method is applied to deal with the nonlinear characteristics of the pneumatic system, and the frictional compensator is applied to compensate for the friction force in the pneumatic actuator. The friction force is estimated based on a dynamic friction model (the LuGre model). Both simulation and experimental studies are done to evaluate the new controller. The evaluation results indicate significant improvement in the tracking position error of the new controller comparing to the multiple-surface sliding controller without friction compensation and other nonlinear controllers.
Keywords: pneumatic actuator, nonlinear control, friction compensation, dynamic friction model

Highlights
- *The new controller with friction compensation is proposed to control the position of a pneumatic cylinder.*
- *A minimal position peak error of 1 mm in steady-state condition can be obtained by the new controller with the step desired positions.*
- *A minimal position peak error of 2.2 mm in steady-state condition can be obtained by the new controller with the sinusoidal desired positions.*
- *By using the new controller, the relative position peak error is reduced by 10 %, and the relative root means squared (RMS) error is reduced by 6.5 % in comparison to those of the multiple-surface sliding (MSS) controller without friction compensation.*

0 INTRODUCTION

Pneumatic systems are widely used in industrial environments because they can provide many advantages, including low cost, high power-to-weight ratio, cleanness, ease of maintenance and replacement, cheap and available supply of air sources [1]. The pneumatic systems are also preferred in hot and/or humid environments where electric systems cannot be applied [2]. However, the compressibility of air, the nonlinearity of valves and friction in the pneumatic actuator are disadvantages of pneumatic systems. They cause the system to have high nonlinearities and modelling uncertainties [3] to [5]. Therefore, the application of linear control strategies is not suitable for achieving fast and highly accurate responses for the pneumatic actuators' position [6] to [8]. Many nonlinear and advanced control strategies have been employed to overcome the nonlinearities and uncertainties of the pneumatic systems. Bobrow and Jabbari [9] applied an adaptive control method based on the linear dynamics of the system to control the position of a pneumatic actuator. An adaptive fuzzy-proportional-derivative (PD) controller was applied by Gao and Feng [10] for a one-degree pneumatic actuator. The full-state feedback was used in the control law for simultaneous parameter identification and tracking control. A combination of an adaptive control strategy and neural network was proposed by Chen et al. [11] for an electro-pneumatic servo system; the neural network was used to compensate for constructing a linearized model of the nonlinear system, and the robust adaptive controller was used to perform the model-matching for the uncertain linearized model of the system. Gross and Rattan [12] applied multilayer neural networks to compensate for the nonlinear nature of the dynamic system in conjunction with a proportional-integral-derivative (PID) feedback controller. The advantages of the above-advanced control strategies are that they allow updating system parameters and controller parameters. However, the quality of control performances greatly depends on the accuracy of the mathematical model of the system.

For the sliding mode control method, the first positioning application for pneumatic actuators was made by Paul et al. [13], Tang and Walker [14], and Surgenor and Vaughan [15]. This robust control method allows handling nonlinearities and compensates for the mismatched uncertainties of the mathematical model. However, one of the main drawbacks of this kind of control strategy for pneumatic systems is the need for acceleration feedback. To overcome this difficulty, Acarman et al. [16] and Liu et al. [17] used observers to estimate the acceleration and Pandian et al. [18] proposed the use of differential pressure feedback

*Corr. Author's Address: Hanoi University of Science and Technology, No. 1, Dai Co Viet str., Hai Ba Trung dist., Hanoi city, Vietnam, bo.tranxuan@hust.edu.vn

instead of acceleration feedback. Recently, Tsai and Huang [19] proposed a multiple-surface sliding controller (multiple-surface sliding (MSS) controller) for a pneumatic servo system. This controller was designed based on three sliding surfaces of position, velocity, and force, and this controller can exhibit the smallest control error among the controllers proposed thus far for the pneumatic actuators. However, the friction force was omitted in designing the MSS controller.

Armstrong-Helouvry [20] has shown that the control performances of a mechanical system can be significantly improved when the system controller is designed with friction compensation. Koch and Reichhartinger [21] and Ayalew and Jablokow [22] have applied the sliding model control method combined with model-based friction compensation in the controlling position of hydraulic actuators; they have achieved improved control performances. However, only simple nonlinear friction models such as static or Coulomb friction models were used in these studies. Tran and Yanada [23] have shown that the static friction models are not enough or useless in predicting dynamic friction behaviours in pneumatic cylinders, especially in the cases where the cylinders operate at low and oscillating velocity conditions. Therefore, dynamic friction models must be used to achieve highly accurate control performances for the pneumatic cylinder position. To date, many dynamic friction models have been proposed [24] to [29]. Among these, the dynamic LuGre friction model [25] is most used. This dynamic friction model can observe basic friction characteristics in most mechanical systems such as pre-sliding displacement, stick-slip motion, varying break-away force, and hysteresis. In addition, this model is quite suitable for theoretical calculations and is easy to implement. Tran and Yanada [23] have also experimentally examined the friction characteristics in pneumatic cylinders and have shown that the LuGre friction model can relatively adequately simulate all the measured friction characteristics. However, according to the author's survey, the application of the LuGre friction model combined with the MSS control method for controlling the position of the pneumatic actuators has not been studied.

In this paper, the multiple-surface control method combining with friction compensation based on the LuGre friction model for controlling the position of a pneumatic cylinder is studied. An electro-pneumatic servo system with a double-acting pneumatic cylinder and two pneumatic proportional flow control valves is considered to carry out this work. A general mathematical model of the system is built first. The control law of the new controller is then designed, and the absolute stability of the system is analysed. The new controller is evaluated using both simulations and experiments. The control performances of the new controller are compared with those of the MSS controller and other nonlinear controllers. Finally, the effectiveness of the new controller is shown.

The rest of this paper is organized as follows. In Section 1, the electro-pneumatic servo system is introduced, and its mathematical model is developed. Section 2 shows the synthesis of the system controller. A stable analysis of the closed-loop system is also shown in this section. The simulation evaluations are shown in Section 3, and the experimental evaluations are shown in Section 4. Finally, the main conclusion is drawn in Section 5.

1 SYSTEM MODEL

In this paper, we consider an electro-pneumatic servo system, as shown in Fig. 1. In this system, a double-acting pneumatic cylinder is used to drive a load mass M.

The motion of the cylinder piston is controlled by two 3/2 electro-pneumatic proportional flow control valves, Valves 1 and 2. Valve 1 is connected to the left chamber, and Valve 2 is connected to the right chamber of the cylinder. The valves' operation is controlled by the voltage signals u_1 and u_2. According to the characteristics of the valves used in the experimental

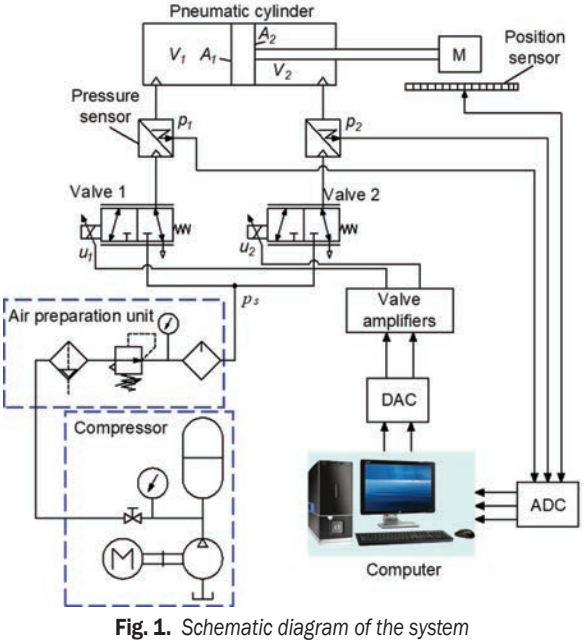

Fig. 1. *Schematic diagram of the system*

system, as shown later in Section 4.1, the voltage values of u_1 and u_2 vary from 0 to 5 VDC. If $2.5 \le u_i \le 5$ VDC (i = 1 and 2), the valves operate at the left side position, letting air from the compressor flow into the cylinder chambers; and if $0 \le u_i < 2.5$ VDC, the valves operate at the right-side position, releasing air from the cylinder chambers to the atmosphere. Therefore, the cylinder piston will extend if $2.5 \le u_1 \le 5$ VDC and $0 \le u_2 < 2.5$ VDC. Conversely, the cylinder piston will extract if $0 \le u_1 < 2.5$ VDC and $2.5 \le u_2 \le 5$ VDC. The flow rates through the valves depend on the voltage values of u_1 and u_2.

To develop a mathematical model of the system, the following assumptions are used:

a) The used air is an ideal gas, and its kinetic energy is negligible in the cylinder chambers.
b) The leakages of the cylinder are negligible.
c) The temperature variation in cylinder chambers is negligible with respect to the supply temperature.
d) The pressure and the temperature in the cylinder chambers are homogeneous.
e) The evolution of the gas in each chamber is a polytropic process.
f) The supply and ambient pressures are constant.

The mass flow rate $\dot{m}_i$ (i = 1 and 2) that flows into or flows out from the chambers of the pneumatic cylinder can be derived in terms of the voltage inputs u_i of the two valves as follow:

$$\dot{m}_i = \begin{cases} \beta_{ib} p_s \sqrt{\dfrac{k}{RT}} H_{V1}\left(u_i - 2.5\right), & 2.5 \le u_i \le 5 \\ \beta_{ie} p_i \sqrt{\dfrac{k}{RT}} H_{V2}\left(u_i - 2.5\right), & 0 \le u_i < 2.5 \end{cases}, \quad (1)$$

where p_s and p_i are respectively the supply air pressure and the pressure in the cylinder's chambers, k is the specific heat ratio, R is the gas constant, and T is the temperature of the supply source. H_{V1} and H_{V2} are respectively the valve coefficients. β_{ib} and β_{ie} are the pressure coefficients and are given by:

$$\beta_{ib} = \begin{cases} \sqrt{\dfrac{2}{k-1}\left(\dfrac{p_i}{p_s}\right)^{\frac{k+1}{2k}} \sqrt{\left(\dfrac{p_i}{p_s}\right)^{\frac{1-k}{k}} - 1}}, & \dfrac{p_i}{p_s} \ge \left(\dfrac{2}{k+1}\right)^{k/k-1} \\ 0.58, & \dfrac{p_i}{p_s} < \left(\dfrac{2}{k+1}\right)^{k/k-1} \end{cases}, \quad (2)$$

$$\beta_{ie} = \begin{cases} \sqrt{\dfrac{2}{k-1}\left(\dfrac{p_{atm}}{p_i}\right)^{\frac{k+1}{2k}} \sqrt{\left(\dfrac{p_{atm}}{p_i}\right)^{\frac{1-k}{k}} - 1}}, & \dfrac{p_{atm}}{p_i} \ge \left(\dfrac{2}{k+1}\right)^{k/k-1} \\ 0.58, & \dfrac{p_{atm}}{p_i} < \left(\dfrac{2}{k+1}\right)^{k/k-1} \end{cases}, \quad (3)$$

where p_{atm} is the atmosphere pressure.

The dynamic relationship between the mass flow rates $\dot{m}_1$, $\dot{m}_2$ and the pressures p_1, p_2 in the cylinder chambers can be given by continuous equation as follows:

$$\dot{p}_1 = \frac{k}{V_1}\left(RT\dot{m}_1 - p_1 A_1 v\right),$$
$$\dot{p}_2 = \frac{k}{V_2}\left(RT\dot{m}_2 + p_2 A_2 v\right), \quad (4)$$

where v is the piston velocity, A_1 and A_2 are the piston areas. V_1 and V_2 are respectively to the volumes in the left and right chambers of the cylinder and are given as follows:

$$V_1 = V_{10} + A_1 x,$$
$$V_2 = V_{20} + A_2 (L - x), \quad (5)$$

where L is the piston stroke, x is the piston position, V_{10} and V_{20} are, respectively, the dead volumes in the left and right chambers of the cylinder. The motion equation of the cylinder piston according to Newton's second law is given by:

$$Ma = p_1 A_1 - p_2 A_2 - F_{fr}, \quad (6)$$

where M is the load mass of the piston, a is the piston acceleration and F_{fr} is the friction force. In **[23]**, Tran and Yanada have measured the friction characteristics of the pneumatic cylinders and have shown that most of the measured characteristics can be simulated by the dynamic LuGre friction model with relatively good accuracy. Therefore, in this study, the LuGre model is used to describe the friction force F_{fr} in the pneumatic cylinder. The LuGre friction model is described as follows:

$$\dot{w} = v - \frac{\sigma_0 w}{q(v)}|v|, \quad (7)$$

$$q(v) = F_{cl} + \left(F_{st} - F_{cl}\right)\exp^{-(v/v_s)^n}, \quad (8)$$

$$F_{fr} = \sigma_0 w + \sigma_1 \dot{w} + \sigma_2 v, \quad (9)$$

where w is the mean deflection of the elastic bristle between two surfaces made in contact, σ_0 is the stiffness of the elastic bristle, $q(v)$ is the Stribeck function, F_{st} is the static friction force, F_{cl} is the Coulomb friction force, v_s is the Stribeck velocity, n is the exponent that affects the slope of the Stribeck curve, σ_1 is the micro-viscous friction coefficient, and σ_2 is the viscous friction coefficient.

Setting the valve signals u_1 and u_2 according to the control law u of the system as follows:

$$u_1 = 2.5 + u,$$
$$u_2 = 2.5 - u, \tag{10}$$

then substituting Eq. (10) into Eq. (1) and along with Eq. (4), we obtain:

$$\dot{p}_1 = -\frac{kA_1 p_1 v}{V_1} + \frac{k\sqrt{kRT}}{V_1}\begin{bmatrix}(1+sign(u))\beta_{1b} p_s H_{V1} \\ +(1-sign(u))\beta_{1e} p_1 H_{V2}\end{bmatrix} u,$$
$$\dot{p}_2 = \frac{kA_2 p_2 v}{V_2} + \frac{k\sqrt{kRT}}{V_2}\begin{bmatrix}(1-sign(u))\beta_{2b} p_s H_{V1} \\ -(1+sign(u))\beta_{2e} p_2 H_{V2}\end{bmatrix} u, \tag{11}$$

By setting $x_1 = x$; $x_2 = \dot{x}_1$ and $x_3 = p_1 A_1 - p_2 A_2$, Eq. (6) then becomes:

$$\dot{x}_1 = x_2,$$
$$\dot{x}_2 = \frac{1}{M} x_3 - \frac{F_{fr}}{M}, \tag{12}$$

Taking time derivative of x_3 along with Eq. (11) can be achieved as follows:

$$\dot{x}_3 = P(\mathbf{x}, t) + B(\mathbf{x}, t)u, \tag{13}$$

where $\mathbf{x} = [x_1 \quad x_2 \quad x_3]$ is state-vector and

$$P(\mathbf{x}, t) = -\frac{k\mathrm{A}_1^2 p_1 x_2}{V_1} - \frac{k\mathrm{A}_2^2 p_2 x_2}{V_2}, \tag{14}$$

$$B(\mathbf{x}, t) = k\sqrt{kRT}\begin{bmatrix}\dfrac{1+\mathrm{sgn}(u)}{2}\left(\dfrac{\beta_{1b} p_s H_{V1}\mathrm{A}_1}{V_1} + \dfrac{\beta_{2e} p_2 H_{V2}\mathrm{A}_2}{V_2}\right) \\ +\dfrac{1-\mathrm{sgn}(u)}{2}\left(\dfrac{\beta_{1e} p_1 H_{V2}\mathrm{A}_1}{V_1} + \dfrac{\beta_{2b} p_s H_{V1}\mathrm{A}_2}{V_2}\right)\end{bmatrix}. \tag{15}$$

It can be realized from Eqs. (1) to (15) that the dynamics of the electro-pneumatic servo system are highly nonlinear due to the effects of compressibility of air in the cylinder chambers, the nonlinearity of the valves, and friction in the pneumatic cylinder.

2 CONTROL STRATEGY

2.1 Control Design

In this section, we design a controller so that the piston position x_1 can track the desired trajectory x_{1d} with high accuracy under the effect of the system nonlinearities (the compressibility of air in the cylinder chambers and the nonlinearity of the valves) and under the existence of friction. In [19], Tsai and Huang have applied the MSS controller to deal with the system nonlinearities and have obtained the smallest position error of 5 mm to sinusoidal desired position trajectories among the controllers proposed thus far for the pneumatic cylinders. However, the friction force was considered as a bounded uncertain force in the controller design. It is shown by Armstrong-Helouvry [20] that a controller combining with a friction compensator has the potential to improve the control performances of a control system. Therefore, in this study, we propose a new position controller of the cylinder piston by combining the MSS control method with a friction observer. The friction observer is designed based on the dynamic LuGre friction model. The block diagram of the closed-loop system using the new controller is shown in Fig. 2.

To design the new controller, the following assumptions of the system parameters are considered: i) the mass load is bounded by $M_{\min} \le M \le \mathrm{M}_{\max}$; ii) the piston velocity is bounded by $|x_2| \le \alpha_1$; iii) the friction force is bounded by $|F_{fr}| \le F_{st}$; iv) the pressures

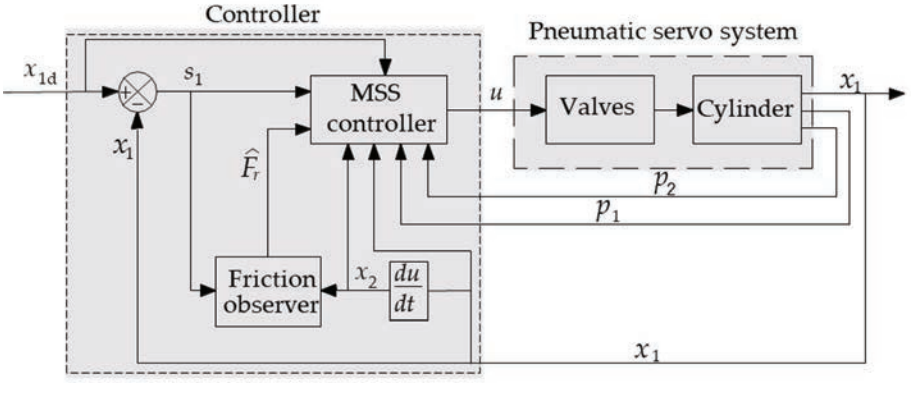

Fig. 2. *Block diagram of the closed-loop system using new controller*

in the cylinder chambers are bounded by $p_{atm} \le p_i \le p_s$, i = 1 and 2. Basing on these assumptions, the bounds for F_{fr}/M and $P(\mathbf{x},t)$ can be identified as follows:

$$\left|\frac{F_{fr}}{M}\right| \le \frac{F_{st}}{M_{\min}} = \alpha_2, \tag{16}$$

$$\left|P(\mathbf{x},t)\right| \le \frac{kp_s A_1^2 \alpha_1}{V_{10}} + \frac{kp_s A_2^2 \alpha_1}{V_{20}} = \alpha_3. \tag{17}$$

The bound for $B(\mathbf{x},t)$ can be found as:

$$0 < B_{\min} \le B(\mathbf{x},t) \le B_{\max}, \tag{18}$$

where $B_{\min}$ and $B_{\max}$ are determined from Eqs. (2), (3) and (15) as:

$$B_{\max} = 0.58 p_s k\sqrt{kRT}\left(\frac{H_{V1}A_1}{V_{10}} + \frac{H_{V2}A_2}{V_{20}}\right),$$

$$B_{\min} = 0.58 p_{atm}\left(\frac{2}{k+1}\right)^{\frac{k}{k-1}} k\sqrt{kRT}\left(\begin{array}{l}\dfrac{H_{V1}A_1}{V_{10}+A_1L} \\ +\dfrac{H_{V2}A_2}{V_{20}+A_2L}\end{array}\right), \tag{19}$$

Let choosing an estimation $\widehat{B}$ of the gain $B(\mathbf{x},t)$ as the mean of the above bounds:

$$\widehat{B} = (B_{\min} B_{\max})^{1/2}, \tag{20}$$

then bounds in Eq. (18) can be written in the form:

$$\lambda^{-1} \le \frac{B(\mathbf{x},t)}{\widehat{B}} \le \lambda, \tag{21}$$

where $\lambda = \left(B_{\max}/B_{\min}\right)^{1/2}$.

Defining three sliding surfaces of position, velocity, and applied force as follows:

$$\begin{aligned} s_1 &= x_1 - x_{1\mathrm{d}}, \\ s_2 &= x_2 - x_{2\mathrm{d}}, \\ s_3 &= x_3 - x_{3\mathrm{d}}, \end{aligned} \tag{22}$$

with the desired velocity and applied force are selected as follows:

$$x_{2\mathrm{d}} = \dot{x}_{1\mathrm{d}} - \tau_1 \frac{s_1}{\theta_1}, \tag{23}$$

$$x_{3d} = M\dot{x}_{2d} + \widehat{F}_{fr} - \tau_2 \frac{s_2}{\theta_2}, \tag{24}$$

where τ_i (i = 1 and 2) are positive constants and θ_i are the boundary layer thicknesses of the surfaces s_i. $\widehat{F}_{fr}$ is the friction force that is estimated by the observer basing on the LuGre model as follows:

$$\widehat{F}_{fr} = \sigma_0 \hat{w} + \sigma_1 \dot{\hat{w}} + \sigma_2 \dot{x}_1, \tag{25}$$

$$\dot{\hat{w}} = \dot{x}_1 - \frac{\sigma_0 \hat{w}}{q(\dot{x}_1)}\left|\dot{x}_1\right| - \tau_z s_1, \tag{26}$$

where τ_z is a positive constant. By introducing $\tilde{w} = w - \hat{w}$ as the estimating error of the mean deflection of the contacting bristle and by combining with Eqs. (7) and (26), the time derivative of the error $\tilde{w}$ can be obtained as:

$$\dot{\tilde{w}} = -\frac{\left|\dot{x}_1\right|\sigma_0 \tilde{w}}{q(\dot{x}_1)} + \tau_z s_1. \tag{27}$$

Taking time derivatives of x_{2d} and x_{3d} along with Eq. (12) obtains:

$$\dot{x}_{2d} = \ddot{x}_{1d} - \frac{\tau_1}{\theta_1}\left(x_2 - \dot{x}_{1d}\right), \tag{28}$$

$$\begin{aligned} \dot{x}_{3d} = M\dddot{x}_{1d} + M\frac{\tau_1}{\theta_1}\ddot{x}_{1d} + \frac{\tau_2}{\theta_2}\dot{x}_{2d} \\ -\left(M\frac{\tau_1}{\theta_1} + \frac{\tau_2}{\theta_2}\right)\left(\frac{1}{M}x_3 - \frac{F_{fr}}{M}\right) + \dot{\hat{F}}_{fr}. \end{aligned} \tag{29}$$

Defining

$\dot{x}_{3d1} = M\dddot{x}_{1d} + M\frac{\tau_1}{\theta_1}\ddot{x}_{1d} + \frac{\tau_2}{\theta_2}\dot{x}_{2d} - \left(M\frac{\tau_1}{\theta_1} + \frac{\tau_2}{\theta_2}\right)\frac{x_3}{M}$, as known part and $\dot{x}_{3d2} = \left(M\frac{\tau_1}{\theta_1} + \frac{\tau_2}{\theta_2}\right)\frac{F_{fr}}{M} + \dot{\hat{F}}_{fr}$, as unknown part of $\dot{x}_{3d}$, then we have:

$$\dot{x}_{3d} = \dot{x}_{3d1} + \dot{x}_{3d2}. \tag{30}$$

In the ideal case where there is no friction force, the bounds of $\dot{x}_{2d}$, $\dot{x}_{3d1}$ and $\dot{x}_{3d2}$ can be identified as

$$\left|\dot{x}_{2d}\right| \le \ddot{x}_{1d\max} + \frac{\tau_1}{\theta_1}\left(\alpha_1 + \dot{x}_{1d\max}\right) = \dot{x}_{2d\max}, \tag{31}$$

$$\begin{aligned} \left|\dot{x}_{3d1}\right| \le M_{\max}\dddot{x}_{1d\max} + M_{\max}\frac{\tau_1}{\theta_1}\ddot{x}_{1d\max} + \frac{\tau_2}{\theta_2}\dot{x}_{2d\,\mathrm{ma}} \\ +\left(M_{\max}\frac{\tau_1}{\theta_1} + \frac{\tau_2}{\theta_2}\right)\frac{p_s A_1 - p_{atm}A_2}{M_{\min}} = \dot{x}_{3d1\max}, \end{aligned} \tag{32}$$

$$\left|\dot{x}_{3d2}\right| = 0. \tag{33}$$

Taking the Eqs. (12) and (13) into consideration, the time derivatives of three sliding surfaces can be derived as

$$\dot{s}_1 = s_2 - \tau_1 \frac{s_1}{\theta_1}, \tag{34}$$

$$\dot{s}_2 = \frac{1}{M}s_3 - \frac{1}{M}\left(F_{fr} - \widehat{F}_{fr}\right) - \frac{1}{M}\tau_2 \frac{s_2}{\theta_2}, \tag{35}$$

$$\dot{s}_3 = P(\mathbf{x},t) + B(\mathbf{x},t)u - \dot{x}_{3d}. \quad (36)$$

Eqs. (27) and (31) to (36) will be used later in Section 2.2 to analyse the stable properties of the closed-loop system. The control law of the system is proposed as follows:

$$u = \frac{1}{\widehat{B}}\left(\dot{x}_{3d1} - P(\mathbf{x},t) - \tau_3 \frac{s_3}{\theta_3}\right). \quad (37)$$

where θ_3 is the boundary thickness of the sliding surface s_3, and τ_3 is a positive constant. It can be noted that adding the friction force estimate $\widehat{F}_{fr}$ in calculating the desired force x_{3d} in Eq. (24) affects the control law u of the system in Eq. (37) through the sliding surface s_3.

2.2 Stability Analysis

This section presents the analysis of the stability properties of the closed-loop system basing on the Lyapunov direct method **[30]**. First, let us consider a Lyapunov function for the third sliding surface s_3 as $G_3 = \frac{1}{2}s_3^2$. Taking the time derivative of G_3 and combining it with the Eqs. (30), (36), and (37), we obtain:

$$\dot{G}_3 = s_3\left[\left(1-\frac{B(\mathbf{x},t)}{\widehat{B}}\right)P(\mathbf{x},t) + \left(\frac{B(\mathbf{x},t)}{\widehat{B}}-1\right)\dot{x}_{3d1} - \dot{x}_{3d2}\right] - \frac{B(\mathbf{x},t)}{\widehat{B}}\frac{\tau_3}{\theta_3}s_3^2. \quad (38)$$

By selecting

$$\tau_3 = \frac{1}{\lambda}\left[(1+\lambda)\alpha_3 + (1+\lambda)\dot{x}_{3d1\max} + \gamma_3\right] \quad \text{with} \quad \gamma_3 > 0$$

along with Eqs. (31) to (33), then we obtain:

$$\dot{G}_3 \le -|s_3|\left[\begin{matrix}(1+\lambda)\alpha_3 \\ +(1+\lambda)\dot{x}_{3d1\max}\end{matrix}\right]\left(\frac{|s_3|}{\theta_3}-1\right) - \gamma_3\frac{s_3^2}{\theta_3}, \quad (39)$$

if we choose $\theta_3 \le |s_3|$ then $\dot{G}_3 \le -\gamma_3 s_3^2/\theta_3 < 0$. This means that s_3 converges asymptotically to its boundary layer, i.e., the force x_3 converges to the desired force x_{3d}. Similarly, let us consider a Lyapunov function for the second sliding surface s_2 as $G_2 = \frac{1}{2}s_2^2$. Taking the time derivative of G_2 and combining it with Eq. (35), we obtain:

$$\dot{G}_2 = s_2\dot{s}_2 = s_2\left[\frac{1}{M}s_3 - \frac{1}{M}\left(F_{fr} - \widehat{F}_{fr}\right) - \frac{1}{M}\tau_2\frac{s_2}{\theta_2}\right]. \quad (40)$$

By assuming that the estimated friction force is bounded by $|\widehat{F}_{fr}| \le F_{st}$ and by selecting $\tau_2 = M_{\max}\left[\frac{1}{M_{\min}}\theta_3 + \frac{1}{M_{\min}}2F_{st} + \gamma_2\right]$ with $\gamma_2 > 0$, then,

$$\dot{G}_2 \le |s_2|\frac{1}{M_{\min}}\left[\left(|s_3| - \theta_3\frac{|s_2|}{\theta_2}\right) + \left(1-\frac{|s_2|}{\theta_2}\right)2F_{st}\right] - \gamma_2\frac{s_2^2}{\theta_2}. \quad (41)$$

If we choose $\theta_2 \le \frac{\theta_3}{|s_3|}|s_2|$ then $\dot{G}_2 \le -\gamma_2\frac{s_2^2}{\theta_2} < 0$. This proves that s_2 converges to its boundary layer asymptotically, i.e., the cylinder velocity x_2 converges to the desired velocity x_{2d}. Finally, a Lyapunov function for the first sliding surface s_1 is defined as $G_1 = \frac{1}{2}s_1^2 + \frac{1}{2\tau_z}\tilde{w}^2$. Taking the time derivative of G_1 and combining it with Eqs. (27) and (34), we obtain:

$$\dot{G}_1 = s_1 s_2 - \tau_1\frac{s_1^2}{\theta_1} - \frac{|\dot{x}_1|\sigma_0\tilde{w}^2}{\tau_z q(\dot{x}_1)} + \tilde{w}s_1. \quad (42)$$

By selecting $\tau_1 = \theta_2 + \gamma_1$ with $\gamma_1 > 0$ and noting that $\tilde{w}s_1 \le \frac{1}{2}\tilde{w}^2 + \frac{1}{2}s_1^2$, then we obtain:

$$\dot{G}_1 \le |s_1|\left(|s_2| - \theta_2\frac{|s_1|}{\theta_1}\right) - \left(\frac{\gamma_1}{\theta_1} - \frac{1}{2}\right)s_1^2 - \left(\frac{\alpha_2\sigma_0}{\tau_z q(\dot{x}_1)} - \frac{1}{2}\right)\tilde{w}^2. \quad (43)$$

It can be noted in Eq. (8) that the Stribeck function $q(\dot{x}_1)$ is strictly positive and is bounded by $0 < F_{cl} \le q(\dot{x}_1) \le F_{st}$. So, if we select $\theta_1 \le \frac{\theta_2}{|s_2|}|s_1|$, $\gamma_1 > \frac{\theta_1}{2}$ and $\tau_z < \frac{2\alpha_2\sigma_0}{q(\dot{x}_1)}$ then $\dot{G}_1 < 0$. Therefore, s_1 converges asymptotically to its boundary layer, i.e., the piston position x_1 converges to the desired position x_{1d}. This result, therefore, verifies the system's stability.

3 SIMULATION EVALUATION

In this section, simulation studies are carried out to evaluate the effectiveness of the new controller. Simulations were done by MATLAB/Simulink software. Both the new controller and the MSS controller were simulated with the same desired position inputs. The step and sinusoidal desired position inputs with different amplitudes and frequencies were used. The parameters of the system used in simulations are listed in Table 1. The maximum velocity of the piston was set to be $\alpha_1 = 1$ m/s according to the cylinder's specification. The static parameters of the LuGre friction model were given by $F_{st} = 30$ N, $F_{cl} = 5.6$ N, $v_s = 0.01$ m/s, $n = 2.5$, $\sigma_2 = 25$ Ns/m for the positive velocity direction (i.e., for extending stroke of the piston) and by $F_{st} = 25$ N,

F_{cl}=5.8 N, v_s=0.015 m/s, n=1.2, σ_2=25 Ns/m for the negative velocity direction (i.e., for extending stroke of the piston). The dynamic parameters of the LuGre model were given by σ_0=8×10³ N/m and σ_1=0.1 Ns/m for both directions of the velocity. These parameters of the LuGre friction model were identified in advance for the pneumatic cylinder in a previous study [23]. The parameters of the controllers used in simulations were chosen as σ_1=0.002, σ_2=0.1, σ_3=0.5, γ_1=0.01, γ_2=γ_3=1, α_2= 60 and the parameter of the friction force observer was chosen as τ_z= 5000.

Table 1. *System parameters used in simulation*

Parameter [unit]	Value	Parameter [unit]	Value
M [kg]	0.5	H_{V1} [m²/V]	5×10^{-7}
A_1 [m²]	4.9×10^{-4}	H_{V2} [m²/V]	6×10^{-7}
A_2 [m²]	4.12×10^{-4}	T [K]	295
L [m]	0.3	R [Nm/(kgK)]	287
V_{10} [m³]	9.8×10^{-7}	p_s [bar]	5
V_{20} [m³]	8.24×10^{-7}	p_{atm} [bar]	0.1
k	1.3997		

Fig. 3 shows a comparison of the control performances obtained by simulations between the new controller and the MSS controller with a step desired position input of the piston position x_{1d}=0.25 m. The piston is set at an initial position of 0 m. Fig. 3a shows that both the controllers exhibit good control performances with no overshoot. However, it can be observed that the rise time achieved by the new controller (0.26 s) is smaller than that of the MSS controller (0.5 s). In addition, the maximum tracking error in steady-state achieved by the new controller (0.5 mm) is also smaller than that of the MSS controller (1 mm) (Fig. 3b).

Fig. 4 shows simulation comparisons of the control performances between the new controller and the MSS controller for four different constant desired positions: x_{1d} = 0.01 m (Fig 4a), 0.05 m (Fig. 4b), 0.1 m (Fig. 4c) and 0.2. m (Fig. 4c). The initial positions of the piston are 0 m. Fig. 4 shows that the controller can provide shorter rise times and smaller position errors for four cases of the desired position. The maximum tracking errors obtained under steady-state conditions are also 0.5 mm for the new controller and 1 mm for the MSS controller.

Fig. 5 shows a comparison between the new controller and the MSS controller for a sinusoidal desired input x_{1d} = 0.15 + 0.1sin(2πft) m at the frequency f = 0.1 Hz. The figure shows that the new controller can track the desired position faster, i.e., a shorter rise time, than the MSS controller. In addition, the tracking error achieved in a steady-state condition of the new controller is much smaller than that by the MSS controller. The maximum tracking error in the steady-state condition of the new controller is 1.5 mm, whereas the maximum tracking error of the MSS controller is 4.8 mm. Other comparisons between two controllers with higher frequencies of the desired position input x_{1d} = 0.15 + 0.1sin (2πft) m are shown in Figs. 6 and 7. The position amplitude remains the same as in Fig. 5, but the frequency is increased to 0.5 Hz and 1 Hz. As compared with Fig. 5, although the abilities to track the desired position of the two controllers are inferior when the frequency is increased, the new controller also provides smaller errors than the MSS controller. In Fig. 6 for f = 0.5 Hz, the maximum error in a steady-state condition is 2.8 mm for the new controller and is 6.5 mm for the MSS controller. In Fig. 7 for f = 1 Hz, the maximum error in a steady-state condition is 4.5 mm for the new controller and is 7.8 mm for the MSS controller. The results obtained in Figs. 3 to 7 verify by simulation that the new controller can provide better control performances than the MSS controller.

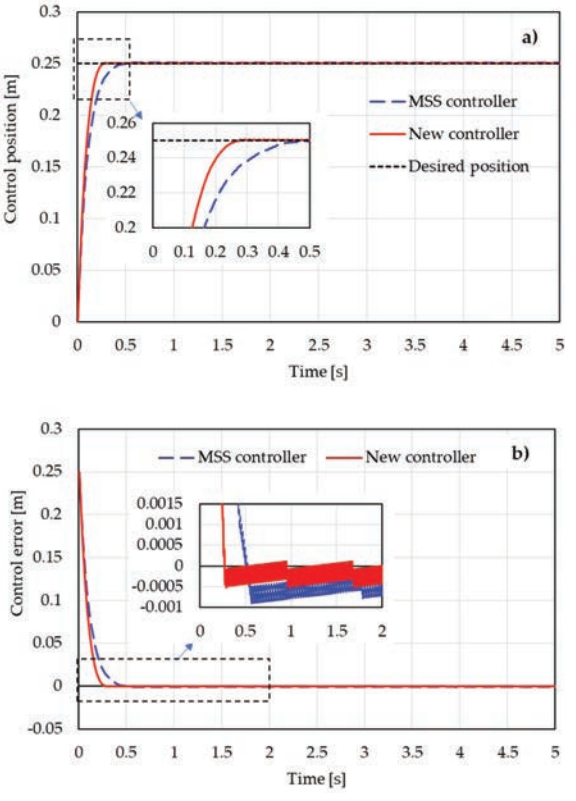

Fig. 3. *Comparing control results of the new controller and the MSS controller with a step desired position input x_{1d} = 0.25 m; a) piston position, b) control position error (simulation)*

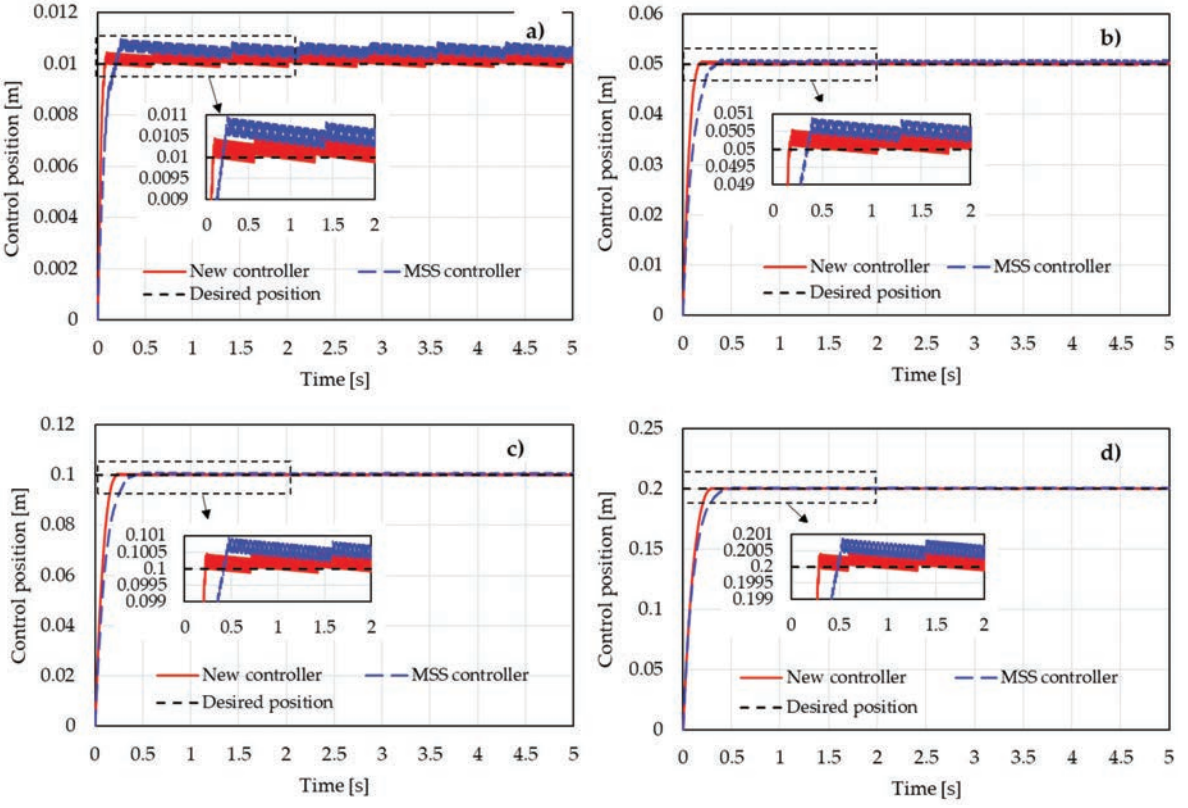

Fig. 4. *Control results of the new controller and the MSS controller for different step desired positions; a)* $x_{1d} = 0.01$ m, *b)* $x_{1d} = 0.05$ m; *c)* $x_{1d} = 0.1$ m; *d)* $x_{1d} = 0.2$ m *(experiment)*

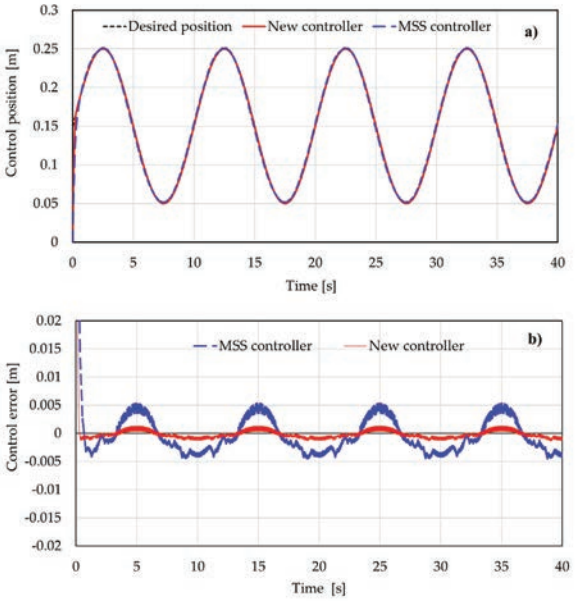

Fig. 5. *Control performances of the new controller and of the MSS controller with a sinusoidal desired position* $x_{1d} = 0.15 + 0.1\sin(2\pi ft)$ m, $f = 0.1$ Hz *by simulation; a) tracking position; b) tracking error*

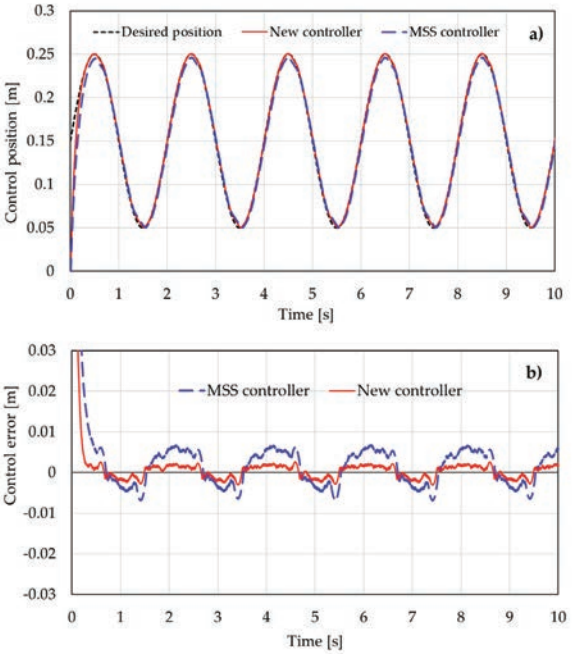

Fig. 6. Control performances of the new controller and of the MSS controller with a sinusoidal desired position $x_{1d} = 0.15 + 0.1\sin(2\pi ft)$ m, $f = 0.5$ Hz by simulation; a) tracking position; b) tracking error.

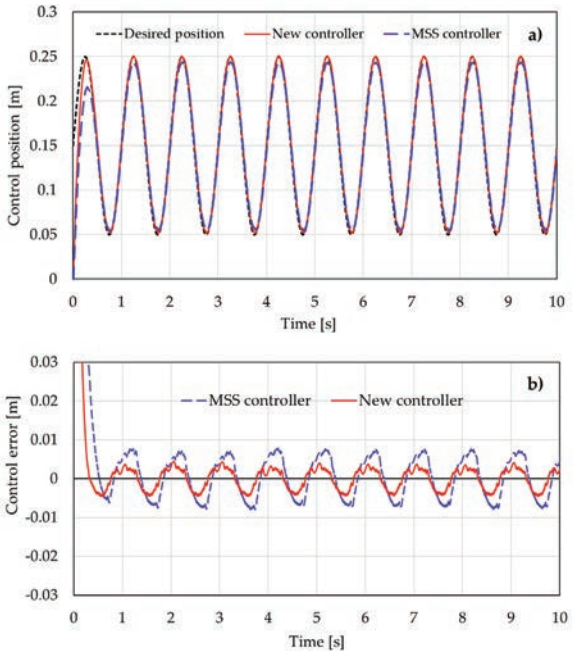

Fig. 7. *Control performances of the new controller and of the MSS controller with a sinusoidal desired position* $x_{1d} = 0.15 + 0.1\sin(2\pi ft)$ m, $f = 1$ Hz *by simulation; a) tracking position; b) tracking error*

4 EXPERIMENTAL EVALUATION

4.1 Experimental System

Fig. 8 shows the experimental system used for the experimental evaluation of the new controller. The system used a pneumatic double-acting cylinder (1). The piston rod was connected to a load mass (2) which slides on a guiding bar (3). The load mass was set at 0.5 kg. Two proportional pneumatic valves (4) were used to control flow rates supplying to the cylinder chambers. These valves were controlled by current signals ranging from 0 A to 1 A. The current signals were supplied by two amplifiers (5). The input signals of the valve amplifiers are voltage values ranging from 0 VDC to 5 VDC. For the flow characteristic of the valves, it is noted that if the valves' inputs vary from 0.5 A to 1 A (corresponding to 2.5 VDC to 5 VDC of the valve amplifiers' inputs), the valves will provide air from the supply source into the cylinder chambers and if the valves' inputs vary from 0 A to 0.5 A (corresponding to 0 VDC to 2.5 VDC of the valve amplifiers' inputs), the valves will release air from the cylinder chambers to the atmosphere. A position sensor with a measuring range from 0 m to 0.3 m (6) was used to measure the piston displacement. Two pressures, p_1 and p_2, in the cylinder chambers were measured by two pressure sensors (7). A data acquisition card (8) that includes both 12 bits analogue-to-digital converter (ADC) and 12 bits digital-to-analogue converter (DAC) was used to acquire the displacement and the pressure signals from the sensors and to send the voltage signals to the valve amplifiers. The data acquisition device was connected to a personal computer (9). The main technical specifications of the devices are listed in Table 2. Microsoft Visual C++ software was used to communicate between the data acquisition device and the computer. Each step of the experimental programme was executed in a period of 1.16 ms.

The piston velocity that is used in calculating the control law was not measured in this experimental system. It was calculated by an approximate

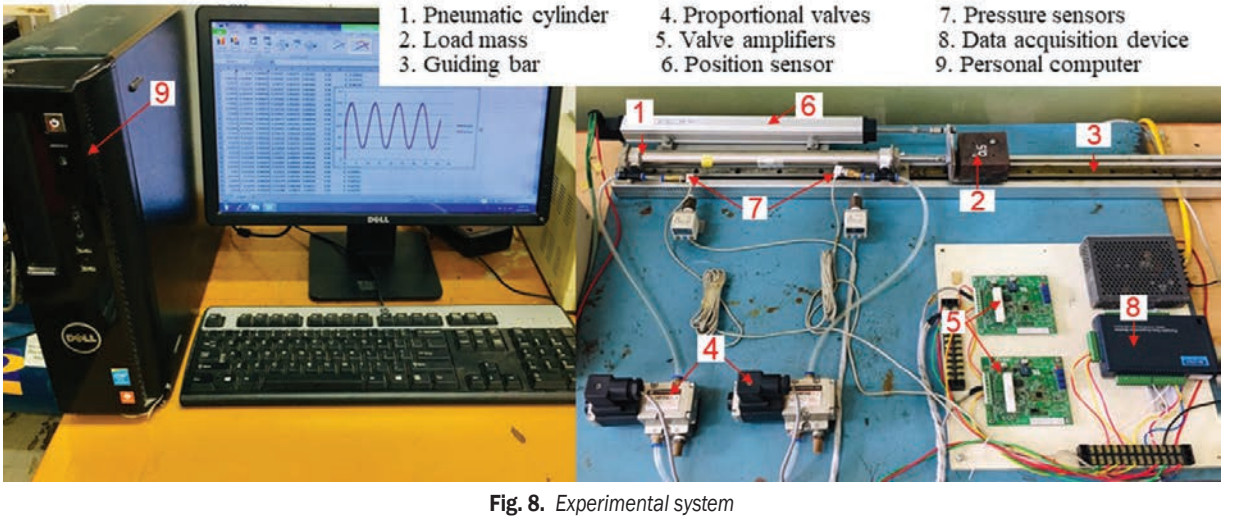

Fig. 8. *Experimental system*

Table 2. *Main equipment used in the experimental system*

Equipment	Model	Main technical specifications	Manufacturer
Compressor	PK 1090A	Maximum pressure: 10 bar Maximum flow rate: 185 l/min	PUMA
Air preparation unit	GC 600-20	Maximum pressure: 10 bar Maximum flow rate: 1000 l/min Filter element: 40 m	AIRTAC
Pneumatic cylinder	CM2L25-300	Piston diameter: 0.025 m Rod diameter: 0.01 m Piston rod: 0.3 m	SMC
Proportional pneumatic valves	VEF3121-1-02	Maximum pressure: 10 bar Maximum flow rate: 720 l/min Current input: 0 A to 1 A	SMC
Valve amplifier	VEA 250	Voltage input: 0 VDC to 5 VDC Curent output: 0 A to 1 A Accuracy: ± 1 % F.S	SMC
Position sensor	LWH0300	Measurement range: 0 m to 0.3 m Accuracy: 0.4 % F.S	NOVOTECHNIK
Pressure sensor	PSE 540	Measurement range: 0 bar to 10 bar Accuracy: 2 % F.S	SMC
Data acquisition card (ADC/DAC)	USB4711	Analog input channels: 16 Analog output channels: 2	ADVANTECH
Personal computer	Dell Vostro 260	CPU: Intel Core I3-2120 3.3 GHz Memory: 8GB RAM	DELL

differentiation of the measured piston displacement. The noise in the calculated velocity signal was filtered using an acausal low-pass filter with a bandwidth of 30 Hz. The compressed air was supplied to the system by a compressor through an air preparation unit, and the supply pressure p_s was set at 5 bar.

4.2 Experimental Results

In this section, experimental performances of the new controller and the MSS controller are compared to evaluate the effectiveness of the new controller. Similarly to simulation, constant and sinusoidal desired position inputs were used. In addition, the control performances of the new controller are also compared to those of the other nonlinear controllers. The values of the controller's parameters and the parameters of the LuGre friction model were given as the same as those used in the simulation.

Fig. 9 compares the experimental performances between the new controller and the MSS controller with a desired step position input of x_{1d} = 0.25 m. Similarly to the results obtained in the simulation results in Fig. 3, both controllers exhibit accurate position tracking with the maximum tracking errors in a steady-state condition below 1 mm, but the rise time of the piston obtained by the new controller (0.2 s) is less than the rise time of the MSS controller (0.3 s). It is additionally noted in Fig. 9 that at the beginning, the piston remains at its original position for 0.1 s. This result may be caused by the compressibility of the air in the cylinder chamber and/or by the delay characteristic of the pneumatic valves.

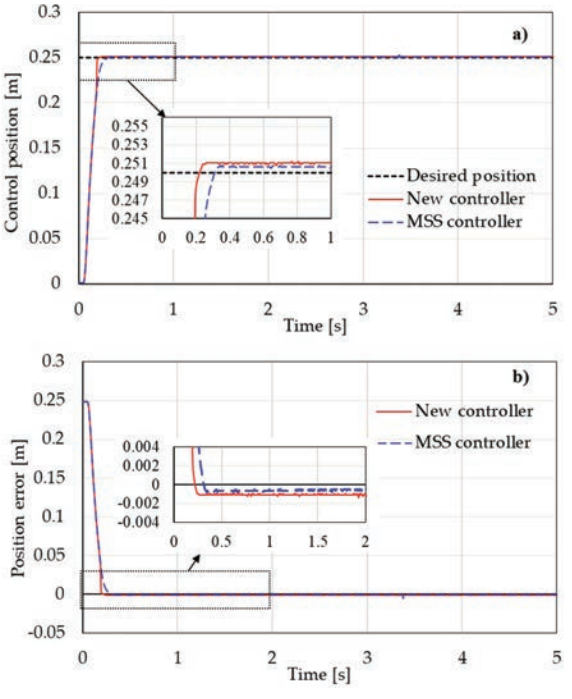

Fig. 9. *Comparing control results of the new controller and the MSS controller with a desired constant position input* x_{1d} = 0.25 m; *a) piston position, b) control position error (experiment)*

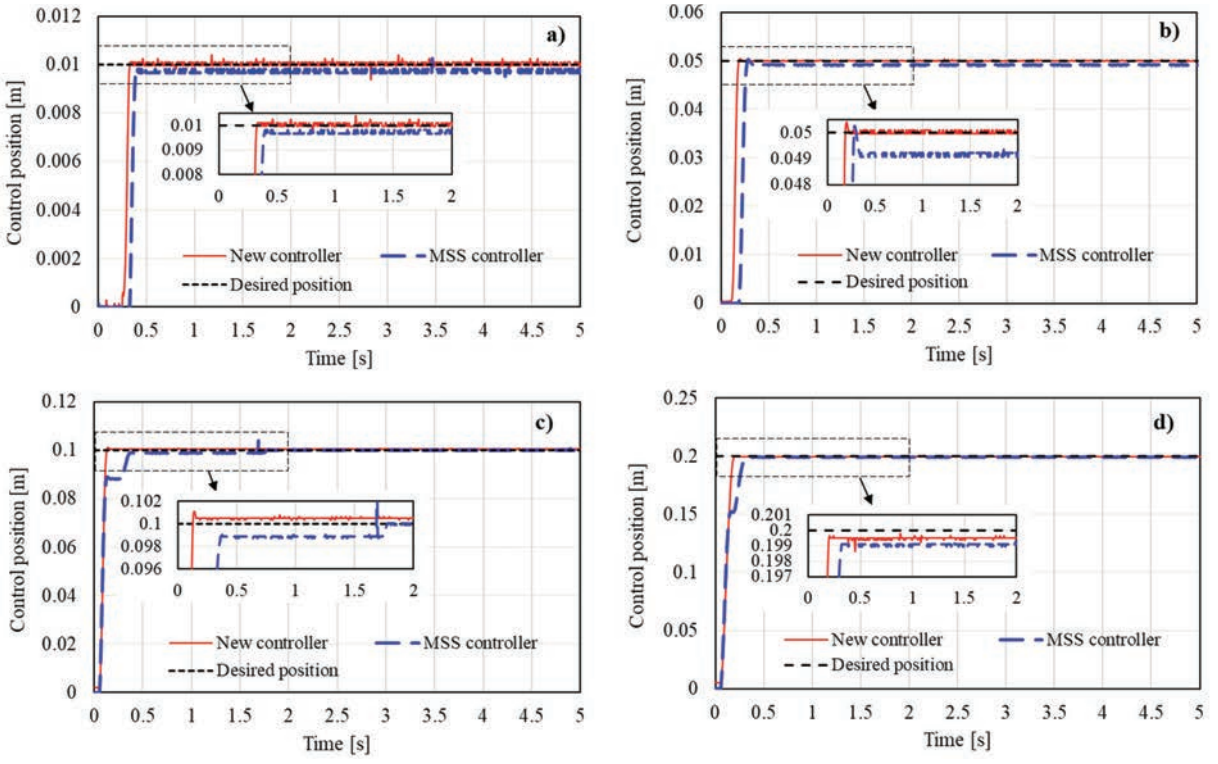

Fig. 10. *Control results of the new controller and the MSS controller for different desired step position inputs; a)* $x_{1d} = 0.01$ m, *b)* $x_{1d} = 0.05$ m; *c)* $x_{1d} = 0.1$ m; *d)* $x_{1d} = 0.2$ m *(experiment)*

Fig. 10 compares the experimental performances between the new controller and the MSS controller at four step-desired positions: 0.01 m (Fig. 10a), 0.05 m (Fig. 10b), 0.1 m (Fig. 10c), and 0.2 m (Fig. 10d). Similarly to the simulation results in Fig. 4, Fig. 10 shows that the new controller provides better control performance than the MSS controller with shorter rise times and smaller steady-state errors in all cases. The maximum position errors in steady-state conditions are 0.5 mm for the new controller and 1 mm for the MSS controller. It can be additionally noted in Fig. 10 that the period at which the piston remains at its initial position is increased by reducing the desired position. This result can be explained by that when the desired position is reduced, the initial flow rate supplied to the cylinder is small and thus increases the delay time of the piston.

Fig. 11 shows an experimental comparison between the new controller and the MSS controller with a sinusoidal desired position $x_{1d} = 0.15 + 0.1\sin(2\pi ft)$ m at a frequency $f = 0.1$ Hz. Fig. 11 shows that the peak position error obtained in a steady-state condition is 8.4 mm (corresponding to 4.2 % of the maximum cross displacement) for the MSS controller and is 4.8 mm (2.4 %) for the new controller. When

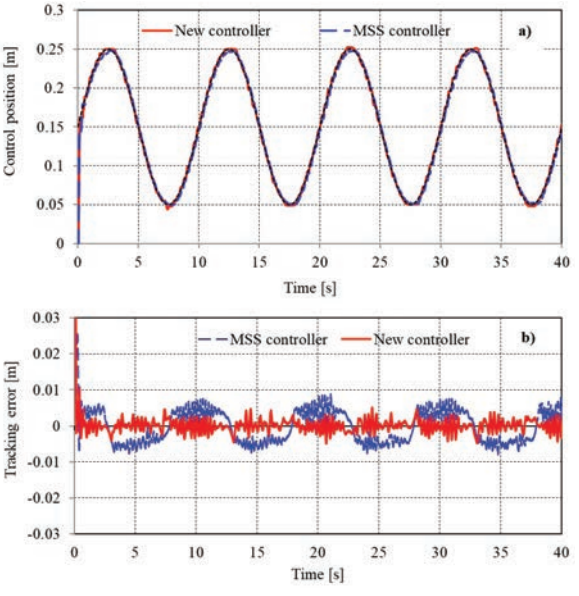

Fig. 11. *Control performances of the MSS controller and the new controller with a sinusoidal input* $x_{1d} = 0.15 + 0.1\sin(2\pi ft)$ m, $f = 0.1$ Hz *by experiments; a) control position; b) tracking error*

calculating the root means squared error (RMS error) in a steady-state condition, the results show that the

RMS error obtained for the MSS controller is 3.7 mm (1.85 % of the maximum cross displacement) while the RMS error obtained for the new controller is 2.1 mm (1.05 %). The calculated velocity and the estimated friction force by the new controller are shown in Fig. 12. When the piston starts moving, the friction force is suddenly increased to a very larger value of about 30 N in the first haft cycle of the piston motion. After that, the friction force reduces and varies under a trapezoidal form between the value from -13 N to 20 N in the steady-state condition. The maximum friction force at the positive velocity direction is larger than at the negative velocity direction. In Fig. 11, the large values of the tracking error obtained by the MSS controller appear mainly at high velocities, and they can be eliminated by the new controller. At high velocities, the friction force becomes large due to the effect of the viscous friction force. Thus, the compensation of friction to the MSS controller significantly reduces the tracking error at these velocities. The tracking errors of the two controllers achieved by experiments are larger than those achieved by simulation in Fig. 3. However, like the simulation results, the experimental result also shows the improvement in the control performances of the new controller comparing with the MSS controller.

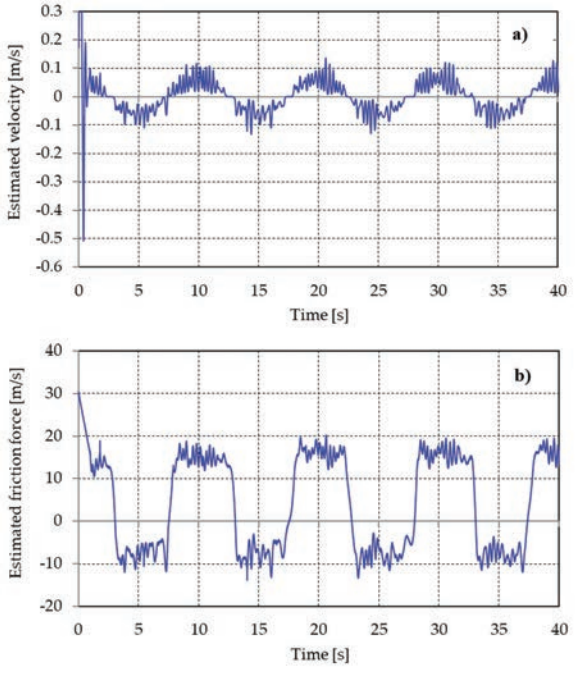

Fig. 12. *Control performances of the MSS controller and the new controller with a sinusoidal input* $x_{1d} = 0.15 + 0.1\sin(2\pi ft)$ m, $f = 0.1$ Hz *by experiments; a) control position; b) tracking error*

Fig. 13 compares the percentage rates of the peak position error and of the RMS error in steady-state condition between two controllers at different displacement amplitude values (A) of the desired position input $x_{1d} = 0.15 + A\sin(2\pi ft)$ m. The varying frequency is fixed at $f = 0.1$ Hz. The results show that both the peak error and the RMS error of both controllers increase with decreasing the displacement amplitude A. However, these errors are significantly reduced when using the new controller. When the amplitude A varies from 0.01 m to 0.1 m, the peak error can be reduced from 1.8 % to 10 %, and the RMS error can be reduced from 0.8 % to 6.5 %. The minimum peak error of 2.2 mm can be obtained at the amplitude $A = 0.01$ m. This result of the new controller indicates better control performances than other nonlinear and robust control methods [9] to [21].

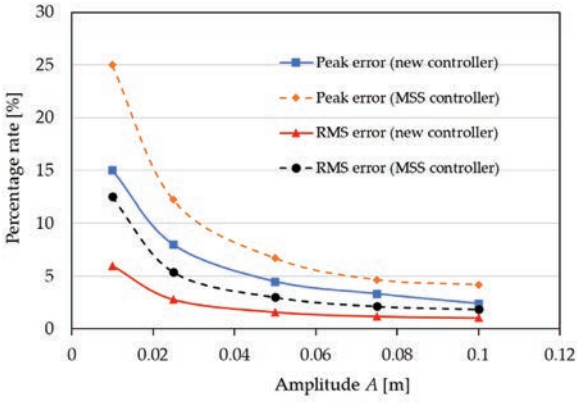

Fig. 13. *Comparison of the percentage rate of peak error and RMS error between the new controller and the MSS controller at different displacement amplitudes* A *and fixed frequency* 0.1 Hz *of the desired position input* $x_{1d} = 0.15 + A\sin(2\pi ft)$ m

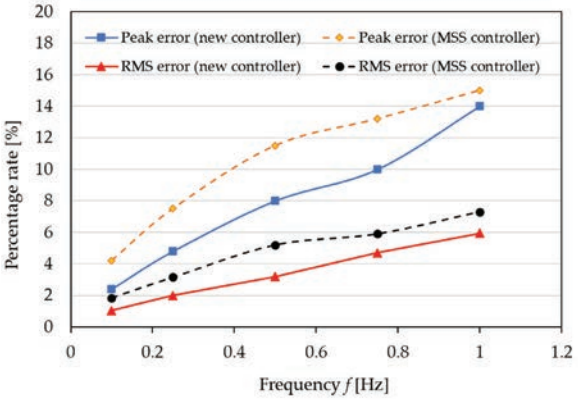

Fig. 14. *Comparison of the percentage rate of peak error and RMS error between the new controller and the MSS controller at different frequencies f and fixed displacement amplitude* $A = 0.1$ m *of the desired position input* $x_{1d} = 0.15 + 0.1\sin(2\pi ft)$ m

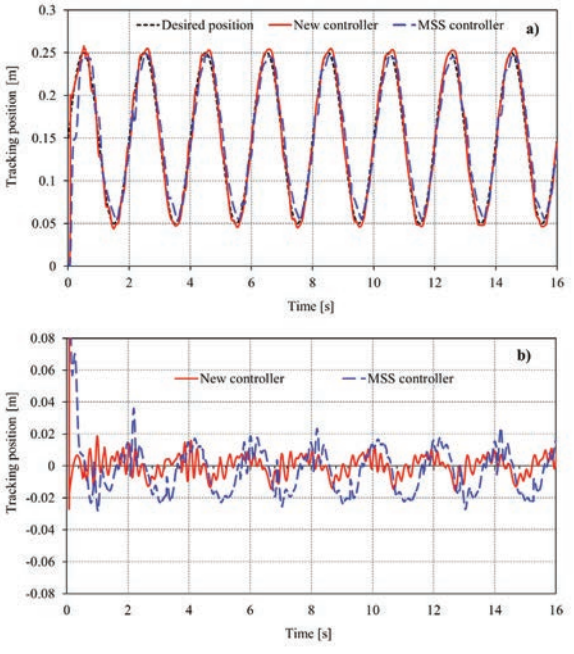

Fig. 15. *Control performances of the MSS controller and the new controller with a sinusoidal input* $x_{1d} = 0.15 + 0.1\sin(2\pi ft)$ m, $f = 0.5$ Hz *by experiments; a) control position; b) tracking error*

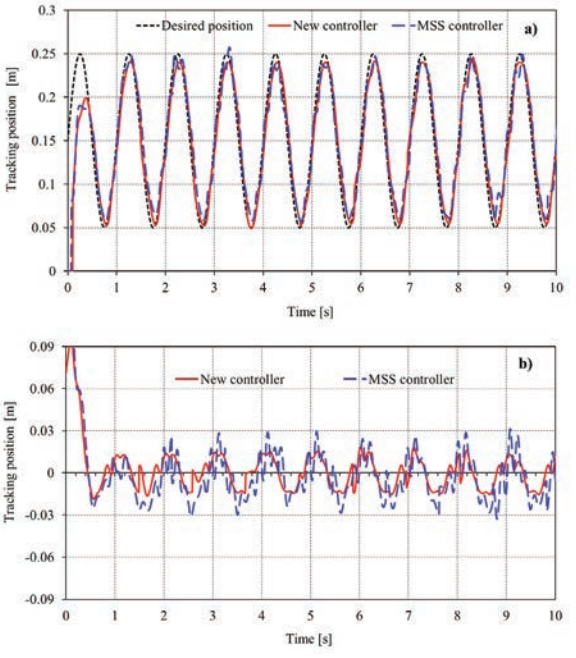

Fig. 16. *Control performances of the MSS controller and the new controller with a sinusoidal input* $x_{1d} = 0.15 + 0.1\sin(2\pi ft)$ m, $f = 1$ Hz *by experiments; a) control position; b) tracking error*

Fig. 14 compares the percentage rates of the peak position error and of the RMS error in steady-state condition between two controllers at different frequencies (f) of the desired position input $x_{1d} = 0.15 + A\sin(2\pi ft)$ m. The displacement amplitude is fixed at $A = 0.1$ m. The results show that both the peak error and the RMS error of both controllers grow with increasing the frequency. However, the peak error and the RMS error are also significantly reduced when using the new controller. When the frequency f varies from 0.1 Hz to 1 Hz, the peak error can be reduced from 1 % to 3.5 % and the RMS error can be reduced from 0.8 % to 2 %. Figs. 15 and 16 show the control performances of two controllers at two frequencies 0.5 Hz and 1 Hz.

5 CONCLUSIONS

In this study, a new controller was proposed for improving position control performances of a pneumatic cylinder. It was designed by combining the multiple-surface sliding control method with a model-based friction compensator, which was designed based on the dynamic LuGre friction model. Both simulation and experimental studies were performed to evaluate the new controller. The study results show that by using the new controller, the relative position peak error is reduced 10 %, and the relative RMS error is reduced by 6.5 % when comparing those of the MSS controller without friction compensation. The new controller also provides improved control error compared to other nonlinear and advanced controllers with a minimal peak error of 2.2 mm. It is noted that the parameters of the LuGre model used in the friction observer in this study were identified in advance. Therefore, a methodology for online parameter estimation of the LuGre model when implementing the new controller will be considered in the future.

6 ACKNOWLEDGEMENTS

This research was an extension of the work in [31]. This research was funded by the Hanoi University of Science and Technology (HUST) under Project number T2020-PC-014.

7 NOMENCLATURES

a	piston acceleration, [m/s^2]
A_i	piston area ($i = 1, 2$), [m^2]
$B_{\max}$	maximum value of the function $B(\mathbf{x},t)$
$B_{\min}$	minimum value of the function $B(\mathbf{x},t)$
$\hat{B}$	estimated value of the function $B(\mathbf{x},t)$
F_{cl}	coulomb friction force, [N]

F_{fr} friction force, [N]
$\widehat{F}_{fr}$ estimated friction force, [N]
F_{st} : maximum static friction force, [N]
G_i : Lyapunov function ($i=1,2,3$)
H_{Vi} : valve coefficient ($i=1,2$), [m²/V]
k : specific heat ratio
L : piston stroke, [m]
M : load mass, [kg]
$M_{\max}$ maximum load mass, [kg]
$M_{\min}$ minimum load mass, [kg]
$\dot{m}_i$ mass flow rate ($i=1,2$), [kg/s]
n exponent for Stribeck curve
p_{atm} atmosphere pressure, [bar]
p_i pressure ($i=1,2$), [bar]
p_s supply pressure, [bar]
$P(\mathbf{x},t)$ function of the states'
$B(\mathbf{x},t)$ function of the states'
$q(v)$ Stribeck function, [N]
R gas constant, [Nm/(kgK)]
s_i sliding surface ($i=1,2,3$)
T Temperature, [K]
u control law, [V]
u_i valve control input ($i=1,2$), [V]
v piston velocity, [m/s]
V_i volume of the cylinder chamber ($i=1,2$), [m³]
V_{i0} dead volume in the cylinder chamber ($i=1,2$), [m³]
v_s : Stribeck velocity, [m/s]
x : piston position, [m]
$\mathbf{x}$: state vector
x_1 : piston position, [m]
x_{1d} : desired position of the piston, [m]
x_2 : piston velocity, [m/s]
x_{2d} : desired velocity of the piston, [m/s]
$\dot{x}_{2d\max}$ maximum value of $\dot{x}_{2d}$, [m/s²]
x_3 : piston force generated by the pressures, [N]
x_{3d} : desired force, [N]
$\dot{x}_{3d1}$ known part of $\dot{x}_{3d}$
$\dot{x}_{3d1\max}$ maximum value of $\dot{x}_{3d1}$
$\dot{x}_{3d2}$ unknown part of $\dot{x}_{3d}$
w mean deflection of bristles, [m]
$\hat{w}$ estimated mean deflection of bristles, [m]
$\tilde{w}$ estimating error of the mean deflection of bristles, [m]
α_1 maximum cylinder velocity, [m/s]
α_2 maximum value of F_{fr}/M, [N/kg]
α_3 maximum value of $P(\mathbf{x},t)$
β_{ib} pressure coefficient ($i=1,2$)
β_{ie} pressure coefficient ($i=1,2$)
γ_i : positive constant ($i=1,2,3$)
λ : constant
σ_0 : stiffness of bristles, [N/m]
σ_1 micro-viscous friction coefficient for bristles, [Ns/m]
σ_2 viscous friction coefficient, [Ns/m]
τ_i positive constant ($i=1,2,3$)
τ_z positive constant
θ_i boundary layer thickness of the surfaces s_i ($i=1,2,3$)

8 REFERENCES

[1] Beater, P. (2007). *Pneumatic Drives: System Design, Modelling and Control*. Springer, Berlin, **DOI:10.1007/978-3-540-69471-7**.

[2] Karponis, D., Koya, Y., Miyazaki, R., Kanno, T., Kawashima, K. (2019). Evaluation of a pneumatic surgical robot with dynamic force feedback. *Journal of Robotic Surgery*, vol. 13, p. 413-421, **DOI:10.1007/s11701-018-0878-2**.

[3] Tressler, J.M., Clement, T., Kazerooni, H., Lim, M. (2002). Dynamic behavior of pneumatic systems for lower extremity extenders. *Proceedings of IEEE International Conference on Robotics and Automation*, p. 3248-3253, **DOI:10.1109/ROBOT.2002.1013727**.

[4] Rao, Z., Bone, G.M. (2008). Nonlinear modeling and control of servo pneumatic actuators. *IEEE Transaction on Control Systems Technology*, vol. 16, no. 3, p. 562-569, **DOI:10.1109/TCST.2007.912127**.

[5] Harris, P.G., O'Donnell, G.E., Whelan, T. (2012). Modelling and identification of industrial pneumatic drive system. *The International Journal of Advanced Manufacturing Technology*, vol. 58, p. 1075-1086, **DOI:10.1007/s00170-011-3447-7**.

[6] Wang, J., Pu, J., Moore, P. (1999). A practical control strategy for servo-pneumatic actuator systems. *Control Engineering Practice*, vol. 7, no. 12, p. 1483-1488, **DOI:10.1016/S0967-0661(99)00115-X**.

[7] Chillari, S., Guccione, S., Muscato, G. (2001). An experimental comparison between several pneumatic position control methods. *Proceedings of the IEEE Conference on Decision and Control*, vol. 2, p. 1168-1173, **DOI:10.1109/CDC.2001.981043**.

[8] Merola, A., Colacino, D., Cosentino, C., Amato, F. (2018). Model-based tracking control design, implementation of embedded digital controller and testing of a biomechatronic device for robotic rehabilitation. *Mechatronics*, vol. 52, p. 70-77, **DOI:10.1016/j.mechatronics.2018.04.006**.

[9] Bobrow, J.E.; Jabbari, F. (1991). Adaptive pneumatic force actuation and position control. *ASME Journal of Dynamic Systems, Measurement, and Control*, vol. 113, no. 2, p. 267-272, **DOI:10.1115/1.2896374**.

[10] Gao, X., Feng, Z.J. (2005). Design study of an adaptive fuzzy-PD controller for pneumatic servo system. *Control Engineering Practice*, vol. 13, no. 1, p. 55-65, **DOI:10.1016/j.conengprac.2004.01.001**.

[11] Chen, Y., Tao, G., Liu, H. (2019). High precision adaptive robust neural network control of a servo pneumatic system. Appled Sciences., vol. 9, no. 17, p. 1-17, **DOI:10.3390/app9173472**.

[12] Gross, D.C., Rattan, K.S. (1997). Pneumatic cylinder trajectory tracking control using a feedforward multilayer neural network,

Proceedings of IEEE Aerospace and Electronics Conference, vol. 2, p. 777-784, **DOI:10.1109/NAECON.1997.622728**.

[13] Paul, A.K., Mishra, J.K.; Radke, M.G. (1994). Reduce order sliding mode control for pneumatic actuator. *IEEE Transaction on Control Systems Technology*, vol. 2, no. 3, p. 271-276. **DOI:10.1109/87.317984**.

[14] Tang, J.J., Walker, G.G. (1995). Variable structure control of a pneumatic actuator. *ASME Journal of Dynamic Systems, Measurement, and Control*, vol. 117, no. 1, p. 88-92, **DOI:10.1115/1.2798526**.

[15] Surgenor, B.W., Vaughan, N.D. (1997). Continuous sliding mode control of a pneumatic actuator. *ASME Journal of Dynamic Systems, Measurement, and Control*, vol. 119, no. 3, p. 578-581, **DOI:10.1115/1.2801298**.

[16] Acarman, T., Hatipoglu, C., Ozguner, U. (2001). A robust nonlinear controller design for a pneumatic actuator. *Proceedings of the IEEE American Control Conference*, vol. 6, p. 4490-4495, **DOI:10.1109/ACC.2001.945686**.

[17] Liu, Y.T, Kung, T.T, Chang, K.M., Chen, S.Y. (2013). Observer-based adaptive sliding mode control for pneumatic servo system. *Precision Engineering*, vol. 37, no. 3, p. 522-530, **DOI:10.1016/j.precisioneng.2012.12.003**.

[18] Pandian, S.R., Hayakawa, Y., Kanazawa, Y., Kamoyama, Y., Kawamura, S. (1997). Practical design of a sliding mode controller for pneumatic actuators. *ASME Journal of Dynamic Systems,Measurement, and Control*, vol. 119, no. 4, p. 666-674, **DOI:10.1115/1.2802376**.

[19] Tsai, Y.C., Huang, A.C. (2008). Multiple-surface sliding controller design for pneumatic servo systems. Mechatronics, vol. 18, no. 9, p. 506-512, **DOI:10.1016/j.mechatronics.2008.03.006**.

[20] Armstrong-Helouvry, B. (1991). Control of Machines with Friction, Springer, Boston, **DOI:10.1007/978-1-4615-3972-8**.

[21] Koch, S., Reichhartinger, M. (2016). Observer-based sliding mode control of hydraulic cylinders in the presence of unknown load forces, *e & i Elektrotechnik und Informationstechnik*, vol. 133, p. 253-260, **DOI:10.1007/s00502-016-0418-6**.

[22] Ayalew, B., Jablokow, K.W. (2006). Cascaded robust nonlinear position tracking control of an electrohydraulic actuator: sliding mode and feed forward. *Proceedings of the ASME International Mechanical Engineering Congress and Exposition. Fluid Power Systems and Technology*, p. 95-102, **DOI:10.1115/IMECE2006-13943**.

[23] Tran, X.B., Yanada, H. (2013). Dynamic friction behaviors of pneumatic cylinders. *Intelligent Control and Automation*, vol. 4, no. 2, p. 180-190, **DOI:10.4236/ica.2013.42022**.

[24] Armstrong-Helouvry, B., Dupont, P., Canudas de Wit, C. (1994). A survey of models analysis tools and compensation methods, for the control of machines with friction. *Automatica*, vol. 30, no. 7, p. 1083-1138, **DOI:10.1016/0005-1098(94)90209-7**.

[25] Canudas de Wit, C., Olsson, H., Aström, K.J., Lischinsky, P. (1995). A new model for control of systems with friction. *IEEE Transaction on Automatic Control*, vol. 40, no. 3, p. 419-425, **DOI:10.1109/9.376053**.

[26] Lampaert, V., Swevers, J., Al-Bender, F. (2002). Modification of the Leuven integrated friction model structure. *IEEE Transaction on Automatic Control*, vol. 47, no. 4, p. 683-687, **DOI:10.1109/9.995050**.

[27] Dupont, P., Hayward, V., Armstrong, B., Altpeter, F. (2002). Single state elastoplastic friction models. *IEEE Transactions on Automatic Control*, vol. 47, no. 5, p. 787-792, **DOI:10.1109/TAC.2002.1000274**.

[28] Al-Bender, F., Lampaert, V., Swevers, J. (2005). The generalized Maxwell-slip model: a novel model for friction simulation and compensation. *IEEE Transaction on Automatic Control*, vol. 50, no. 11, p. 1883-1887, **DOI:10.1109/TAC.2005.858676**.

[29] Tran, X.B., Hafizah, N., Yanada, H. (2012). Modeling of dynamic friction behaviors of hydraulic cylinders. *Mechatronics*, vol. 22, no. 1, p. 65-75, **DOI:10.1016/j.mechatronics.2011.11.009**.

[30] Slotine, J.J.E., Li, W. (1991). *Applied Nonlinear Control*, Prentice Hall, London.

[31] Tran, X.B., Nguyen, V.L., Nguyen, N.C., Pham, D.T., Phan, V.L. (2020). Sliding mode control for a pneumatic servo system with friction compensation. In: Sattler, K.U., Nguyen, D., Vu, N., Tien Long, B., Puta, H. (eds). *Advances in Engineering Research and Application. ICERA 2019. Lecture Notes in Networks and Systems*, vol. 104. Springer, Cham, **DOI:10.1007/978-3-030-37497-6_75**.

Vsebina

Strojniški vestnik - Journal of Mechanical Engineering
letnik 67, (2021), številka 9
Ljubljana, september 2021
ISSN 0039-2480

Izhaja mesečno

Razširjeni povzetki (extended abstracts)

Khurram Ali, Adeel Mehmood, Israr Muhammad, Sohail Razzaq, Jamshed Iqbal: Upravljanje antropomorfnega manipulatorja z modelom trenja LuGre – zasnova in eksperimentalna validacija SI 53
Dragan Milčić, Amir Alsammarraie, Miloš Madić, Vladislav Krstić, Miodrag Milčić: Napovedovanje količnika trenja pri hidrodinamičnem radialnem drsnem ležaju z uporabo umetnih nevronskih mrež SI 54
Almatbek Kydyrbekuly, Gulama-Garip Alisher Ibrayev, Tangat Ospan, Anatolij Nikonov: Večparametrična dinamična analiza sistema kotalnih ležajev SI 55
Youyu Liu, Yi Li, Xuyou Zhang, Bo Chen: Sledilno vodenje za manipulatorje na osnovi mehke ekvivalence in terminalnega drsnega režima SI 56
Yanxiong Liu, Yuwen Shu, Wentao Hu, Xinhao Zhao, Zhicheng Xu: Aktivni nadzor vibracij pri mehanski visokohitrostni servostiskalnici za natančno štancanje SI 57
Xuan Bo Tran: Nelinearno vodenje pnevmatskega aktuatorja na osnovi dinamičnega modela trenja SI 58

Strojniški vestnik - Journal of Mechanical Engineering 67(2021)9, SI 53
© 2021 Strojniški vestnik. Vse pravice pridržane.
Prejeto v recenzijo: 2021-05-28
Prejeto popravljeno: 2021-08-17
Odobreno za objavo: 2021-08-18

Upravljanje antropomorfnega manipulatorja z modelom trenja LuGre – zasnova in eksperimentalna validacija

Khurram Ali[1] – Adeel Mehmood[1] – Israr Muhammad[1] – Sohail Razzaq[1] – Jamshed Iqbal[2,*]

[1]Univerza COMSATS v Islamabadu, Oddelek za elektrotehniko in računalništvo, Pakistan
[2]Univerza v Hullu, Znanstveno-tehniška fakulteta, Oddelek za računalništvo in tehnologijo, Združeno kraljestvo

Zasluga za nedavni napredek fleksibilne avtomatizacije gre predvsem robotskim rokam in manipulatorjem. Avtonomija teh manipulatorjev je povezana z napredkom na področju nelinearnih regulacijskih sistemov. Cilj pričujoče raziskave je oblikovanje predloga za robusten regulacijski algoritem robotske roke s petimi prostostnimi stopnjami, ki bo zagotavljal vrhunsko zmogljivost in zanesljivost v prisotnosti trenja. Predstavljena sta predlog in izvedba nelinearne regulacije robotskega manipulatorja na osnovi kompenzacije trenja.

Za zasnovo integralnega regulatorja drsnega režima za antropomorfni manipulator je bil uporabljen prilagojeni model LuGre s kompenzacijo trenja, ki zagotavlja sledenje želeni trajektoriji v prisotnosti trenja. Najprej je bil po modelu trenja LuGre izpeljan matematični model avtonomne zglobne robotske izobraževalne platforme (AUTAREP) ED-7220C s petimi prostostnimi stopnjami. Nato je bil zasnovan robustni regulator za kompenzacijo dinamičnih tornih pojavov, ki upravlja položaj in hitrost za doseganje želene trajektorije.

Kompenzacija negotovosti parametrov in obremenitvenih momentov sistema je izvedena z integralnim zakonom SMC na osnovi funkcije po Lyapunovu.

Izkazalo se je, da so parametri prehodnih pojavov (čas maksimalnega prevzpona, odstotek prenihaja, čas ustalitve itd.) znotraj predvidenih mej. Regulator s kompenzacijo trenja ima boljši čas ustalitve in zmogljivost kot zakon na osnovi SMC brez kompenzacije trenja. Predlagani regulacijski zakon je bil preizkušen tudi na namenskem preizkuševališču s programsko opremo LabVIEW in strojno opremo NI-myRIO.

Večina modelov robotskih sistemov v literaturi obravnava trenje s teoretičnega in konceptualnega vidika kot motnjo in ne kot stanje. V pričujočem članku je podan predlog matematičnega modela, ki kombinira dinamični model robota z dvema stanjema in dinamični model trenja z enim stanjem. Predstavljene so zasnova, simulacija in hardverska izvedba robustnega regulacijskega zakona, ki upošteva trenje. Robotski manipulator po meri s petimi prostostnimi stopnjami je bil tudi fizično izveden.

V prihodnjih raziskavah bo mogoče razviti dinamični model robotskega manipulatorja AUTAREP z različnimi modeli trenja. Trenje je dinamično in njegovo stanje ni merljivo, zato bo mogoče zasnovati opazovalca za ocenjevanje njegove vrednosti.

Ključne besede: regulacija drsnega režima, prostostna stopnja, model trenja LuGre, avtonomna zglobna robotska izobraževalna platforma (AUTAREP)

*Naslov avtorja za dopisovanje: Univerza v Hullu, Znanstveno-tehniška fakulteta, Oddelek za računalništvo in tehnologijo, HU6 7RX, Združeno kraljestvo, j.iqbal@hull.ac.uk

Strojniški vestnik - Journal of Mechanical Engineering 67(2021)9, SI 54
© 2021 Strojniški vestnik. Vse pravice pridržane.
Prejeto v recenzijo: 2021-04-19
Prejeto popravljeno: 2021-07-13
Odobreno za objavo: 2021-08-20

Napovedovanje količnika trenja pri hidrodinamičnem radialnem drsnem ležaju z uporabo umetnih nevronskih mrež

Dragan Milčić[1,*] – Amir Alsammarraie[2] – Miloš Madić[1] – Vladislav Krstić[3] – Miodrag Milčić[1]

[1] Fakulteta za strojništvo, Univerza v Nišu, Srbija
[2] Univerza v Tikritu, Tehniška fakulteta, Irak
[3] Ljubex International, Srbija

Hidrodinamični ležaji nosijo vrtečo se gred in vse pripadajoče obremenitve s pomočjo tlačnega polja v mazivu, ki fizično ločuje trdne površine. Radialni drsni ležaji, izdelani iz zlitine kositer-babbitt (Tegotenax V840), se pogosto uporabljajo v pogojih hidrodinamičnega mazanja pri kompresorjih, turbinah, črpalkah, elektromotorjih, električnih generatorjih, mlinih za rudo itd. Drsno trenje na kontaktnih površinah med tečajem in pušo je kompleksen disipativen proces, ki ga spremlja vrsta mehanskih, fizikalno-kemičnih, električnih, metalurških in toplotnih pojavov, za katere je značilno obrabljanje udeleženih teles.

Na količnik trenja pomembno vplivajo normalne obremenitve, geometrija, relativno gibanje površin, drsna hitrost, površinska hrapavost tornih površin, vrsta materiala, togost sistema, temperatura, pojav stik-slip, relativna vlažnost, mazanje in vibracije. Članek preučuje vplive frekvence vrtenja tečaja v puši in radialne obremenitve radialnega drsnega ležaja, izdelanega iz zlitine kositer-babbitt (Tegotenax V840) v pogojih hidrodinamičnega mazanja. Na preizkuševališču za rotacijske elemente (radialne in drsne ležaje) je bil opravljen eksperimentalni preskus tornih lastnosti radialnega drsnega ležaja.

Za določitev matematične odvisnosti med eksperimentalnimi parametri preskusa radialnega drsnega ležaja v pogojih hidrodinamičnega trenja sta bila razvita dva modela z umetnimi nevronskimi mrežami (ANN). Prvi model je namenjen napovedovanju količnika trenja, drugi pa temperaturi ležaja. Za učenje in testiranje mrež so bili uporabljeni rezultati meritev količnika trenja μ in temperature ležaja T, ki so trajale 18.000 sekund, in sicer v funkciji sprememb radialne obremenitve FN in vrtilne hitrosti gredi n.

Množica razpoložljivih vhodnih/izhodnih podatkov je bila pri razvoju modela ANN naključno razdeljena v dve množici: prvo za učenje in drugo za testiranje modela ANN. 295 podatkov je bilo uporabljenih za učenje ANN, 43 pa za testiranje naučenega modela mreže ANN.

Za učenje ANN je bil izbran algoritem Levenberg-Marquardt, ki se odlikuje z visoko točnostjo in hitro konvergenco. Proces učenja ANN je bil ponovljen večkrat za razrešitev problema (počasne) konvergence z različnimi začetnimi utežmi, določenimi po metodi Nguyen-Widrow. Med procesom učenja ANN je bilo ugotovljeno, da kljub izbrani vrednosti največjega števila iteracij 1000 zadostuje že bistveno manjše število iteracij.

Z uporabo nevronske mreže z vzvratnim postopkom učenja na osnovi eksperimentalnih podatkov so bili razviti modeli ANN za napovedovanje odvisnosti količnika trenja in temperature ležajev od radialne obremenitve in vrtilne hitrosti. Na podlagi eksperimentalno določenih vrednosti količnika trenja, s katerimi je bilo opravljeno učenje ANN, so bile pridobljene dobro naučene mreže s srednjo absolutno odstotno napako 0,0054 % pri učenju in 0,0085 % pri testiranju. Po optimizaciji modela ANN je bil ugotovljen najvišji količnik trenja 0,1513 pri obremenitvi ležaja 1072 N in vrtilni hitrosti 3000 vrt/min, medtem ko je bil najnižji količnik trenja 0,00288 ugotovljen pri maksimalni obremenitvi 4000 N in vrtilni hitrosti 1675,22 vrt/min.

Model za napovedovanje temperature ležajev nakazuje naraščajoči trend spremembe s podaljševanjem časa drsnega trenja in vrtilne hitrosti. Temperatura ležaja T se povečuje s časom t in se po nekaj manj kot 1 uri (približno 4000 s) stabilizira pri približno 50 °C pri vseh vrednostih obremenitve in vrtilne hitrosti ležaja.

Ključne besede: umetna nevronska mreža, hidrodinamični radialni drsni ležaj, zlitina babbitt-kositer, količnik trenja

*Naslov avtorja za dopisovanje: Fakulteta za strojništvo, Univerza v Nišu, Aleksandra Medvedeva 14, Niš, Srbija, dragan.milcic@masfak.ni.ac.rs

Strojniški vestnik - Journal of Mechanical Engineering 67(2021)9, SI 55
© 2021 Strojniški vestnik. Vse pravice pridržane.
Prejeto v recenzijo: 2021-03-21
Prejeto popravljeno:2021-06-24
Odobreno za objavo: 2021-09-17

Večparametrična dinamična analiza sistema kotalnih ležajev

Almatbek Kydyrbekuly[1] – Gulama-Garip Alisher Ibrayev [1] – Tangat Ospan[1] – Anatolij Nikonov[2,*]

[1] Al-Farabi Kazahstanska narodna univerza, Kazahstan
[2] Fakulteta za industrijski inženiring Novo mesto, Slovenia

Pri načrtovanju rotacijskih strojev je ena najpomembnejših mehanskih komponent, ki jih opisujejo nelinearni modeli, elastična podpora, ki zagotavlja delovanje in zanesljivost sistema. Pri analizi linearnih rotorskih sistemov z valjčnimi ležaji se najpogosteje uporablja približna ocena togostnih in dušilnih lastnosti ležajev, medtem ko je v resnici togost ležaja močno odvisna od obremenitve, to je od načina delovanja rotorskega sistema, od geometrije in velikosti zračnosti ležajev, velikosti prileganja notranjega in zunanjega obroča v ležaju ter drugih dejavnikov.

Za podroben opis dinamičnega procesa sistema kotalnih ležajev je potrebno upoštevati vpliv dejavnikov, kot so neuravnoteženost, asimetrija rotorja na gredi, zunanje trenje, spremembe vztrajnostnih parametrov in položajne sile različnih vrst. V prispevku smo preučevali vpliv velikosti reže, vrtilne frekvence na frekvenčne spektre in amplitudno-frekvenčne značilnosti poljubnega rotorskega sistema na kotalne ležaje. Matematični modeli ležajev, ki upoštevajo faktorje nelinearnosti, se odlikujejo po kompleksnosti, predvsem pa po obremenitvah, ki jih upoštevajo.

Razvita je metoda za izračun amplitud in konstrukcijo frekvenčnih karakteristik vsiljenih in samovzbujenih vibracij sistema »rotor-tekočina-temelj« na kotalnih ležajih z nelinearno karakteristiko, ki temelji na metodi kompleksnih amplitud in harmonskega ravnovesja. Izpeljane so nelinearne enačbe gibanja sistema »rotor-tekočina-temelj«, za katere so predstavljene analitične metode reševanja. Določene so frekvence osnovne in ultra harmonične resonance. Ocenjeni so intervali med frekvencami samovzbujenih nihanj. V prispevku je prikazana odvisnost amplitud od količine tekočine v votlini rotorja, mase temeljev, linearne neuravnoteženosti, vrednosti koeficienta togosti in koeficienta dušenja. Proučene so tudi posebnosti nelinearnega dinamičnega obnašanja, za katere so značilne ultra harmonične vibracije. Za optimalne vrednosti amplitud so bili v celoti določeni optimalni parametri linearne neuravnoteženosti, mase temeljev, prostornine tekočine v votlini rotorja, togosti in koeficienta dušenja.

Ugotovljeno je bilo, da v prisotnosti zanemarljivo majhne količine tekočine v votlini opazimo tri cone samovzbujenih nihanj in tri resonančne amplitude za rotor in za temelj. Največje amplitude vsiljenih nihanj rotorja in temelja opazimo, ko je tretjina votline rotorja napolnjena s tekočino. Poleg tega je bilo ugotovljeno, da zmanjšanje prostornine tekočine vodi do premika tretje resonance proti nižjim krožnim frekvencam. Prav tako se ob znatnem zmanjšanju koeficienta dušenja pojavi premik tretje resonance proti višjim kotnim hitrostim. Zlasti pri rotorju, napolnjenem s tekočino do tretjine prostornine, omenjeno resonanco opazimo pri isti frekvenci kot pri praznem rotorju, kar je značilnost nelinearnih vibracij.

Dinamična analiza je pokazala, da z naraščanjem vrednosti neuravnoteženosti za red velikosti amplitudno frekvenčno karakteristiko rotorja in temelja določa nelinearnost progresivnega tipa. Tako s povečanjem linearne neuravnoteženosti samovzbujena nihanja, ki izvirajo iz delovanja tekočine, zamrejo zaradi vsiljenih vibracij. V tem primeru se značilna razčlenitev amplitud premakne proti višjim frekvencam sistema. Nadalje se po razčlenitvi zaradi učinka samocentriranja delovanje sistema stabilizira, pri čemer se pojavijo vibracije z amplitudo, ki nekoliko presega amplitudo samovzbujenih nihanj.

Ključne besede: vsiljena nihanja, resonanca, tekočina, kotalni ležaj, samovzbujena nihanja, ultra harmonično nihanje

*Naslov avtorja za dopisovanje: Fakulteta za industrijski inženiring Novo mesto, Šegova ulica 112, 8000 Novo mesto, Slovenija, anatolij.nikonov@fini-unm.si

Strojniški vestnik - Journal of Mechanical Engineering 67(2021)9, SI 56
© 2021 Strojniški vestnik. Vse pravice pridržane.
Prejeto v recenzijo: 2021-04-08
Prejeto popravljeno: 2021-08-21
Odobreno za objavo: 2021-08-24

Sledilno vodenje za manipulatorje na osnovi mehke ekvivalence in terminalnega drsnega režima

Youyu Liu[1,2,*] – Yi Li[1,2] – Xuyou Zhang[1,2] – Bo Chen[1,2]

[1] Državni laboratorij za napredno senzoriko in pametno upravljanje visokotehnološke opreme, Ministrstvo za izobraževanje, Kitajska
[2] Politehnika Anhui, Šola za strojništvo, Kitajska

Za zmanjšanje poskakovanja v pogojih težkih obremenitev in zagotavljanje primerne točnosti vodenja zgibov, hitrosti konvergence napak in robustnosti je bil podan predlog metode za vodenje manipulatorjev na osnovi mehke ekvivalence in terminalnega drsnega režima (FETSM).

Sistemi za regulacijo drsnega režima so obremenjeni s pojavom poskakovanja. Danes obstaja več metod za odpravo poskakovanja, ki pa imajo vse svoje pomanjkljivosti. Metoda, ki uporablja zakon približevanja s funkcijo FAL (ali SAL), ima tako npr. slabost, da je težko izbrati položaj za uvajanje pojemka. Druga metoda, ki uporablja mehka pravila za ravnanje z eksponentom v potenčnih zakonih približevanja in, ki funkcijo predznaka zamenja s funkcijo hiperboličnega tangensa, ne more zmanjšati amplitude poskakovanja. Tretja metoda z adaptivno kompenzacijo napak (ali z nevronsko mrežo BP) je povezana z občutnim povečanjem računske kompleksnosti.

Na osnovi člena za preklapljanje ESM je bila uvedena matrika z mehkimi parametri, ki se obdeluje s preprostimi mehkimi pravili, in določen je bil mehki člen za preklapljanje. S seštevanjem mehkega člena za preklapljanje ter ekvivalentnega člena ekvivalence in terminalnega drsnega režima (ETSM) je bil določen regulacijski zakon FETSM za manipulatorje. Na tej osnovi je bila analizirana stabilnost sistema s funkcijo po Lyapunovu in izpeljan je bil njen končni čas prihoda. Na podlagi domneve zagotavljanja stabilnosti sistema so bila oblikovana mehka pravila in članske funkcije za mehke konstante. Uporabnost in učinkovitost predlagane metode sta bili preverjeni s primerjavo sledenja trajektoriji in vhodnega momenta za več obstoječih metod.

Rezultati in ugotovitve:

(1) Predlagano metodo regulacije FETSM je mogoče uporabiti za sledenje dejanskemu položaju vsakega zgiba glede na njegovo idealno trajektorijo. Ta tehnologija je praktično uporabna pri manipulatorjih, ki so med obratovanjem izpostavljeni velikim obremenitvam.

(2) Rezultati simulacij kažejo, da je celotna natančnost sledenja po predlagani metodi FETSM za 3,56 % boljša v primerjavi z ETSM, celotna robustnost pa se je izboljšala za 30,24 %. Hitrost konvergence napake je praktično enaka. Celotna natančnost sledenja se je s predlagano metodo FETSM izboljšala za 89,30 %, celotna robustnost se je izboljšala za 96,83 %, hitrost konvergence napak pa za 83,13 % v primerjavi z ESM. Celotna natančnost sledenja s predlagano metodo FETSM se je v primerjavi s PID-regulacijo izboljšala za 92,78 %. Hitrost konvergence napak in celotna robustnost sta boljši kot pri PID-regulaciji. Predlagana metoda FETSM lahko zagotavlja zadostno natančnost sledenja trajektoriji, hitrost konvergence napak in robustnost.

(3) Pri predlagani metodi FETSM prihaja do poskakovanja le pod pogojem, da sistem ne doseže površine drsnega režima. Metoda FETSM lahko v primerjavi z ETSM v povprečju skrajša čas poskakovanja za 94,75 %. V primerjavi z regulacijo PID se maksimalna amplituda poskakovanja pri metodi FETSM zmanjša za vsaj 99,21 %. Predlagana metoda FETSM lahko torej omeji poskakovanje sistema in optimizira regulacijo vhodnega momenta.

Praktični učinek predlagane metode pri manipulatorjih, ki obratujejo v pogojih težkih obremenitev, ni bil preverjen in to bo predmet nadaljnjih raziskav.

Določen je zakon regulacijskega sistema FETSM za manipulatorje. Preverjena sta stabilnost in končni čas prihoda sistema FETSM. Z mehkimi pravili so ocenjene zunanje motnje in negotovosti sistema. Predlagana metoda regulacije omogoča omejitev poskakovanja sistema v drsnem režimu. Sistem FETSM je primeren za manipulatorje, ki obratujejo v pogojih težkih obremenitev.

Ključne besede: regulacija drsnega režima, mehki člen za preklapljanje, poskakovanje, manipulator, sledenje trajektoriji, hitrost konvergence napake, robustnost

*Naslov avtorja za dopisovanje: Politehnika Anhui, Šola za strojništvo, Wuhu 241000, Kitajska, liuyyu@ahpu.edu.cn

Strojniški vestnik - Journal of Mechanical Engineering 67(2021)9, SI 57
© 2021 Strojniški vestnik. Vse pravice pridržane.
Prejeto v recenzijo: 2020-10-01
Prejeto popravljeno: 2021-01-04
Odobreno za objavo: 2021-01-07

Aktivni nadzor vibracij pri mehanski visokohitrostni servostiskalnici za natančno štancanje

Yanxiong Liu[1,3] – Yuwen Shu[1,3] – Wentao Hu[1,3] – Xinhao Zhao[1,2,*] – Zhicheng Xu[1,3]

[1]Tehniška univerza v Wuhanu, Državni laboratorij province Hubei
za napredno tehnologijo avtomobilskih komponent, Kitajska
[2]Tehniška univerza v Wuhanu, Šola za materiale in inženiring, Kitajska
[3]Tehniška univerza v Wuhanu, Sodelovalno inovacijsko središče province Hubei
za tehnologijo avtomobilskih komponent, Kitajska

Proces natančnega štancanja je napreden preoblikovalni proces, ki daje izdelku končno ali skoraj dokončno obliko, v industriji pa se je uveljavil zaradi visoke učinkovitosti in kakovosti izdelkov. Z višanjem frekvence delovnih gibov so vse močnejše tudi vibracije stiskalnic za natančno štancanje. Znano je, da vibracije stiskalnice ne vplivajo le na kakovost izdelkov s povzročanjem razpok na površini reza in zmanjševanjem dimenzijske točnosti – skrajšujejo tudi življenjsko dobo strojev. Hrup, ki ga povzročajo vibracije stroja, poleg tega otežuje delovne pogoje in vpliva na zdravje ljudi. Nadzor nad vibracijami mehanskih stiskalnic za natančno štancanje ni ustrezno raziskan, zato obstaja nujna potreba po rešitvah za nadzor nad vibracijami teh visokohitrostnih stiskalnic.

V članku sta opisani pasivna in aktivna metoda za nadzor nad vibracijami visokohitrostne stiskalnice za natančno štancanje, ki omejujeta vibracije celega stroja zaradi elastičnih sil med procesom natančnega štancanja.

V članku je predstavljeno samoadaptivno krmiljenje z upoštevanjem motnje za simulacijo aktivnega nadzora nad vibracijami mehanske stiskalnice za natančno štancanje. Opisano je načelo nadzora nad vibracijami in določen je krmilni algoritem. Vzpostavljen je tudi mehanski model vibracij stroja za natančno štancanje kot objekta regulacije. Parametri vzbujanja in mehanski model so bili določeni s simulacijo po metodi končnih elementov in z eksperimentalnimi meritvami vibracij stiskalnice. Končno je opravljena še numerična simulacija in analiza aktivnega nadzora vibracij v okolju MATLAB.

Vibracije celotnega stroja so se učinkovito zmanjšale z uporabo aktivnega nadzora – v časovni domeni za več kot 95 % in v frekvenčni domeni za več kot 80 %. Učinkovitost pri zmanjševanju vibracij je torej očitna, posledično pa se izboljša točnost obdelave, prihrani veliko energije in zmanjša škart.

Predlagana metoda bi bila primerna tudi za nadzor nad vibracijami pri gradbenih strojih in pri opremi za končno obdelavo. V prihodnjih raziskavah bo mogoče uporabiti naprednejše metode regulacije za še boljši učinek regulacije.

Tokrat je bil prvič vzpostavljen mehanski model vibracij stroja za natančno štancanje. Parametri dinamičnega modela mehanskega stroja za natančno štancanje so bili pridobljeni z analizo po metodi končnih elementov in z empirično formulo. Razvit je bil adaptivni regulator vibracij z upoštevanjem motnje, ki je bil uporabljen za aktivni nadzor nad vibracijami stroja za natančno štancanje. S tem so bile učinkovito zmanjšane vibracije stiskalnice in posledično se lahko izboljša točnost obdelave, prihrani veliko energije in zmanjša škart.

Ključne besede: aktivni nadzor vibracij, mehanski model vibracij, visokohitrostna mehanska servostiskalnica za natančno štancanje, samoadaptivno krmiljenje z upoštevanjem motnje

*Naslov avtorja za dopisovanje: Tehniška univerza v Wuhanu, Wuhan, Kitajska, zhaoxh@whut.edu.cn

Strojniški vestnik - Journal of Mechanical Engineering 67(2021)9, SI 58
© 2021 Strojniški vestnik. Vse pravice pridržane.
Prejeto v recenzijo: 2021-04-26
Prejeto popravljeno: 2021-08-04
Odobreno za objavo: 2021-09-01

Nelinearno vodenje pnevmatskega aktuatorja na osnovi dinamičnega modela trenja

Xuan Bo Tran

Znanstveno-tehniška univerza v Hanoju, Šola za transport, Oddelek za fluidno tehniko in avtomatizacijo, Vietnam

Pnevmatski sistemi se množično uporabljajo v industriji zaradi mnogih prednosti, kot so nizka cena, visoka moč na enoto mase, čistoča, preprosto vzdrževanje in zamenjava delov ter poceni in razpoložljiva oskrba z zrakom. Prednost imajo tudi v vročih in/ali vlažnih okoljih, kjer električni sistemi niso primerni. Zanje pa sta značilni tudi kompleksna dinamika in visoka nelinearnost zaradi vplivov stisljivosti zraka, nelinearnosti pnevmatskih ventilov in trenja v pnevmatskem aktuatorju. Točno vodenje položaja, hitrosti in sil pnevmatskega aktuatorja zato ni preprosta naloga.

V pričujočem članku je predstavljen predlog novega regulatorja za vodenje položaja pnevmatskega valja. Zasnovan je po metodi drsne regulacije z več površinami v kombinaciji s kompenzatorjem trenja. Metoda drsne regulacije z več površinami obvladuje nelinearne lastnosti pnevmatskega sistema, kot sta stisljivost zraka in nelinearnost pnevmatskega ventila. Kompenzator trenja omogoča kompenzacijo sile trenja v pnevmatskem valju. Ta je ocenjena na podlagi dinamičnega modela trenja LuGre.

V predstavljeni študiji je bil obravnavan elektropnevmatski servosistem z dvosmernim pnevmatskim valjem in dvema pnevmatskima proporcionalnima ventiloma za regulacijo pretoka. Najprej je bil postavljen splošni matematični model sistema, nato pa je bil oblikovan regulacijski zakon novega regulatorja in analizirana absolutna stabilnost sistema. Novi regulator je bil ovrednoten s simulacijami v programski opremi MATLAB/Simulink. Novi regulator in drsni regulator z več površinami sta bila simulirana z enakimi položajnimi vhodi, in sicer s koračnim in sinusoidnim položajnim vhodom z različnimi amplitudami in frekvencami. Zmogljivost novega regulatorja je bila primerjana z zmogljivostjo drsnega regulatorja z več površinami. Novi regulator je bil končno preverjen še eksperimentalno. Za to je bil postavljen eksperimentalni sistem in novi regulator je bil preverjen v enakih pogojih kot pri simulaciji. Eksperimentalno določena zmogljivost novega regulatorja je bila primerjana z zmogljivostjo drsnega regulatorja z več površinami in drugih nelinearnih regulatorjev.

Rezultati študije so: i) največja napaka relativnega položaja se z novim regulatorjem zmanjša za 10 %, koren srednje kvadratne napake pa se zmanjša za 6,5 % v primerjavi z drsnim regulatorjem z več površinami brez kompenzacije trenja; ii) novi regulator dosega pri koračnem položajnem vhodu minimalno največjo napako 1 mm v stacionarnih pogojih; iii) novi regulator dosega pri sinusoidnem položajnem vhodu minimalno največjo napako 2,2 mm v stacionarnih pogojih; iv) novi regulator ima v primerjavi z ostalimi nelinearnimi in naprednimi regulatorji manjšo napako regulacije. Parametri modela trenja LuGre, uporabljeni v opazovalcu trenja, so bili določeni vnaprej.

V prihodnje bo vključena še metodologija za sprotno ocenjevanje parametrov modela trenja LuGre pri novem regulatorju.

Prispevek študije je v predlogu nove metode za regulacijo položaja v kombinaciji s kompenzacijo trenja na osnovi modela trenja, ki lahko izboljša kakovost regulacije položaja pnevmatskih valjev. Rezultate te študije bo mogoče uporabiti za izboljšanje kakovosti regulacije avtomatskih pnevmatskih strojev in sistemov v industriji.

Ključne besede: pnevmatski valj, nelinearno vodenje, kompenzacija trenja, dinamični model trenja

*Naslov avtorja za dopisovanje: Znanstveno-tehniška univerza v Hanoju, No. 1, Dai co Viet str., Hai Ba Trung dist., Hanoi city, Vietnam, bo.tranxuan@hust.edu.vn

Guide for Authors

All manuscripts must be in English. Pages should be numbered sequentially. The manuscript should be composed in accordance with the Article Template given above. The maximum length of contributions is 12 pages (approx. 5000 words). Longer contributions will only be accepted if authors provide justification in a cover letter. For full instructions see the Information for Authors section on the journal's website: http://en.sv-jme.eu .

SUBMISSION:

Submission to SV-JME is made with the implicit understanding that neither the manuscript nor the essence of its content has been published previously either in whole or in part and that it is not being considered for publication elsewhere. All the listed authors should have agreed on the content and the corresponding (submitting) author is responsible for having ensured that this agreement has been reached. The acceptance of an article is based entirely on its scientific merit, as judged by peer review. Scientific articles comprising simulations only will not be accepted for publication; simulations must be accompanied by experimental results carried out to confirm or deny the accuracy of the simulation. Every manuscript submitted to the SV-JME undergoes a peer-review process.

The authors are kindly invited to submit the paper through our web site: http://ojs.sv-jme.eu. The Author is able to track the submission through the editorial process - as well as participate in the copyediting and proofreading of submissions accepted for publication - by logging in, and using the username and password provided.

SUBMISSION CONTENT:

The typical submission material consists of:

- A **manuscript** (A PDF file, with title, all authors with affiliations, abstract, keywords, highlights, inserted figures and tables and references),
- Supplementary files:
  - a **manuscript** in a WORD file format
  - a **cover letter** (please see instructions for composing the cover letter)
  - a ZIP file containing **figures** in high resolution in one of the graphical formats (please see instructions for preparing the figure files)
  - possible **appendicies** (optional), cover materials, video materials, etc.

Incomplete or improperly prepared submissions will be rejected with explanatory comments provided. In this case we will kindly ask the authors to carefully read the Information for Authors and to resubmit their manuscripts taking into consideration our comments.

COVER LETTER INSTRUCTIONS:

Please add a **cover letter** stating the following information about the submitted paper:

1. Paper **title**, list of **authors** and their **affiliations**. **One** corresponding author should be provided.
2. **Type of paper**: original scientific paper (1.01), review scientific paper (1.02) or short scientific paper (1.03).
3. A **declaration** that neither the manuscript nor the essence of its content has been published in whole or in part previously and that it is not being considered for publication elsewhere.
4. State the **value of the paper** or its practical, theoretical and scientific implications. What is new in the paper with respect to the state-of-the-art in the published papers? Do not repeat the content of your abstract for this purpose.
5. We kindly ask you to suggest at least two **reviewers** for your paper and give us their names, their full affiliation and contact information, and their scientific research interest. The suggested reviewers should have at least two relevant references (with an impact factor) to the scientific field concerned; they should not be from the same country as the authors and should have no close connection with the authors.

FORMAT OF THE MANUSCRIPT:

The manuscript should be composed in accordance with the Article Template. The manuscript should be written in the following format:

- A **Title** that adequately describes the content of the manuscript.
- A list of **Authors** and their **affiliations**.
- An **Abstract** that should not exceed 250 words. The Abstract should state the principal objectives and the scope of the investigation, as well as the methodology employed. It should summarize the results and state the principal conclusions.
- 4 to 6 significant **key words** should follow the abstract to aid indexing.
- 4 to 6 **highlights;** a short collection of bullet points that convey the core findings and provide readers with a quick textual overview of the article. These four to six bullet points should describe the essence of the research (e.g. results or conclusions) and highlight what is distinctive about it.
- An **Introduction** that should provide a review of recent literature and sufficient background information to allow the results of the article to be understood and evaluated.
- A **Methods** section detailing the theoretical or experimental methods used.
- An **Experimental section** that should provide details of the experimental set-up and the methods used to obtain the results.
- A **Results** section that should clearly and concisely present the data, using figures and tables where appropriate.
- A **Discussion** section that should describe the relationships and generalizations shown by the results and discuss the significance of the results, making comparisons with previously published work. (It may be appropriate to combine the Results and Discussion sections into a single section to improve clarity.)
- A **Conclusions** section that should present one or more conclusions drawn from the results and subsequent discussion and should not duplicate the Abstract.
- **Acknowledgement** (optional) of collaboration or preparation assistance may be included. Please note the source of funding for the research.
- **Nomenclature** (optional). Papers with many symbols should have a nomenclature that defines all symbols with units, inserted above the references. If one is used, it must contain all the symbols used in the manuscript and the definitions should not be repeated in the text. In all cases, identify the symbols used if they are not widely recognized in the profession. Define acronyms in the text, not in the nomenclature.
- **References** must be cited consecutively in the text using square brackets [1] and collected together in a reference list at the end of the manuscript.
- **Appendix(-icies)** if any.

SPECIAL NOTES

Units: The SI system of units for nomenclature, symbols and abbreviations should be followed closely. Symbols for physical quantities in the text should be written in italics (e.g. *v*, *T*, *n*, etc.). Symbols for units that consist of letters should be in plain text (e.g. ms^{-1}, K, min, mm, etc.). Please also see: http://physics.nist.gov/cuu/pdf/sp811.pdf .

Abbreviations should be spelt out in full on first appearance followed by the abbreviation in parentheses, e.g. variable time geometry (VTG). The meaning of symbols and units belonging to symbols should be explained in each case or cited in a **nomenclature** section at the end of the manuscript before the References.

Figures (figures, graphs, illustrations digital images, photographs) must be cited in consecutive numerical order in the text and referred to in both the text and the captions as Fig. 1, Fig. 2, etc. Figures should be prepared without borders and on white grounding and should be sent separately in their original formats. If a figure is composed of several parts, please mark each part with a), b), c), etc. and provide an explanation for each part in Figure caption. The caption should be self-explanatory. Letters and numbers should be readable (Arial or Times New Roman, min 6 pt with equal sizes and fonts in all figures). Graphics (submitted as supplementary files) may be exported in resolution good enough for printing (min. 300 dpi) in any common format, e.g. TIFF, BMP or JPG, PDF and should be named Fig1.jpg, Fig2.tif, etc. However, graphs and line drawings should be prepared as vector images, e.g. CDR, AI. Multi-curve graphs should have individual curves marked with a symbol or otherwise provide distinguishing differences using, for example, different thicknesses or dashing.

Tables should carry separate titles and must be numbered in consecutive numerical order in the text and referred to in both the text and the captions as Table 1, Table 2, etc. In addition to the physical quantities, such as *t* (in italics), the units [s] (normal text) should be added in square brackets. Tables should not duplicate data found elsewhere in the manuscript. Tables should be prepared using a table editor and not inserted as a graphic.

REFERENCES:

A reference list must be included using the following information as a guide. Only cited text references are to be included. Each reference is to be referred to in the text by a number enclosed in a square bracket (i.e. [3] or [2] to [4] for more references; do not combine more than 3 references, explain each). No reference to the author is necessary.

References must be numbered and ordered according to where they are first mentioned in the paper, not alphabetically. All references must be complete and accurate. Please add DOI code when available. Examples follow.

Journal Papers:

Surname 1, Initials, Surname 2, Initials (year). Title. Journal, volume, number, pages, DOI code.

[1] Hackenschmidt, R., Alber-Laukant, B., Rieg, F. (2010). Simulating nonlinear materials under centrifugal forces by using intelligent cross-linked simulations. *Strojniški vestnik - Journal of Mechanical Engineering,* vol. 57, no. 7-8, p. 531-538, DOI:10.5545/sv-jme.2011.013.

Journal titles should not be abbreviated. Note that journal title is set in italics.

Books:

Surname 1, Initials, Surname 2, Initials (year). Title. Publisher, place of publication.

[2] Groover, M.P. (2007). *Fundamentals of Modern Manufacturing*. John Wiley & Sons, Hoboken.

Note that the title of the book is italicized.

Chapters in Books:

Surname 1, Initials, Surname 2, Initials (year). Chapter title. Editor(s) of book, book title. Publisher, place of publication, pages.

[3] Carbone, G., Ceccarelli, M. (2005). Legged robotic systems. Kordić, V., Lazinica, A., Merdan, M. (Eds.), Cutting Edge Robotics. Pro literatur Verlag, Mammendorf, p. 553-576.

Proceedings Papers:

Surname 1, Initials, Surname 2, Initials (year). Paper title. Proceedings title, pages.

[4] Štefanić, N., Martinčević-Mikić, S., Tošanović, N. (2009). Applied lean system in process industry. *MOTSP Conference Proceedings*, p. 422-427.

Standards:

Standard-Code (year). Title. Organisation. Place.

[5] ISO/DIS 16000-6.2:2002. *Indoor Air – Part 6: Determination of Volatile Organic Compounds in Indoor and Chamber Air by Active Sampling on TENAX TA Sorbent, Thermal Desorption and Gas Chromatography using MSD/FID.* International Organization for Standardization. Geneva.

WWW pages:

Surname, Initials or Company name. Title, from http://address, date of access.

[6] Rockwell Automation. Arena, from *http://www.arenasimulation.com,* accessed on 2009-09-07.

EXTENDED ABSTRACT:

When the paper is accepted for publishing, the authors will be requested to send an **extended abstract** (approx. one A4 page or 3500 to 4000 characters or approx. 600 words). The instruction for composing the extended abstract are published on-line: http://www.sv-jme.eu/information-for-authors/ .

COPYRIGHT:

Authors submitting a manuscript do so on the understanding that the work has not been published before, is not being considered for publication elsewhere and has been read and approved by all authors. The submission of the manuscript by the authors means that the authors automatically agree to transfer copyright to SV-JME when the manuscript is accepted for publication. All accepted manuscripts must be accompanied by a Copyright Transfer Agreement, which should be sent to the editor. The work should be original work by the authors and not be published elsewhere in any language without the written consent of the publisher. The proof will be sent to the author showing the final layout of the article. Proof correction must be minimal and executed quickly. Thus it is essential that manuscripts are accurate when submitted. Authors can track the status of their accepted articles on http://en.sv-jme.eu/.

PUBLICATION FEE:

Authors will be asked to pay a publication fee for each article prior to the article appearing in the journal. However, this fee only needs to be paid after the article has been accepted for publishing. The fee is 380 EUR (for articles with maximum of 6 pages), 470 EUR (for articles with maximum of 10 pages), plus 50 EUR for each additional page. The additional cost for a color page is 90.00 EUR (only for a journal hard copy; optional upon author's request). These fees do not include tax.

Strojniški vestnik -Journal of Mechanical Engineering
Aškerčeva 6, 1000 Ljubljana, Slovenia, e-mail: info@sv-jme.eu

9 770039 248001
ISSN 0039-2480

http://www.sv-jme.eu

Contents

Papers

401 Khurram Ali, Adeel Mehmood, Israr Muhammad, Sohail Razzaq, Jamshed Iqbal: **Control of an Anthropomorphic Manipulator using LuGre Friction Model - Design and Experimental Validation**

411 Dragan Milčić, Amir Alsammarraie, Miloš Madić, Vladislav Krstić, Miodrag Milčić: **Predictions of Friction Coefficient in Hydrodynamic Journal Bearing Using Artificial Neural Networks**

421 Almatbek Kydyrbekuly, Gulama-Garip Alisher Ibrayev, Tangat Ospan, Anatolij Nikonov: **Multiparametric Dynamic Analysis of a Rolling Bearings System**

433 Youyu Liu, Yi Li, Xuyou Zhang, Bo Chen: **Trajectory-Tracking Control for Manipulators Based on Fuzzy Equivalence and a Terminal Sliding Mode**

445 Yanxiong Liu, Yuwen Shu, Wentao Hu, Xinhao Zhao, Zhicheng Xu: **Active Vibration Control of a Mechanical Servo High-speed Fine-Blanking Press**

458 Xuan Bo Tran: **Nonlinear Control of a Pneumatic Actuator Based on a Dynamic Friction Model**